

ERCOFTAC

*Bulletin*

March 2013

94

---

## European Research Community on Flow, Turbulence and Combustion

---

ERCOFTAC is a leading European association of research, education and industry groups in the technology of flow, turbulence and combustion. The main objectives of ERCOFTAC are: To promote joint efforts of European research institutes and industries with the aim of **exchanging technical and scientific information**; to promote **Pilot Centres** for collaboration, stimulation and application of

research across Europe; to stimulate, through the creation of **Special Interest Groups**, wellcoordinated European-wide research efforts on specific topics; to stimulate the creation of advanced training activities; and to be influential on funding agencies, governments, the European Commission and the European Parliament.

[www.ercoftac.org](http://www.ercoftac.org)

### Honorary Presidents

Mathieu, J.

Spalding, D.B.

### Executive Committee

#### Chairman

Tomboulides, A.  
University of Western  
Macedonia, Greece  
Tel: +30 246 105 6630  
atompoulidis@uowm.gr  
ananiast@auth.gr

#### Deputy Chairman

Von Terzi, D.

#### Deputy Chairman

Hirsch, C.

#### Treasurer

Hämäläinen, J.

#### Deputy Treasurer

Ooms, G.

#### SPC Chairman

Geurts, B.J.

#### SPC Deputy Chairman

Sagaut, P.

#### IPC Chairman

Geuzaine, P.

#### IPC Deputy Chairman

Oliemans, R.V.A.

#### Horizon 10 Chairman

Jakirlic, S.

#### Ind. Engagement Officer

Seoud, R.E.

#### Knowledge Base Editor

Rodi, W.

#### Bulletin Editor

Elsner, W.

### ERCOFTAC Seat of the Organisation

#### Director

Hirsch, C.  
Numea International  
Chaussée de la Hulpe 189  
Terhulpesteenweg  
B-1170 Brussels  
Belgium  
Tel: +32 2 643 3572  
Fax: +32 2 647 9398  
ado@ercoftac.be

#### Secretary

Jakubczak, M.  
magdalena.jakubczak@ercoftac.org

### Scientific Programme Committee

#### Chairman

Geurts, B.J.  
University of Twente  
Mathematical Sciences  
PO Box 217  
NL-7500 AE Enschede  
The Netherlands  
Tel: +31 53 489 4125  
b.j.geurts@utwente.nl

#### Deputy Chairman

Sagaut, P.

### Industrial Programme Committee

#### Chairman

Geuzaine, P.

#### Deputy Chairman

Oliemans, R.V.A.

#### Engagement Officer

Seoud, R.E.  
ERCOFTAC  
Crown House  
72 Hammersmith Road  
London W14 8TH  
United Kingdom  
Tel: +44 207 559 1430  
Fax: +44 207 559 1428  
richard.seoud-ieo@ercoftac.org

### ERCOFTAC Central Administration Development & Outreach

ERCOFTAC CADO  
Crown House  
72 Hammersmith Road  
London W14 8TH  
United Kingdom  
Tel: +44 207 559 1427  
Fax: +44 207 559 1428

#### CADO Manager and Industrial Engagement Officer

Richard Seoud  
Tel: +44 207 559 1430  
Richard.Seoud-ieo@ercoftac.org

#### Admin Manager

Magdalena Jakubczak  
Tel: +44 207 559 1429  
Fax: +44 207 559 1428  
magdalena.jakubczak@ercoftac.org

---

## TABLE OF CONTENTS

<b>Special Theme: Plasma Aerodynamics</b>	<b>3</b>
<i>K.-S. Choi</i>	
<b>PLASMAERO European Project</b>	<b>4</b>
<i>D. Caruana, C. Tropea, C. Hollenstein, J-P. Bœuf, E. Moreau, F. Rogier and M. Forte</i>	
<b>Surface Dielectric Barrier Discharge Plasma Actuators</b>	<b>5</b>
<i>E. Moreau, A. Debien, N. Bénard, T. Jukes, R. Whalley, K.-S. Choi, A. Berendt, J. Podliński and J. Mizeraczyk</i>	
<b>Nanosecond Pulsed Plasma Actuators</b>	<b>11</b>
<i>N. Benard, E. Moreau, N. Zouzou, H. Rabat, J. Pons, D. Hong, A. Leroy-Chesneau, P. Peschke and C. Hollenstein</i>	
<b>The Plasma Synthetic Jet Actuator for Separation Control</b>	<b>17</b>
<i>D. Caruana, J.P. Cambronne, P. Barricau and A. Belinger</i>	
<b>Numerical Modeling Of Plasma Actuators</b>	<b>23</b>
<i>K. Kourtzanidis, F. Rogier, G. Dufour, J.P. Bœuf and T. Unfer</i>	
<b>Coupling of CFD with advanced plasma models</b>	<b>29</b>
<i>J.C. Kok, P. Catalano, K. Kourtzanidis, F. Rogier and T. Unfer</i>	
<b>Trailing-Edge Separation Control Of A NACA 0015 Airfoil Using Dielectric-Barrier-Discharge Plasma Actuators</b>	<b>35</b>
<i>R. D. Whalley, A. Debien, J. Podliński, T. N. Jukes, K.-S. Choi, N. Bénard, E. Moreau, A. Berendt, J. Mizeraczyk</i>	
<b>Mid-Chord Separation Control Using PSJ And DBD Plasma Actuators</b>	<b>41</b>
<i>M. Forte, A. Debien, D. Caruana, N. Bénard, P. Barricau, C. Gleyzes and E. Moreau</i>	
<b>Fully Separated Flow Control Using DBD Plasma Actuators Located At The Leading Edge Of An Airfoil</b>	<b>47</b>
<i>A. Leroy, P. Audier, D. Hong, J. Podliński, A. Berendt, and J. Mizeraczyk</i>	
<b>Wing Tip Vortex Control By Plasma Actuators</b>	<b>53</b>
<i>P. Molton, A. Leroy-Chesneau, J. Pons, Y. Carpels, P. Barricau, C. Gleyze, M. Forte and D. Caruana</i>	
<b>Boundary Layer Transition Control With Steady And Unsteady DBD Plasma Actuation</b>	<b>59</b>
<i>M. Forte, A. Seraudie, O. Vermeersch, A. Kurz, S. Grundmann, C. Tropea, J. Pons and A. Leroy</i>	
<b>Attenuation Of Noise From An Airfoil Equipped With A High-Lift Device Using Plasma Actuators</b>	<b>65</b>
<i>P. Chen, X. Zhang, S. Chappell, Z. Cai and D. Angland</i>	
<b>High Voltage Pulsed DBD Effects On The Aerodynamic Performances And On The Shock Buffet</b>	<b>70</b>
<i>A. Marino, P. Peschke, F. De Gregorio, P. Leyland, P. Ott, C. Hollenstein and R. S. Donelli</i>	
<b>Unmanned Aerial Vehicle for Plasma Flow Control</b>	<b>77</b>
<i>W. Friedrichs, S. Grundmann, C. Tropea</i>	

EDITOR	Marek, M.
TECHNICAL EDITOR	Kuban, Ł.
CHAIRMAN	Elsner, W.
EDITORIAL BOARD	Armenio, V. Dick, E. Geurts, B.J.
DESIGN & LAYOUT	Borhani, N. Nichita, B.A.
COVER DESIGN	Aniszewski, W.

**SUBMISSIONS**

ERCOFTAC Bulletin  
 Institute of Thermal Machinery  
 Częstochowa University of Technology  
 Al. Armii Krajowej 21  
 42-201 Częstochowa  
 Poland  
 Tel: +48 343 250 507  
 Fax: +48 343 250 507  
 Email: [ercoftac@imc.pcz.czyst.pl](mailto:ercoftac@imc.pcz.czyst.pl)

**HOSTED, PRINTED & DISTRIBUTED BY**



**CZĘSTOCHOWA UNIVERSITY OF TECHNOLOGY**

The reader should note that the Editorial Board cannot accept responsibility for the accuracy of statements made by any contributing authors

### NEXT ERCOFTAC EVENTS

*ERCOFTAC Spring Festival  
 and Committee Meetings  
 10-11th April 2013  
 Toulon, France*



# The ERCOFTAC Best Practice Guidelines for Industrial Computational Fluid Dynamics

The Best Practice Guidelines (BPG) were commissioned by ERCOFTAC following an extensive consultation with European industry which revealed an urgent demand for such a document. The first edition was completed in January 2000 and constitutes generic advice on how to carry out quality CFD calculations. The BPG therefore address mesh design; construction of numerical boundary conditions where problem data is uncertain; mesh and model sensitivity checks; distinction between numerical and turbulence model inadequacy; preliminary information regarding the limitations of turbulence models etc. The aim is to encourage a common best practice by virtue of which separate analyses of the same problem, using the same model physics, should produce consistent results. Input and advice was sought from a wide cross-section of CFD specialists, eminent academics, end-users and, (particularly important) the leading commercial code vendors established in Europe. Thus, the final document can be considered to represent the consensus view of the European CFD community.

Inevitably, the Guidelines cannot cover every aspect of CFD in detail. They are intended to offer roughly those 20% of the most important general rules of advice that cover roughly 80% of the problems likely to be encountered. As such, they constitute essential information for the novice user and provide a basis for quality management and regulation of safety submissions which rely on CFD. Experience has also shown that they can often provide useful advice for the more experienced user. The technical content is limited to single-phase, compressible and incompressible, steady and unsteady, turbulent and laminar flow with and without heat transfer. Versions which are customised to other aspects of CFD (the remaining 20% of problems) are planned for the future.

The seven principle chapters of the document address numerical, convergence and round-off errors; turbulence modelling; application uncertainties; user errors; code errors; validation and sensitivity tests for CFD models and finally examples of the BPG applied in practice. In the first six of these, each of the different sources of error and uncertainty are examined and discussed, including references to important books, articles and reviews. Following the discussion sections, short simple bullet-point statements of advice are listed which provide clear guidance and are easily understandable without elaborate mathematics. As an illustrative example, an extract dealing with the use of turbulent wall functions is given below:

- Check that the correct form of the wall function is being used to take into account the wall roughness. An equivalent roughness height and a modified multiplier in the law of the wall must be used.
- Check the upper limit on  $y^+$ . In the case of moderate Reynolds number, where the boundary layer only extends to  $y^+$  of 300 to 500, there is no chance of accurately resolving the boundary layer if the first integration point is placed at a location with the value of  $y^+$  of 100.

- Check the lower limit of  $y^+$ . In the commonly used applications of wall functions, the meshing should be arranged so that the values of  $y^+$  at all the wall-adjacent integration points is only slightly above the recommended lower limit given by the code developers, typically between 20 and 30 (the form usually assumed for the wall functions is not valid much below these values). This procedure offers the best chances to resolve the turbulent portion of the boundary layer. It should be noted that this criterion is impossible to satisfy close to separation or reattachment zones unless  $y^+$  is based upon  $y^*$ .
- Exercise care when calculating the flow using different schemes or different codes with wall functions on the same mesh. Cell centred schemes have their integration points at different locations in a mesh cell than cell vertex schemes. Thus the  $y^+$  value associated with a wall-adjacent cell differs according to which scheme is being used on the mesh.
- Check the resolution of the boundary layer. If boundary layer effects are important, it is recommended that the resolution of the boundary layer is checked after the computation. This can be achieved by a plot of the ratio between the turbulent to the molecular viscosity, which is high inside the boundary layer. Adequate boundary layer resolution requires at least 8-10 points in the layer.

All such statements of advice are gathered together at the end of the document to provide a 'Best Practice Checklist'. The examples chapter provides detailed expositions of eight test cases each one calculated by a code vendor (viz FLUENT, AEA Technology, Computational Dynamics, NUMECA) or code developer (viz Electricité de France, CEA, British Energy) and each of which highlights one or more specific points of advice arising in the BPG. These test cases range from natural convection in a cavity through to flow in a low speed centrifugal compressor and in an internal combustion engine valve.

Copies of the Best Practice Guidelines can be acquired from:

ERCOFTAC CADO  
Crown House  
72 Hammersmith Road  
London W14 8TH, United Kingdom  
Tel: +44 207 559 1429  
Fax: +44 207 559 1428  
Email: Richard.Seoud-ieo@ercoftac.org

The price per copy (not including postage) is:

ERCOFTAC members		
First copy		Free
Subsequent copies		65 Euros
Students		49 Euros
Non-ERCOFTAC academics		
		90 Euros
Non-ERCOFTAC industrial		
		230 Euros

# SPECIAL THEME: PLASMA AERODYNAMICS

K.-S. Choi

*Faculty of Engineering, University of Nottingham, University Park, Nottingham NG7 2RD, UK*

`Kwing-so.choi@nottingham.ac.uk`

Flow control using DBD (Dielectric-Barrier-Discharge) plasma actuators is a relatively new, but rapidly expanding area of research. DBD plasma actuators are all-electric devices without the need of pneumatics, hydraulics or moving parts. They are light and fast reacting, ideal for active control of flow over aerodynamic bodies. Moreover, DBD plasma actuators are very thin, which can be either attached on or integrated into the aerodynamic body. DBD plasma actuators are therefore simple, yet powerful devices that make novel aerodynamic applications possible. The purpose of this Theme Issue is to review the latest developments of DBD and spark-jet plasma actuators and their applications for aerodynamics.

All articles are based on the presentations given at the Joint ERCOFTAC/PLASMAERO Workshop<sup>1</sup>, organised by K-S Choi, D. Caruana, C. Tropea and C. Hollenstein. This took place on 10-12 December 2012 in Toulouse, France (Workshop Report will appear in the next volume of ERCOFTAC Bulletin). They summarise and synthesise the numerical and experimental results obtained from PLASMAERO project. The analysis of the operation of plasmas actuators and their effect on

flow control are also described. The research subjects covered by the articles include:

- design and development of DBD plasma actuators, nano-second DBD plasma actuators and spark-jet plasma actuators;
- physical understanding and numerical modelling of plasma actuators and their interaction with air flows;
- evaluation of the plasma technology for aerodynamic flow control of flow separation, wing-tip vortex, boundary layer transition, slat noise and aerofoil buffet;
- validation of plasma technology by large wind tunnel tests at realistic Reynolds and Mach numbers;
- demonstration of DBD plasma flow control system using unmanned aerial vehicles (UAVs).

---

<sup>1</sup>[http://www.ercoftac.org/special\\_interest\\_groups/20\\_drag\\_reduction\\_and\\_flow\\_control/upcoming\\_events/joint\\_workshop/](http://www.ercoftac.org/special_interest_groups/20_drag_reduction_and_flow_control/upcoming_events/joint_workshop/)

# PLASMAERO EUROPEAN PROJECT

D. Caruana<sup>1</sup>, C. Tropea<sup>2</sup>, C. Hollenstein<sup>3</sup>, J-P. Boeuf<sup>4</sup>, E. Moreau<sup>5</sup>, F. Rogier<sup>1</sup> and M. Forte<sup>1</sup>

<sup>1</sup>ONERA, Toulouse Centre, 2 Av. Edouard Belin, 31055 Toulouse, France

<sup>2</sup>Center of Smart Interfaces, Technische Universität Darmstadt, 62347 Griesheim, Germany

<sup>3</sup>Ecole Polytechnique Fédérale de Lausanne (EPFL), CH-1015 Lausanne, Switzerland

<sup>4</sup>LAPLACE, UMR 5213, University of Toulouse - 118 route de Narbonne - 31062 Toulouse - France

<sup>5</sup>Pprime, University of Poitiers, CNRS, ISAE-ENSMA, Téléport 2, 86962, Futuroscope, France

PLASMAERO coordinator and work packages leaders & deputies  
(Contact: [daniel.caruana@onera.fr](mailto:daniel.caruana@onera.fr))

## Abstract

With the continued objective of increasing aircraft performances whilst reducing the environmental impact, research is being carried out to find innovative solutions to influence air flow using simple actuators. If the aerodynamic configuration of future aircraft could be modified in real time in flight, then the aircraft's performance could be continually adapted to provide optimum aerodynamic characteristics.

Among the innovative solutions, the use of plasma technologies has shown itself to be very promising from both a performance point of view and in terms of the diversity in potential applications such as external and internal flow control, combustion enhancement and noise attenuation. The main advantages of plasmas devices are their manufacturing and integration simplicity, low power consumption and ability for real time control at high frequency.

PLASMAERO "PLASMas for AERODynamic control" (<http://www.plasmaero.eu>) is a European project of the Seventh Framework Programme under grant agreement 234201, co-funded by the European Commission. It is coordinated by ONERA supported by ART-TIC. The total budget is about 5M€. The project consortium is composed of eleven organisations from seven European countries which gathers the key players from the plasma and aerodynamic scientific community of Europe, CIRA, CNRS (EPEE, LAPLACE and PPRIME laboratories), University of Darmstadt, EPFL, Institut Maszyn Przeplywowych (IMP), NLR, University of Nottingham, ONERA, SNECMA, University of Southampton. The project began in October 2009 and ended in December 2012 with the successful joint ERCOFTAC/PLASMAERO workshop. It sought to demonstrate how DBD and spark-discharge plasma actuators could be used to control aircraft aerodynamic flows. This was achieved through an enhanced understanding of their physical characteristics and an in-depth study of how they may be optimised to influence the air flow properties.

More specifically, the project objectives were to:

- understand, model and classify, through experimental and numerical studies, the most relevant physical characteristics of plasma actuators capable of influencing flow;
- perform comparative experimental tests and numerical studies of different actuators and flow configurations;
- demonstrate through wind tunnel experimentations and computational fluid dynamics the ability of plasma devices to significantly improve or control the aerodynamics;
- demonstrate the integration of these actuators in a reduced-size flight platform and their use in real atmospheric conditions;
- provide exhaustive recommendations on future work to be performed to achieve the implementation of this technology.

The obtained results show that actuation using the studied plasma technology for flow control is very promising.

## Acknowledgements

We thank the project officer of the European Commission, Dietrich Knoerzer, for his insightful guidance at all stages of the project. I would also like to express my very great appreciation to all project partners, participants and reviewers for their valuable skills, enthusiasm and commitment during the planning and development of this research work. I wish to address special thanks to Nicolas Benard, Jean-Pascal Cambronne, Pietro Catalano, Kwing-So Choi, Raffaele Donelli, Guillaume Du-four, Michel Dumas, Isabelle Forcier, Christian Gleyzes, Sven Grundman, Hugo Hart, Johan Kok, Annie Leroy, Penelope Leyland, Jerzy Mizeraczyk, Pascal Molton, Janusz Podliński and Xin Zhang.

# SURFACE DIELECTRIC BARRIER DISCHARGE PLASMA ACTUATORS

E. Moreau<sup>1</sup>, A. Debien<sup>1</sup>, N. Bénard<sup>1</sup>, T. Jukes<sup>2</sup>, R. Whalley<sup>2</sup>, K.-S. Choi<sup>2</sup>,  
A. Berendt<sup>3</sup>, J. Podliński<sup>3</sup>, J. Mizeraczyk<sup>3</sup>

<sup>1</sup>*Prime, University of Poitiers, CNRS, ISAE-ENSMA, Téléport 2, 86962, Futuroscope, France*

<sup>2</sup>*Faculty of Engineering, University of Nottingham, University Park, Nottingham, NG7 2RD, UK*

<sup>3</sup>*Institute of Fluid Flow Machinery, Polish Academy of Sciences, Fiszerka 14, 80-231 Gdansk, Poland*

## Abstract

This paper presents a part of the works conducted in the Plasmaero European project (task 1.1) on surface dielectric barrier discharge actuators applied to airflow control. The study is divided into several parts. In the first part, the goal is to enhance the electric wind produced by a typical single DBD actuator by optimization of the active electrode shape. For instance, the use of a thin wire instead of a plate air-exposed electrode has shown that the body force can be increased from 65 to 97 mN/m for a power consumption of 1 W/cm. Secondly, plasma vortex generators are presented. The interaction between the spanwise-directed body force and the oncoming boundary layer is illustrated. In the third part, the interest of using three-electrode based sliding discharges for large-scale applications is highlighted. The final part deals with multi-DBD actuators that result in an increase of the electric wind velocity up to 10.5 m/s. This has been previously limited to about 7 m/s until now.

## 1 Introduction

Surface dielectric barrier discharge (DBD) plasma actuators are widely investigated for their ability to manipulate airflow [1, 2]. Their main advantages are their very short response time and their low power consumption. The well-known single DBD plasma actuator is composed of two plate electrodes asymmetrically mounted on both sides of a dielectric and supplied by an ac voltage. As a sufficient voltage is applied, a discharge occurs on the air-exposed surface. An electrohydrodynamic (EHD) body force is created and momentum transfer occurs from charged particles to neutral particles, leading to an electric wind with maximum velocity up to about 6 m/s. The present paper briefly describes a part of the works performed in the task 1.1 of the Plasmaero European project. The objective of this task was to optimize and characterize DBD plasma actuators, and to develop new actuators based on various DBD designs, such as multi-electrode DBD actuators and DBD vortex generators. The experimental works have mainly consisted of characterizing the velocity and the topology of the produced flow by time-averaged and timeresolved methods, such as particle image velocimetry. Direct measurements and indirect estimations of the EHD force have also been conducted. This paper is divided into four parts. In the first part, the goal is to enhance the mechanical performances of a single DBD actuator by modification of the active electrode shape. Thin wire electrodes and serrated electrodes have been investigated. In both cases, the use of these new electrodes results in a strong modification

of the discharge behaviour. By using a thin wire, the discharge becomes filament-free, whilst a serrated electrode enables streamer locations to be regulated. As a result, this should increase the induced EHD body force and the resulting electric wind. In the second part, the goal is to explore DBD plasma actuators that create streamwise vortices, like vane-type vortex generators. This is an old flow control concept which has found many applications in industry because stream wise vortices have remarkable organisation and longevity. These DBD actuators are oriented to produce a body force at some yaw angle to the oncoming flow. This increases mixing between the boundary layer and the free-stream to reenergize the near-wall region with fluid from the outer flow. In the third part, three-electrode based actuators are presented. This type of electrode configuration has been inspired by devices used to produce sliding discharges for laser applications [3]. The three-electrode based actuator is supplied by an ac high voltage, plus a dc component. Two electrodes are flush mounted on each side of a dielectric, like the single DBD device, but a second air-exposed electrode is added and supplied by a dc voltage. This results in a “sliding“ of the space charge between both air-exposed electrodes. The main advantage of this discharge is that it can be used in largescale applications because the discharge extension may be increased up to the gap between both air-exposed electrodes. Finally, the fourth part deals with multi-DBD plasma actuators. There are two goals here: an enhancement of the electric wind velocity and an enlargement of the plasma surface in order to be useful for large-scale applications. Multi-DBD actuators are usually composed of several DBD in series in order to cumulate the velocity produced by every single DBD. Innovative multi-DBD designs that have been perfected during this project will be presented and discussed. Velocity higher than 10 m/s has been measured with these configurations, which is the highest induced velocity that has ever been recorded.

## 2 Single DBD actuators

Two active electrode shapes were tested in order to increase the body force produced by a single DBD. The effects are summarized in the following sections.

### 2.1 Wire active electrode

DBD actuators are composed of two electrodes asymmetrically flush mounted on each side of a dielectric plate (3 mm-thick PMMA, Figure 1). The grounded electrode (span 90 mm, width 20 mm) is insulated with an epoxy resin. A small gap of 2 mm separates the active electrode

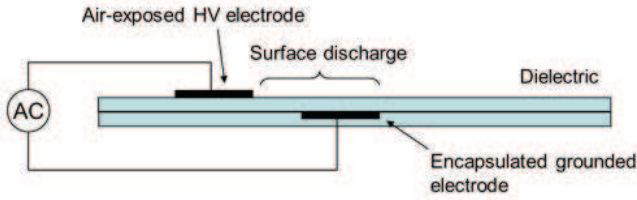


Figure 1: Schematic of a single DBD actuator

and the grounded one. For the baseline case, the active electrode is a rectangular aluminum foil (10 mm-wide, 80  $\mu\text{m}$ -thick). For the new design investigated at University of Poitiers, the air-exposed electrode was replaced by a thin wire in order to increase the local electric field at the vicinity of the high voltage electrode (tungsten wire with diameter of 300, 100, 50, 25 and 13  $\mu\text{m}$ ). The voltage waveform was sinusoidal with high voltage amplitudes from 14 to 22 kV (frequency of 1 and 1.5 kHz).

The surface dielectric barrier discharge has been experimentally investigated by electrical and optical diagnostics, electrohydrodynamic force measurements and produced electric wind characterization from time-averaged and time-resolved measurements. Major results are going to be presented in this paper. For more details, see [4]. First, measurements of the discharge current highlighted that the discharge regime is quite different. For instance, the number of streamers that occur during the positive going-cycle decreases with the wire diameter, resulting in a filament-free regime when a 13  $\mu\text{m}$  wire was used. Figure 2 shows the thrust produced by different actuators versus their electrical power consumption. The use of a thin wire electrodes results in higher thrust for a same electrical power consumption as the plate electrode. The force is larger as the wire diameter decreases. The actuator effectiveness, that corresponds to the mean produced force divided by the electrical power consumption, is increased from 0.65 mN/W to 0.97 mN/W. Then the resulting electric wind is fully modified (Figure 3). The suction effect above the surface discharge is enhanced (vertical velocity drops from -0.9 to -1.3 m/s) and the maximum horizontal velocity measured at 0.6 mm above the dielectric wall increases to about 7 m/s. Finally, the most interesting result is presented in Figure 4 that plots the time history of the electric wind at 1 mm above the wall and 5 mm downstream the active electrode. In the case of a plate-to-plate DBD, the velocity increases during the negative-going cycle (when the negative discharge ignites) and it decreases during the positive one because the streamers does not contribute efficiently to body force production (the force is negative during the positive discharge). With a wire-to-plate DBD, the velocity increases during both half cycles, with a velocity growth when the discharge occurs and a decrease when there is no discharge. Moreover, the maximum velocity is produced during the positive discharge, showing that the filament-free discharge is most efficient means of velocity production.

## 2.2 Serrated active electrode

DBD plasma actuators were investigated at Institute of Fluid Flow Machinery to compare the velocity of electric wind induced by a single DBD actuator with an active plate electrode having either smooth (Figure 5a) or serrated (Figure 5b) edge. In this paper, selected results are presented. For more details, see [5]. The actuators consisted of two electrodes (made of a 50  $\mu\text{m}$  thick cop-

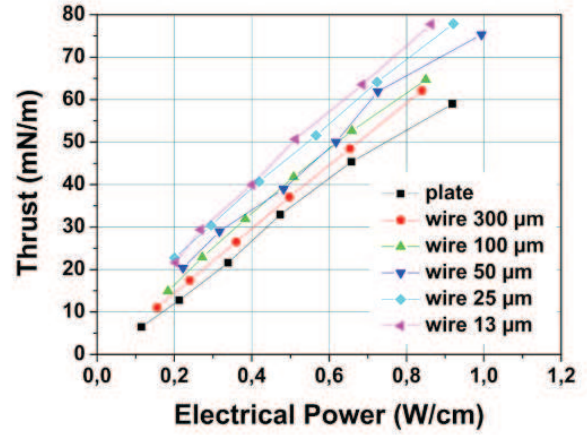


Figure 2: Discharge thrust versus electrical power (frequency = 1.5 kHz, voltages from 12 to 22 kV)

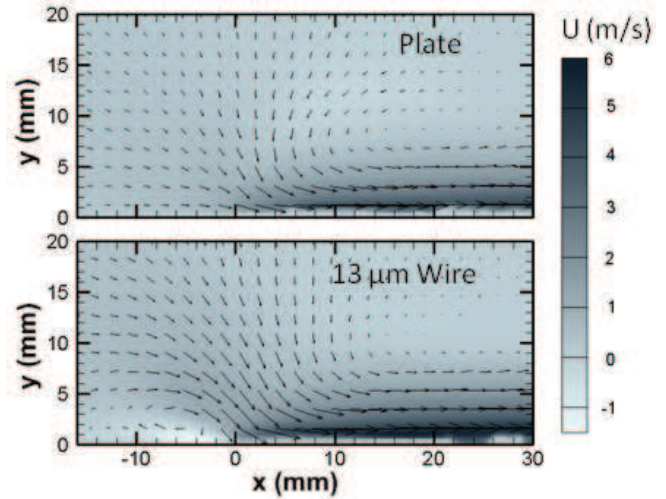


Figure 3: Velocity fields measured by PIV in stagnant air with a plate active electrode and a wire active electrode (22 kV, 1.5 kHz, scale in millimeter, edge of the active electrode at  $x = 0$  and  $y = 0$ )

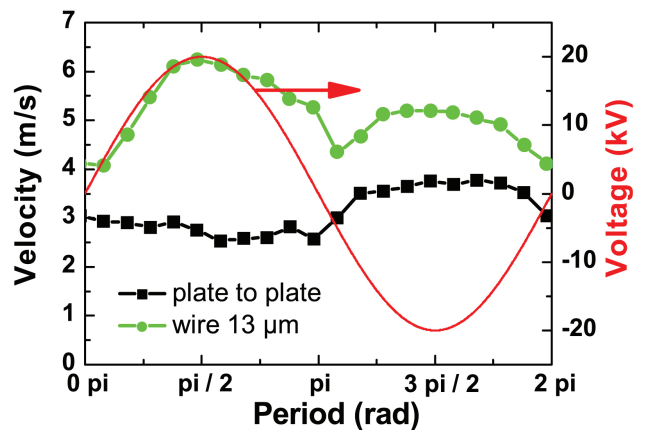


Figure 4: Velocity versus time at  $x = 5$  mm and  $y = 1$  mm

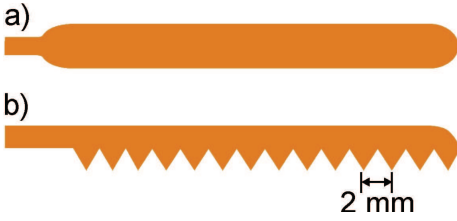


Figure 5: Top view of a smooth and serrated active electrode used in the DBD plasma actuators

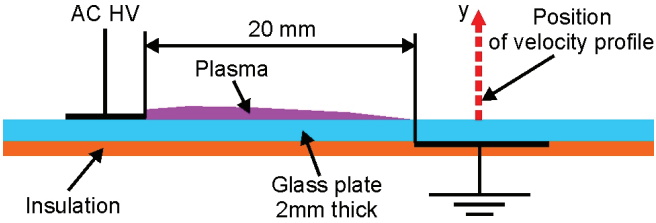


Figure 6: Schematic side view of the DBD actuator with 20 mm shift between the edges of the active and grounded electrode

per tape) flush mounted on a 2 mm thick glass plate (Figure 6). The active electrode was exposed to ambient air while the 10 mm wide grounded electrode (on the bottom side) was insulated. The width of the active electrode was equal to 6 mm and the gap between the edges of the active and grounded electrodes was 20 mm. The length of the electrodes in the span wise direction was 50 mm.

When the sine high voltage is applied to the actuators, a surface DBD is generated. The discharge generated by the actuator with serrated active electrode ignites at a lower voltage than the smooth active electrode. Moreover, the discharge starts from every saw-tooth of the serrated electrode and therefore, the plasma generated along the serrated electrode is quite homogenous (Figure 7b). When a smooth active electrode is used, the plasma is clearly non-uniform (Figure 7a).

A 2D PIV method was used to measure velocity fields of electrohydrodynamic (EHD) flow generated by the DBD actuators in quiescent air. In Figure 8, velocity profiles of the electric wind measured with both the smooth (a) and serrated (b) active electrodes are presented. These profiles are taken 25 mm downstream the edge of the active electrode (see Figure 6). As it can be seen in Figure 8, the velocity of the EHD flow induced by the DBD actuator with serrated active electrode is higher than for the actuator with smooth active electrode in all cases. The clearest difference in flow velocity is for low voltages. For example, when the applied voltage is 22 kV (frequency 1.5 kHz), the maximum induced flow velocity obtained for the actuator with smooth electrode is

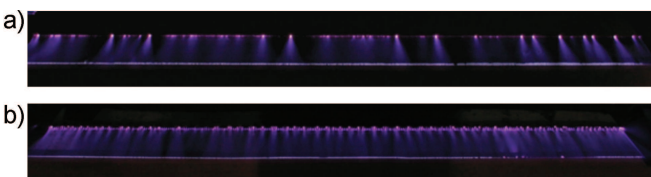


Figure 7: Images of the DBD obtained in the actuator with smooth (a) and serrated (b) active electrode. The amplitude of the applied sine-wave voltage was 26 kV, frequency 1.5 kHz

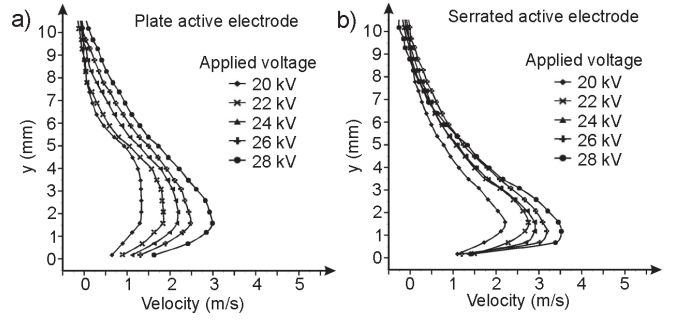


Figure 8: Velocity profiles of the EHD flow induced by the DBD actuator with smooth (a) and serrated (b) active electrode

1.8 m/s, while for the actuator with serrated electrode it reaches 2.7 m/s.

### 3 DBD vortex generators

The DBD vortex generator (DBD-VG) studied at University of Nottingham is a standard asymmetric DBD actuator like shown in Figure 1, oriented with component of body force perpendicular to the oncoming flow. This force vectoring interacts with the oncoming boundary layer to produce a longitudinal vortex, as depicted in Figure 9. Four key parameters affect the formation of streamwise vortex and its flow control capability: the plasma jet velocity  $W_p$  (which depends on the geometry and excitation parameters), the free-stream velocity  $U_\infty$ , the electrode yaw angle  $\beta$ , and the DBD-VG length  $l$ . Actuators with a range of  $E$ ,  $U_\infty$ ,  $\beta$  and  $l$  were studied and DBD-VGs were produced as co-rotating and counter-rotating vortex generator arrays. Further details and complete results are given in [6]. DBD-VG characterisation was carried out in a lowspeed wind tunnel over a 1 m long by 0.284 m wide smooth flat plate. The DBD-VGs were flush-mounted into the upper surface of the plate, 0.6 m from the leading edge. The free-stream velocity was set in the range  $2 \leq U_\infty \leq 15 \text{ m/s}$ , where the local laminar boundary layer thickness at the DBD-VGs was  $4.2 \leq \delta \leq 11.5 \text{ mm}$ . Global flow field measurements were made with timeresolved PIV in the streamwise ( $x$ - $y$ ), cross-stream ( $y$ - $z$ ), and wall-parallel ( $x$ - $z$ ) planes. Particular emphasis was placed on the vortex formation mechanisms and the growth/decay of the vortex downstream. Figure 10 shows a typical cross-stream slice through the vortex at the trailing-edge of a DBD-VG. The upper electrode is drawn in black where the electrode edge is located at the origin. Plasma forms in the region  $0 < z/l < 0.05$ ,  $y/l < 0.02$ . It is clear that the DBD-VG produces a concentrated streamwise vortex. This has counterclockwise rotation in the plane of Figure 10 (black isocontour shows  $\Omega_x = -100 \text{ s}^{-1}$ ). The vortex takes less than 0.1 s to initiate (depending on  $U_\infty$ ) and is very stable with time. The core meandered by less than  $\pm 2 \text{ mm}$  whilst the plasma was on and the flow field in Figure 10 can be considered a steady-state phenomenon. When the plasma is switched off the vortex rapidly shrunk to the wall, so that longitudinal vortices can be simply turned on and off by intermittently energizing DBD-VGs. The strongest vortices were created when the DBD-VG is aligned with the flow ( $\beta = 90^\circ$ ), so that the DBD induced a body force predominantly in the spanwise direction. This creates a spanwise directed wall-jet flow, as can be seen in Figure 10 for  $y/l < 0.05$ . The upper part of this wall jet ( $-\Omega_x$ ) rolls-up into the

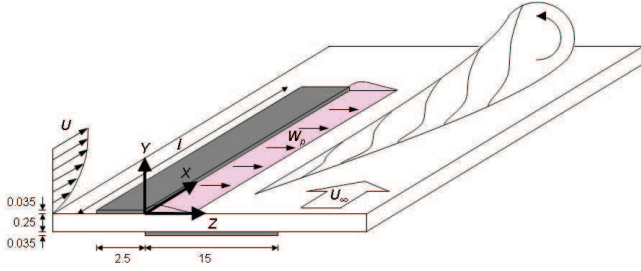


Figure 9: Schematic of a DBD-VG. Dimensions in mm

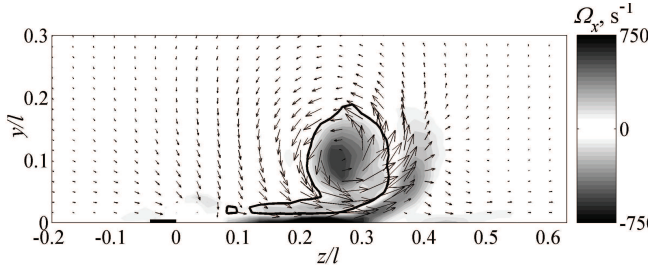


Figure 10:  $\Omega_x$  with VW velocity vectors at trailing-edge of a DBD-VG.  $\beta = 90^\circ$ ,  $l = 60$  mm,  $x = 60$  mm,  $E = 7.5$  kV<sub>p-p</sub>,  $f = 23$  kHz,  $U_\infty = 2.2$  m/s

streamwise vortex whilst the lower part of the wall jet ( $+\Omega_x$ ) becomes lifted from the wall on the outboard side to wrap around the core ( $z/l > 0.3$ ).

Figure 11 plots the  $\lambda_2$  vortex indicator, which shows the vortex is spanwise-oriented at the DBD-VG tip. This suggests that the vortex is formed as a result of lifting and twisting of spanwise vorticity ( $-\Omega_z$ ) in the incoming boundary layer over the virtual blockage of the wall jet created by the plasma. This lifting is non-uniform across the span due to jet thickening, so the spanwise vortex filaments are increasingly lifted into region of higher  $U$  velocity with  $z$ , causing a reorientation of  $-\Omega_z$  into  $\Omega_x$ . This combines with  $-\Omega_x$  is the outer region of the wall-jet, which supplies vorticity along the length of the DBD-VG. In addition, the DBD-VG includes a wall-ward motion into the plasma ( $-V$ ) because the plasma is a source of momentum, not mass. Thus fluid is drawn into the DBD from above to replace that accelerated laterally by the body force. The suction into the DBD is quite unlike other vortex generators and causes a dramatic thinning of the boundary layer in the downstream, as can be seen in the  $U$  iso-contours and deflection of the streamline towards the wall at  $z/l \approx 0$ . This action occurs in addition to the cross-stream mixing of the streamwise vortex, which has proved beneficial for flow separation control [7].

## 4 Sliding discharges

Sliding discharge actuators are composed of two electrodes flush mounted on each side of a dielectric such as a single DBD device, plus a second air-exposed electrode supplied by a dc voltage. This results in a "sliding" of the space charge between both air-exposed electrodes [3]. These discharge are as stable as a single DBD and have the advantage that they can be used in large-scale applications because the discharge extension may be increased across the entire gap between both air-exposed electrodes. However, until now, no work has investigated accurately the flow produced by these discharges compared to that induced by a single DBD. This was the objective of the

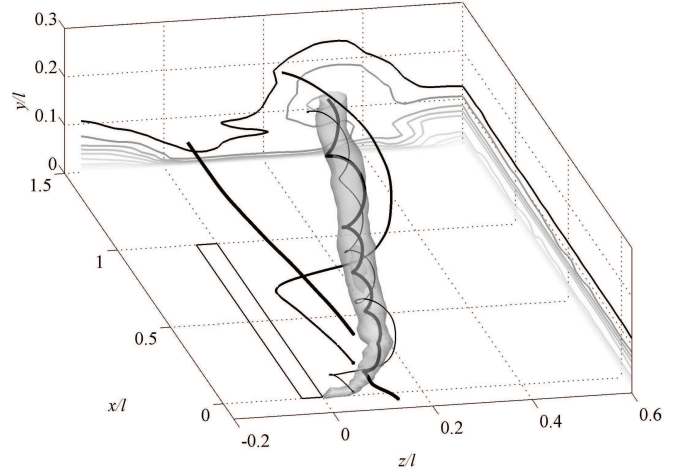


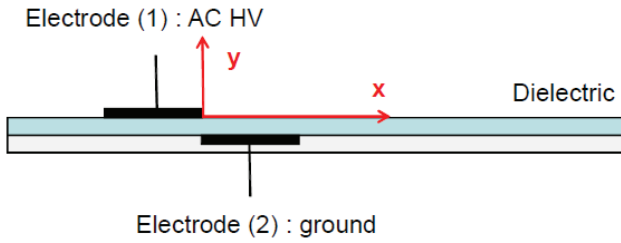
Figure 11:  $\lambda_2$  iso-surface with streamlines and  $U$  iso-contours ( $0 \leq U/U_\infty \leq 0.9$ ).  $\beta = 90^\circ$ ,  $l = 60$  mm,  $E = 7.5$  kV<sub>p-p</sub>,  $f = 23$  kHz,  $U_\infty = 2.2$  m/s. DBD-VG upper electrode in box

present study conducted at University of Poitiers. Lots of configurations have been tested. Only one is presented here. For further detail, see [8]. Figure 12 presents a schematic of a sliding discharge, with a 4-cm gap between electrodes (1) and (3). Others geometrical parameters are similar to described in Section 2.1. Figure 13 shows the velocity vector fields for a single DBD and the design of Figure 12b. One can see that the use of a third electrode, in certain conditions, can result in significant effects. First, the suction effect above and upstream the discharge is strongly increased compared to a typical single DBD. Moreover, the region where the suction is visible is strongly enlarged. Secondly, the electric wind wall jet is thickened (its height is multiplied by two). Third, the maximum electric wind velocity is slightly increased, from 4.2 to 5.5 m/s here. However, it is located 2 mm above the flat plate when it is measured at  $y \approx 0.5$  mm with a single DBD. This increase in velocity is due to the fact that the tangential wall jet separates from the wall at the edge of electrode (3) because a weak counter-wind is produced at this electrode. Then friction between the wall and electric wind decreases, resulting in the electric wind velocity growth.

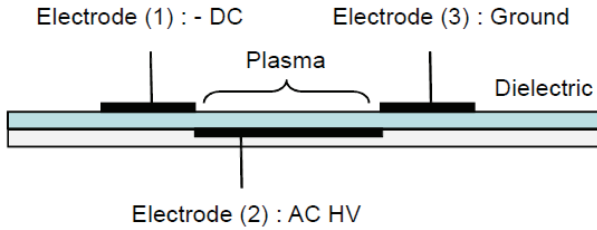
## 5 Multi-DBD

The goal of multi-DBD actuators is twofold: an enhancement of the electric wind velocity and an enlargement of the plasma layer in order to be useful for large-scale applications. Multi-DBD actuators are composed of several DBD in series in order to cumulate the velocity produced by every single DBD. Two innovative multi-DBD designs have been perfected during the project.

The first one, studied at University of Poitiers, consists of four successive single DBD. To take advantages of the cumulative effect, the DBD have to be close to each other, but in this case mutual interactions between electrodes can limit the velocity accumulation. This is caused by a counteracting wind caused by backdischarge from each air-exposed electrode toward the grounded electrode of the previous single DBD. In the new design proposed here, two points have been optimized compared to usual multi-DBD. First, the plate active electrodes have been replaced by thin wires (diameter of 25  $\mu\text{m}$ ) in order to enhance the electric wind produced by each single DBD according to the results presented previously



(a)



(b)

Figure 12: Sketch of a single DBD (a) and a sliding discharge (b)

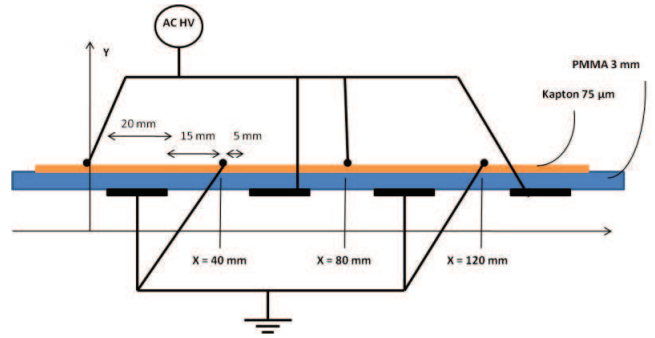


Figure 14: Sketch of the multi-DBD actuator based on four single wire-to-plate DBD

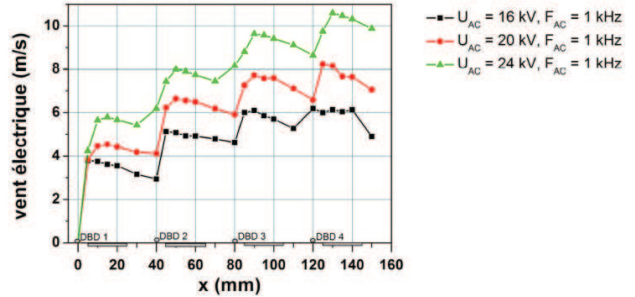
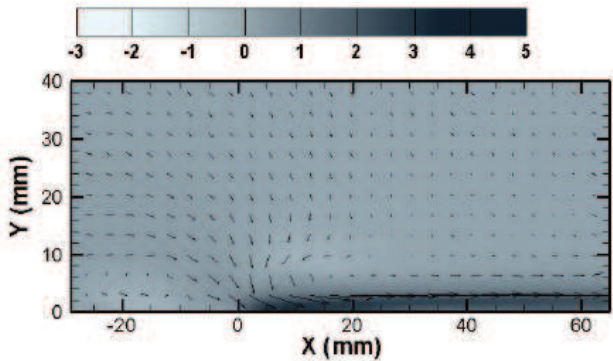
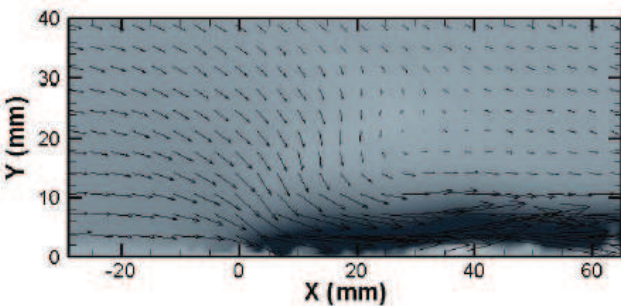


Figure 15: Horizontal velocity profiles measured 0.6 mm above a multi-DBD actuator for  $V_{AC} = 16, 20$  and  $24$  kV



(a)



(b)

Figure 13: Velocity vector fields measured for a single DBD with  $V_{AC} = 24$  kV (a) and a sliding discharge with  $V_{AC} = 24$  kV,  $V_{DC} = -24$  kV (b)

in Section 2.1. Secondly, interaction between successive DBD has been cancelled by alternating the HV electrode and the grounded one, from one DBD to the successive one (see Figure 14). In such conditions, velocity measurements have been conducted with a Pitot tube. For instance, Figure 15 presents horizontal velocity profiles measured 0.6 mm above the wall, from  $x = 0$  (position of the first wire HV electrode) to  $x = 145$  mm (25 mm downstream the right edge of the last grounded electrode) for three different voltages. From  $x = 0$  to about 15 mm, the velocity increases from zero to 6 m/s for 24 kV and then decreases because there is no EHD force downstream the plasma extension. Then each successive single DBD add velocity that cumulates up to 10.5 m/s downstream the last single DBD, when voltage equal to 24 kV.

The second multi-DBD actuator presented in this section consists of three successive single DBD sets with two inter-electrodes at floating potential placed between them (Figure 16). This new design has been proposed by the Institute of Fluid Flow Machinery. The grounded electrodes and the floating inter-electrodes are exposed to ambient air. The grounded electrodes are serrated (similar to that presented in Figure 5b) while the floating inter-electrodes consist of a series of separated sawteeth. The grounded and floating electrodes are partially insulated, as presented in Figure 16. The high voltage plate electrodes are on the bottom side of the actuator. They are insulated with Kapton tape. The floating electrodes are so placed over the high voltage electrodes that only their saw tips stuck out 1 mm downstream from the edge of the high voltage electrodes. Such an arrangement reduces mutual interactions between successive single DBD sets and allow us to decrease the spacing between them. Moreover, additional DBDs are generated between the floating inter-electrodes and the grounded electrodes. The flow induced by these addi-

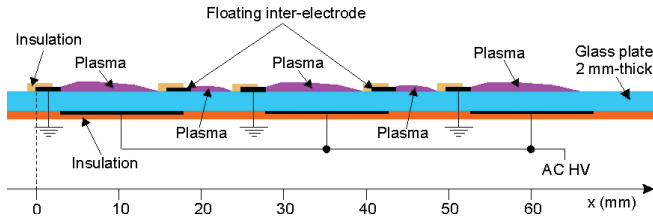


Figure 16: Schematic side view of the multi-DBD actuator with floating inter-electrodes

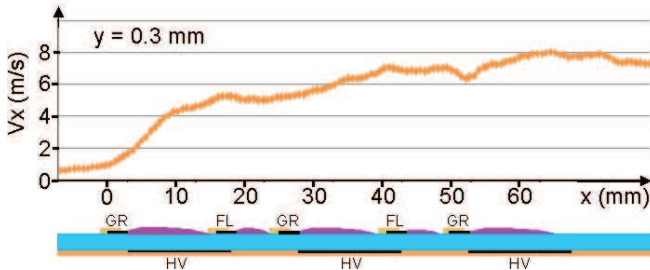


Figure 17: The horizontal time-averaged velocity profile taken 0.3 mm above actuator surface. The applied voltage 26 kV, the frequency 1.5 kHz

tional DBDs interacts coherently with the flow produced by the DBDs from grounded active electrodes, enhancing the total induced airflow. For more details see [9]. A 2D PIV system was used to characterize the total induced flow. An example of time-averaged horizontal velocity profile taken 0.3 mm above the dielectric surface is presented in Figure 17. In this case the voltage amplitude is equal to 26 kV and the frequency is set to 1.5 kHz. It can be observed that the induced airflow is almost continuously accelerated by the successive DBDs (placed close one to each other) comprising the multi-DBD actuator. The counteracting between successive DBD sets is not observed. The maximum velocity is equal to 8 m/s (just after the last grounded electrode). However, the produced velocity can be increased by increasing the ac frequency. At a frequency of 2.35 kHz, the maximum velocity was 10.1 m/s.

## 6 Conclusion

The works conducted in Plasmaero European project task 1.1 allowed us to investigate innovative plasma actuator designs. The body force induced by single DBD has been enhanced. Velocity above 10 m/s has been reached with both multi-DBD actuators. It is the highest velocity that has ever been measured in the case of a surface

discharges. DBD-VGs have also been characterized. All of these actuators have been used for flow control applications in subsequent Plasmaero work packages.

## Acknowledgments

The work has been carried out as a part of PlasmAero program with funding from the European Community's Seventh Framework Programme FP7/2007-2013 under grant agreement nr. 234201.

## References

- [1] E. Moreau, 2007, *Airflow Control by Non-Thermal Plasma Actuators*, Journal of Physics D: Applied Physics, Vol. 40, pp. 605-636.
- [2] N. Bénard, E. Moreau, 2012, *EHD Force and Electric Wind Produced by Plasma Actuators Used for Airflow Control*, 6th AIAA Flow Control Conference, paper AIAA-2012-3136.
- [3] E. Moreau, R. Sosa, G. Artana, 2008, *Electric wind produced by surface plasma actuators: a new dielectric barrier discharge based on a three-electrode geometry*, J. Phys. D: Appl. Phys., 41, 115204 .
- [4] A. Debien, N. Bénard, E. Moreau, 2012, *Streamer inhibition for improving force and electric wind produced by DBD actuators*, J. Phys. D: Appl. Phys. 45, 215201.
- [5] A. Berendt, J. Podliński, J. Mizeraczyk, 2011, *Comparison of airflow patterns produced by DBD actuators with smooth and saw-like electrode*, J. Phys.: Conf. Series, 301, 012018
- [6] T. N. Jukes & K.-S. Choi, 2012, *Dielectric-Barrier-Discharge Vortex Generators: Characterisation and Optimisation for Flow Separation Control*, Exp. Fluids, 52, 329-345.
- [7] T. Jukes, T. Segawa & H. Furutani, 2012, *Flow Control on a NACA 4418 Using Dielectric Barrier Discharge Vortex Generators*, AIAA-2012-1139 and accepted for publication in AIAA J.
- [8] A. Debien, R. Sosa, N. Benard, E. Moreau, 2011, *Electric wind produced by sliding discharges*, Proc. ISNPEDADM, Nov. Nouméa, France.
- [9] A. Berendt, J. Podliński, J. Mizeraczyk, 2011, *Elongated DBD with floating interelectrodes for actuators*, Eur. Phys. J. Appl. Phys., 55, 13804.

# NANOSECOND PULSED PLASMA ACTUATORS

N. Benard<sup>1</sup>, E. Moreau<sup>1</sup>, N. Zouzou<sup>1</sup>, H. Rabat<sup>2</sup>, J. Pons<sup>3</sup>, D. Hong<sup>2</sup>,  
A. Leroy-Chesneau<sup>4</sup>, P. Peschke<sup>5</sup> and C. Hollenstein<sup>5</sup>

<sup>1</sup>*Pprime, University of Poitiers, CNRS, ISAE-ENSMA, Téléport 2, 86962, Futuroscope, France*

<sup>2</sup>*GREMI, UMR 7344, CNRS, University of Orleans, Orléans, France*

<sup>3</sup>*EPEE FR776, CNRS, University of Orleans Cedex 2, France*

<sup>4</sup>*PRISME, UPRES 4229, University of Orleans, Orléans, France*

<sup>5</sup>*Ecole Polytechnique Fédéral de Lausanne (EPFL), CH-1015 Lausanne, Switzerland*

## Abstract

This paper summarizes the results of Plasmaero (EU project) partners on the characterization of plasma actuators based on nanosecond pulsed discharges. Results cover electrical aspects, optical discharge visualizations and measurements of the plasma-induced pressure wave, this for quiescent and transonic flow regimes. Among the results, this study demonstrates that the induced pressure wave is composed of over and under pressure of 1600 and -600 Pa, respectively. In transonic regime, the capability of the discharge to produce a pressure wave remains but this one is convected by the freestream flow.

## 1 Introduction

The PLASMAERO European project looks at a further understanding of plasma physics for flow manipulation by non-thermal surface discharges. On the margin of typical AC Dielectric Barrier Discharge (DBD) plasma actuators that are based on the produced electric wind [1], different actors of the project are interested in the development of pulsed discharges with rising time in the nanosecond scale order. This type of actuator has demonstrated promising influence to mitigate flow separation at Reynolds numbers related to realistic flight speed conditions [2-4], where AC-DBD have shown only little or no effect. Recent literature suggests that nanosecond pulsed DBD can produce a localized pressure wave that propagates in the medium at speed of sound [5-8] while the induced momentum transfer related to neutral/charged particle collision remains marginal. In the framework of PLASMAERO, different nanosecond pulsed DBDs have been investigated in terms of electrical characteristics for quiescent flow condition. A variety of electrical parameters such as the voltage amplitude, rising time or polarity have been considered. Each partner has used different optical systems that permit detailed qualitative and quantitative descriptions of the propagating pressure waves suspected to be responsible for the control effect and control authority at high speed flow conditions. Later in the project, the behavior of this type of DBD has been investigated in presence of transonic flow. The present paper summarizes the main results obtained in PLASMAERO EU project.

## 2 Nanosecond pulsed DBD operated in quiescent flow condition

In this first section, different nanosecond pulsed DBD are investigated for initial quiescent flow conditions. As ns-DBD is very flexible, important discharge parameters can be chosen independently. For instance, parameters such as voltage amplitude, rise time or polarity are investigated here.

### 2.1 Electrical aspects

The electrical measurements for a surface dielectric barrier discharge composed of two electrodes (copper foil with thickness of 40  $\mu\text{m}$ ) flush mounted on both sides of a 127  $\mu\text{m}$  thick Kapton layer are shown in figure 1. The gas thermalization at the surface of the dielectric is the result of HV pulse produced by a commercial generator (DEI PVX-4110) connected to a DC power that can supply voltage amplitude up to  $\pm 10$  kV (Matsuda, 10P30, 30 mA). Results are presented for both positive and negative voltage pulses (absolute voltage amplitudes of 8 and 4 kV, pulse width of 200 ns and rise time about 50 ns).

For a single pulse, two current peaks occur in the total current evolution as shown in Figure 1b. The first one is due to air ionization when the electric field is sufficient to initiate air breakdown. Following the first current peak, charges are deposited at the dielectric surface. When the potential difference between the upper electrode and the charged surface is sufficient, a new discharge propagates on the dielectric. This is verified regardless of the polarity of the HV pulse. The positive voltage pulse presents an asymmetry in the current peak amplitude of the rising and decaying periods. Indeed, a larger amplitude is observed for the primary current peak that results in a significant increase in consumed electrical power (Figure 1c). Oppositely, the amplitude of the current peaks remains of a similar level when DBD is supplied by a negative pulse. Calculation of deposited energy per plasma length indicates that positive HV pulse is more efficient than negative HV pulse, this regardless of the applied voltage amplitude (Figure 1d). As indicated by the discharge current, the first current peak is the main contributor to the energy deposited on the wall surface during an HV pulse. It is suspected that the deposited energy is the key metric for characterizing nanosecond pulsed

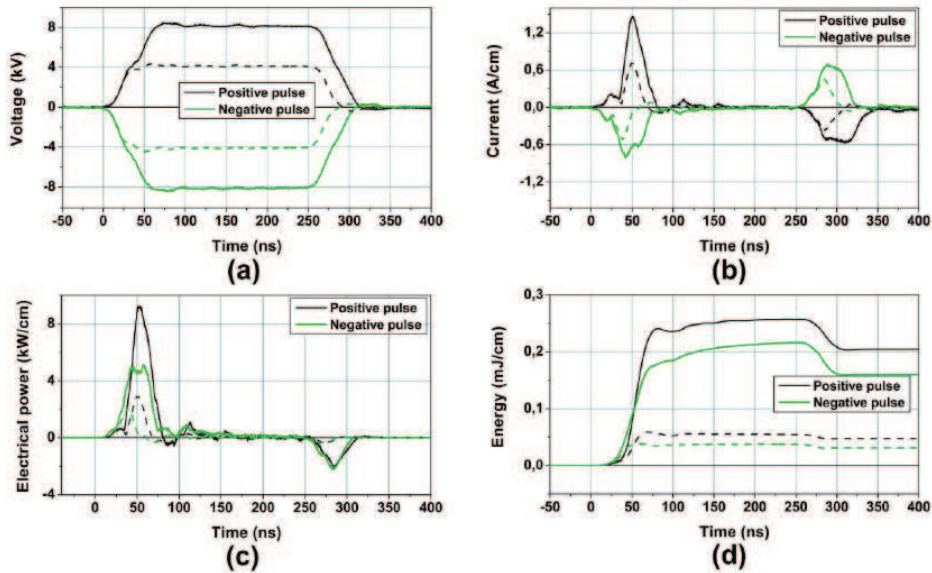


Figure 1: Electrical aspects of positive and negative pulse discharges operated at voltage amplitude of  $\pm 8$  kV (filled lines) and  $\pm 4$  kV (dashed lines) with pulse width of 200 ns. (a) Voltage amplitude, (b) Total current (discharge plus displacement currents), (c) Consumed electrical power and (d) Energy deposition

DBD for flow control applications. Indeed, it seems that the pressure wave intensity is directly correlated with the amplitude of the deposited energy [7].

Among the electrical parameters having demonstrated an influence on the pressure wave formation, the rise time of the high voltage pulse is of primary importance as numerically demonstrated by Unfer and Boeuf [9]. Indeed, by reducing the rising time of the input signal, the produced pressure wave should be reinforced by a faster energy deposition into a relatively small volume. The effects of the rising and decaying time are investigated by adding a high voltage resistor in series with the exposed electrode (Figure 2). The amplitude of the signal is adjusted to compensate the voltage drop through the resistor while maintaining a constant output (9.350.15 kV). As illustrated in the figure, the deposited energy reduces in an exponential manner with the time-scale of the rising/decaying period of the voltage signal. By increasing the rising time,  $t_r$ , by 25 ns from 50 ns, the deposited energy is reduced by 56%. The results indicate that more energy is dissipated, and then potentially converted into gas heating, by reducing the time to attain the maximal (or minimal) voltage amplitude. Furthermore, it was found that a voltage pulse with a steeper slope causes a much shorter and more intense discharge with higher streamer propagation speed. This is illustrated in figure 3, which shows the discharge light emission intensity for two voltage pulses of different rise times  $t_r$ .

## 2.2 Plasma morphology

The temporal and spatial discharge development created by the nanosecond pulsed DBD was investigated using ICCD cameras. Measurements are performed for an homebuilt pulse generator constructed using existing power electronics (Mosfet switch). This generator can provide pulse with rise time of a few 10's of nanoseconds, discharge currents up to 30-50 A, frequencies up to 10-20 kHz and voltage amplitude up to 10 kV. In addition, commercial pulse generator is also investigated. This commercial system (described in section 2.1) produces high voltage pulses up to 10 kV amplitude while the rise time is 50 nanoseconds. An illustration of the

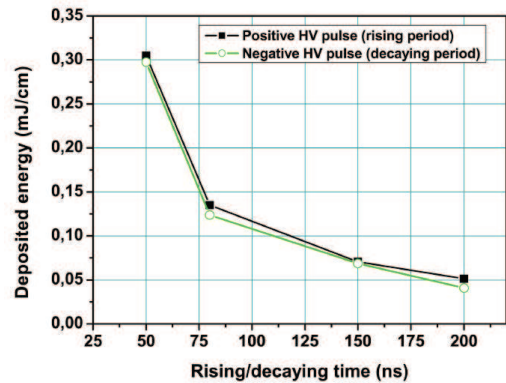


Figure 2: Deposited energy at the dielectric wall according to the rising time (positive high voltage pulse) or decaying time (negative high voltage pulse) for voltage amplitude,  $U$ , of  $\pm 10$  kV

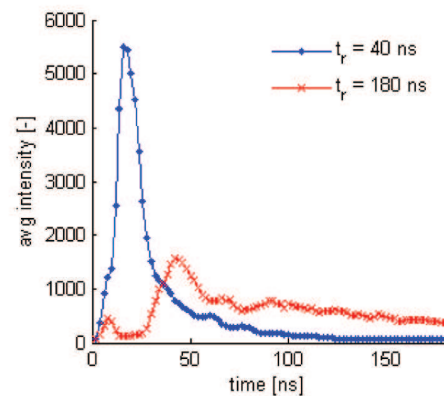


Figure 3: Effect of the rise time on the light emission intensity of a ns-DBD actuator ( $U = +7$  kV)

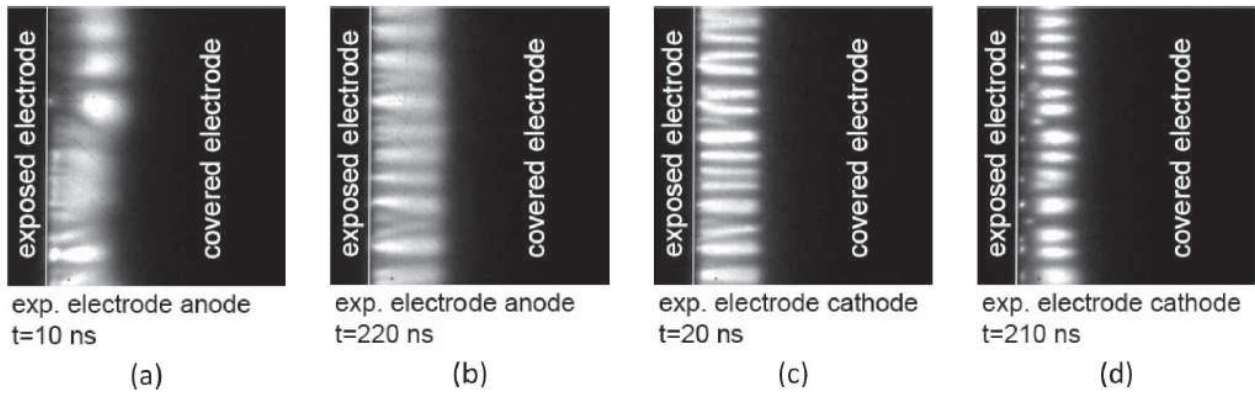


Figure 4: Top-view of the discharge development for homebuilt pulse generator. Cathode directed discharge during voltage rise (a) and fall (b). Anode directed discharge during voltage rise (c) and fall (d)

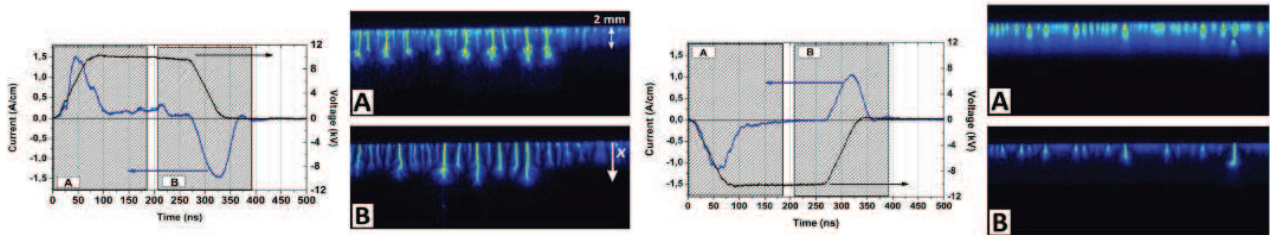


Figure 5: Current evolution and top-view of the discharge development for commercial pulse generator (exposure time of 180 ns). Top figure corresponds to a positive pulse of 10 kV while the bottom plot refers to a negative pulse of -10 kV (pulse width of 200 ns)

plasma discharge obtained by using the homebuilt system is provided in Figure 4. The figure shows the general pattern of the discharge during voltage rise and fall. During voltage rise (Figure 4a), a streamer discharge develops very fast, showing inhomogeneous light emission. The streamers start to develop from the edge of the upper electrode (anode) and propagate along the surface of the dielectric over the lower electrode (cathode). The emission intensity is very high close to the streamer heads. Between these and some bright spots at the edge of the upper electrode, almost no light is emitted. This first discharge is followed by a dark period also referred as “silent period” in [10]. When the voltage pulse ends, a second discharge develops showing a more homogeneous plasma distribution but also a slower propagation speed (Figure 4b). For the negative HV pulse (Figures 4c and 4d), the plasma exhibits an homogeneous pattern made of straight ionization channels.

Typical current evolution and top-view of the gas ionization at the dielectric surface are provided in Figure 5 for DBD actuator supplied by a commercial pulse generator. For the positive HV pulse, the rising and decaying periods produce a filamentary discharge. In its initial stage, the discharge is composed of many streamers distributed along the length of the exposed electrode and superimposed with a corona-like discharge. The straight filaments propagate up to 4 mm, at high speed (0.33 mm/ns in the first instants of the discharge) in the direction of the grounded electrode. During the decaying period of the positive voltage pulse, new plasma forms due to collection of positive charges deposited during the streamer propagation. The plasma is composed again by straight filaments with propagating speed of 0.1 mm/ns. However, the propagation line of the plasma discharge presents a wavy front. This may relate to a non-homogeneous deposition of charged particles at the di-

electric wall following the rising period. Nevertheless, the light emitted during the rising voltage period is stronger than the one for the decaying period. This is confirmed by the amplitude of the positive and negative current peaks (1.54 and 1.28 A/cm, respectively).

For the negative HV pulse, the plasma is diffuse and homogeneous along the edge of the active electrode, but some ionization channels are observed. These channels issued from corona spots and propagate with a plume shape that extends up to 2.5 mm. By comparison with a positive high voltage pulse, the filamentary regime, and then occurrence of streamer channels is here significantly reduced. The reduction in streamers results in a shortened discharge propagation that may explain that less energy is deposited on the wall surface.

Finally, the two experiments performed by using two different pulse generators produce differentiated plasma morphology. Results are in agreement when the first discharge is considered. One can say that a streamer discharge develops at voltage rise, while an homogeneous discharge forms at voltage decay. However, the plasma morphology is changed for the discharge related to the second current peak. The difference between the two experiments may result from a larger pulse width with the homebuilt pulse generator that permit a higher relaxation of charged species deposited by the first discharge and then reduce the occurrence of streamers during the voltage decay for positive pulse and voltage rise for negative high voltage pulse.

### 2.3 Induced pressure wave by nanosecond pulsed DBD

For DBD actuators supplied by high voltage nanosecond pulses, the produced local flow remains weak, subsequently it cannot be considered as the key parameter

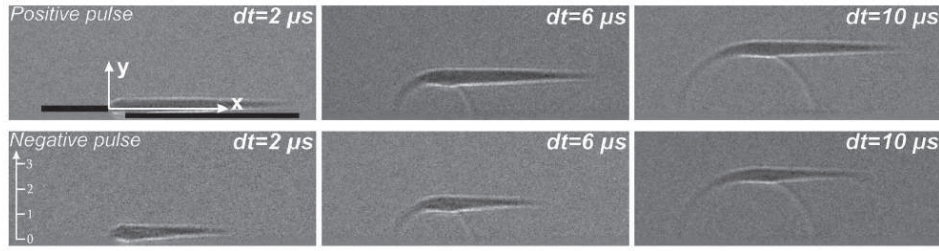


Figure 6: Zoomed visualizations of the propagating pressure wave for positive and negative pulses with width of 200 ns and amplitude of  $\pm 10$  kV (side view, scale in mm)

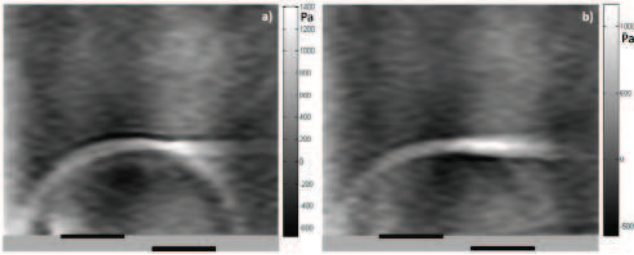


Figure 7: Pressure levels for +15 kV (left) and -15 kV (right) pulses at  $t = 20 \mu s$

in flow control scenario. As experimentally and numerically demonstrated, pulsed DBD conduces to a rapid energy deposition at the dielectric surface causing a sudden change in the pressure [11, 12]. This abrupt change in the pressure distribution gives rise to a localized pressure wave. It is actually presumed that the mechanism responsible for mitigation or elimination of flow separation is due to the interactions of the pressure wave with coherent flow structures when the wave propagates in the aerodynamic flow. More certainly, such actuator can have particular interest for delaying/promoting laminar-to-turbulent transition. In both cases, the mechanical quantity of primary importance for flow control applications is the produced pressure wave, its intensity and propagation speed. A series of experiments have been conducted to visualize and quantify these pressure waves. They are introduced in this section.

The propagation of the pressure wave produced by the nanosecond pulsed DBD is illustrated in Figure 6 for positive and negative HV pulses (side view). The shadowgraphy images give only qualitative views of the physical phenomenon but they show that the topology of the wave is composed of two distinct parts: A straight region at the top of an hemispheric region. The plate region initiates at the dielectric surface regardless of the pulse polarity. This plate region extends further in the case of a positive HV pulse in agreement with ICCD visualizations. It can be postulated that this part of the pressure wave relates to the streamer developing at the dielectric surface. Calculation of the propagation speed gives a value of 343 m/s, this suggesting that the pressure wave could relate to aeroacoustic noise propagation. This propagation speed is similar for positive and negative pulses of high voltage.

For convenient overpressure field value estimation a time-resolved interferometric imaging setup has been assembled (Mach-Zehnder interferometer). The expanded beam of a 632.8 nm He-Ne laser has been used to produce parallel fringes of equal thickness on a translucent screen at the apparatus outlet. The fringes have been arranged orthogonally to the actuator surface. The cmos sensor

(Photron Fastcam SA5 1000K-M2) is used to acquire the interference figure displayed on the screen. When the pressure wave is generated, the consecutive compression or expansion of the air inside the wave front results in refraction index modifications, which appear in the interference figure as fringe distortions. By measuring fringe shifts,  $\Delta\varphi$ , it is therefore possible to deduce the related index variations,  $\Delta n$ , with the following relation:

$$\Delta n = n - n_0 = \Delta\varphi \times \frac{\lambda}{2\pi L} \quad (1)$$

where  $n$  and  $n_0$  are refractive indices of respectively perturbed and unperturbed air (the latter is taken at room temperature),  $\lambda$  the laser wavelength and  $L$  the perturbation length. To use this equation it is assumed that the perturbation is independent from the coordinate orthogonal to the picture plane (2D assumption). For an ideal gas the pressure  $p$  is related to the refractive index by the Gladstone-Dale equation:

$$n = 1 + \frac{pK}{RT} \quad (2)$$

where  $K$  is the Gladstone-Dale constant for the laser wavelength and gas composition of interest,  $R$  the ideal gas constant and  $T$  the gas temperature. The latter is assumed to be constant and uniform, which is reasonable if dielectric heating consecutive to discharge running can be neglected. Finally, pressure variation can be deduced from phase shift by the following relation:

$$\Delta p = p_0 \times \frac{\Delta\varphi \times \lambda}{(n_0 - 1) \times 2\pi L} \quad (3)$$

Here, the acquisition system is used for an actuator with 100-mm long, 6-mm wide copper electrodes placed at a mutual gap distance of 3 mm on each side of a 0.4-mm thick dielectric (combination of 0.3-mm thick Mylar and two 50  $\mu m$  thick polyimide layers). The voltage pulse consisted in a nanosecond rise ramp (30 ns) followed by a millisecond range decay [13]. The pulse is obtained by triggering the closure of a fast Thyatron switch (Thyatron Perkin-Elmer HY-3002), in series with the actuator and a capacitor bank. The applied voltage peak value is  $\pm 15$  kV. The peak power value associated with this pulse is approximately 200 kW, and the corresponding dissipated energy per pulse is close to 0.3 mJ/cm.

According to this processing technique, the overpressure fields have been deduced and results for the two polarities at  $t = 20 \mu s$  are shown in Figure 7. The front shape is similar to those already observed with shadowgraphy (Figure 6) or Schlieren techniques [6]. It shows a pressure excess on one half of the circular part and on the planar part, and a pressure deficit on the second half of the circular part, situated above the plasma. The

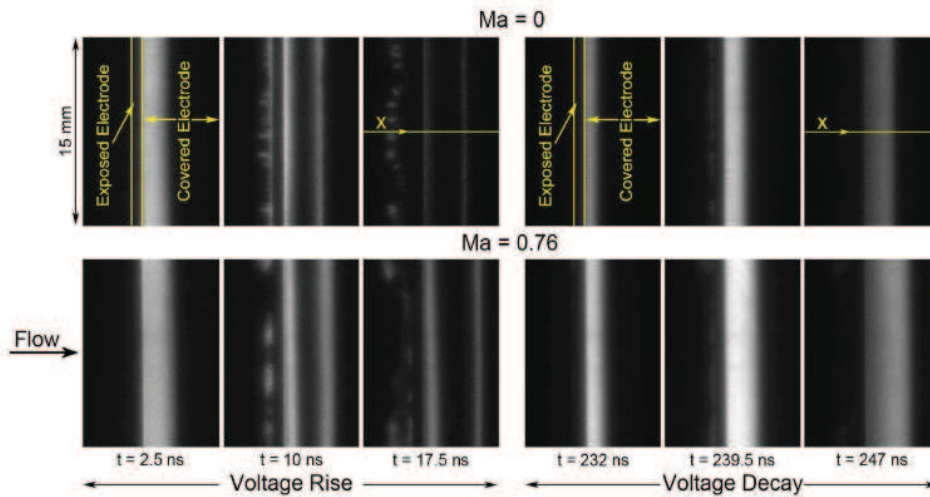


Figure 8: Impact of the flow on the plasma development during voltage rise (left) and fall (right)

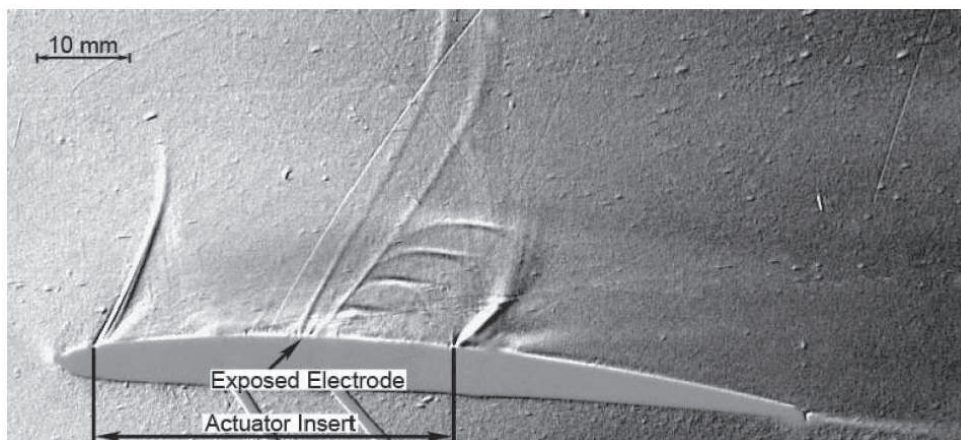


Figure 9: Influence of the flow on the DBD-generated pressure wave ( $Ma = 0.76$ ,  $\alpha = 4^\circ$ )

maximum pressure is obtained at the junction of cylindrical and planar parts. In the present conditions it is estimated to about 1500 Pa with positive pulse and 600 Pa with negative pulse. The minimum is about -600 Pa for positive pulses, and -200 for negative pulses. It confirms that negative discharges transfer a lower amount of energy to the pressure wave. Values agreeing well with simulations found in the literature [9] even if further setup improvements focusing on increasing phase shifts associated to pressure variations should be done to achieve a better resolution in pressure fields.

### 3 Nanosecond pulsed DBD operated in situation of transonic flow

Experiments in a transonic wind tunnel have been performed to investigate the characteristics of the ns-DBD in presence of a high speed flow ( $Ma=0.76$ ). The actuator is integrated on the suction side of a NACA 3506 (span of 40 mm and a length of 77.57 mm).

#### 3.1 Plasma morphology

Phase-averaged images of the discharge development were acquired with a Princeton Instruments PiMax ICCD camera. Figure 8 summarizes the development

of the discharge in the absence and presence of flow. An inhomogeneous discharge forms at voltage rise, with a discharge-front that separates from the plasma at the edge of the exposed electrode, whereas a homogeneous discharge is observed at voltage decay, which corresponds to the findings of the experiments without flow. However, the discharge propagation speed, its intensity as well as its extension are increased.

#### 3.2 Induced pressure wave

The propagation of the actuator induced pressure wave was investigated with phase-averaged schlieren images. The behaviour of the ns-DBD generated pressure wave in the presence of flow is shown in figure 9. It is the result of 4 superimposed phase-averaged schlieren images acquired from  $t = 10 \mu s$  to  $t = 40 \mu s$  after the discharge. The shape of this wave is similar to the experiments without flow but it moves downstream with the flow. The propagation speed normal to the DBD surface is still about 330 m/s and the downstream movement of its center corresponds to the flow speed. Due to the highly averaged nature of the schlieren images conclusions of the effect of the actuator on the flow cannot be drawn.

## 4 Conclusion

The present paper contributes to the body of knowledge on nanosecond pulsed DBD for flow control applications. In particular, it is demonstrated that the actuator can produce a pressure wave presumably useful for flow separation control, this by using different technologies of pulse generators. For the first time, a measure of the pressure level of the induced pressure wave is proposed. Furthermore, it is shown that pressure wave can also be produced in condition of transonic flow regime. However, several partners of the project had to face with difficulties when such actuators are used in wind-tunnel experiments. Indeed, this type of discharge can produce electromagnetic interferences resulting in strong signature of HV pulses in the acquired data or perturbations on the acquisition system.

## Acknowledgments

The work has been carried out as a part of PLASMAERO program with funding from the European Community's Seventh Framework Programme FP7/2007-2013 under grant agreement nr. 234201.

## References

- [1] N. Benard, E. Moreau, 2012, *EHD Force and Electric Wind Produced by Plasma Actuators Used for Airflow Control*, AIAA paper 2012-3136.
- [2] D. Roupasov, A. Nikipelov, M. Nudnova, and A. Starikovskii, 2009, *Flow separation control by plasma actuator with nanosecond pulsed-periodic discharge*, AIAA J., Vol. 47, pp. 168-185.
- [3] J. Little, K. Takashima, M. Nishihara, I. Adamovich, and M. Samimy, 2012, *Separation Control with Nanosecond-Pulse-Driven Dielectric Barrier Discharge Plasma Actuators*, AIAA J., Vol. 50, pp. 350-365.
- [4] S.M. Aulchenko, V.P. Zamuraev, and A.P. Kalinina, 2009, *Control of the aerodynamic characteristics of wing airfoils by nonstationary energy supply in transonic flow*, J. Engineering Physics and Thermophys., Vol. 82, pp. 16, 20.
- [5] I.A. Znamenskaya, D.F. Latfullin, A.E. Lutskii, and I.V. Musenkova, 2010, *Energy deposition in boundary gas layer during initiation of nanosecond sliding surface discharge*, Techn. Phys. Letters, Vol. 36, pp. 795-797.
- [6] K. Takashima, Y. Zuzeeq, W.R. Lempert, and I.V. Adamovich, 2011, *Characterization of surface dielectric barrier discharge plasma sustained by repetitive nanosecond pulses*, Plasma Source Sci. Technol., Vol. 20, pp. 055009.
- [7] N. Benard, N. Zouzou, A. Claverie, J. Sotton, and E. Moreau, 2012, *Optical visualization and electrical characterization of fast-rising pulsed dielectric barrier discharge for airflow control applications*, J. Applied Physics, Vol. 111, 033303.
- [8] J. Little, and R. Dawson, 2012, *Characterization of Nanosecond Pulse Driven Dielectric Barrier Discharge Plasma Actuators for Aerodynamic Flow Control*, AIAA paper 2012-188
- [9] T. Unfer, and J.P. Boeuf, 2010, *Modeling and comparison of sinusoidal and nanosecond pulsed surface dielectric barrier discharges for flow control*, Plasma Phys. Control. Fusion, Vol. 52, pp. 124019.
- [10] A.Y. Starikovskii, A.A. Nikipelov, M.M. Nudnova, M.M., and D.V. Roupasov, 2009, *SDBD plasma actuator with nanosecond pulse-periodic discharge*, Plasma Sources Sci. Technol., Vol. 18, pp. 034015.
- [11] I.A. Znamenskaya, D.F. Latfullin, A.E. Lutskii, A.E., and I.V. Musenkova, 2010, *Energy deposition in boundary gas layer during initiation of nanosecond sliding surface discharge*, Techn. Phys. Letters, Vol. 36, pp. 795-797.
- [12] T. Unfer, and J.P. Boeuf, 2009, *Modelling of a nanosecond surface discharge actuator*, J. Physics D Applied Physics, Vol.42, pp.194017.
- [13] H. Rabat, J. Pons, D. Hong, and A. Leroy, 2011, *Study of an atmospheric surface barrier discharge actuator using a nanosecond rising high-voltage power supply*, Proc. 20th Int. Symp. in Plasma Chem., Philadelphia, USA, July 24-29, 2011.

# THE PLASMA SYNTHETIC JET ACTUATOR FOR SEPARATION CONTROL

D. Caruana<sup>1</sup>, J.P. Cambronne<sup>2</sup>, P. Barricau<sup>1</sup> and A. Belinger<sup>2</sup>

<sup>1</sup>ONERA - DMAE department - Toulouse Centre - 2, Av. Edouard Belin - 31055 Toulouse - France

daniel.caruana@onera.fr

<sup>2</sup>LAPLACE, UMR 5213, Toulouse University - 118 route de Narbonne - 31062 Toulouse - France

jeanpascal.cambronne@laplace.univ-tlse.fr

## Abstract

Practical application of active flow control is dependent upon the development of robust actuators that are reliable, small, easy to integrate, have no delay. ONERA/DMAE department and CNRS/Laplace laboratories study and develop Plasma Synthetic Jet actuators, PSJ, in order to demonstrate the potential of such electrical devices to act on aerodynamic phenomena like separated flows. The characterisation of the pulsed jet produced by a PSJ actuator is investigated with experimental techniques, helping the validation of theoretical and numerical studies carried out in parallel. This article mainly describes experimental studies on the characterization of the PSJ device with and without flow and on the ability of the PSJ actuators to reduce separated flow region on a decelerating ramp. The PSJ actuators efficiency has been quantified using the PIV technique in order to estimate the decrease of the separated flow region induced by the actuation and consequently the drag reduction.

## Nomenclature

C	=capacity of the power supply's capacitor
E	=energy transferred to the Plasma Synthetic Jet
IGBT	=insulated-gate bipolar transistor
F	=frequency of the discharge (Hertz)
M0, U0	=free stream Mach number, velocity (m/s)
PIV	=Particle Image Velocimetry
T	=temperature (K)
V	=plasma jet velocity (m/s)
V <sub>b</sub>	=Voltage breakdown of the air gap (Volt)

## 1 Introduction

Flow control with active actuators requires efficient, robust, easy to integrate and low energy consumption devices. Inspired by the "sparkjet" device, proposed by Grossman [1] from the Hopkins University of Applied Physics Laboratory, ONERA, in cooperation with CNRS/LAPLACE laboratory, studies and develops a very promising synthetic jet plasma generator, which can produce a high-velocity synthetic jet without any moving part and without any external fluid injection. In order to determine the operational characteristics of this actuator needed for flow control and to improve its conception, several studies are conducted by ONERA/DMAE and CNRS/LAPLACE in the framework of the PLASMAERO project funded by the European Community into a specific task which deals with the demonstration

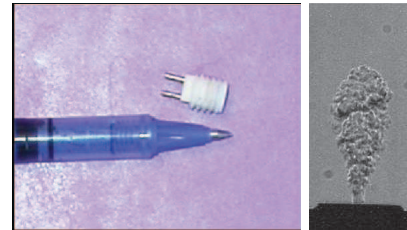


Figure 1: PSJ device ( $\phi = 8\text{mm}$ ), generated micro-jet

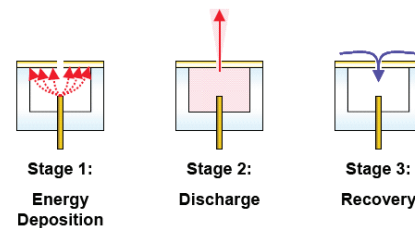


Figure 2: Principle of functioning of the PSJ

for these devices to be able to postpone the trailing edge separation phenomenon occurring in a high lift configuration (low velocity, high incidence angle).

## 2 Description and principle of the PSJ actuator

PSJ is a zero-net-mass-flux device mainly composed of 2 electrodes embedded in a cavity manufactured in a ceramic material, in connection with the external medium with the help of a small dedicated orifice (fig. 1). By applying a voltage difference greater than the disruptive voltage of the gas located inside the cavity (5 kV for ONERA's actuators), an electrical arc is created between the 2 electrodes, leading to an increase of the internal energy. Because the air is confined, the temperature and the pressure increase very quickly inside the cavity. The fluid relaxation can be realized through the dedicated orifice, producing a pulsed air jet. At the end of this blowing phase, the cavity pressure drops under the external pressure value, activating a suction stage inside the cavity. The actuator is ready for another cycle (fig. 2).

The characteristics of this device depend on the cavity geometry, the energy deposition and on the electrical parameters. In order to create the discharge, a high power supply is essential. Developed by Laplace laboratory, the solution using a low voltage power supply associated to a high voltage transformer (m) and a transistor (IGBT) has been chosen, (fig. 3) [2]. The IGBT can be easily

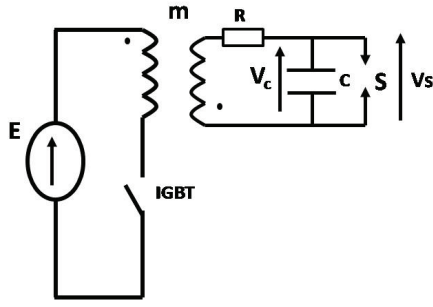


Figure 3: Capacitive power supply

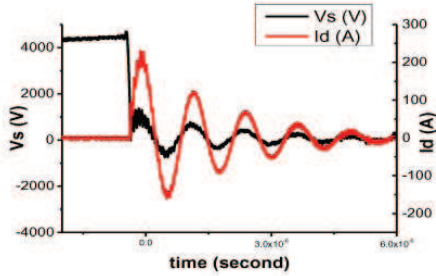


Figure 4: Discharge and current voltage - C=15 nF

controlled to adjust the frequency and the energy accumulated in the transformer. This power supply can control the frequency, the phase and the energy dissipated in the discharge for each device itself. The maximum of frequency actuation is 2000 Hertz for a capacitor value of 20nF and can be increased for lower capacitor values. The delay can be undependably fixed for each PSJ (the precision is less than one micro-second).

### 3 Electrical characterization of the PSJ

PSJ actuator is connected to the capacitor by a wire, which is modeled as an inductance of  $2 \mu\text{H}$  and a resistance of  $0.5\Omega$ . These considerations allow the calculation of the voltage of the discharge from the current and the capacity voltage measurement. During the ignition time, discharge voltage falls to zero in a few nanoseconds (fig. 4). Following ignition, the current and the voltage discharge are sinusoidal and in phase. This suggests that plasma in the PSJ actuator behave as a resistance. Calculations, not provided in this paper, show that the value of the resistance can amount to several ohms. Therefore, the plasma is very conductive. This explains that the temperature of the plasma is higher than 10 000K.

Furthermore, the maximum current is proportional to the breakdown voltage, and in all the case higher than 100 A during a few nano-seconds.

The evolution of the luminosity of the discharge has been obtained using short exposure time photography taken with an intensified CCD camera (Fig. 5). The maximum luminosity is however three times more intense for 15 nF than for 5 nF. It is relevant that the luminosity of the discharge decreases with the time; indeed the current diminishes also with the time. For the two cases, the behaviour is similar; the discharge looks cylindrical as the luminosity is shared out symmetrically between the two electrodes. After the ignition ( $t > 600 \text{ ns}$ ), the discharge is homogenous and the diameter of the discharge does not change. Furthermore the height

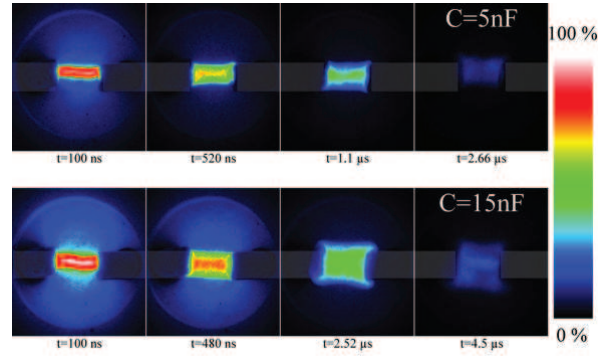


Figure 5: ICCD images of light emission for two different capacitances (5nF and 15 nF)

of the discharge is wider for 15nF (and covers the electrodes) than for 5 nF. Consequently the 15 nF discharge heats larger volume of gas and for longer times than the 5 nF discharge.

### 4 Aerodynamic characterization of the PSJ

The characteristics of the micro-jet produced by the PSJ actuator are closely connected to the electrical energy ' $E_c$ ' loaded in a capacitor before being transferred to the device after the breakdown outbreak. This energy level depends on the breakdown voltage ' $V_b$ ' and the capacitor value ' $C$ ' according to the following formula:  $E_c = 0.5 \times C \times V_b^2$ . The maximal jet velocity can reach  $280 \text{ m.s}^{-1}$  with a temperature level of about 400K (figure 6-up), depending on the capacitor value and the running frequency which can be up to 2000 Hertz. For a given frequency, a saturation effect appears on the velocity levels when the capacitor value is increased, because the heating of the device induces a dropping of the breakdown voltage and consequently a decrease of the electrical energy transferred during the spark discharge. The heating is also responsible of the velocity decrease induced when the running frequency is increased. As the PSJ actuator produces a pulsed jet with a quasi-constant duration of  $150 \mu\text{s}$ , the duty cycle increases linearly with the frequency as it can be noticed on the figure 6 - down [3] and [4].

### 5 Flow control strategy - PSJ/flow interaction

The strategy retained to delay the flow separation in subsonic configuration, is to use PSJ actuators as vortex generator devices. The produced longitudinal vortices should increase the momentum in the lower part of the turbulent boundary layer, in order to reduce its sensitivity to adverse pressure gradients as showed by Lin [5]. Even if experimental and numerical results about synthetic jets are less widespread, these devices have received a great amount of attention from the fluid dynamics community as mentioned by Gilarranz [6].

The vortex generated by the interaction between the main flow and the jet produced by a PSJ actuator embedded in a model has been characterized in subsonic flow, for a zero pressure gradient configuration, by using the PIV technique. This experimental work was conducted into a subsonic ONERA wind tunnel. For these

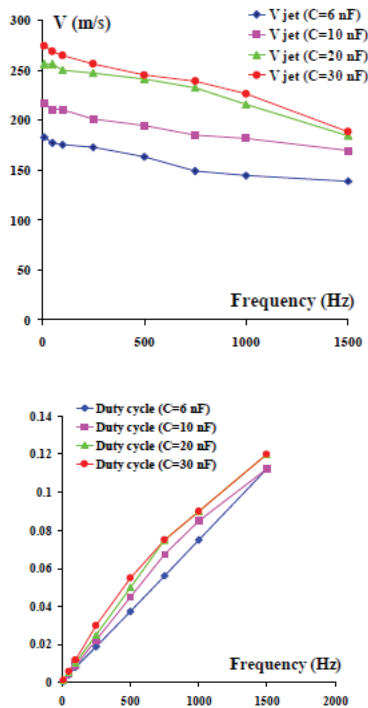


Figure 6: Micro-jet velocities and duty cycle versus PSJ running frequency

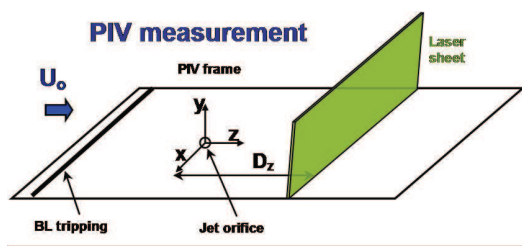


Figure 7: Geometric configuration implemented for the PIV measurements

tests, a flat plate has been mounted into the test section equipped with glass windows dedicated to optical diagnostic techniques. The PSJ actuator was located 250 mm downstream the leading edge of the flat plate. The values of the pitch " $\alpha$ " and skew " $\beta$ " angles for the jet exhaust were fixed at  $30^\circ$  and  $60^\circ$  respectively, in order to produce a vortex issued from the interaction between the jet and the main flow. Because these angular values have been chosen from computation results performed on a continuous jet blowing configuration, complementary tests have been carried out in order to check the suitability of this exhaust jet direction and particularly of this brief impacting generated pulsed jet. The incoming boundary layer was tripped with a 0.8 mm diameter cylindrical rod located 200 mm upstream the PSJ actuator in order to obtain a fully developed turbulent boundary layer in the vicinity of the jet. In this case, the boundary layer thickness was 8 mm for an upstream velocity equal to 40 m/s. The 3-component PIV technique has been implemented to characterize the formation of the vortex and also its convection by the main flow, by using phase-shifting time-averaged measurements. The spark discharge into the PSJ actuator has been chosen for the origin of the time scale (" $T_0$ "). The figure 7 shows the geometric configuration implemented for the PIV technique. The acquisition of phase-averaged ve-

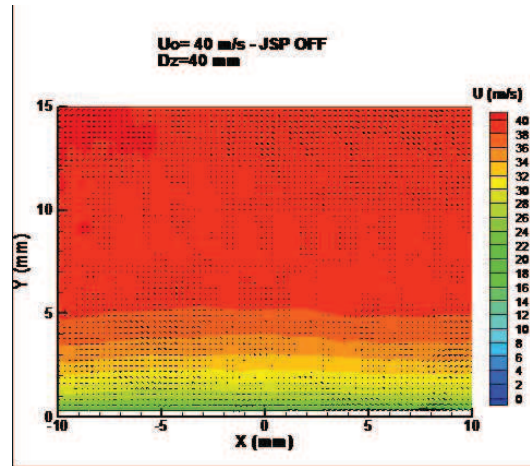


Figure 8: Baseline  $V_{flow} = 40\text{m/s}$  - JSP Off

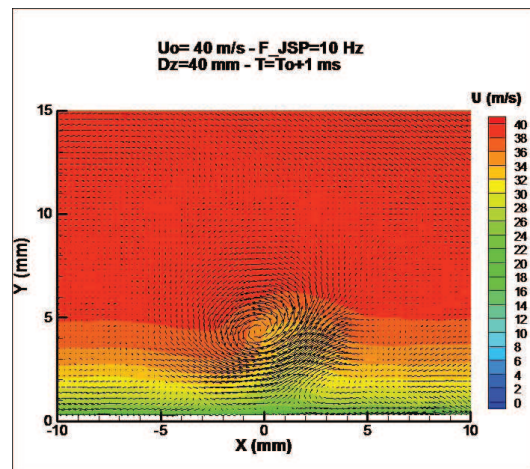


Figure 9: Micro-jet / flow interaction - Generated vortex ( $U$  velocity) -  $V_{flow} = 40\text{m/s}$  - JSP On

locity fields has been done in a cross plane configuration, for 5 equidistant " $D_z$ " stations, from 20 mm to 100 mm downstream the jet exhaust. The frequency of the spark discharge and then for the jet production was fixed at 10 Hz. The delay " $T$ " defined to capture phase averaged PIV measurements has been varied from 0 to 1.6 ms with a 50 ms step. The figures 8, 9, 10 and 11 present the results obtained at  $D_z=40$  mm station for a capacitor value of 20 nF mounted in the power supply circuit. This capacitor value leads to an energetic level of 90 mJ transferred to the actuator. The figure 8 shows the velocity field obtained with PSJ actuator switched-off (baseline case). The figures 9 and 10 describe the evolution of the vortex (velocity and vorticity). The detection of the vortex can be realized by using vorticity computation on PIV data. A vertical velocity profile obtained at  $X=-2$  mm for a delay value of  $T=T_0+1$  ms is presented in figure 11, showing the momentum increase into the boundary layer, generated by the vortex issued from the interaction between the JSP actuator and the flow. These PIV results have been exploited to extract the duration of the vortex in the different cross planes ( $500 \mu\text{s}$ ). Also, the elevation of the vortex along the longitudinal axis has been brought to light. If we make the assumption that this coherent structure is convected with a velocity close to the upstream velocity (40 m/s), we can determine its trajectory along the flat plate. The figure 12-up shows the vortex location estimated at the different cross plane stations implemented for the PIV technique. The

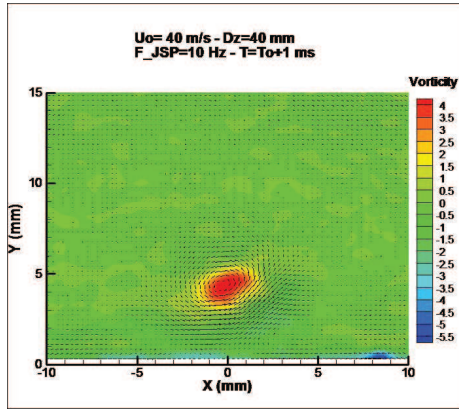


Figure 10: Micro-jet / flow interaction - Generated vortex (vorticity) -  $V_{flow} = 40m/s$  - JSP On

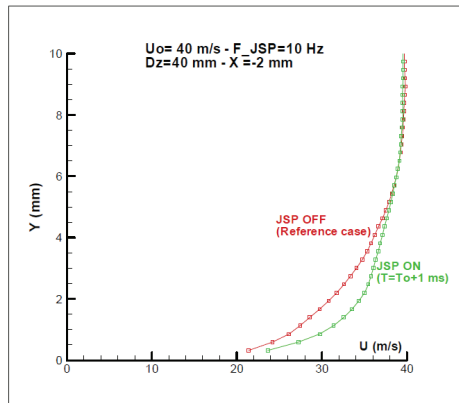


Figure 11: Micro-jet / flow interaction - Generated vortex (Velocity profile) -  $V_{flow} = 40m/s$

colours are connected to the vorticity levels. We can notice that the vortex comes up to 6 mm away from the wall at  $Dz=100$  mm station. As this elevation remains too important to get sufficient momentum from the external part of the boundary layer in order to make it more stable and then to delay the separation. The vortex generated by a less energetic PSJ actuator has been investigated, using a smaller value for the capacitor ( $C=5$  nF /  $E_c=20$  mJ) mounted into the electric circuit dedicated to the power supply of the PSJ actuator.

The figure 12-down shows the location of the vortex generated by the PSJ actuator for 2 energy levels (20 mJ and 90 mJ), obtained at 3 different "Dz" stations ( $Dz=20$  mm,  $Dz=40$  mm,  $Dz=60$  mm). We can notice that reducing the energy level does not really impact the elevation of the vortex but leads to a decrease of the vorticity levels. For the lower energy case, the vortex vanishes earlier. As the jet remains very impacting, even with a lower energy level, the trajectory seems to be fixed by the orientation angles of the jet exhaust.

## 6 Assessment of the PSJ actuators efficiency on separation - Separation delay on a ramp

In order to investigate the efficiency on separation of the vortices generated by the interaction between the jet produced by PSJ actuators and the main flow, a ramp model has been manufactured and wind tunnel tests performed. This model is composed with 2 parts. The first one con-

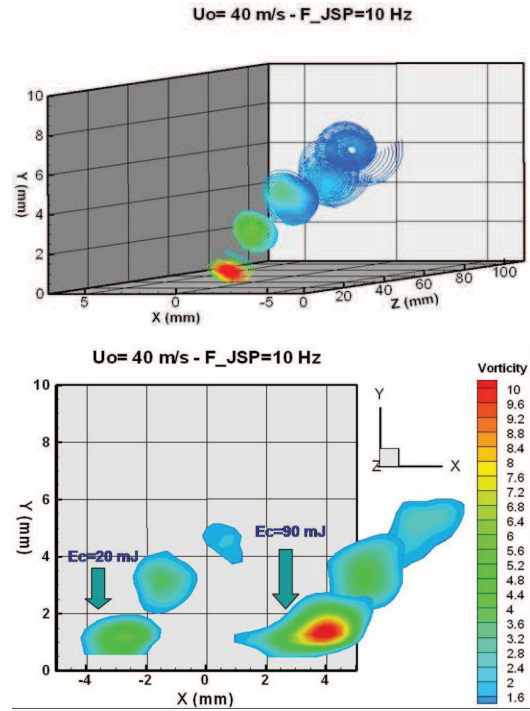


Figure 12: Micro-jet / flow interaction - Generated vortex (vorticity) -  $V_{flow} = 40m/s$  - JSP On



Figure 13: Ramp model into the WT test section

cerns the accelerating ramp followed by a plateau. In the downstream region of this plateau, an insert has been manufactured in order to receive 5 PSJ actuators (Fig. 13 & 14). The second part concerns the decelerating ramp with an angle of 20 degrees. RANS computations have been performed to optimize the geometry of the model.

Five PSJ exhausts have been distributed along 2 lines (fig. 14). The incidence and skew angles for the PSJ exhausts remain the same compared to the previous experiments carried out for the zero pressure gradient configuration ( $\alpha=30^\circ$ ;  $\beta=60^\circ$ ). The boundary layer has been tripped in order to have a fully turbulent boundary layer in the vicinity of the actuators. Experimental results have been obtained for three different upstream velocities (20 m/s, 30m/s and 37 m/s), using the 2-component PIV technique in order to characterize the separation generated in the decelerating ramp area (Fig. 15 & 16).

For each aerodynamic configuration, the baseline case (PSJ OFF) shows the expansion of the separated flow in the decelerating ramp region, represented in dark blue in the figures. In the lower velocity case (20 m/s), the separated region starts very closely to the edge of the decelerating ramp. The decrease of the size of the separated

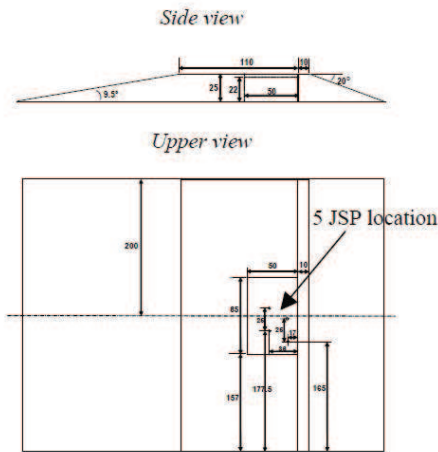


Figure 14: Geometry of the ramp model and location of the PSJ exhausts

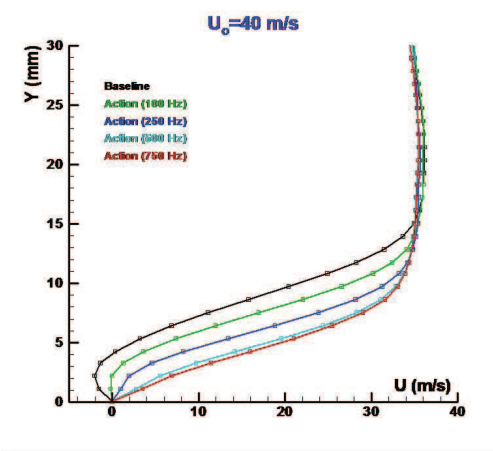
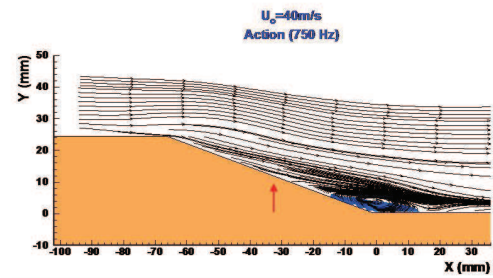
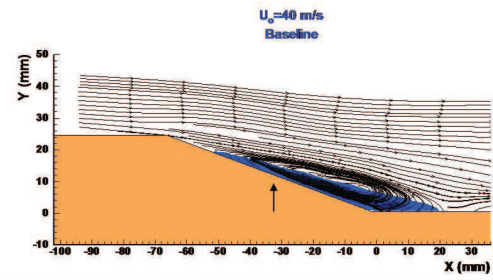


Figure 16: PIV measurements of the streamlines and the separation area, PSJ off and on -  $V_{flow} = 40m/s$

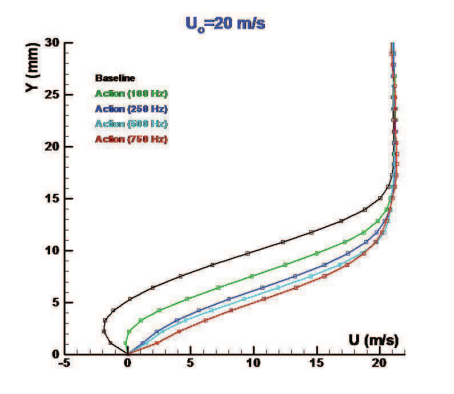
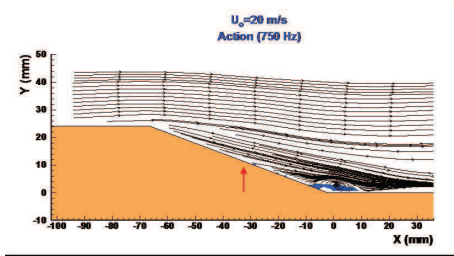
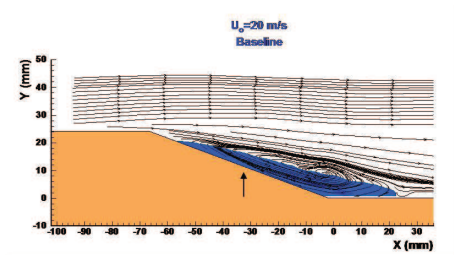


Figure 15: PIV measurements of the streamlines and the separation area, PSJ off and on -  $V_{flow} = 20m/s$

flow area induced by the PSJ action is very significant as it can be noticed on the mean velocity field obtained with the PIV technique. Vertical profiles of the longitudinal velocity obtained in the middle of the decelerating ramp are given. The effect of the PSJ actuators running frequency is clearly demonstrated on these profiles. Even at low frequency levels (100 Hz), the separated region is reduced. The best reduction is obtained for the maximal frequency tested (750 Hz) even if a saturated level seems to be achieved from the frequency of 500 Hz. In this case, the separated region is confined in the lower part of the decelerating ramp. The implementation of PSJ actuators in the middle of the decelerating ramp could cancel this small separated flow region. The PSJ efficiency is also demonstrated for higher velocity configurations (up to 37 m/s) even if the remaining separated area located in the lower end of the ramp is larger than in the case of the low velocity configuration. In these cases, we can also notice the saturation effect on the decrease of the separated area, obtained for a running frequency greater than 500 Hz.

This experimental facility should be helpful to study the interaction between the vortices generated by a group of PSJ actuators and the mean flow, one of the keys of control strategy description.

## 7 Conclusions

During PLASMAERO project, the PSJ has been developed and characterised in order to delay airfoil leading edge separation. Mass flow creation by plasma is used to add energy to the flow to improve it. The general physics of the PSJ in flow concerns the generation of a series of vortices produced at the pulse frequency which induces a transfer of momentum towards the wall, with a stabilizing effect on the turbulent boundary layer, quite similarly as continuous jets, with of course the advantage of zero mass flow. It is expected that the reaction of the flow to the generated micro-jet is the key point for understanding the influence of the various parameters. The basic ramp configuration has been a very useful tool to understand better the physics of this action and to determine the parameters driving the efficiency of these devices. The efficiency of PSJ devices on high lift airfoil separation is demonstrated in M. Forte & All. paper by following in this document.

## Acknowledgments

The present work has been performed within the framework of the PlasmAero project ([www.plasmaero.eu](http://www.plasmaero.eu)) funded by the European Community's Seventh Frame-

work Program FP7/2007-2013 under grant agreement nr. 234201.

## References

- [1] Grossman K.R., Cybyk B.Z. and Wie D.M.V. *Spark-Jet actuators for flow control*, AIAA 2003-0057.
- [2] A. Belinger & al.- *Influence of the energy dissipation rate in the discharge of a plasma synthetic jet actuator*. J.Phys.D : Appl. Phys. 44
- [3] D. Caruana & al. - *The "Plasma Synthetic Jet" Actuator - Aero-thermodynamic characterisation and first Flow Control Application* - AIAA-2009-1307
- [4] P. Hardy & al. *Plasma Synthetic Jet for Flow Control* - AIAA-2010-5103
- [5] Lin J.C. *Control of Turbulent Boundary-Layer Separation using Micro-Vortex Generator*, AIAA 99-3404
- [6] Gilarranz J.L. & All, *A New Class of Synthetic Jet Actuators*, Journal of Fluids Engineering, March 2005, Vol. 127 /377-387.

# NUMERICAL MODELING OF PLASMA ACTUATORS

K. Kourtzanidis<sup>1,2,3</sup>, F. Rogier<sup>1</sup>, G. Dufour<sup>1</sup>, J.P. Bœuf<sup>2</sup>, T. Unfer<sup>2</sup>

<sup>1</sup>ONERA - DMAE department - Toulouse Centre - 2, Av. Edouard Belin - 31055 Toulouse - France

François.Rogier@onera.fr

<sup>2</sup>LAPLACE, UMR 5213, Toulouse University - 118 route de Narbonne - 31062 Toulouse - France

Jean-Pierre.Boeuf@laplace.univtlse.fr

<sup>3</sup>I.S.A.E. - 10 Avenue Edouard Belin - 31400 Toulouse - France

k.kourtzanidis@onera.fr

## Abstract

Plasma actuators provide an innovating and promising method for flow control applications in aeronautics. In this article, numerical models for three different types of such actuators (DBD, DBD-nanosecond, PSJ) are presented. These models are based on the coupling of plasma equations with fluid ones under different assumptions and numerical schemes for each case, having as goal accurate simulations in reduced CPU time. With these models, parametric studies along with simulations that demonstrate the actuators' promising effects for flow control could be performed and are also presented here.

## Nomenclature

C	=capacity of the power supply's capacitor
E	=energy transferred to the Plasma Synthetic Jet
IGBT	=insulated-gate bipolar transistor
F	=frequency of the discharge (Hertz)
M0, U0	=free stream Mach number, velocity (m/s)
PIV	=Particle Image Velocimetry
T	=temperature (K)
V	=plasma jet velocity (m/s)
V <sub>b</sub>	=Voltage breakdown of the air gap (Volt)

## 1 Introduction

Practical applications of active flow control depends on the development of robust actuators that are reliable, small, easy to integrate and have no delay.

The modeling was mainly divided in two tasks corresponding to two kinds of plasma actuators. The first one was dedicated to the development of sinusoidal and nanosecond DBD actuators and the second one was concerned by the Plasma Synthetic jet.

A code has been developed in LAPLACE and the objective was to use this code to perform simulations of DBD actuators in various configurations. The output of the code provide the body force as well as the amount of energy deposited by the plasma that serves as input to compute the action of the flow by a CFD code. Parametric studies have been systemically done and compared with experimental results. These computations provide a database that will be useful to analyze any actuator's effects. A floating electrodes configuration (concept proposed by IMP) as well as a ns-DBD (Dielectric Barrier Discharge operating with nanosecond rise-time voltage pulses) actuator were also simulated.

A code describing the operation of the plasma syn-

thetic jet has been written during the project. Numerical results have been successfully compared with experimental results and the quasi static regime has been determined. But, this study will be complete when a characterization of the JSP will be achieved. Until now, the trends with PSJ parameters, like frequency, capacity and geometry are correct. It provides also some results about the optimal geometry of the neck to improve the performances of this actuator.

## 2 Modeling of Dielectric Barrier Discharge

The sinusoidal DBD regime is based on momentum transfer from ions to the neutral gas along the dielectric surface of the DD. This form of action takes place under typical DBD operating conditions, i.e. for sinusoidal voltages with frequencies in the [0.1-10 kHz] range. The action of the plasma on the flow can be computed as the result of a "body force" that appears in the right hand side of the flow momentum equation.

In the case of ns-DBD, the voltage between the electrodes increases in a very short time (ns) and the discharge regime is quite different from the one described above for a sinusoidal voltage waveform. A large amount of energy is deposited by the discharge at the tip of the top electrode and is quickly converted into gas heating. The plasma effect is then represented by adding to the energy equation the heating power due to the plasma.

The model used to calculate the body force of surface DBDs and of the energy deposited by ns-DBDs has been developed at LAPLACE laboratory and is based on the detailed description of charged particle transport in a coalitional plasma (including charging of the dielectric surface) coupled with Poisson's equation for the electric field. One consider only one type of positive ion and one type of negative ion with a basic chemistry including ionization, attachment, and recombination (Ref. [1]). These simulations require to integrate the different times scales of all particles which are active in the plasma. Then, the price to pay is the large computational time. To deal with this, a specific numerical method has been developed at LAPLACE using the concept of asynchronous adaptive model (Ref. [2] and figure 1 show the mesh used in a typical simulation of a sinusoidal DBD). Such modeling has the great advantage to provide predictable results, in the contrary of empirical models developed by others groups. The code ASYNCO from LAPLACE has been intensively used to perform these simulations: it integrates the plasma equations

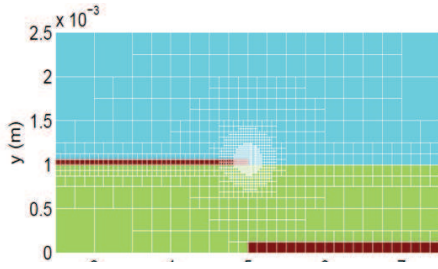


Figure 1: Mesh used in a typical simulation of a sinusoidal DBD

and a new version coupling Navier-Stokes equations and plasma equations have been also implemented. It serves to some validations in simple cases.

### Test case computation for sinusoidal DBD

The test case with 500 $\mu$ m dielectric layer and 15kV at 2 kHz was chosen to serve as an illustrative example. The evolution in time of the total time averaged horizontal force and its space distribution at  $t=2$ ms is shown on Figures 2. The first chart shows that after 3 to 4 periods of the sinusoidal voltage the time-averaged force has reached a steady state value. It also shows that the negative part (upstream) of the force is negligible whereas in the space distribution, negative forces are present with high values. However these negative forces are located in a very small volume near to the electrode tip. This is mainly due to the presence of a cathode sheath in the phases where the upper electrode plays the role of a cathode (negative phase).

The sinusoidal DBD regime is based on momentum transfer from ions to the neutral gas along the dielectric surface of the DBD. This form of action takes place under typical DBD operating conditions, i.e. for sinusoidal voltages with frequencies in the [0.1-10 kHz] range. The action of the plasma in the flow can be computed as the result of a "body force" that appears in the right hand side of the flow momentum equation.

In the case of ns-DBD, the voltage between electrodes increases in a very short time (ns) and the discharge regime is quite different from the one described above for a sinusoidal voltage waveform. A large amount of energy is deposited by the discharge at the tip of the top electrode and is quickly converted into gas heating. The plasma effect is then represented by adding to the energy equation the heating power due to the plasma.

## 3 Parametric study over a 1mm thick dielectric plate

A parametric study has been conducted to compute the total time-averaged force created by a DBD made of a 1mm thick dielectric layer ( $\epsilon_r=5$ , corresponding to PVC for instance) and driven by different voltages and frequencies. Three different frequencies have been studied 2, 5 and 10 kHz with applied voltage amplitudes ranging from a few kV to 30 kV. The results of this parametric study are shown on Figure 2a and compare well to experimental measurements (figure 2b). The plasma code has been strongly coupled with a Navier-Stokes solver and fully coupled plasma/airflow simulations have been performed. Some investigations have also been done recently for the conventional DBD, the main issue is as usual the computational time. With recent optimisation it is possible to simulate the first few cycles of the dis-

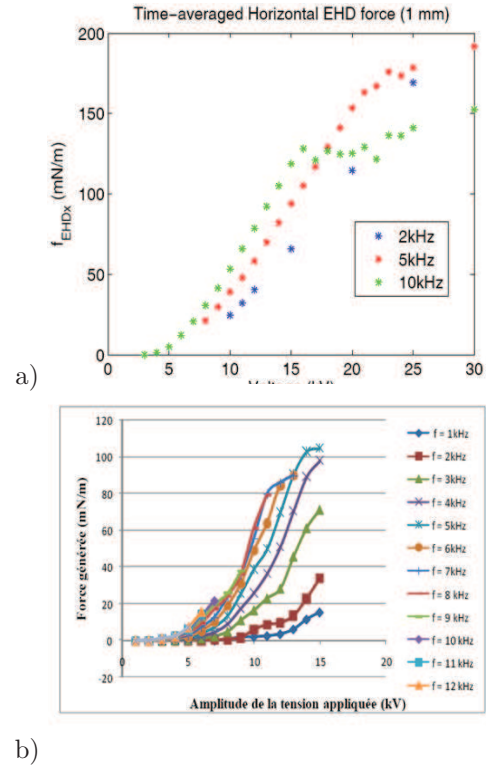


Figure 2: Parametric study on voltage and frequency for a sinusoidal 1mm thick DBD - a) Numerical results; b) Experimental results

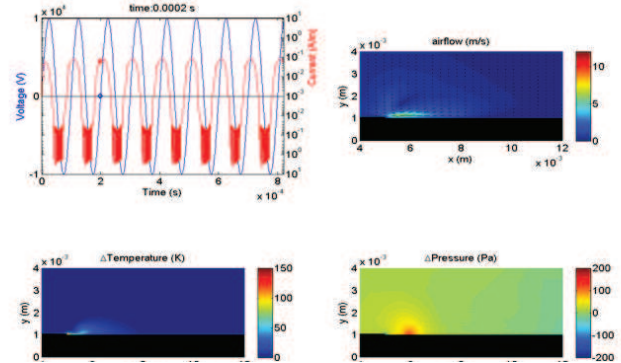


Figure 3: Numerical results for a 2kHz/10kV sinus applied on a 500 $\mu$ m thick DBD actuator

charge in a fully coupled manner. Two test cases have been simulated a 2kHz/10kV sinus applied on a 500 $\mu$ m thick DBD (Figures 3) and a 10kHz/10kV sinus applied on a 1mm thick DBD.

## 4 Simulation of the sinusoidal DBD experiment with floating electrodes (IMP experiment)

We recently tried to simulate the multi-stage DBD experiment done at IMP with a floating electrode. New features have been added to the code to properly take into account the floating electrodes. Basically it consists in adding one more equation in addition to Poisson's to also solve for the floating electrode potentials. These equations are simply Gauss' law applied to the floating electrodes, the total charge on the floating electrode being deduced from the plasma simulation.

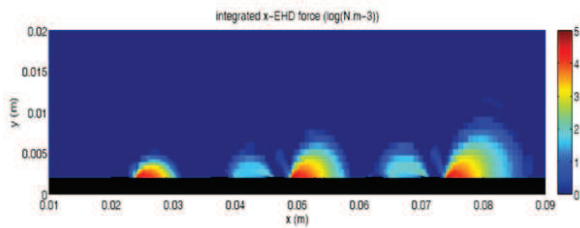


Figure 4: Time-averaged horizontal EHD force - Floating electrode configuration

The distribution of the time-averaged horizontal EHD force is displayed on Figure 6. The total integrated horizontal force is in this case 186 mN/m which corresponds to an average of 62 mN/m per stage. This value is reasonable when comparing with the parametric study of section 3 (in this case the dielectric thickness is 2 mm not 1). The use of floating electrode successfully prevented the backstroke from the next grounded upper electrode. There is indeed a pull between the end of the floating electrode and the next grounded electrode, but this force is 2 to 3 order of magnitude smaller.

## 5 Nano Pulsed Dielectric Barrier Discharge

If the voltage between electrodes increases in a very short time, the discharge regime is quite different from the one described above for a sinusoidal voltage waveform. While the sinusoidal DBD regime can be compared with a transient corona regime (sometimes interrupted by streamers developing along the surface), the “nanosecond regime” is characterized by the development of synchronized, high current streamers at each rise or decay of the voltage, without any corona phase. Due to the fast rise of the applied voltage, the discharges are initiated at a voltage much higher than the breakdown voltage, leading to a high current pulse. Because there is no corona phase, the momentum transfer from ions to the neutral gas is small, and the “ion wind” generated by these discharges is negligible. Ion wind can only be generated in unipolar regions (regions where the density of one species, positive or negative ions, is dominant). Such regions exist in corona discharges, but not in streamer discharges where the plasma is quasineutral and the force due to electrons and negative ions balances the force due to positive ions, leading to a zero net EHD force.

Nevertheless, recent experiments have shown that these discharges can have a significant effect on a flow (e.g. reattachment) for higher flow velocities than sinusoidal DBDs. Our recent work, Ref. [3], shows that during nanosecond discharges, a large amount of energy is deposited by the discharge at the tip of the top electrode. A large part of this energy is quickly converted into gas heating. The numerical models (discharge model + Navier Stokes equations) show that the fast heating in this small region is responsible for the generation of micro-shock waves. These pressure waves could be responsible for the observed effect on the flow (work is still necessary to understand how these micro-shock wave generated by the discharge pulses interact with an external flow). Some preliminary FRP DBD experiments have been done at EPFL and the objective is to provide simulations results. The DBD is placed in the middle of the volume so that a discharge can developed on the up-

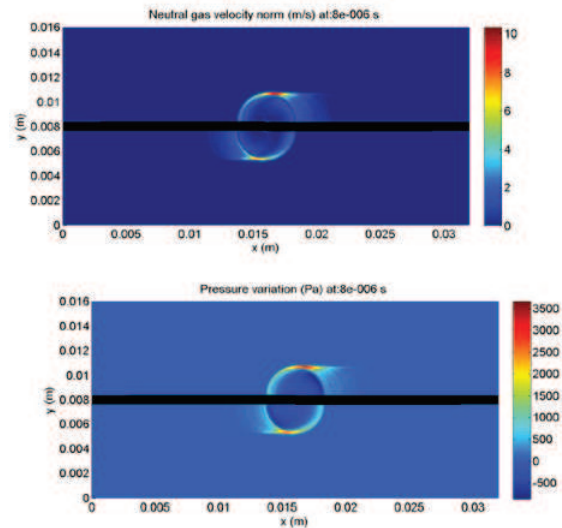


Figure 5: Shock wave formation for a nanosecond DBD actuator

per electrode side and also on the lower electrode side. A 10kV nanosecond pulse is applied on the upper electrode with a 21 ns rising time and a 23 ns setting time. The whole pulse duration is 444 ns. Between 0 and 21 ns the voltage is rising then there is a plateau phase for 400 ns and the potential is falling for 23 ns, the main difference of this experiment with respect to those of Starikovskii et al is that the plateau phase is much longer. In this case the second discharges occur in a much weaker plasma. The relative permittivity of the dielectric is 10 which correspond roughly to alumina. The minimum cell size used is 15  $\mu\text{m}$ . The upper discharge is a positive streamer whereas the lower discharge is a negative streamer. The negative discharge is faster because in this case the electrons are driven towards the surface. The discharge currents on both electrodes show that the first discharges (rising potential) are stronger than the second discharges (falling potential). The shock waves formation is presented on Figure 5. Both sides have experienced a positive and a negative discharge, so the structure of the wave is identical and is composed of a flat wave and a cylindrical wave centered on the electrode tip. As they develop with time it becomes clearer that the upper discharge is stronger than the lower discharge. It seems to be more efficient to have first a positive discharge followed by a negative discharge than the opposite.

## 6 Plasma synthetic Jet modeling

A full model of the PSJ actuator has been developed by ONERA. It contains physical insights (real gas effect, discharge modeling...) and provides information on the gas into the cavity as well as in the plume. The objective of the modeling was to get a better understanding the transformation of the thermal energy supplied by the arc discharge to the gas. Information on spark-discharge actuators can be found in Ref. [4].

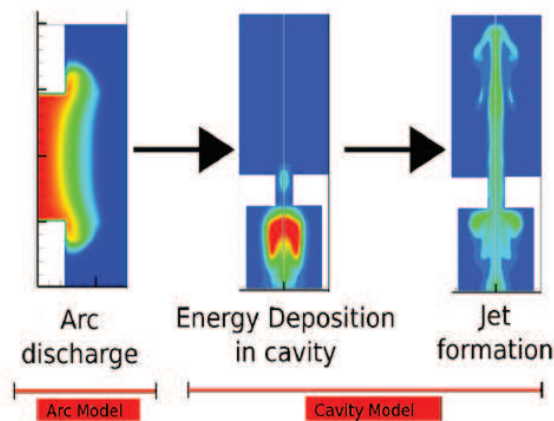


Figure 6: Coupled solvers for the PSJ actuator

The model has been split into two coupled sub-models (see figure 6) . The first one deals with the energy deposition through electric arcing in the vicinity of the electrodes in absence of the cavity. It describes the plasma formation between both electrodes in an axisymmetrical configuration. This model is coupled to the RLC circuit equations describing the electrical supply by the external generator. The second submodel, focuses on the flow heating into the cavity and the working of the actuator. It uses the energy distribution computed by the first sub-model as source term and calculates the resulting effects on the actuator. It provides the flow mass rate, momentum and energy at the PSJ's exhaust versus time.

To perform a full PSJ's simulation both codes are used. A simulation of the arc is first done and then the PSJ's simulation is performed. The modeling relies on a certain number of assumptions. First of all, the arc created in the PSJ cavity, which corresponds to the location of the energy deposit, is supposed to be elongated and characterized by an azimuthal symmetry. Because of the strong current and the short gap between the electrodes, we assume that the arc is cylindrical as well. In this case, the complexity of the problem can be reduced to the solving of a 2D axisymmetric problem where all the variables only depend on the radius  $r$  and the height  $z$  (Figure 11). The real configuration is genuinely 3D because of the way the electrodes are placed inside the cavity. The amount of heating provided by the arc discharge is so large that real gases properties have to be taken into account in the description of the flow. The ionisation and dissociation reactions at higher temperatures cause very strong non-linearities in the evolution of the thermodynamic coefficients. As a consequence, one generally considers a "real gas" modeling to compute transport and thermodynamic coefficients which have to be injected in the system. In this case, the "real gas" representation has been made using coefficients depending on pressure and temperature calculated by D'Angola et al. (2008) on a range going from 300 to 60 000 K and from 0.01 to 100 atm . More information on the model can be found in Ref. [5].

### Non-confined Arc modeling

The arc geometry is still considered as a 2D axisymmetric problem. Moreover, the arc is considered to be in local thermal equilibrium (LTE) by looking at the high temperatures and pressures that generally characterize this type of device. Therefore, there is no distinction between the heavy particles and electrons behaviour.

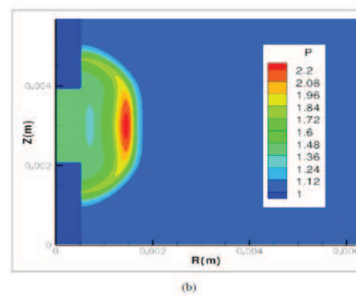


Figure 7: Pressure wave at  $t=5\text{ns}$

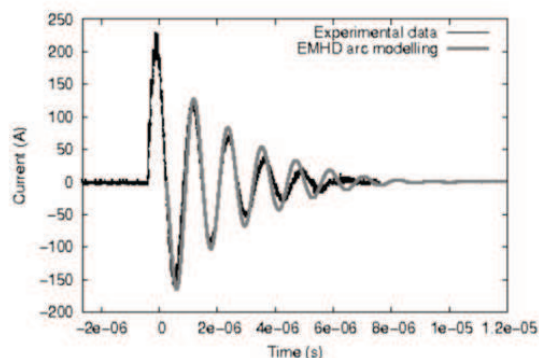


Figure 8: Experimental and computed current discharge

This assumption then gives the possibility to take into account a unique temperature to represent the thermal behaviour of all the species as a global single fluid. The viscosity effects are neglected . So, the flow evolution is governed by the 2D inviscid Euler equations with thermal diffusion and Joule heating. Radiative energy losses are also taken into account proportionally to the net emission coefficient (NEC) whose value is given by tables depending on  $T$  and  $P$  provided by LAPLACE. The plasma resistance results from the conductivity that depends analytically from the temperature between the electrodes. The current  $I$  is then obtained by the RLC circuit equations and the electric field from the discharge current using Ohm's law. The modeling is not able to describe the arc formation phase during the first nanoseconds. It is assumed, that the initial state of the arc is known after the first current pulse. Figure 7 show the pressure wave resulting from the energy deposition by the electrical circuit at  $t=5\text{ns}$ .

Figure 8 show a comparison between experimental and computed current discharge. It has to be noticed that to obtain these results, it has been necessary to add a virtual resistance to represents the voltage drops occurring in the areas close to the electrodes and which cannot be solved by the modeling (presence of sheaths).

### Simulations of the plasma Synthetic Jet

The simulation of the PSJ operation is performed using first the non confined arc modeling. An energy source distribution term is computed and introduced as input in the PSJ solver. Because of the cavity's geometry, its cooling is only possible through convective heat transfers at the walls (heat transfer at electrodes is neglected). A thermal flux has been prescribed on the wall PSJ.

At that point, the arc discharge is not delivering power anymore and the fluid behaviour is only governed by pressure and thermal gradients. This energy deposition generates an over pressure inside the cavity (on the order of 0.4 bar) which forces the flow at high

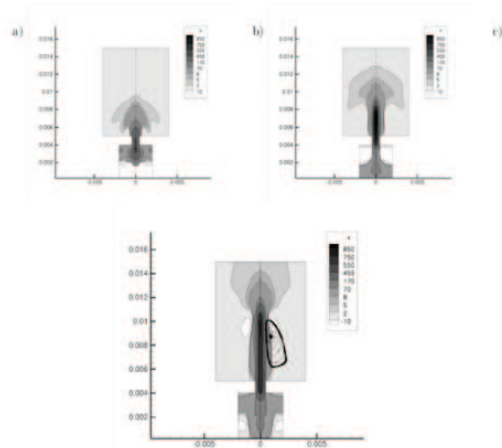


Figure 9: Velocity contours of the jet's evolution

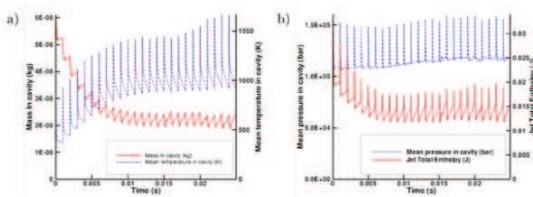


Figure 10: Mass, mean temperature, mean pressure in cavity and jet's total enthalpy over time

velocity outside the cavity. This creates velocities inside the core of the jet as high as 700 m/s (Figure 9) although the tip of the jet moves much slower (around 160 m/s) between 0.5 and 1 cm outside the neck of the cavity, this value corresponds to the measurements for a low frequency actuator). The high velocity jet assumes an arrow-shape which is visible. Simulations of more than one discharge pulse led to the quasi-static periodic behaviour of the actuator after approximately 25 pulses. The breakdown voltage depends on the initial gas state as an analytical function. So, after one pulse the gas in the cavity has been heated and the initial condition of the breakdown voltage will change. A simple breakdown voltage law have been introduced in the modeling to take into account the modification of the gas properties after the pulse. The quasi-static behaviour of the actuator is readily visible on 2D visualizations of the flow. However, some gaps such as the total mass contained and the mean fluid temperature inside the cavity show this periodicity even more clearly. This simulation has been carried for an actuator operating at 1 kHz frequency, using a 15 nF capacitor and a constant breakdown voltage of 2.7 kV. Once the quasi-static behaviour is obtained, 7 mJ of electric energy are deposited in the fluid during each pulse. For these graphs, fluid in the nozzle has been taken into account as well. Quasi-static behaviour is obtained after roughly 10 ms (or 10 pulses) for all represented graphs. Starting from this moment, the jet is truly synthetic, as seen on Figure 10 (i.e. its net mass flow is null over one period). Afterwards, the jet expels about 5.2 mg (8.5% of the PSJ's initial mass) during each pulse, at a mass flow rate of approximately 49 mg/s. The fluid inside the cavity gets relatively hot with a temperature never falling below 900 K. This figure also demonstrates that periodic regime has been obtained : electric energy to enthalpy conversion, jet total enthalpy and enthalpy gained through refill keep constant magni-

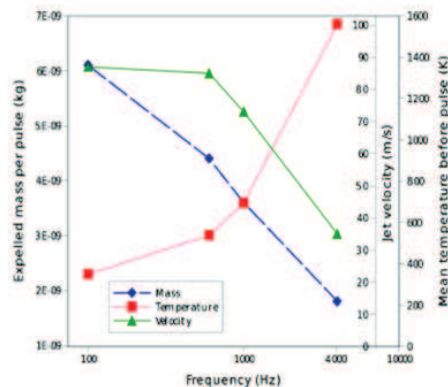


Figure 11: Parametric study over frequency on mass expelled per pulse, mean temperature before each pulse and jet's velocity

tudes over the last 5 periods. Figure 16 clearly shows that cavity refill and fluid cooling are strongly correlated.

### Parametric study

A qualitatively study of the influence of several parameters on both energy deposition and cavity geometry is presented. These parameters were chosen around a reference actuator, composed of a 15 nF capacitor operating at 1 kHz, with a cavity ended by a cylindrical neck 1 mm wide. It should be kept in mind that because of the inaccuracy of the energy deposition phase (energy loss in sheaths and constant breakdown voltage), only qualitative differences between the different configurations are presented.

### Operating frequency

The behaviour of the actuator for several operating frequencies seems physically correct (Figure 11) : qualitatively we observe that, the higher the frequency, the hotter the cavity and the less mass is expelled (because of the less efficient refill). Experimentally, the actuator should deposit less and less energy.

### Actuator's geometry

Simulations in this section are done for several geometries of the cavity's neck (figure 12). Three different half cone angle were used for this converging section : 90(no cone), 45 and 27 (designated respectively by Cyl, Col45 and Col27 on figure). Arguably, this introduces a variation in the volume of the cavity. Even if the cavity volume changes slightly, figure 13 shows that, with the same entry section, the refill is much more efficient in the case of converging cavity shape.

## 7 Conclusions

A numerical model of DBDs in sinusoidal and nanosecond pulsed regimes has been developed at LAPLACE and improved in the frame of the PLASMAERO project. This model includes a description of the plasma as well as the gas flow and gas heating. It is based on an asynchronous time stepping technique which allows an efficient treatment of the different time and spatial scales of the problem. This model has been used to provide a database of EHD force as a function of applied voltage amplitude and frequency in the sinusoidal regime, and to understand the differences between the mechanisms lead-

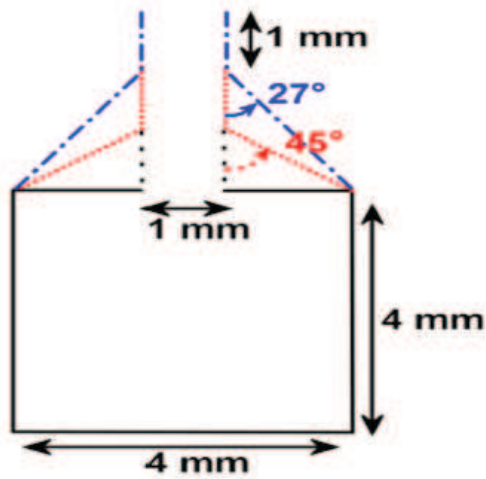


Figure 12: Different geometries of the cavity's neck studied

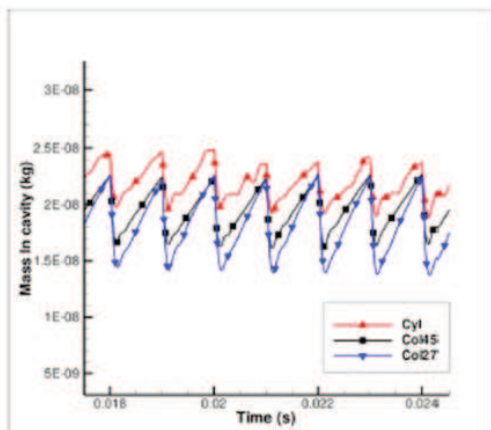


Figure 13: Refilling of the cavity with different neck's shape

ing to flow modification in the sinusoidal (ion wind) and nanosecond (fast gas heating) regimes of DBDs. A useful continuation of this work would be to fit the numerical results concerning the distribution of the EHD force in sinusoidal regimes into analytical laws depending on the main parameters, i.e. voltage amplitude, frequency, dielectric thickness etc...

The operation of the Plasma Synthetic Jet actuator has been numerically described by two models: One describing the arc development and one coupling it via a Joule heating source term with the Euler equations. Comparisons with experimental results show a good qualitative agreement, but the lack of PSJ's characterization make a precise comparison hazardous. The computational cost of such simulation is until now reasonable because the assumptions of ETL provide plasma and flow time scales of the same order.

So, such tool could be useful to be used in an optimization loop. More work is needed to increase the robustness of the model. This concerns the initial arc description at some ns and the sheaths which are roughly described in the present model.

Parametric studies on the geometrical aspects of the actuator as well as its electrical inputs have been performed, optimizing its efficiency and resulting to a semi-permanent pulsed regime.

## Acknowledgments

The present work has been performed within the framework of the PlasmAero project ([www.plasmaero.eu](http://www.plasmaero.eu)) funded by the European Community's Seventh Framework Program FP7/2007- 2013 under grant agreement nr. 234201.

## References

- [1] *Electrohydrodynamic force and aerodynamic flow acceleration in surface dielectric barrier discharge*, Journal of Applied Physics, 97, 103307, 2005.
- [2] *Multi-scale gas discharge simulations using asynchronous adaptive mesh refinement*, T. Unfer, J.P. Boeuf, F. Rogier and F.Thiver, Computer Physics Communications Volume 181, Issue 2, February 2010, Pages 247-258.
- [3] *Modelling of a nanosecond surface discharge actuator*, T. Unfer and JP Boeuf, J. Phys. D: Appl. Phys. 42 No 19 (7 October 2009) 194017 (12pp).
- [4] *SparkJet actuators for flow control*, Grossman K.R., Cybyk B.Z. and Wie D.M.V. , AIAA 2003-0057.
- [5] *Physics and models for plasma synthetic jets*, F.Rogier, G.Dufour, G.Quint, Int. J. of Aerodynamics, 2013 Vol.3, No.1/2/3, pp.47 - 70.

# COUPLING OF CFD WITH ADVANCED PLASMA MODELS

J.C. Kok<sup>1</sup>, P. Catalano<sup>2</sup>, K. Kourtzanidis<sup>3</sup>, F. Rogier<sup>3</sup>, and T. Unfer<sup>4</sup>

<sup>1</sup>*NLR, Amsterdam, The Netherlands, johan.kok@nlr.nl*

<sup>2</sup>*CIRA, Capua, Italy, p.catalano@cira.it*

<sup>3</sup>*ONERA, Toulouse, France, francois.rogier@onera.fr*

<sup>4</sup>*LAPLACE, Université de Toulouse, Toulouse, France, thomas.unfer@laplace.univ-tlse.fr*

## Abstract

Advanced plasma models are coupled with CFD to determine the effect of plasma actuators on the flow. Two kinds of actuators are considered: Dielectric Barrier Discharge (DBD) actuators and Plasma Synthetic Jets (PSJ). For DBD actuators, a 2D plasma model is used that describes the transport of charged particles in a collisional plasma. A time-averaged body-force field is obtained from this plasma model and added as a source term to the Navier–Stokes equations. For PSJs, a 2D axisymmetric model describes the discharge in the microcavity and provides the mass flow and the heat flow at the exhaust. The effect of the PSJ on the CFD is introduced as an unsteady boundary condition for the Navier–Stokes equations at the PSJ orifice by the output of the PSJ’s model.

## 1 Introduction

For DBD actuators, CFD computations presented in the literature commonly use phenomenological or simplified models to obtain the body force exerted by the plasma on the flow, such as the models of Shyy *et al.* [1], Suzen *et al.* [2], and Orlov [3]. Although such models are very cheap, they are not self-contained and therefore must be tuned for each (type of) DBD actuator. A self-contained first-principle plasma model, on the other hand, does not require any tuning, but it is considerably more expensive. In this paper, the first-principle model of Unfer and Boeuf [4] has been coupled with CFD.

For PSJ actuators, a full model of the actuator has been developed, that provides information on the gas in the cavity as well as in the plume. To couple this model with CFD, the PSJ is represented as a dynamical boundary condition located at the orifice aperture.

## 2 DBD actuator

### 2.1 Plasma model

For DBD actuators, a first-principle 2D plasma model is used, which is based on the detailed description of charged particle transport in a collisional plasma (including charging of the dielectric surface) coupled with Poisson’s equation for the electric field [4].

These simulations require to integrate the different time scales of all particles which are active in the plasma. Then, the price to pay is the large computational time. To deal with this, a specific numerical method has been developed at LAPLACE using the concept of an asynchronous adaptive model [5]. Such modelling has the great advantage to provide predictable results; this is

not the case for the phenomenological or simplified models developed by other groups.

The plasma model delivers a body-force field which is averaged over time.

### 2.2 Coupling with CFD

To model plasma actuators in a CFD method, the time-averaged body-force field is added to the compressible Reynolds-averaged Navier–Stokes (RANS) equations as a source term. The body force  $\mathbf{f}_b$  appears directly in the momentum equation and the work done by the body force appears in the energy equation, as follows:

$$\frac{\partial \rho \mathbf{u}}{\partial t} + \nabla \cdot (\rho \mathbf{u} \mathbf{u}) + \nabla p = \nabla \cdot \boldsymbol{\tau} + \mathbf{f}_b,$$
$$\frac{\partial \rho E}{\partial t} + \nabla \cdot (\rho \mathbf{u} E) + \nabla \cdot (\mathbf{u} p) = \nabla \cdot (\boldsymbol{\tau} \cdot \mathbf{u} - \mathbf{Q}) + \mathbf{f}_b \cdot \mathbf{u},$$

with  $\rho$  the density,  $\mathbf{u}$  the velocity vector,  $p$  the pressure,  $E$  the total energy per unit mass,  $\boldsymbol{\tau}$  the stress tensor, and  $\mathbf{Q}$  the heat flux vector.

The body-force field is transferred from the unstructured plasma grid to the CFD grid using bilinear interpolation. Note that including a time-averaged body-force field implies that possible interaction between the high-frequency unsteadiness of the plasma and the flow turbulence is not taken into account.

To compute the flow around airfoils and wings with plasma actuators, two in-house flow solvers are used: NLR’s ENSOLV and CIRA’s UZEN, which are both based on multi-block structured grids. In ENSOLV, the RANS equations are solved together with the TNT EARSM turbulence model [6], whereas in UZEN the Menter SST turbulence model is used. In both solvers, the flow equations are discretized in space with a second-order cell-centre finite-volume method. The discrete equations are solved with a multi-grid method using as relaxation operator a Runge–Kutta scheme accelerated by local time stepping and implicit residual averaging.

### 2.3 Flat plate with stream-wise forcing

As most basic case, the flow induced by a DBD plasma actuator over a flat plate has been considered with and without a background flow. In the experiment by E. Moreau *et al.* [7], there is no background flow, so that one can consider only the jet induced by the actuator. In the experiment, a plasma DBD actuator was used with a dielectric thickness of 4 mm and a voltage signal of 11 kV and 11.7 kHz. A turbulent computation compares well to the experiment, as shown in 1. The thickness of the wall jet is consistent with the experiment at the first station (10 mm downstream) indicating that the effect of the actuator on the flow is correctly captured. The

velocity profiles at the subsequent stations also compare reasonably well with the experiment, indicating that the decay of the wall jet is correctly captured. Note that this decay is determined by the turbulence model and does not depend on the plasma model.

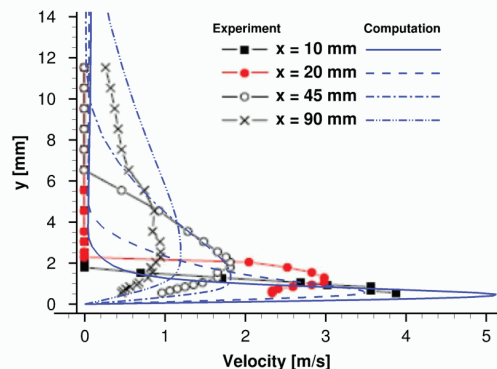
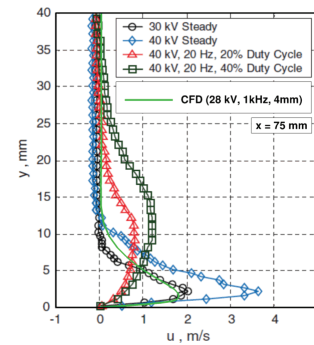


Figure 1: Velocity along flat plate induced by plasma actuator in the absence of a background flow (turbulent computation ENSOLV; experiment by Moreau *et al.* [7]) **Need permission to reproduce picture!**

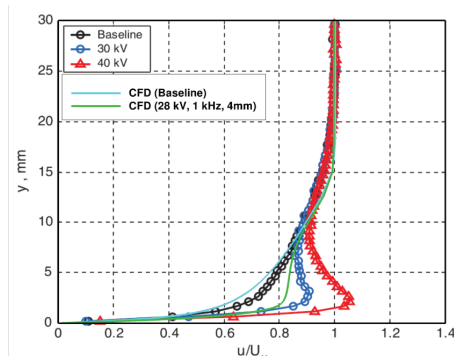
In the experiment by Schatzman and Thomas [8], there is a turbulent boundary layer developing over the flat plate, in addition to a case without flow. A plasma DBD actuator was used with a dielectric thickness of 3.175 mm and a voltage signal of 30 or 40 kV and 2 kHz. For the flow computations, similar but not identical actuator settings were available: 4 mm, 28 kV, and 1 kHz. Both computations with and without flow have been performed. The velocity profiles at 75 mm downstream of the actuator are compared to the experiment in 2. Without flow, the computation compares well to the experiment, just like in the previous case. With flow, the actuation effect is fairly well reproduced in the computation, considering the slightly different settings of the actuator.

## 2.4 NACA0015 with stream-wise forcing

For the NACA0015 airfoil, the control of weak trailing-edge separation has been considered (chord length 50 cm, free-stream velocities 10 m/s and 30 m/s, angle of attack up to 17°). Fully turbulent computations have been performed with the TNT EARS model (ENSOLV) and the Menter SST Model (UZEN). Two actuator locations have been considered ( $x/c = 0.7$  and  $x/c = 0.9$ ) with the actuator forcing in chord-wise direction. A body-force field computed for a dielectric thickness of 1.0 mm and a voltage signal of 10 kV and 2 kHz has been employed. At a velocity of 10 m/s, the actuation is effective in delaying the separation if the actuator is placed close to the separation location (Figure 3(a)). As a consequence, the lift coefficient is also increased (Figures 3(b) and 3(c)). At a velocity of 30 m/s, however, there is only a weak delay of separation and the effect on the lift coefficient is negligible. Note that similar results have been obtained with both flow solvers. Validation of the method for this case has been found difficult. Comparison has been made to an experiment of Pprime at 20 m/s and 12°. The actuator in the experiment had a dielectric thickness of 4.0 mm and a voltage signal of 28 kV and 1 kHz. Using these same actuator settings in the computation resulted in unsatisfactory results with a strong underprediction of the actuation effect compared to the experiment. This is contradictory to the results for the



(a) Without background flow



(b) With background flow (5 m/s)

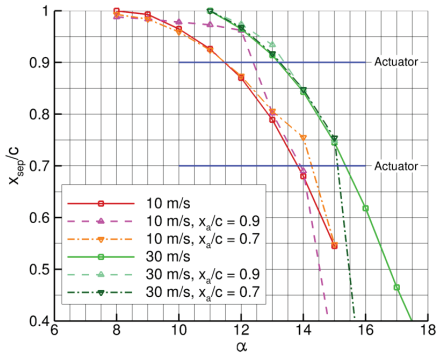
Figure 2: Velocity along flat plate induced by plasma actuator (turbulent computation ENSOLV; experiment by Schatzman and Thomas [8]) **Need permission to reproduce picture!**

flat plate with flow, where the same actuator settings provided a fair comparison with experiment. The total body force in the computation amounted to 20 mN/m. If the level is increased to 80 mN/m (a common level for DBD actuators) by scaling the body-force field, then the computations show a similar actuation effect as the experiment (4). The question that remains is whether the plasma model underestimates the level of the body force or whether there is another reason for the mismatch between computation and experiment, e.g., an interaction between the unsteady plasma and the turbulence.

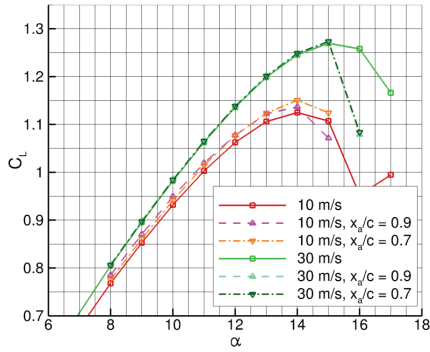
## 2.5 Plasma vortex generator

The application of plasma vortex generators (PVG), as introduced by the University of Nottingham, has been considered for the NACA0012 and NACA0015 airfoils using ENSOLV.

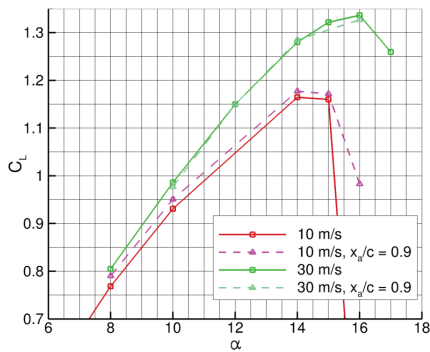
For the NACA0012, a chord of 10 cm is used with a free-stream velocity of 6.5 m/s ( $M = 0.019$ ,  $Re = 4.4 \cdot 10^4$ ). The actuators have a chord-wise extent from 10% to 88% chord and have a span-wise spacing of 25% chord. Both co-forcing and counter-forcing PVGs have been considered. The 2D plasma body-force field (1mm, 10 kV, 2 kHz) has been extended to 3D in chord-wise direction to model the PVGs. Stream-wise vortices are generated as illustrated in Figure 5(a) for the counter-forcing PVG. This results in an increase of the lift, as can be seen from the wing pressure distribution (Figure 5(b)). For the NACA0015, an experiment has been performed at Pprime with the PVGs of Nottingham (chord 50 cm, velocity 20 m/s, angle of attack 12°). The actuators have a chord-wise extent from 66% to 75% chord and have a span-wise spacing of 9% chord. Again



(a) Location of separation (ENSOLV)



(b) Lift coefficient (ENSOLV)



(c) Lift coefficient (UZEN)

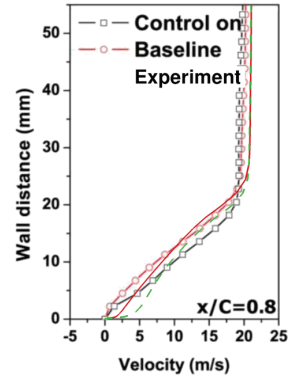
Figure 3: Location of trailing-edge separation and lift coefficient for NACA0015 airfoil with and without plasma actuator

both co-forcing and counter-forcing have been considered. The actuator settings of the experiment (0.76 mm Cirlex, 35 kV, 1 kHz) have also been used for the computations, except for a slightly higher voltage (42 kV). An illustrative comparison with the experiment is shown in 6 for the counter-forcing setup, showing a similar weakening of the wake. Finally, the PVG leads to an increase of lift at a constant drag as shown in 7, in particular for the counter-forcing PVG.

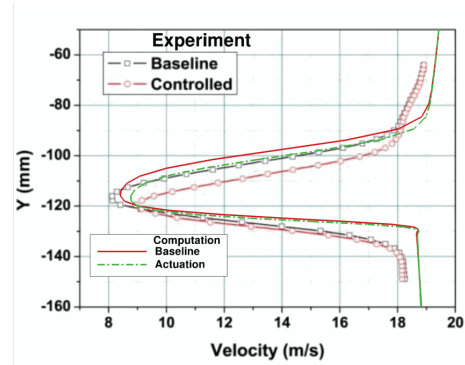
### 3 Plasma Synthetic Jet

#### 3.1 Plasma model

When the potential difference applied between the PSJ's electrodes reaches the disruptive voltage of air (about 4 kV for ONERA's actuators), the fluid is ionised and an electrical arc is created. This discharge leads to a large increase of the internal energy. Since the air is confined,



(a)  $x/c = 0.8$



(b)  $x/c = 1.2$

Figure 4: Velocity profiles for NACA0015 airfoil at 20 m/s and  $12^\circ$  with and without actuation (experiment by Pprime: lines with symbols; computations ENSOLV: lines without symbols) **Need permission to reproduce picture!**

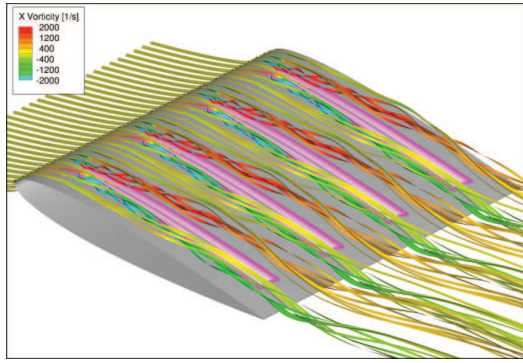
the pressure and the temperature increase rapidly inside the PSJ cavity.

A full model of the PSJ actuator has been developed (see 8). It contains physics insights (real gas effect, discharge modelling, ...) and provides information on the gas in the cavity as well as in the plume. The model has been split into two coupled sub-models. The first one deals with the energy deposition through electric arcing in the vicinity of the electrodes in absence of the cavity. It describes the plasma formation between both electrodes in an axisymmetrical configuration. This model is coupled to the RLC circuit equations describing the electrical supply by the external generator. The second sub-model focuses on the flow heating into the cavity and the working of the actuator. It uses the energy distribution computed by the first sub-model as source term and calculate the resulting effects on the actuator. It provides the flow mass rate, momentum and energy at the PSJ's exhaust versus time[9].

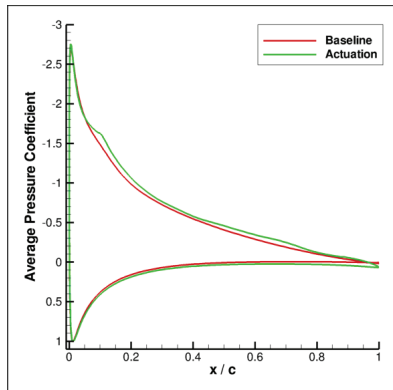
#### 3.2 Coupling with CFD

The density, momentum, and temperature are computed by the PSJ modelling at the orifice during one cycle and serve as input for a 3D CFD simulation. Therefore, the plasma synthetic jet is represented as a dynamical boundary condition located at the orifice aperture.

The simulation of the PSJ working is performed using first the non confined arc modelling. An energy source distribution term is computed and introduced as input in the PSJ solver. Because of the cavity's geometry, its cooling is only possible through convective heat trans-

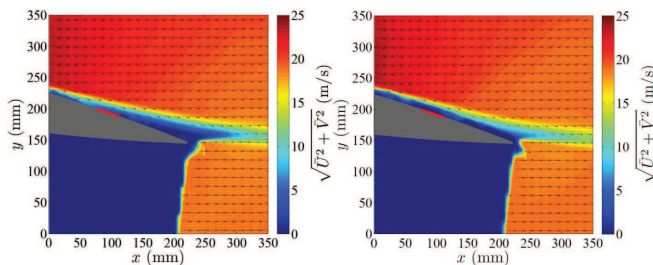


(a) Streamribbons coloured with x-component of vorticity



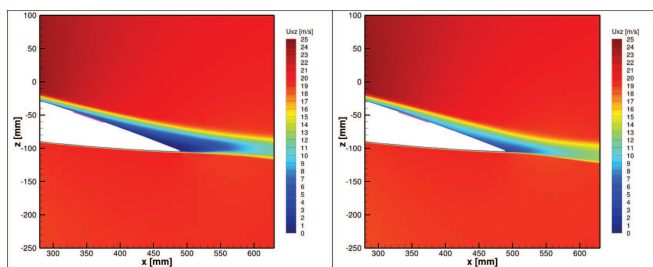
(b) Pressure coefficient averaged in span

Figure 5: NACA0012 with counter-forcing plasma vortex generators (velocity 6.5 m/s, angle of attack 8°, computation ENSOLV)



(a) Experiment: Baseline

(b) Experiment: Actuation



(c) Computation: Baseline

(d) Computation: Actuation

Figure 6: Velocity magnitude in plane between actuators for NACA0015 with counter-forcing PVG (20 m/s, 12°) (experiment of Nottingham; computation ENSOLV) **Need permission to reproduce picture!**

fers at walls (heat transfer at electrodes is neglected). A thermal flux has been prescribed on the wall PSJ. At this point, the arc discharge is not delivering power anymore and the fluid behaviour is only governed by pressure and thermal gradients. This energy deposition generates an

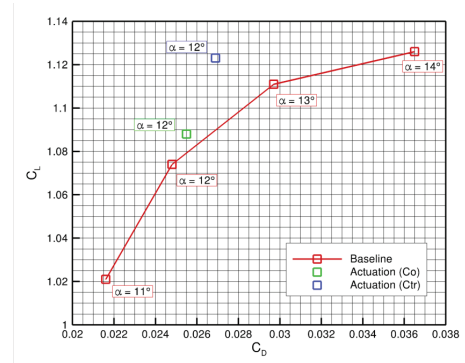


Figure 7: Lift versus drag polar for NACA0015 without actuator and with co-forcing (Co) and counter-forcing (Ctr) PVG actuators (20 m/s, computation ENSOLV)

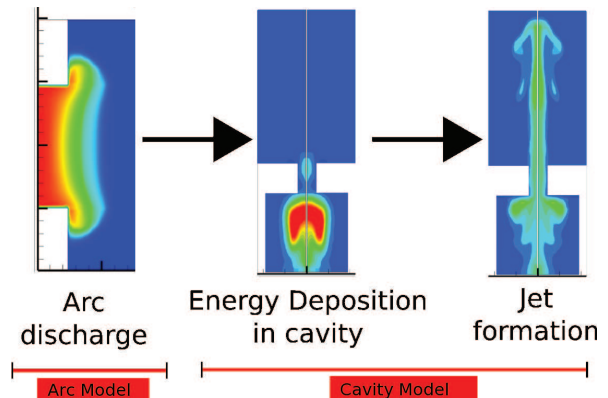


Figure 8: Scheme of the PSJ modelling

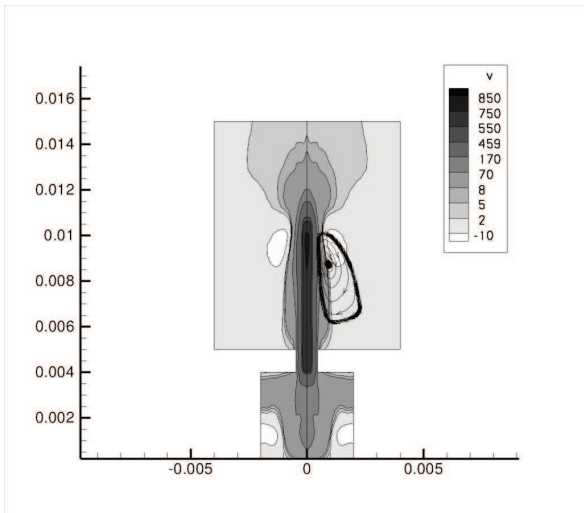
over pressure inside the cavity (in order of 0.4 bar) which forces the flow at high velocity outside the cavity. This creates velocities inside the core of the jet as high as 700 m/s, although the tip of the jet moves much slower (around 160 m/s) between 0.5 and 1 cm outside the neck of the cavity (this value corresponds to the measurements for a low frequency actuator). The high velocity jet and the temperature of the flow are shown in 9.

### 3.3 Results

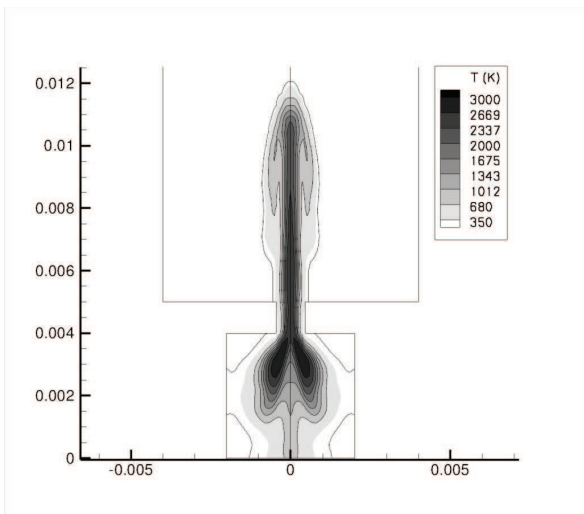
The interaction between the incompressible flow over a flat plate and a plasma synthetic jet has been considered. The free-stream velocity is 40 m/s, the length of the flat plate is 400 mm and the resulting Reynolds number is  $1.095 \cdot 10^6$ . The jet is located at the centre of the flat plate at a distance of 250 mm from the inlet and has a circular shape with a diameter of the orifice of 1 mm.

A computational mesh of about  $3.5 \cdot 10^6$  cells has been generated. As prescribed in the experiments the transition has been imposed at a distance of 50 mm. from the inlet. The TNT  $k-\omega$  turbulence model has been employed. An URANS simulation by the CIRA UZEN code has been performed. The time period of the PSJ has been divided in 720 steps, which means that the computation has been advanced in time with a non-dimensional time step of  $4.17 \cdot 10^{-5}$ .

An anti-clockwise rotating vortex is formed as the result of the interaction between the main flow and the plasma synthetic jet. A comparison between numerical and experimental data is shown in 10. The stream-wise velocity field at the plane  $x = 270$  mm is presented. The agreement for the velocity field is acceptable and also the position of the vortex is reasonable. The evolution of the



(a) Velocity



(b) Temperature

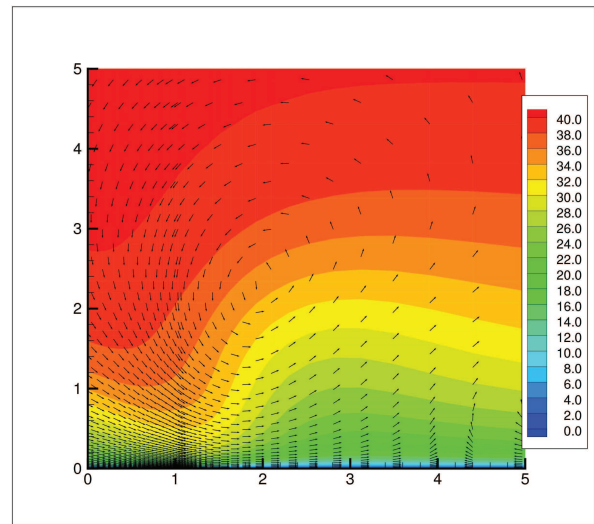
Figure 9: Velocity field and temperature distribution at  $t = 39\mu s$

vortex in the stream-wise direction, as noted in the numerical simulations, is to move away from the wall as the distance from the PSJ increases.

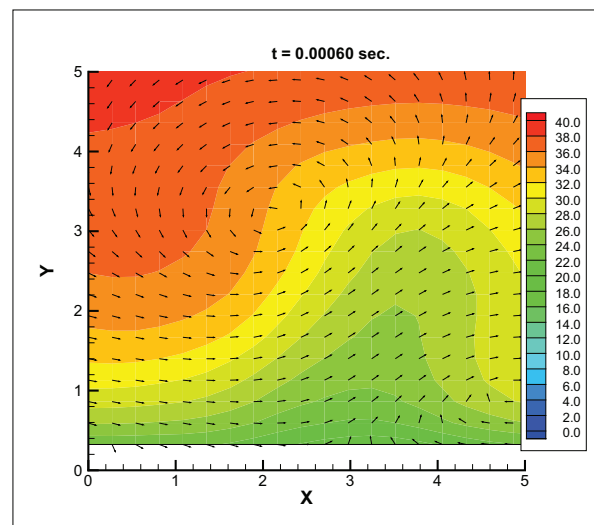
The numerical simulation has returned an anti-clockwise rotating vortex as in the experiments. The dynamics of the vortex, mainly the movement towards the wall observed in the experiments, has not been reproduced correctly. Likely the artificial viscosity employed in the adopted numerical method has prevented the presence of the vortex close to the wall. On the other hand, the boundary condition developed to simulate a plasma synthetic jet should be applied to less CPU-expensive test cases in order to check if the momentum of the PSJ is correctly transferred to the flow.

## 4 Conclusions

For DBD actuators, a first-principle model has been coupled with CFD through a time-averaged body force. The validation of this modelling approach has been definitively achieved in a quiescent gas or in a flow past a flat plate. The results obtained show a good estimation of the total body force and of the flow velocity in simple configurations. Nevertheless, some discrepancy have been noticed in a NACA0015 airfoil simulation. The



(a) Numerical



(b) Experimental

Figure 10: Velocity field generated by plasma synthetic jet at 270 mm downstream of actuator (colours indicate streamwise component [m/s]; computation UZEN)

DBD modelling has been applied to the simulation of plasma vortex generators (actuators working in spanwise direction), showing qualitatively similar results as in the experiments.

For PSJ actuators, a full model of the actuator has been coupled with CFD through a time-dependent boundary condition at the orifice. The 3D simulation of the PSJ actuator placed in a flat plate using this modelling approach has been done and shows the development of a vortex, as expected based on the experiment. Other simulations requiring advanced CFD modelling will be useful to improve these preliminaries results.

## Acknowledgement

The research presented in this paper has received funding from the European Community's Seventh Framework Program FP7/2007-2013 under grant agreement nr. 234201, project PLASMAERO.

## References

- [1] W. Shyy, B. Jayaraman, and A. Anderson, “Modeling of glow-discharge induced flow dynamics,” *Journal of Applied Physics*, vol. 92, no. 11, pp. 6434–43, 2002.
- [2] Y. B. Suzen, P. G. Huang, J. D. Jacob, and D. E. Ashpis, “Numerical simulations of plasma based flow control applications,” in *35<sup>th</sup> AIAA Fluid Dynamics Conference and Exhibit*, (Toronto, Canada), 6–9 June 2005. AIAA 2005-4633.
- [3] D. M. Orlov, *Modelling and simulation of single dielectric barrier discharge plasma actuators*. PhD thesis, University of Notre Dame, Notre Dame, Indiana, October 2006.
- [4] T. Unfer and J. Boeuf, “Modeling and comparison of sinusoidal and nanosecond pulsed surface dielectric barrier discharges for flow control,” *Plasma Physics and Controlled Fusion*, vol. 52, p. 124019, 2010.
- [5] T. Unfer, J.-P. Boeuf, F. Rogier, and F. Thivet, “Multi-scale gas discharge simulations using asynchronous adaptive mesh refinement,” *Computer Physics Communications*, vol. 181, no. 2, pp. 247 – 258, 2010.
- [6] H. S. Dol, J. C. Kok, and B. Oskam, “Turbulence modelling for leading-edge vortex flows,” in *40<sup>th</sup> Aerospace Sciences Meeting & Exhibit*, (Reno, NV), 14–17 January 2002. AIAA paper 2002-0843.
- [7] E. Moreau, R. Sosa, and G. Artana, “Electric wind produced by surface plasma actuators: a new dielectric barrier discharge based on a three-electrode geometry,” *Journal of Physics D: Applied Physics*, vol. 41, p. 115204 (12pp), 7 June 2008.
- [8] D. M. Schatzman and F. O. Thomas, “Turbulent boundary-layer separation control with single dielectric barrier discharge plasma actuators,” *AIAA Journal*, vol. 48, pp. 1620–1634, August 2010.
- [9] G. Dufour, P. Hardy, G. Quint, and F. Rogier, “Physics and models for plasma synthetic jets,” *Int. J. for AeroDynamics*, vol. 3, pp. 47–70, 2012.

# TRAILING-EDGE SEPARATION CONTROL OF A NACA 0015 AIRFOIL USING DIELECTRIC-BARRIER-DISCHARGE PLASMA ACTUATORS

R. D. Whalley<sup>1</sup>, A. Debien<sup>2</sup>, J. Podliński<sup>3</sup>, T. N. Jukes<sup>1</sup>, K.-S. Choi<sup>1</sup>,  
N. Bénard<sup>2</sup>, E. Moreau<sup>2</sup>, A. Berendt<sup>3</sup> and J. Mizeraczyk<sup>3</sup>

<sup>1</sup>*Faculty of Engineering, University of Nottingham, University Park, Nottingham, NG7 2RD, UK*

<sup>2</sup>*Pprime, Université de Poitiers, CNRS, ISAE-ENSMA, Téléport 2, 86962, Futuroscope, France*

<sup>3</sup>*Institute of Fluid Flow Machinery, Polish Academy of Sciences, Fiszerka 14, 80-231 Gdańsk, Poland*

## Abstract

This paper presents a part of the works conducted in the Plasmaero European project (task 3.1), where the trailing-edge flow separation of a NACA 0015 airfoil has been controlled using four different dielectric-barrier-discharge (DBD) actuator types at three institutions across Europe. The results show that it is possible to enhance the aerodynamic performance of aircraft at speeds up to 40 m/s. Dielectric-barrier-discharge vortex generators (DBD VGs) have been used to create streamwise vortices that entrain the high-speed fluid from outside the boundary layer into the separated region causing flow reattachment. The DBD VGs have shown the ability of flow separation control by reducing the drag of the NACA 0015 airfoil up to 45%. Singledielectric-barrier-discharge (SDBD) and multi-dielectricbarrier-discharge (MDBD) plasma actuators have been used to re-energize the separated region by introducing high streamwise velocity close to the wall. The novel MDBD actuators create an induced velocity above 10 m/s. This significant improvement in actuator authority has yielded flow separation control at a Reynolds number of  $Re_c = 1.33 \times 10^6$ , where a drag reduction of 10% was observed.

## 1 Introduction

Dielectric-barrier-discharge (DBD) plasma actuators are unique. They are completely electrical devices that are fast acting, cheap to manufacture and can be retrofitted to existing airframes. Their design is simple requiring an upper and lower electrode separated by a thin dielectric layer. The plasma actuators induce a jet flow providing the ability to manipulate the airflow around aerodynamic bodies. For these reasons there has been enormous interest over the past decade in the use of DBD actuators for flow control in the aerospace industry [1, 2]. Trailing-edge flow separation is usually turbulent and highly three-dimensional. Therefore, the separating region is dynamic and moves in both space and time. This makes the control of trailing-edge flow separation challenging with well-established flow control techniques involving the stimulation of shear-layer instabilities [3] not readily applicable. The objective of this research investigation is to control the trailing-edge flow separation of a NACA 0015 airfoil at flow speeds up to 40 m/s. This has been achieved using four different types of DBD plasma actuators. The first DBD actuator type is DBD VGs, which create streamwise vortices, like vane-type vortex generators [4]. This is an old flow control

concept which has found many applications in industry since streamwise vortices have remarkable organisation and longevity [5]. Here, the DBD actuators are oriented to produce a body force in the spanwise direction. This generates the roll up of fluid into a coherent streamwise vortex. The streamwise vortex increases mixing between the boundary layer and the free-stream to re-energize the near-wall region with fluid from outside the boundary layer. Consequently, these actuators can be effective over long streamwise distances so are particularly suited to applications requiring trailing-edge separation control. The second, third and fourth actuator types are SDBD and two types of MDBDs, respectively. The SDBD actuator has been studied extensively: see Moreau [1] and Corke et al [2]. The MDBD actuators consist of multiple SDBDs and allow accumulation of induced velocity above 10 m/s. The SDBDs and MDBDs are orientated to produce a body force in the streamwise direction. This introduces high streamwise velocity close to the wall and re-energizes the separated region. All of these types of actuators were developed as part of Plasmaero task 1.1.

## 2 Experimental Set-up

Experiments using DBD VGs, SDBD and MDBD plasma actuators have been conducted on a NACA 0015 airfoil with a chord of  $c = 500$  mm and span of 1.2 m at the high-speed test facility at the Université de Poitiers. Experiments are performed at a free-stream velocity of  $U_0 = 20$  m/s to  $U_0 = 40$  m/s, providing a Reynolds number based on chord length of  $Re_c = 0.67 - 1.33 \times 10^6$ . A boundary-layer trip consisting of Carborundum fixes the transition point over the airfoil and ensures a fully developed turbulent boundary layer before the onset of plasma actuation. This guarantees that the control mechanism with the plasma actuators is not the tripping of the flow into a turbulent regime. A schematic representation of the DBD VGs is shown in figure 1. The DBD VGs consist of upper and lower electrodes separated by 0.76 mm thick Cirlex dielectric in a symmetric arrangement, figure 1 (a). The DBD VGs contain 12 upper electrodes separated by a spanwise wavelength of  $\lambda = 45$  mm. The active length of each DBD is  $L = 40$  mm. The DBD VGs are orientated in the streamwise direction and produce spanwise forcing, figure 1 (b). A schematic representation of the SDBD and MDBD actuators are shown in figure 2 (a) and figure 2 (b), respectively. The SDBD actuator consists of an upper and lower electrode separated by 4 mm thick PMMA dielectric in an asymmetric arrangement. The MDBD actuator consists of three SDBDs with alternating high voltage

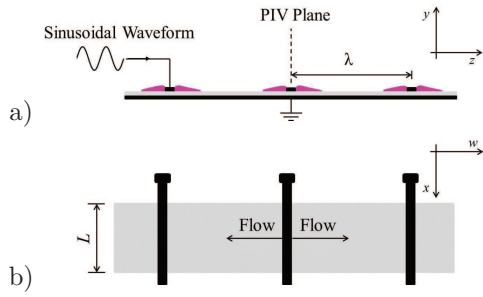


Figure 1: Schematic representation of DBD VGs (a) side view and (b) plan view

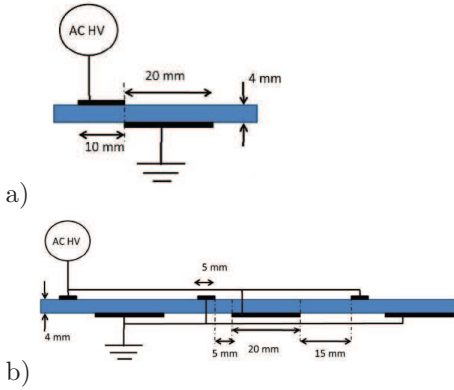


Figure 2: Schematic representation of (a) SDBD actuator and (b) MDBD actuator

and grounded upper electrodes to prevent the formation of plasma upstream of the activated upper electrode [6]. The SDBD and MDBD actuators are orientated in the spanwise direction and produce streamwise forcing.

The DBD VGs, SDBD and MDBD actuators are operated with an applied voltage of  $E = 35 \text{ kV}_{p-p}$ ,  $E = 56 \text{ kV}_{p-p}$  and  $E = 48 \text{ kV}_{p-p}$ , respectively. Each actuator is driven with a sinusoidal waveform at  $f = 1 \text{ kHz}$  with 100% duty. The DBD VGs require  $0.47 \text{ W/cm}$  and produce an induced velocity of  $3.5 \text{ m/s}$ . The SDBD actuator requires  $2.5 \text{ W/cm}$  and produces an induced velocity of  $6 \text{ m/s}$ , and the MDBD requires  $3.5 \text{ W/cm}$  and produces an induced velocity of  $7.5 \text{ m/s}$ . The DBD VGs are flush mounted over the upper surface of the NACA 0015 airfoil. The DBD begins at  $x/c = 68\%$  and ends at  $x/c = 76\%$ . The SDBD actuator and the first DBD in the MDBD plasma actuator are located at  $x/c = 60\%$ . Measurements are obtained with a high-resolution 2D PIV system. This consists of a  $2048 \times 2048$  pixel Pulnix/Jai RM-4200 CL camera and a  $250 \text{ mJ/pulse}$  Big Sky Laser. Data are acquired at  $5\text{--}7 \text{ Hz}$  (depending on the camera buffer), with 500 image pairs taken both with and without control. The time delay between image pairs varies from  $30\text{--}120 \mu\text{s}$  depending on the flow speed. Data processing is performed using Dantec Dynamic Studio with a  $16 \times 16$  pixel interrogation area providing a spatial resolution of  $1.41 \text{ mm}$ .

Further tests using DBD VGs have been conducted on a NACA 0015 airfoil with a chord of  $c = 300 \text{ mm}$  and span of  $800 \text{ mm}$  at the University of Nottingham. The DBD VGs are flush mounted over the upper surface of the NACA 0015 airfoil and positioned so that the DBD begins at  $x/c = 30\%$  and ends at  $x/c = 63\%$ . Hence, the active length of the DBD is  $L = 100 \text{ mm}$ . Experiments are performed at a free-stream velocity of  $U_0 = 8 \text{ m/s}$ , providing a Reynolds number based on chord length of  $Re_c = 0.16 \times 10^6$ . The transition point of the airfoil is

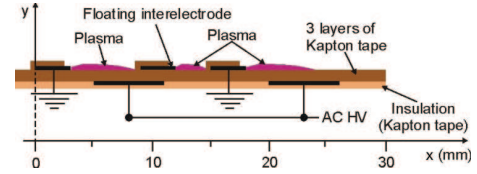


Figure 3: Schematic side view of the MDBD actuator with floating inter-electrode

fixed by a boundary-layer trip, which consists of a stainless steel tube that is  $1.5 \text{ mm}$  in diameter. This provides a Reynolds number based on step height of  $Re_h = 800$ . The trip is placed at  $x/c = 8\%$  and effectively trips the boundary layer into a turbulent regime. It should be noted that surface flow visualisations performed without a boundary-layer trip show a transition line located at  $x/c \approx 8\%$  for angles of attack exhibiting trailing edge separation,  $13^\circ < \alpha < 14.3^\circ$ . Therefore, there is a fully developed turbulent boundary layer before the onset of plasma actuation, with or without a boundary-layer trip. The DBD VGs are operated with an applied voltage of  $E = 7 \text{ kV}_{p-p}$  at  $f = 35 \text{ kHz}$  with a sinusoidal waveform. The DBD VGs are fabricated with  $0.23 \text{ mm}$  thick Cirlex dielectric, figure 1 (a) and are operated with 100% duty cycle. They require  $1.1 \text{ W/cm}$  and produce an induced velocity of  $2.5 \text{ m/s}$ .

A time-resolved 2D PIV system is used to measure the flow velocities. This consists of a Litron LDY302-PIV 100 W Nd:YLF laser and a Vision Research Phantom V12.1 high-speed camera. Olive oil with a nominal diameter of  $1 \mu\text{m}$  is used to seed the flow. Data are acquired at  $500 \text{ Hz}$  with the time delay between image pairs being  $250 \mu\text{s}$ . In total, 500 image pairs are taken both with and without control. Data processing is performed using Dantec Dynamic Studio with a  $32 \times 32$  pixel interrogation area with 50% overlap providing a spatial resolution of  $3.4 \text{ mm}$ .

Experiments using a MDBD actuator [7] with floating inter-electrodes (figure 3) have been conducted on a NACA 0015 airfoil with a chord of  $c = 200 \text{ mm}$  and span of  $595 \text{ mm}$  at the Polish Academy of Sciences. The MDBD actuator is operated with an applied voltage of  $E = 15 \text{ kV}_{p-p}$  at  $f = 1.5 \text{ kHz}$  with a sinusoidal waveform. The MDBD actuator is operated with 100% duty cycle and requires  $0.3 \text{ W/cm}$  to produce an induced velocity of  $6 \text{ m/s}$ . The MDBD actuator is fabricated from 3 layers of  $45 \mu\text{m}$  thick Kapton dielectric. The upper and lower electrodes are  $50 \mu\text{m}$  thick copper tapes that are  $500 \text{ mm}$  in length. The floating and sawtooth grounded electrodes are exposed to the airflow and are partially insulated with Kapton tape: see figure 3. The MDBD actuator is flush mounted on the upper surface of the NACA 0015 airfoil with the first DBD in the MDBD plasma actuator located at  $x/c = 52\%$ . The experiments are conducted with the absence of a boundary-layer trip and the freestream velocity is  $U_0 = 10 \text{ m/s}$ , providing a Reynolds number based on chord length of  $Re_c = 0.13 \times 10^6$ . Measurements are obtained with a 2D PIV system, which consists of a double Nd:YAG Quantel Big Sky Laser, a cylindrical telescope optic to create a laser sheet, a  $1600 \times 1186$  pixel CCD FlowSense M2 camera and a dedicated PC. Cigarette smoke is used to seed the flow. Data are acquired at  $15 \text{ Hz}$  with the time delay between image pairs being  $30 \mu\text{s}$ . In total, 150 image pairs are taken both with and without control. Data processing is performed using Dantec Flow Manager with a  $32 \times 16$  pixel interrogation area with 25% overlap providing a spatial resolution of  $1.7 \times 0.8 \text{ mm}$ .

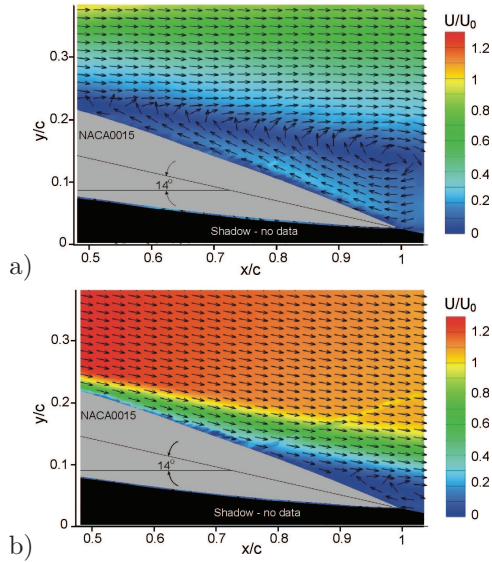


Figure 4: Time-averaged velocity magnitude around a NACA 0015 airfoil at  $Re_c = 0.13 \times 10^6$  and  $\alpha = 14^\circ$ . Showing (a) without control and (b) control with a MDBD actuator with inter-floating electrodes

### 3 Results

The trailing edge separation of a NACA 0015 airfoil has been controlled with four different DBD plasma actuators. Test speeds have ranged from 8 m/s to 40 m/s, providing a range in Reynolds number of  $Re_c = 0.13 - 1.33 \times 10^6$ .

#### 3.1 Control at $Re_c = 0.13 - 0.16 \times 10^6$

Experiments using a MDBD actuator with floating interelectrodes (figure 3) have been conducted at  $Re_c = 0.13 \times 10^6$ . The time-averaged velocity magnitude without control at  $\alpha = 14^\circ$  is shown in figure 4 (a). The recirculation zone extends over 50% of the chord and is clearly visible by the circling arrows of U- and V- components of velocity. On application of the MDBD actuator, figure 4 (b), the recirculation zone is pushed far downstream, covering the last 10% of the chord. This reduces the drag of the NACA 0015 airfoil and increases its lift, improving aerodynamic performance. The MDBD actuator induces a streamwise velocity of 6 m/s, providing a streamwise to free-stream velocity ratio of  $U/U_0 = 60\%$ . The high streamwise velocity re-energizes the separated region causing the reduction in size of the recirculation zone. Experiments using DBD VGs have been conducted at  $Re_c = 0.16 \times 10^6$ . An important parameter of the DBD VGs is the spanwise to free-stream velocity ratio,  $W/U_0$ . The spanwise velocity induced by a single counterrotating DBD VG in quiescent air is  $W = \pm 2.5 \text{ m/s}$ . Therefore, the spanwise to free-stream velocity ratio is  $W/U_0 = 31\%$ . We have previously shown that the DBD VGs generate streamwise vortices [8]. The streamwise vortices entrain the high-speed fluid from outside the boundary layer into the separated region causing flow reattachment. The effect of the DBD VGs on the trailing edge separation of a NACA 0015 airfoil is shown in figure 5. The data presented is taken at the centre of the upper electrode where maximum downwash is expected: see figure 1. The trailing edge separation begins at  $\alpha \approx 13^\circ$  and moves upstream as the angle of attack increases. At  $\alpha = 14.2^\circ$ , figure 5 (a), the separated region covers 45% of the chord.

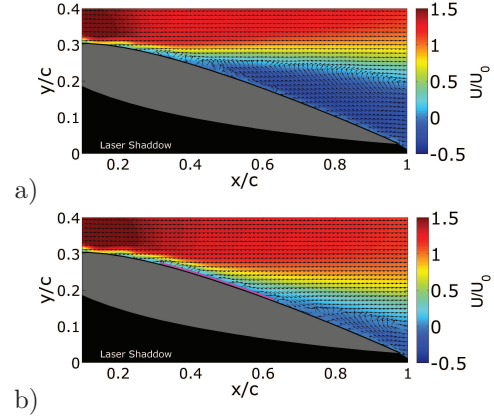


Figure 5: Time-averaged streamwise velocity around a NACA 0015 airfoil at  $Re_c = 0.16 \times 10^6$  and  $\alpha = 14.2^\circ$ . Showing (a) without control and (b) DBD VG control. The magenta line indicates the location of the plasma actuators

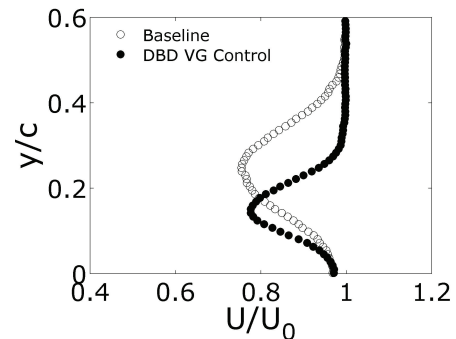


Figure 6: Wake profiles measured at  $x/c = 2$  with and without DBD VGs at  $Re_c = 0.16 \times 10^6$  and  $\alpha = 13.4^\circ$ .

The separated region has a clear recirculation zone, illustrated by time-averaged streamwise velocity and arrows of U- and V-components of velocity. As the DBD VGs are operated, figure 5 (b), the recirculation zone is pushed downstream to  $x/c = 65\%$  by the entrainment of high-speed fluid from the streamwise vortices. The streamwise vortices created by the DBD VGs introduce a highly three-dimensional flow field. Yet, remarkably, PIV data obtained at several spanwise locations across the wavelength of the DBD VGs show similar results. Although it is not shown here for brevity, it is interesting to note that the recirculation zone for  $\alpha < 13.6^\circ$  can be completely removed by the DBD VGs allowing the flow over the airfoil to become fully reattached. In addition, at  $\alpha = 15.2^\circ$ , the recirculation zone encompasses 70% of the chord, extending to  $x/c = 30\%$ , which is the location of the onset of plasma actuation with the DBD VGs. Remarkably, we have found that even at this condition, the DBD VG can push the recirculation zone to  $x/c = 50\%$ . Increasing the angle of attack to  $\alpha = 15.3^\circ$  causes the trailing edge separation to snap to a leading edge stall. Once the airfoil is stalled, the DBD VGs have no effect on the separated region and therefore must be applied upstream of separation.

To quantify the aerodynamic performance of the DBD VGs on the NACA 0015, wake profiles are measured one chord downstream of the trailing edge. The wake profiles at  $\alpha = 13.4^\circ$  are shown in figure 6. The DBD VGs reduce the width of the wake, deflect the wake downwards and slightly increase the streamwise velocity

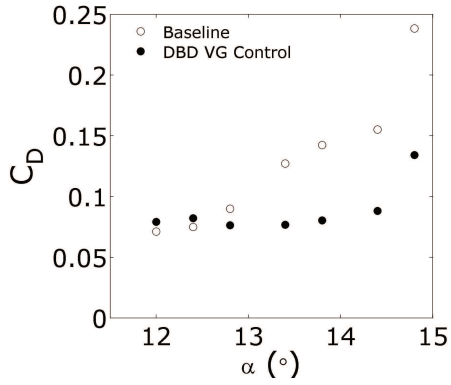


Figure 7: Drag coefficient per unit span with and without DBD VGs at  $Re_c = 0.16 \times 10^6$

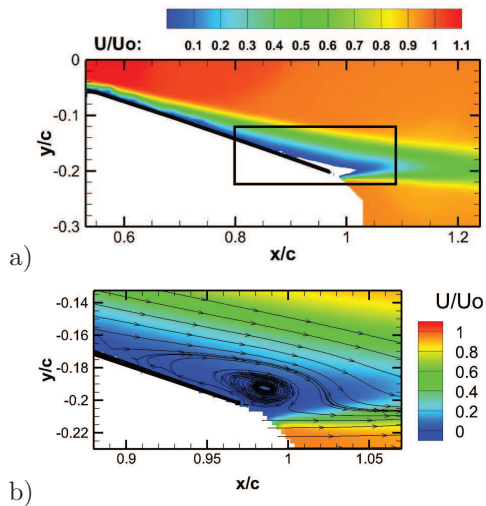


Figure 8: Time-averaged (a) streamwise velocity and (b) streamline patterns of the recirculation region without control at  $Re_c = 0.67 \times 10^6$  and  $\alpha = 12^\circ$ . The black box in (a) indicates the area of the zoomed view in (b)

within the wake. The large change in the wake indicates the significant improvement in aerodynamic performance with DBD VG control. Integration of the wake profiles allows the drag co-efficient per unit span to be quantified and these results are shown in figure 7. With an angle of attack of  $\alpha > 12.8^\circ$ , the DBD VGs begin to have a positive effect on aerodynamic performance and cause the drag co-efficient of the NACA 0015 to decrease by 45% for  $\alpha > 13.8^\circ$ . The drag coefficient for  $\alpha > 14.8^\circ$  is not shown as the wake is greater than the field of view of the PIV measurements.

### 3.2 Control at $Re_c = 0.67 \times 10^6$

Experiments using DBD VGs (figure 1), SDBD and MDBD actuators (figure 2) have been conducted at the Université de Poitiers at  $Re_c = 0.67 \times 10^6$ . Velocity fields of the airflow around the NACA 0015 without control at an angle of attack of  $\alpha = 12^\circ$  are presented in figure 8. Time-averaged streamwise velocity is shown in figure 8 (a) and demonstrates the separated region close to the trailing edge of the airfoil. The white region represents negative streamwise velocity and illustrates the presence of a recirculating zone, which is more clearly highlighted by the time-averaged streamlines of a zoomed view of the trailing edge shown in figure 8 (b).

The SDBD, MDBD and DBD VGs produce an induced velocity of 6 m/s, 7.5 m/s and 3.5 m/s, respectively. The

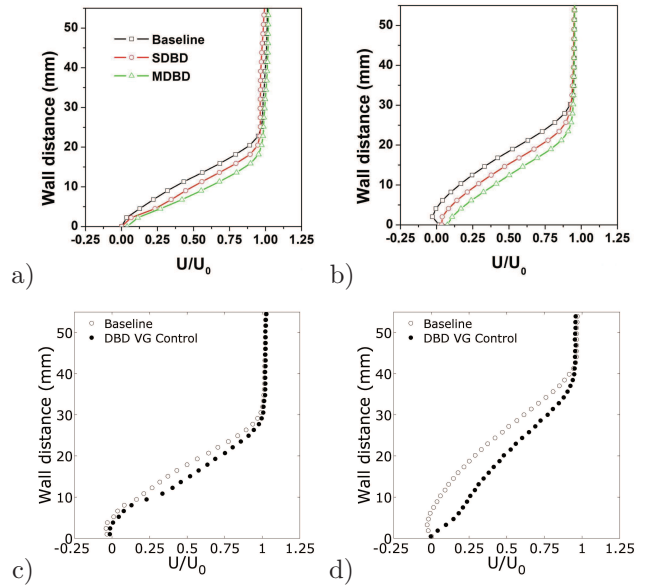


Figure 9: Time-averaged streamwise velocity profiles at (a)  $x/c = 80\%$  and (b)  $x/c = 100\%$  with SDBD and MDBD actuators and at (c)  $x/c = 80\%$  and (d)  $x/c = 100\%$  with DBD VGs at  $Re_c = 0.67 \times 10^6$  and  $\alpha = 12^\circ$

SDBD and MDBD actuators are aligned along the span of the airfoil and produce streamwise forcing, whereas the DBD VGs are aligned along the chord of the airfoil and produce spanwise forcing. Therefore, the SDBD and MDBD actuators produce a streamwise to free-stream velocity ratio of  $U/U_0 = 30\%$  and  $U/U_0 = 37.5\%$ , respectively and the DBD VGs produce a spanwise to free-stream velocity ratio of  $W/U_0 = 17.5\%$ .

Time-averaged streamwise velocity profiles at  $x/c = 80\%$  and  $x/c = 100\%$  are shown in figure 9 at an angle of attack of  $\alpha = 12^\circ$ . The SDBD and MDBD actuators add streamwise momentum to the boundary layer. This increases the velocity close to the wall, figure 9 (a), and removes the recirculation region at the trailing edge of the airfoil, figure 9 (b). On the other hand, the streamwise vortices generated by the DBD VGs entrain high momentum fluid from outside the boundary layer into the recirculation region: see figure 9 (c) and figure 9 (d). As shown in these results, all types of DBD actuators are very effective in re-energising the separated boundary layer at this Reynolds number. The MDBD actuator produces greater actuator authority and is more effective than the SDBD actuator at controlling the trailing edge separation. This is illustrated in figure 10, where the vortices detected in the separated region using the G1 criterion [9] are superimposed onto a background of time-averaged wallnormal velocity. The number of vortices detected in the separated region with MDBD actuation, figure 10 (a), is reduced by more than a factor a ten when compared with uncontrolled flow, figure 10 (b). To quantify the aerodynamic performance of the SDBD, MDBD and DBD VGs at  $Re_c = 0.67 \times 10^6$ , wake profiles have been measured at  $x/c = 1.2$ . The wake profiles with the SDBD and MDBD actuators are shown in figure 11 (a) and the wake profiles for DBD VGs are shown in figure 11 (b). The baseline data sets show discrepancy and are a measure of the repeatability over the experimental campaign. The wake profiles with DBD control are reduced in width and are deflected downwards, indicating that lift increased with all actuator types. The velocity defects within the wake region are reduced by approximately 10% and 22% with the SDBD

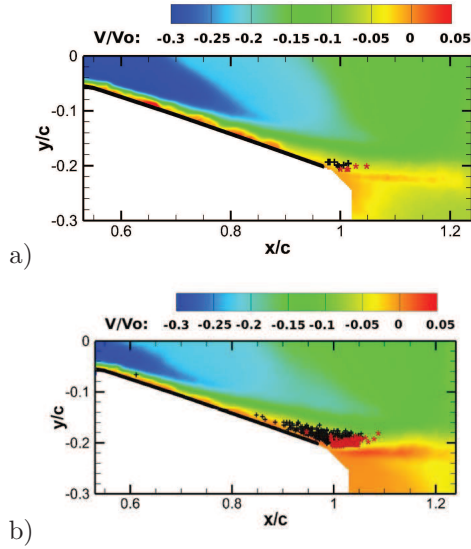


Figure 10: Location of vortices superimposed on time-averaged wall-normal velocity with (a) MDBD actuation and (b) without control at  $Re_c = 0.67 \times 10^6$  and  $\alpha = 12^\circ$

and MDBD actuators, respectively, leading to a drag reduction of 8.3% and 18.5%. The data for the DBD VGs indicates that drag is reduced by 6% up to an angle of attack of  $\alpha = 13^\circ$  with only 50% of the induced plasma velocity used by the SDBD and MDBD actuators.

### 3.3 Control at $Re_c = 1.33 \times 10^6$

To demonstrate the effectiveness of the plasma actuators at higher Reynolds number, the MDBD actuator and DBD VGs are tested at  $Re_c = 1.33 \times 10^6$ . Here, the actuator authority is  $U/U_0 = 18.8\%$  for the MDBD actuator and is only  $W/U_0 = 8.8\%$  for the DBD VGs. Remarkably, with reduced actuator authority, the MDBD actuator fully reattaches the flow at an angle of attack of  $\alpha = 12^\circ$  and results in a drag reduction of 9.8%. Although marginal, the DBD VGs also showed a reduction and downward deflection of the wake at this Reynolds number.

It is interesting to note that the actuator authority with the DBD VGs at  $Re_c = 0.67 \times 10^6$  is similar to the actuator authority of the MDBD actuator at  $Re_c = 1.33 \times 10^6$ . At these Reynolds numbers both actuator types have shown comparable improvements in aerodynamic performance. As we may expect, flow separation control decreases with increasing Reynolds number, mainly due to reduced actuator authority. However, for the DBD VGs there are other important factors that must be considered. The location and coverage of the plasma actuators is critically important for effective control of flow separation. This is particularly important for the DBD VGs since it takes some distance before the streamwise vortices are developed. The DBD VGs were placed between  $x/c = 68\%$  to  $76\%$  of the NACA 0015 airfoil in the experiments conducted at the Université de Poitiers, which was probably too close to the trailing edge. For the experiments conducted at the University of Nottingham, the DBD VGs were moved closer to the leading edge to cover the airfoil between  $x/c = 30\%$  to  $63\%$ . The movement of the plasma actuators further downstream and the reduced coverage along the chord of the airfoil during the higher Reynolds number tests may have resulted in the development of relatively weaker streamwise vortices and could have contributed to lower

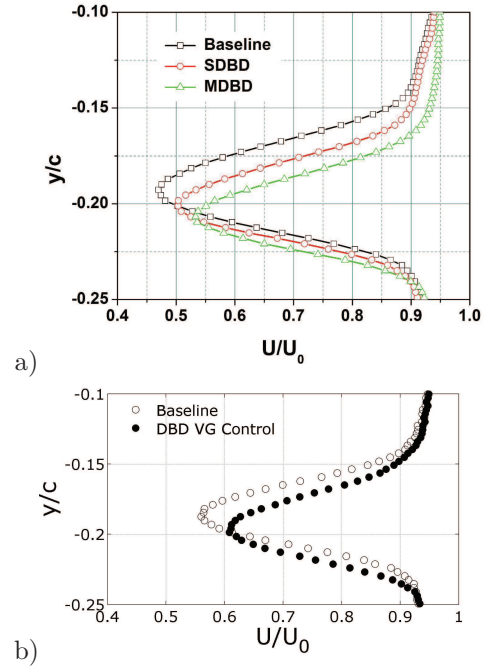


Figure 11: Wake profiles measured at  $x/c = 1.2$  with (a) SDBD and MDBD actuators and (b) DBD VGs at  $Re_c = 0.67 \times 10^6$  and  $\alpha = 12^\circ$

flow separation control observed at higher test speeds. What is clear is that the results at higher Reynolds number are very promising. We have demonstrated that plasma actuators are capable of controlling the trailing edge separation of an airfoil at flow speeds typical for the landing and take-off phases of realistic flight envelopes.

## 4 Conclusions

The trailing edge separation of a NACA 0015 airfoil has been controlled by four different types of DBD plasma actuators, which were developed as part of Plasmaero task 1.1. Experiments have been conducted over a speed range of 8 m/s to 40 m/s, providing a range in Reynolds number of  $Re_c = 0.13 - 1.33 \times 10^6$ . The DBD VGs create streamwise vortices that entrain the high-speed fluid from outside the boundary layer into the separated region causing flow reattachment. At an angle of attack of  $\alpha > 13.8^\circ$  and Reynolds number of  $Re_c = 0.16 \times 10^6$ , the DBD VGs have shown the ability of flow separation control by reducing the drag of the NACA 0015 by 45%. The level of flow separation control reduces as the Reynolds number increases due to actuator authority, location of the DBD VGs and the active length of the DBD. The SDBD and MDBD actuators re-energize the separated region by introducing high streamwise velocity close to the wall. The novel MDBD actuators create an induced velocity above 10 m/s. The increased actuator authority has yielded flow separation control at  $Re_c = 1.33 \times 10^6$ . These results clearly demonstrate that it is possible to control the trailing edge separation of an airfoil up to 40 m/s, a speed found in a typical flight envelope of commercial aircraft.

## Acknowledgments

The work has been carried out as a part of Plasmaero program with funding from the European Community's

## References

- [1] E. Moreau, 2007, *Airflow Control by Non-Thermal Plasma Actuators*, Journal of Physics D: Applied Physics, Vol. 40, pp. 605-636.
- [2] T. C. Corke, C. L. Enloe & S. P. Wilkinson, 2010, *Dielectric barrier discharge plasma actuators for flow control*, Annu. Rev. of Fluid Mech., Vol. 42, pp. 505-529.
- [3] D. Greenblatt & I. J. Wygnanski, *The Control of Separation by Periodic Excitation*, Progress in Aerospace Sciences, Vol. 36, No. 7, 2000, pp. 487-545.
- [4] J. Lin, *Review of Research on Low-Profile Vortex Generators to Control Boundary-Layer Separation*. Progress in Aerospace Science, Vol. 38, 2002, pp. 389-420.
- [5] D. Bushnell, *Longitudinal Vortex Control - Techniques and Applications*, Aeronautical Journal, Vol. 96, 1992, pp. 293-312.
- [6] E. Moreau et al. Surface DBD plasma actuators. Joint ERCOFTAC/PLASMAERO Workshop, 10-12 December, Toulouse, France.
- [7] A. Berendt, J. Podliński, J. Mizeraczyk, 2011, *Elongated DBD with floating interelectrodes for actuators*, Eur. Phys. J. Appl. Phys., 55, 13804.
- [8] T. N. Jukes & K.-S. Choi, *Dielectric-Barrier-Discharge Vortex Generators: Characterisation and Optimisation for Flow Separation Control*, Experiments in Fluids, Vol. 52, 2012, pp. 329-345.
- [9] Gratfieux, L., et al, 2001, *Combining PIV, POD and vortex identification algorithms for the study of unsteady turbulent swirling flows*, Meas. Sci. Technol., Vol. 12, pp. 1422-1429.

# MID-CHORD SEPARATION CONTROL USING PSJ AND DBD PLASMA ACTUATORS

M. Forte<sup>1</sup>, A. Debien<sup>2</sup>, D. Caruana<sup>1</sup>, N. Bénard<sup>2</sup>, P. Barricau<sup>1</sup>,  
C. Gleyzes<sup>1</sup> and E. Moreau<sup>2</sup>

<sup>1</sup>ONERA, Aerodynamics & Energetics Modelling Department, 2 av. Edouard Belin, 31055, Toulouse, France

<sup>2</sup>Pprime, University of Poitiers, CNRS, ISAE-ENSMA, Téléport 2, 86962, Futuroscope, France

## Abstract

This paper presents experimental investigations dealing with mid-chord separation control on a NACA0015 airfoil using two different kinds of plasma actuators: Plasma Synthetic Jets and Dielectric Barrier Discharges. The ability of both actuators to delay this kind of massive separation has been assessed for a realistic chord based Reynolds number of  $Re_c = 1.3 \times 10^6$ . In most cases, the separation point has been delayed towards the trailing edge and the recirculation zone has been reduced. This work has been conducted in the frame of the PlasmAero project funded by European Commission.

## 1 Introduction

Plasma actuators for flow control applications have been studied for more than a decade now. Basically, these actuators can be sorted in two groups depending on the kind of plasma which is generated: non-thermal plasma or thermal plasma. Non-thermal plasma actuators, like Dielectric Barrier Discharge (DBD), are based on the generation of a non-equilibrium surface discharge which induces a body force parallel to the wall inside the boundary layer. This kind of actuators has been widely characterized in quiescent air for different ambient conditions. Moreover, many investigations have shown their ability to control airflows around different kind of bodies: flat plates, cylinders, airfoils. Most of these studies are reported in detailed reviews [1, 2]. Thermal plasma actuators are based on the generation of an equilibrium discharge in order to locally increase the pressure and the temperature of the surrounding gas. For example, Plasma Synthetic Jets (PSJ) actuators are generating a spark discharge inside a small cavity having a pin-hole exit at the wall. The pressure increase inside this cavity induces a wall-normal jet which acts on the boundary layer as a vortex generator. These actuators have been found to generate wall-normal jets with velocities up to 250 m/s at the exit. Moreover, they have shown promising results in controlling several academic aerodynamic configurations just like compressible jets or incompressible separated boundary layers [3, 4]. The originality of the present paper lies in the fact that both kinds of plasma actuators have been used in order to control a specific aerodynamic configuration: PSJ and DBD actuators have been mounted on a NACA0015 model in order to assess their ability to control midchord separation at a realistic chord based Reynolds number.

This work has been performed in the framework of the PlasmAero project funded by the European Commission. One of the main objectives of this project is to study different kinds of plasma actuators and to as-

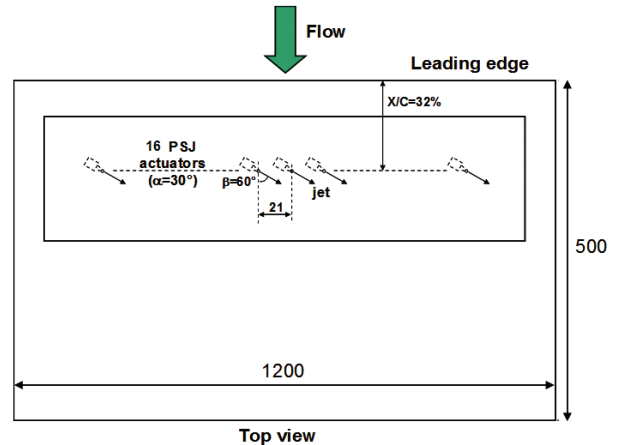


Figure 1: Top view of the model equipped with the PSJ insert

sess their ability to control airflows in order to reduce environmental impact of air transport.

## 2 Experimental setup

The present experiment has been conducted in the "Béton" subsonic closed wind tunnel at the University of Poitiers. This facility operates at ambient conditions and has a large test section which is 2.4 m-high and 2.6 m-wide. A two-dimensional model with a NACA0015 profile is mounted horizontally in the test section between two end-plates which are 2.4 m-high and 5 m-long in the streamwise direction. This model has a chord and span lengths of  $c = 0.5$  mm and  $L = 1.2$  m respectively and includes specific inserts on the suction side. Transition of boundary layer is tripped on both sides of the airfoil with a  $205 \mu\text{m}$ -high zig-zag tape that prevents any uncontrolled effect such as laminar separation bubble for example. Angle of attack has been varied between  $\alpha = 11^\circ$  and  $\alpha = 13^\circ$  and the free-stream velocity adjusted to a constant value of  $U_\infty = 40$  m/s (which gives a chord based Reynolds number of  $Re_c = 1.3 \times 10^6$ ). In these conditions, separation of boundary layer naturally occurs on the suction side at about  $x/c = 0.5$ . Time-averaged PIV measurements have been undertaken in order to access the whole velocity field on the suction side of the airfoil. Velocity measurements have been performed in two overlapping planes using two high-resolution CCD cameras (Pulnix, RM-4200CL,  $2048 \times 2048$ ). Two different inserts, adapted for each sort of plasma actuators, have been realized. The first insert, illustrated in Figure 1, has been equipped with 16 PSJ located on a line

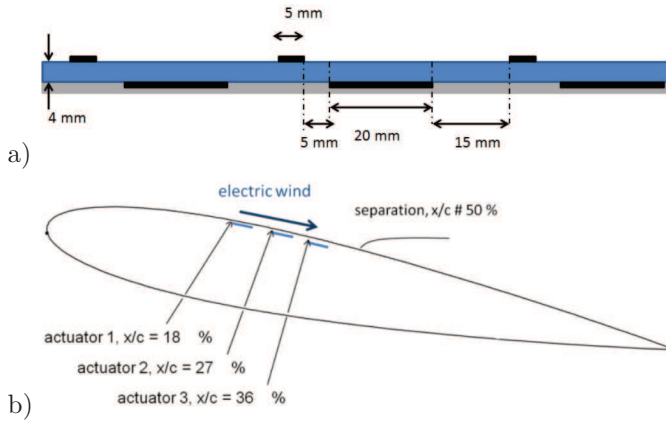


Figure 2: Schematic of the DBD actuators (a) and their locations on the suction side of the airfoil (b)

at  $x/c = 0.32$ . The spacing between each actuator is 21 mm. All PSJ generate in phase synthetic high-velocity jets which act on the boundary layer as vortex generators. The direction of ejection is not normal to the wall: pitch and skew angles are  $\alpha_{PSJ} = 30^\circ$  and  $\beta_{PSJ} = 60^\circ$  respectively. The basic principle and mechanical characterization of PSJ actuators used in this experiment have been well described in previous studies [3, 4].

A second insert in resin has been equipped with a multi-DBD actuator. As illustrated in Figure 2, three successive single DBD that can operate separately or simultaneously are mounted at 18%, 27% and 36% of the chord length. Each single DBD (SDBD) is composed of a 5 mm-wide air-exposed active electrode and a 20 mm-wide encapsulated electrode placed below the dielectric insert. The electrode gap and the dielectric thickness are equal to 5 mm and 4 mm, respectively. The actuation spanwise is equal to 57 cm, corresponding to about 50% of the airfoil span. A sine waveform is applied to every SBDB, with voltage amplitude ranging from 12 kV to 20 kV and frequency between 50 Hz and 1 kHz. In such conditions, a streamwise body force is produced, resulting in a co-flow electric wind oriented toward the trailing edge.

### 3 Baseline flow

For the baseline aerodynamic configuration, the angle of attack is set to  $\alpha = 11.5^\circ$  and the free-stream velocity to  $U_\infty = 40$  m/s, resulting in a chord-based Reynolds number of  $Re_c = 1.33 \times 10^6$ . Figure 3a) shows the time-averaged velocity field of the baseline flow without any control. It highlights the presence of a flow separation that occurs at about mid-chord. In Figure 3b), a  $\Gamma_1$  criterion [6] has been used to detect the centre of the vortices induced by the flow around the profile. The black crosses correspond to the vortices with a clockwise rotation. They form usually at the separation location and they are convected by the flow. As illustrated in Figure 3b), the first vortices are located at about 30% of chord, suggesting that the separation point moves versus time, because the mean separation occurs at mid-chord. The red stars represents the vortices with a counterclockwise rotation, due to the interaction with the flow incoming from the pressure side of the airfoil. Finally, in order to determine accurately the mean separation position, near-wall time-averaged velocity profiles have been plotted at different locations around 50% of chord. (Figure 4). Downstream 50% of chord, the near-wall velocity

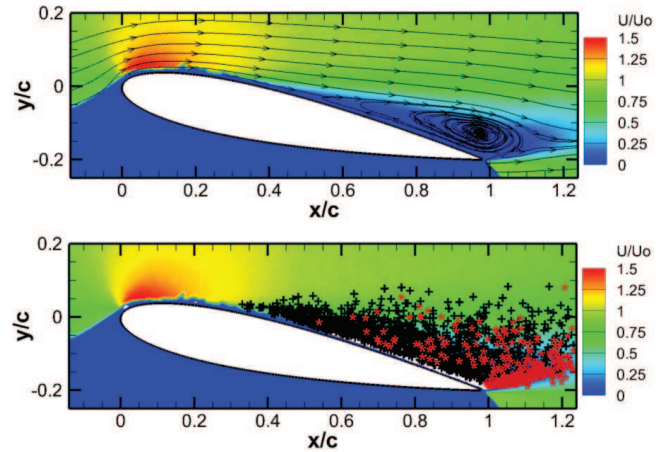


Figure 3: PIV results for the baseline configuration ( $\alpha = 11.5^\circ$ ,  $U_\infty = 40$  m/s): time-averaged field of the horizontal normalized velocity component  $U/U_0$  (a) and detection of vortices by a  $\Gamma_1$  criterion (b)

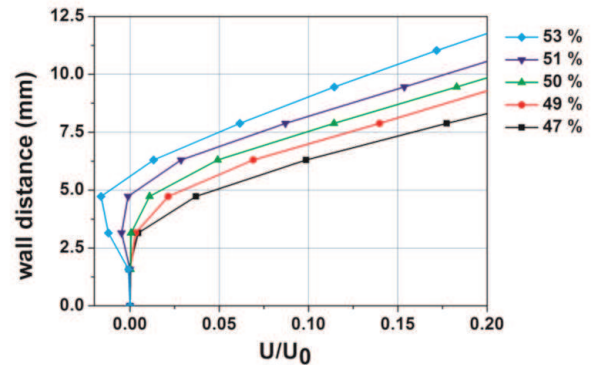


Figure 4: Near-wall velocity profiles at different locations, from 47% to 53% of chord

is negative, highlighting the presence of a recirculation zone. From these profiles, one can deduce that the mean separation point is located exactly at 51% of chord.

### 4 Control by PSJ actuators

This section is related to the experiment with the PSJ actuators insert.

#### 4.1 Effect of the PSJ operating frequency

Figure 5 presents typical results of PIV measurements over the airfoil fitted with the PSJ insert for  $\alpha = 11.5^\circ$  and  $U_\infty = 40$  m/s. The first plot (a) is related to the baseline case without any control while the other plots b) c) and d) are associated to the controlled cases with PSJ pulsing at a frequency of 100 Hz, 250 Hz and 750 Hz respectively. Without control, PIV measurements show a mid-chord separation as presented in the previous test section, generating a massive recirculation zone over the suction side. The separation point seems to be located a little more upstream in this case ( $x/c = 0.45$ ) and this could be explained by the fact that the flow is really unstable in this specific aerodynamic configuration, as discussed in section 3. Nevertheless, separation occurs downstream of the actuators location. When PSJ are

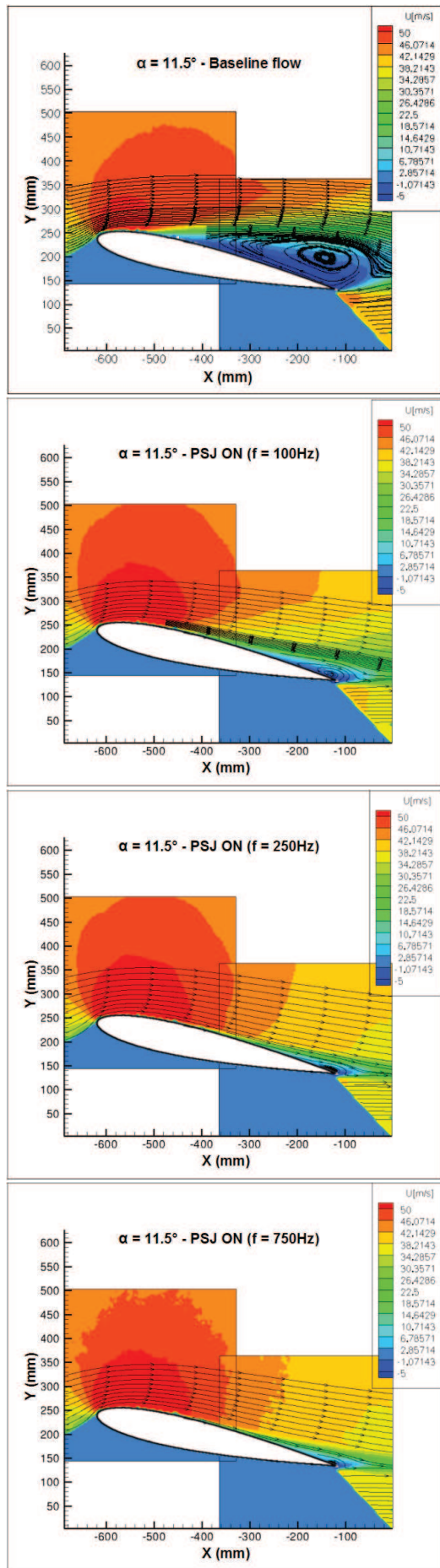


Figure 5: Time-averaged fields of horizontal velocity component and streamtraces ( $\alpha = 11.5^\circ$ ,  $U_\infty = 40\text{m/s}$ ): without control (a) then with PSJ pulsing at  $f=100\text{ Hz}$  (b), at  $f=250\text{ Hz}$  (c) and at  $f=750\text{ Hz}$  (d)

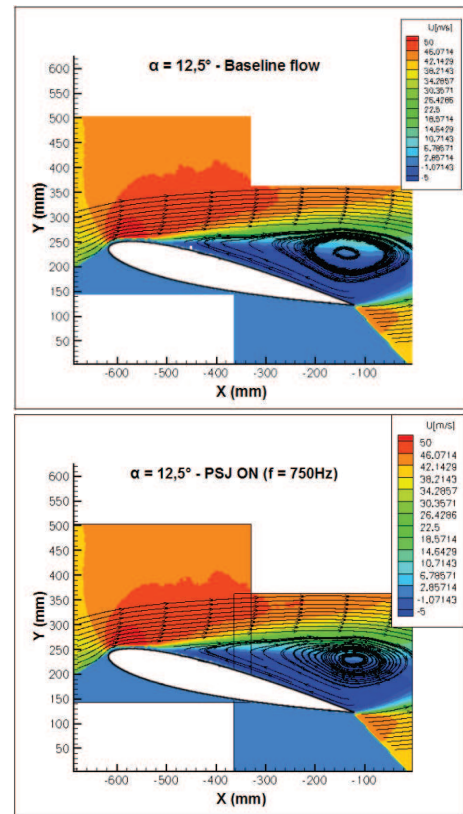


Figure 6: Time-averaged fields of horizontal velocity component and streamtraces ( $\alpha = 12.5^\circ$ ,  $U_\infty = 40\text{m/s}$ ): without control (a) then with PSJ pulsing at  $f=750\text{Hz}$  (b)

turned on, pulsing at a frequency of 100 Hz, the separation point is drastically shifted downstream at  $x/c = 0.8$  and the recirculation zone has been reduced but not totally removed. Separation delay in this case is about 35% of chord. The following plots c) and d) show a clear effect of the operating frequency of PSJ. The location of separation point is progressively shifted downstream when the frequency is increased. In the case where PSJ are pulsing at a frequency of 750 Hz, the separation point is very close to the trailing edge at  $x/c = 0.9$  and the recirculation zone has almost completely disappeared. Increasing this frequency leads to an increase of the mechanical energy induced by the actuators, thus the efficiency of the vortex generators is enhanced. A maximum delay of 45% of chord is achieved with PSJ actuators in this aerodynamic configuration.

## 4.2 Effect of separation point location

In order to study the effect of the separation point location on the PSJ efficiency, a new aerodynamic configuration has been tested. The angle of attack of the model has been slightly increased to a value of  $\alpha = 12.5^\circ$  while the free-stream velocity is kept to the constant value of  $U_\infty = 40\text{ m/s}$  as in the previous experiment. Figure 6 presents the PIV measurements for this aerodynamic configuration in the baseline case (a) and with the PSJ pulsing at a frequency of  $f = 750\text{ Hz}$ . As expected, the separation point without control has been moved upstream compared to the baseline configuration with  $\alpha = 11.5^\circ$  and is located to a value of  $x/c = 0.25$  (upstream of the PSJ location).

When PSJ actuators are turned on at the operating frequency of  $f = 750\text{ Hz}$ , the effect of the actuation is

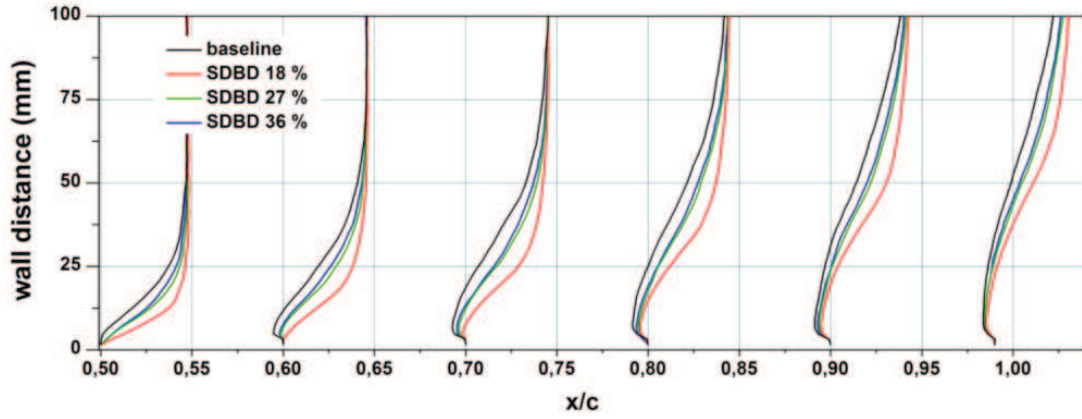


Figure 7: Velocity profiles at several  $x/c$  locations for the baseline and forced flow by the three different SDBD

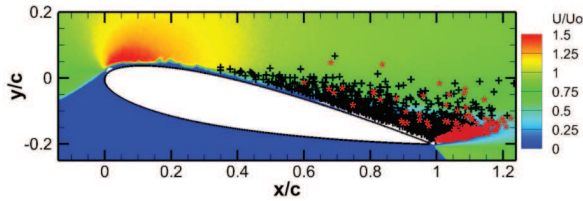


Figure 8: Forced flow by the SDBD located at 18% of chord and detection of vortices by a  $\Gamma_1$  criterion

hardly visible. This experiment demonstrates that the location of the actuation compared to the separation point location is a key parameter. PSJ actuators maximum efficiency is reached when the separation occurs just downstream of the actuation line.

## 5 Control by DBD actuators

In this part, results concerning flow control by surface DBD actuators are given.

### 5.1 Flow control by SDBD

The first investigations concerned flow control by SDBD. Each SDBD is switched on individually in "steady" mode, suggesting that the flow control strategy is only based on streamwise momentum addition within the boundary layer. The actuator is supplied by a sine waveform having an ac frequency of 1 kHz and a voltage amplitude maintained at 20 kV. The electrical power consumed by one SDBD is equal to 0.75 Watt per spanwise centimetre and the electric wind velocity can be estimated to about 4 m/s, corresponding to one tenth of  $U_0$ . Figure 7 presents velocity profiles along the suction side, between 50 to 98% of chord, with and without actuation. First, it highlights that the actuation results in a significant velocity gain inside the boundary layer. Secondly, one can remark that the SDBD located at 18% of chord is more effective than the two others ones. Indeed, for this position, the actuator is always located upstream the flow separation, when the two others ones are sometimes located downstream the separation point due to the high time-dependent behaviour of this point. As a result, the SDBD located at 18% delays the separation up to 64% of chord when it is shifted by only 6% when one of the two others SDBD is used. Finally, Figure 8 presents the vortex locations when the flow is forced with the SDBD located at 18% of chord. It shows that the recirculation

zone has been slightly reduced, but the flow has not been fully reattached.

### 5.2 Flow control by MDBD

In a second set of experiments, the three DBDs operate simultaneously in order to cumulate the velocity induced by every single DBD. Moreover, the interaction between successive SDBD has been cancelled by alternating the high voltage electrode and the grounded one, from one DBD to the successive one, as explained in [5]. At 20 kV and 1 kHz, the electric power consumption is equal to about 2.2 W/cm and the electric wind velocity can be estimated to 6.5 m/s. When the voltage and the frequency are reduced, the electric wind velocity decreases (down to 3 m/s at 12 kV and 1 kHz for instance). The main advantage of using this multi-DBD (MDBD) actuator is that the actuation area is enlarged. The actuation takes place from 18 to 36% of chord. Figure 9 presents velocity profiles of the baseline flow and the forced flow for several voltage values. First, it highlights that the velocity gain increases with the applied voltage. Secondly, one can see that the MDBD is more effective than the SDBD. In Figure 10, the location of the separation point on the suction side is plotted versus the value of the applied voltage. The operating frequency is set to a constant value  $F_{ac} = 1\text{kHz}$ . The dashed line represents the location of separation point in the baseline case, without any actuation. The plot clearly reveals that the separation point moves progressively toward the trailing edge when the voltage is increased. In the best case, separation point is located at 76% of chord. Figure 11 shows the flow field and the location of the vortices when the separation is delayed at 76% of chord. The recirculation region and the vortex number have been significantly reduced compared to the baseline flow (see Figure 3b).

Finally, the effect of an unsteady actuation has been investigated and the results are plotted in Figure 12. First, the operating frequency  $F_{ac}$  has been varied from 50 Hz up to 1 kHz, corresponding to a reduced frequency range of  $0.3 < F_{sep}^+ < 6.13$  (black curve with squares in Figure 7). This reduced frequency is estimated with the following equation:  $F_{sep}^+ = L_{sep} \times F_{ac} / U_\infty$ . Here, the voltage amplitude is set to a constant value  $V = 20\text{kV}$ . From this plot, one can deduce that the most effective separation delay occurs for  $F_{sep}^+ = 3$ , with  $x_{sep}/c = 80\%$ . However, the actuation is not effective for frequencies close to  $F_{sep}^+ = 1$ , as sometimes reported in literature. Secondly, the operating frequency has been set to a constant value as well as the voltage amplitude ( $F_{ac} = 1\text{kHz}$ ,

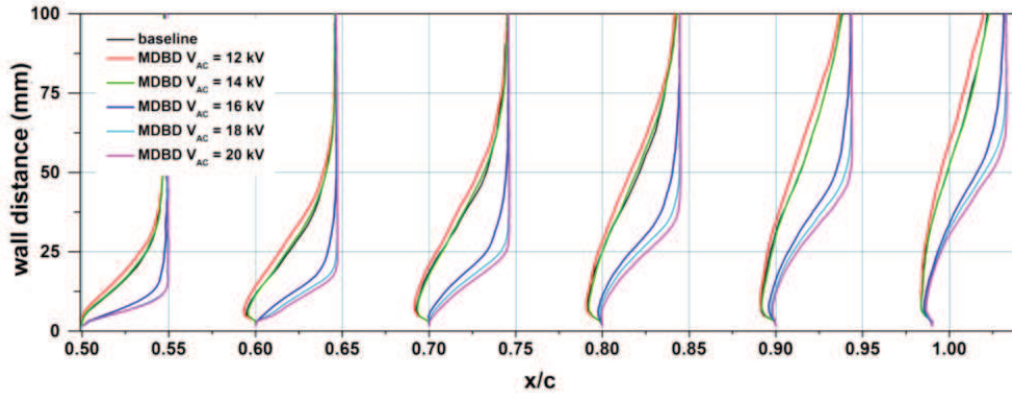


Figure 9: Velocity profiles at several  $x/c$  locations for the baseline flow and forced flow by the MDBD for different voltage values

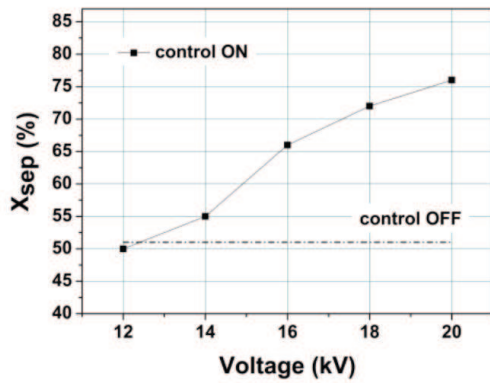


Figure 10: Position of the flow separation versus applied high voltage

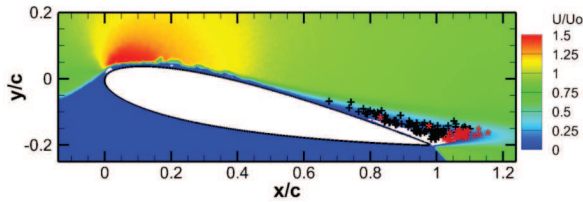


Figure 11: Forced flow by the MDBD and detection of vortices by a  $\Gamma_1$  criterion

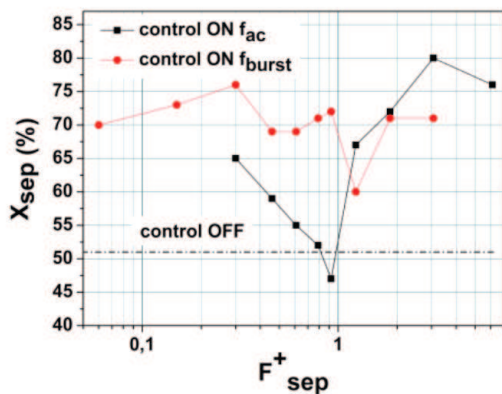


Figure 12: Position  $X_{sep}$  (in % of chord) of the separation versus reduced frequency  $F_{sep}^+$

$V = 20\text{kV}$ ) and this sine signal has been modulated by a gate signal at a lower frequency  $F_{burst}$ . The duty cycle is set to 50%, this resulting in electric wind fluctuations with much larger amplitude and with frequencies scaling with the frequency range of the natural free shear layer forming from the separation point. Here the reduced frequency is estimated with the following equation  $F_{sep}^+ = L_{sep} \times F_{burst} / U_\infty$ . In all the cases, the actuation can reduce the flow separation. A maximal separation postpone is observed for burst actuation at  $F_{sep}^+ = 0.3$  ( $F_{burst} = 50\text{Hz}$ ).

## 6 Conclusion

In this study, two different kinds of plasma actuators, with two different control strategies, have been used in order to control a separation over a NACA0015 airfoil for a realistic chord based Reynolds number of  $Re_c = 1.3 \times 10^6$ . Plasma Synthetic Jets and Dielectric Barrier Discharge actuators have both shown very good results in delaying a massive separation occurring at mid-chord. PSJ actuators, which generate wall-normal jets, achieved a maximum delay of 45% of chord at the highest operating frequency. The investigations about DBD actuator underlined that Multi-DBD is more efficient than Single-DBD thanks to an extended area of actuation and stronger mechanical effect. Thus, a maximum delay of 30% of chord has been achieved using the MDBD actuator with maximum voltage amplitude of 20kV. As this amplitude value has been deliberately limited, better results could be expected with higher voltage amplitudes. Finally, this study has shown that the location of the actuation compared to the separation point is a key parameter for both actuators. Maximum efficiency is reached when the separation occurs just downstream of the actuation line.

## Acknowledgments

The present work has been performed within the framework of the PlasmAero project ([www.plasmaero.eu](http://www.plasmaero.eu)) funded by the 7th Framework Program of European Commission (grant agreement nr. 234201). The authors would like to thank the members of this project for sharing their knowledge and the fruitful discussions.

## References

- [1] E. Moreau, *Airflow Control by Non-Thermal Plasma Actuators*, Journal of Physics D: Applied Physics, Vol. 40, pp. 605-636, 2007.
- [2] N. Bénard and E. Moreau, 2012, *EHD Force and Electric Wind Produced by Plasma Actuators Used for Airflow Control*, Proc. of the 6th AIAA Flow Control Conference, AIAA Paper 2012-3136, 2012.
- [3] D. Caruana, et al., *The Plasma Synthetic Jet actuator. Aero-thermodynamic characterization and first flow control applications*, Proc. of the 47th AIAA Aerospace Sciences Meeting, AIAA Paper 2009-1307, 2009.
- [4] P. Hardy, et al., *Plasma Synthetic Jet for flow control*, Proc. of the 5th AIAA Flow Control Conference, AIAA Paper 2010-5103, 2010.
- [5] E. Moreau, et al., *Surface DBD plasma actuators*, Proc. of the Joint ERCOFTAC PLASMAERO Workshop, Toulouse, France, 2012.
- [6] L. Gratieaux, et al., *Combining PIV, POD and vortex identification algorithms for the study of unsteady turbulent swirling flows* Meas. Sci. Technol., Vol. 12, pp. 1422-1429, 2001.

# FULLY SEPARATED FLOW CONTROL USING DBD PLASMA ACTUATORS LOCATED AT THE LEADING EDGE OF AN AIRFOIL

A. Leroy<sup>1</sup>, P. Audier<sup>2</sup>, D. Hong<sup>2</sup>, J. Podliński<sup>3</sup>,  
A. Berendt<sup>3</sup>, and J. Mizeraczyk<sup>3</sup>

<sup>1</sup>Laboratory PRISME, University of Orleans, 8 rue Léonard de Vinci, 45 072 Orleans, France

<sup>2</sup>GREMI, UMR 7344, CNRS and University of Orleans, 14 rue d'Issoudun, 45 067 Orleans, France

<sup>3</sup>Centre for Plasma and Laser Engineering, The Szwedowski Institute of Fluid Flow Machinery  
Polish Academy of Sciences, Fiszera 14, 80-952 Gdańsk, Poland

## Abstract

In the framework of the PLASMAERO European project, experiments were conducted to investigate the authority of surface DBD plasma actuators to alter a fully separated flow around an airfoil in order to improve its aerodynamic performances in its natural stall regime. In this paper, unsteady excitation control is more specifically investigated. The key control parameter studied here is the burst frequency which periodically imposes switching on and off the actuator. Results show that it is possible to perform a modification of the massively separated flow by unsteady excitation near the leading-edge. However, depending on the forcing frequency and the post-stall regime, two different flow modification mechanisms can be observed leading to either the reduction of the flow separation or the occurrence of a mean large lifting vortex next to the suction side. In both cases, a large lift increase is obtained.

## 1 Introduction

Active flow control technologies based on plasma actuators present the potential to create flow field modifications without the need for mechanical parts and with the ability for real-time control at high frequency. For these reasons, they have received much attention in previous years within research laboratories in aerodynamics and in plasma physics. More recently, references [1-3] provide an overview of the physics of surface DBD plasma actuators and highlight some of their capabilities through examples from experiments and simulations.

Results presented in this paper have been achieved in the framework of the PLASMAERO European project [4]. In order to demonstrate capabilities of typical surface DBD plasma actuators to enhance airfoil aerodynamic performances, different test cases were studied. In this paper are reported results focusing on lift enhancement in a deep post-stall configuration. Post-stall flow control may be very useful to enlarge the range of angles of attack for large wings, more practically, in landing of aircraft and manoeuvring flight. According to the stall regime configuration to be controlled, different kinds of flow modification mechanisms can be effectively observed depending on the operating electrical parameters used to supply plasma actuators. In studies of flow separation control, the actuators are generally implemented at, or near, lines of separation in order that the formation of the shear layer emitted may be modified. A large range

of effective forcing frequencies are reported in the literature via numerical and experimental studies. The goal of the most investigations is to largely reduce the size of the massive separation bubble in order to increase lift and reduce drag [5-11]. However, for certain post-stall regimes, Wu et al [12] argues it is reasonable to assume that shear layer convective instabilities and far wake global instability interact according to a nonlinear process and then a large lifting vortex is formed leading to a large increase in lift. For that, the control is performed near the leading-edge by periodic excitation scaled on the wake flow instability [12-16]. In this paper, unsteady excitation control is therefore more specifically addressed. The key control parameter studied here is the burst frequency which periodically imposes switching on and off the actuator. A single DBD and a multi-DBD actuator with additional floating interelectrodes, located at the vicinity of the leading edge of an NACA0012 airfoil, were tested for Reynolds numbers based on the airfoil chord length varying up to  $8 \times 10^5$ . Aerodynamic force measurements, Particle Imaging Velocimetry and Hot-Wire Anemometry measurements have been performed to quantify the control benefits and to characterize the uncontrolled and controlled flow.

## 2 Experimental set-up

### 2.1 Airfoil model and actuators

Experiments were carried out in the close return wind tunnel at the University of Orléans. The testing part of the tunnel is 5 m long with a cross-section of  $2 \text{ m} \times 2 \text{ m}$ . The operating speed varies from  $10 \text{ m.s}^{-1}$  to  $60 \text{ m.s}^{-1}$  with a turbulence level of the airflow below 0.4%. A Plexiglas window was mounted on one side for measurements using optics and lasers. The wing used in this study had a NACA 0012 profile with the chord dimension of  $C = 0.3 \text{ m}$  and the span-wise length of  $L = 1.1 \text{ m}$ . It was suspended between two large flat plates ensuring a 2D flow configuration. Both plates were linked to a 6 component platform balance (located under the test section) used for time-averaged aerodynamic load measurements.

The actuator consisted of a copper electrodes flush mounted with an asymmetric disposition on both sides of a dielectric panel constituted by four layers of Kapton<sup>®</sup> tape (Fig. 1). A single and a multi-DBD actuator (see Figure 2 and references [17,18]) with saw-like grounded electrodes and floating inter-electrodes were used. Both actuators were operated to obtain a discharge contouring the airfoil leading edge over 90% of the span. The first plasma discharge started at  $x/C = 0$  (x-position in

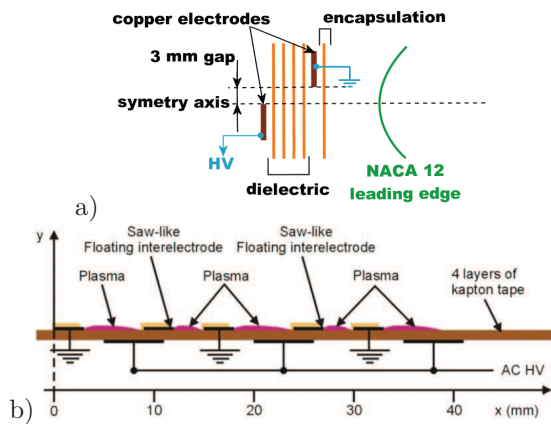


Figure 1: Schematic side view of the single DBD (a) and the multi-DBD (b) actuators mounted on the NACA 0012 airfoil model. ( $x$ ,  $z$ : chord and vertical directions respectively)

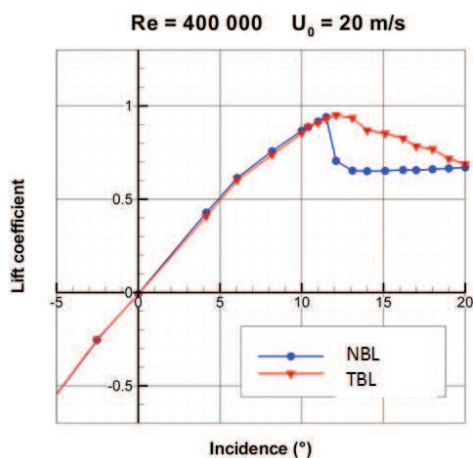


Figure 2: Lift versus incidence in NBL and TBL

chord direction). Discharges were obtained by applying a sinusoidal signal simultaneously to insulated electrodes (on the bottom of the main dielectric for the multi-DBD actuator) with a high voltage amplitude of 8 kV and a frequency of 1 or 2 kHz. With these electrical operating parameters, the thin wall jet is continuously accelerated along the successive discharges with the multi-DBDs. The flow produced tangentially to the model surface in the freestream direction has a mean velocity of about  $8 \text{ m.s}^{-1}$  (without external flow) [17]. The electric power dissipated by the discharges was 15 W per meter for a single DBD. The actuator was operated in steady or unsteady actuation mode. In unsteady actuation, the main control parameter investigated in this study was the burst frequency which periodically imposes switching on and off the actuator. The duty cycle was fixed to 50%.

## 2.2 Measurement systems

Mean load measurements were performed by the aerodynamic balance, which was carefully calibrated. Lift and drag coefficient uncertainties were estimated to be less than 2%. Mean velocity fields around the airfoil were studied from 2D-PIV measurements to analyze flow separation features in the symmetry longitudinal plane. PIV system consisted of a double pulsed Nd:YAG laser emitting pulses of 200 mJ each. The laser light sheet

was placed parallel to the streamwise direction at the median plane. Images were acquired with one or two TSI Power View Plus  $2048 \times 2048$  pixels cameras fitted with a 105 mm lens. With two cameras, the image size was  $431 \text{ mm} \times 248 \text{ mm}$  and it covers the whole separation region around the airfoil. The seeding consisted of submicro-sized olive oil droplets sprayed by a PIVTEC seeding system (around 1 mm in diameter). Data processing to compute instantaneous and time averaged flow velocity fields was made using Insight software. For this configuration 1000 image pairs were recorded to ensure good statistics.

Measurements of temporal flow velocities were made using two single hot-wire probes (Dantec Dynamics, 55P11). The two hot-wire signals were simultaneously processed and recorded via the Dantec Constant-Temperature-Anemometer (Streamline 90N10 Frame). One single hot wire probe was mounted on the moving 3-axis traversing system installed above the test section and was used to perform velocity measurements in the vicinity of the shear layer. The other one was mounted on a system fixed on the floor of the test section near the wake at one chord length downstream the trailing edge. Each velocity measurement consisted of the average of 524288 samples. The acquisition frequency was set to 6 kHz and signals were low-pass filtered at 3 kHz. The sampling rate is high enough to use temporal flow velocity series to calculate Power Spectra Density (PSD) of the fluctuating streamwise velocity.

## 3 Results

### 3.1 Natural and non-controlled flow

As the incidence increases beyond the static stall incidence, fully separated flow develops causing a high lift drop as shown in Figure 2 for a Reynolds number of  $4 \times 10^5$ . Because of possible Reynolds effects in these aerodynamic test conditions, the post-stall separated flow over the airfoil was studied in natural boundary layer (NBL) and artificially tripped boundary layer (TBL) in order to observe differences in actuator authority. At  $20^\circ$  of incidence, in NBL or TBL, the fully separated flow is characterized at least by a shear layer emitted from the leading-edge that corresponds to convective process instability (Kelvin-Helmholtz instability) and a wake flow corresponding to a global instability behavior that causes a large scale vortex shedding (Karman vortex shedding). Figure 3 shows the power spectra density of the fluctuating streamwise velocity at  $20^\circ$  of incidence, corresponding to this deep post stall regime. The presence of both natural frequencies can be observed in the shear layer and in the wake regions. The first one is indicated by PSD versus  $F^+ = f \frac{\text{chord}}{U_\infty}$  plotted in the shear layer and corresponds to instabilities in the shear layer due to the separated boundary layer. The frequency bump is centered around 3 in NBL and 5 in TBL. As the airfoil is in deep stall, the wake shedding of vortices is characterized by the dominant Strouhal number ( $St = f(\text{wake}) \cdot \text{chord} \cdot \sin(\text{incidence}) / U_{\downarrow\infty}$ ) of about 0.2, commonly reported in the literature for bluff bodies. This indicates that there is more than one natural time scale, and consequently, both instabilities have to be considered to achieve flow control, assuming nonlinear interactions between them.

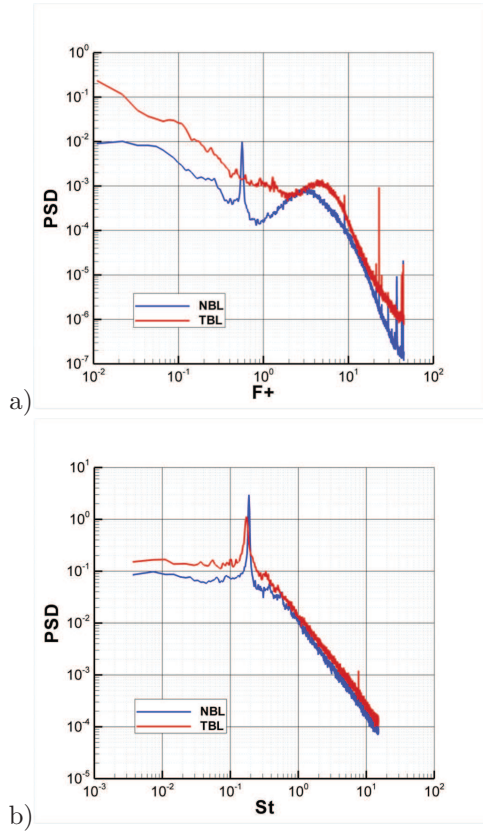


Figure 3: PSD at 20° of incidence in (a) the shear layer and (b) the wake regions

### 3.2 Controlled flow

In this paper, unsteady excitation control is more specifically addressed in the case of the deep stall configuration at 20° of incidence for a Reynolds number of  $4 \times 10^5$ . The controlled flow obtained by varying the burst frequency, keeping constant other electrical operating parameters, is compared to the uncontrolled flow and to the controlled flow with steady actuation. Time-averaged lift and drag coefficient gains for the controlled flow defined by  $\frac{CL - CL_{OFF}}{CL_{OFF}}$  and  $\frac{CD - CD_{OFF}}{CD_{OFF}}$  respectively, are presented in Fig. 4 and 5 as a function of the burst frequency at 20° of incidence in NBL and TBL. CL, CD,  $CL_{OFF}$  and  $CD_{OFF}$  correspond to the aerodynamic coefficients for the controlled and the uncontrolled flow respectively.

These results globally show that the control effects are similar for both actuators. The control is more efficient with unsteady actuation than with steady actuation in terms of a favorable lift coefficient gain whatever the actuator. Drag is either increased or decreased. Considering natural or tripped boundary layer, results seem to exhibit the same range of effective forcing frequencies. However, with the same power input the control is more efficient in the NBL. For this Reynolds number, a probable interaction of the actuator on the boundary layer nature and transition, reinforcing actuation effects, has to be considered as well. Finally, these results indicate a frequency range at which lift and drag gains are maximum, namely around the frequencies in the range of 30-35 Hz. In this deep post-stall configuration, this frequency matches with the bluff body wake shedding of vortices, commonly characterized by the Strouhal number of around 0.2.

Tables I and II summarize lift, drag, lift to drag ratio gains with steady actuation and with unsteady actuation

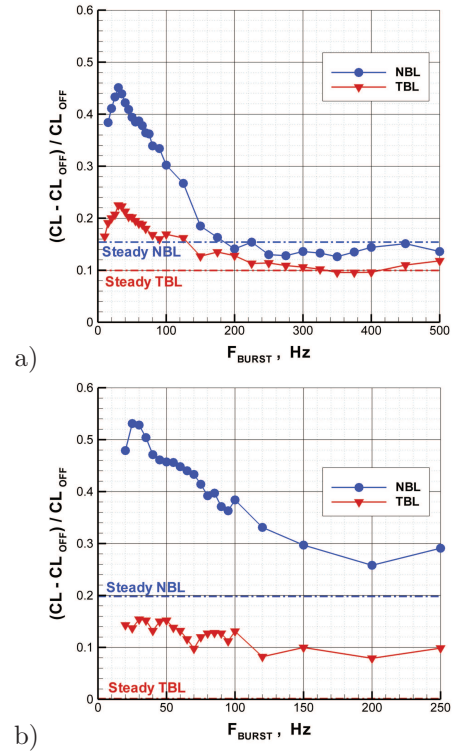


Figure 4: Lift gain versus burst frequency for (a) the single DBD and (b) the multi-DBD actuator.  $Re = 4 \times 10^5$

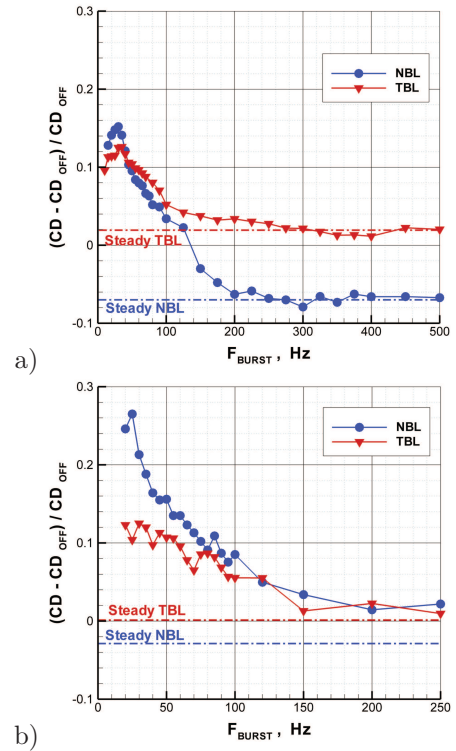


Figure 5: Drag gain versus burst frequency for (a) the single DBD and (b) the multi-DBD actuator.  $Re = 4 \times 10^5$

Table I: Aerodynamic load gains with steady actuation

	Single DBD		Multi DBDs	
	NBL	TBL	NBL	TBL
Lift gain	15%	10%	20%	insignificant
Drag gain	-7%	insignificant	-2.5%	insignificant
Lift/Drag gain	21%	7%	22%	insignificant

Table II: Aerodynamic load gains with unsteady actuation at a burst frequency of 30-35 Hz

	Single DBD Burst frequency of 35 Hz		Multi DBDs Burst frequency of 35 Hz	
	NBL	TBL	NBL	TBL
Lift gain	45%	20%	55%	15%
Drag gain	15%	10%	25%	10%
Lift/Drag gain	26%	9%	26%	3%

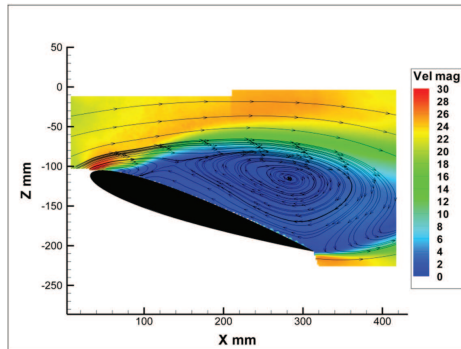


Figure 6: Time averaged velocity contours and streamlines. Uncontrolled flow in TBL

at the burst frequency of 30 Hz respectively. It can be noted, even if the drag is increased with unsteady actuation at the burst frequency corresponding to the wake natural instability, the lift to drag ratio gain remains positive because of the dramatic lift enhancement obtained thanks to the actuation.

In order to exhibit burst modulation effects on the flow topology, examples of mean flow velocity fields are plotted in Figures 6, 7, 8 and 9 at  $20^\circ$  of incidence, for  $Re = 4 \times 10^5$ , in TBL, for the single DBD actuator ( $U_{HV} = 8$  kV,  $F_{HV} = 2$  kHz).

It can be noted that mechanisms involved in the enhancement of the lift coefficient can be different with steady or unsteady actuation. Moreover depending on the forcing frequency, two different flow modification mechanisms can be observed whatever the actuator. With steady actuation or by selecting the burst frequency adjusted to natural shear layer instability frequencies ( $\geq 150$ Hz), the flow tends to reattach on the suction side. It therefore leads to a lift increase and a drag reduction whereas a high lift increase and a drag increase are observed with unsteady actuation based on a burst frequency adjusted to the wake vortex shedding natural frequency (30-35 Hz). In this case, it suggests that an interaction exists between the modified shear layer and

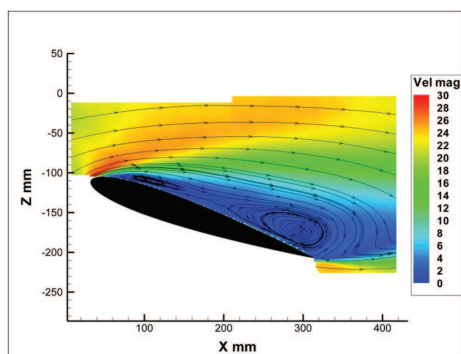


Figure 7: Time averaged velocity contours and streamlines. Steady actuation.

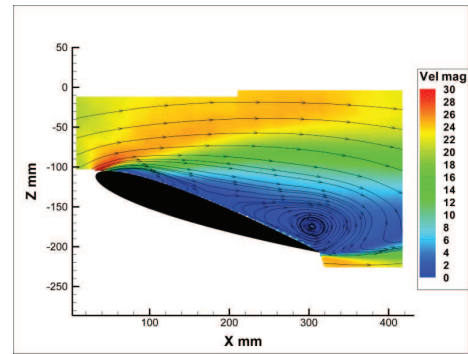


Figure 8: Time averaged velocity contours and streamlines. Unsteady actuation at  $F_{BURST} = 350$  Hz

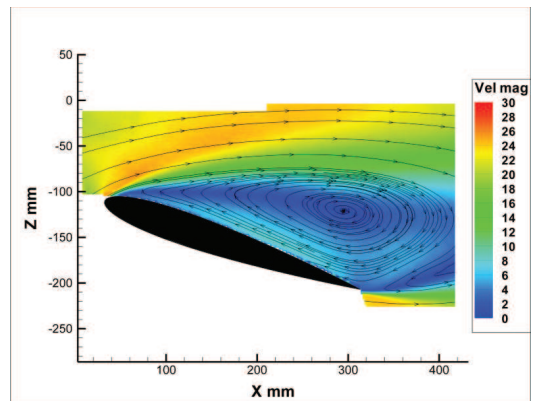


Figure 9: Time averaged velocity contours and streamlines. Unsteady actuation at  $F_{BURST} = 35$  Hz

vortices emitted in the wake leading to a flow field modification favorable to increase the lift. Investigation of aerodynamic flow features suggest that the enhancement of the shear layer vortex rollup in the shear layer leads to the formation of a number of small vortices which merge to form a strong well-developed vortex, namely a mean large lifting vortex, as reported in [12], close to the suction side. This latter is sufficiently close to the airfoil to reinforce flow velocities at its surface. In this case, the lift increase is around twice higher but drag is also increased. Nevertheless, the lift/drag ratio is improved for both cases. Effects of the burst frequencies are presented by plotting in Figures 10 and 11 the power spectral density (PSD) of the fluctuating longitudinal velocity component in the shear layer and wake regions respectively, for the uncontrolled flow and for the flow controlled by steady actuation and unsteady actuation. PSD of the forced flow exhibits strong peaks at the excitation frequency of 35 Hz and its harmonics and shows control process actually contributes to the production of some turbulence over a broad range of scales. The shear layer frequency bump is slightly shifted towards lower frequencies for the controlled flow. It indicates an enhancement of the shear layer vortex rollup and diffusion while the unfavorable bluff body wake shedding of vortices might be disorganized, more particularly with unsteady actuation at  $F_{BURST} = 350$  Hz, whereas it is well established with unsteady actuation at  $F_{BURST} = 30, 35$  and  $40$  Hz, as shown in Figure 11. PSD in the wake region is shown in Figure 11 according to the burst frequencies selected corresponding to a Strouhal number of 0.2 around. It has to be noted that the wake vortex shedding frequency locks on the burst frequency. This phenomenon was not observed for higher forcing frequencies and steady actua-

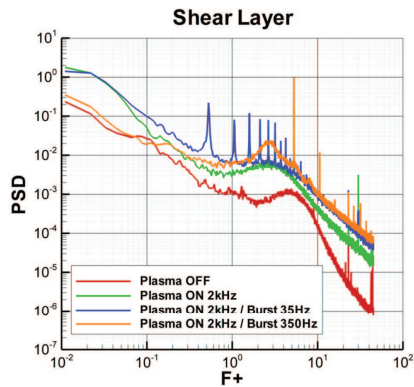


Figure 10: PSD for the uncontrolled and controlled flow. Steady actuation and unsteady actuation ( $F_{HV} = 2$  kHz and  $F_{BURST} = 35$  or  $350$ Hz)

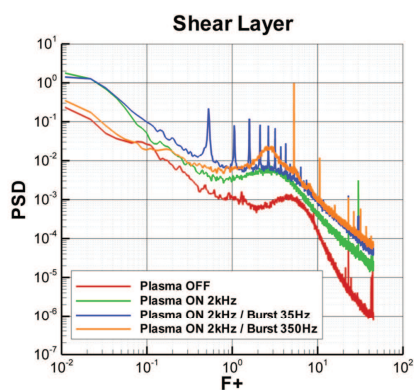


Figure 11: Wake PSD for the controlled flow. Unsteady actuation with  $F_{BURST} = 30, 35, 40$  and  $350$  Hz

tion. This result highlights interaction and resonance between shear layer and wake vortex shedding as discussed in [12] and could be interesting in view of implementing close loop control.

## 4 Conclusion

Results show that it is more suitable to perform a modification of the massively separated flow by using surface DBD actuators with unsteady excitation than steady actuation near the leading-edge of an airfoil. As reported in the literature, when the reduced frequency of excitation  $F^+$  is roughly equal to unity, aerodynamic performances are enhanced. This is the case here. However, depending on the forcing frequency, two different flow modification mechanisms have been observed leading to a high lift increase, based either on a flow reattachment or on the occurrence of a mean large lifting vortex close to the suction side. When a suitable forcing frequency is chosen, in particular close to the natural wake vortex shedding frequency, the wake vortex shedding can lock on the forcing frequency. Nevertheless, a more exhaustive parametric study is necessary to be able to predict the flow response mechanism which will be preponderant in regard to forcing frequencies and post-stall regimes, and to optimize the control benefits as well.

## Acknowledgment

The research leading to these results has received funding from the European Community's Seventh Framework Program FP7/2007-2013 under grant agreement nr. 234201. It was performed in the framework of the research federation FR 0776 - EPEE.

## References

- [1] E. Moreau, *Airflow control by non thermal plasma actuators*, Journal of Physics: Applied Physics, vol. 40, pp. 605-636, 2007.
- [2] G. Touchard, *Plasma actuators for aeronautics applications - State of art review*, I. J. PEST, 2, 1, 2008.
- [3] T.C. Corke, C.L. Enloe, and S.P. Wilkinson, *Dielectric Barrier Discharge plasma actuators for flow control*, Annual Review of Fluid Mechanics, vol. 42, pp. 505-529, 2010.
- [4] D. Caruana, *Plasmas for aerodynamic control*, Plasma Physics and Controlled Fusion, vol. 52, 2010.
- [5] R. Sosa, G. Artana, E. Moreau, G. Touchard, *Stall control at high angle of attack with plasma sheet actuators*, Experiments in Fluids, 2007, vol. 42, 2007.
- [6] D. Greenblatt, I.J. Wygnanski, *The control of flow separation by periodic excitation*, Prog. Aerospace Sciences, vol.36, pp. 487-545, 2000.
- [7] A. Seifert, D. Greenblatt, I.J. Wygnanski, *Active separation control: on overview of Reynolds and mach numbers effects*, Aerospace Science and Technology, vol. 8, pp. 569-582, 2004.
- [8] Patel, M.P et al., *Scaling effects of an aerodynamic plasma actuator*, Journal of Aircraft, Vol. 45, No 1, 2008.
- [9] N. Benard, J. Jolibois, E. Moreau, *Lift and drag performances of an axisymmetric airfoil controlled by plasma actuator*, Journal of Electrostatics, vol. 67, Issue 2-3, pp. 133-139, 2009.
- [10] M. Amitay, A. Glezer, *Role of Actuation Frequency in Controlled Flow Reattachment over a Stalled Airfoil*, AIAA Journal, 0001-1452, vol.40, no.2, pp. 209-216, 2002.
- [11] N. Benard, P. Braud, J. Jolibois, E. Moreau, *Airflow reattachment along a NACA0015 airfoil by Surfaces Dielectric Barrier Discharge actuator - Time resolved PIV Investigation*, 4th Flow Control Conference, Seattle, AIAA Paper n°2008- 4202, 2008.
- [12] J.Z. Wu, X. Lu, A. Denny, M. Fan, J.M. Wu, *Post-Stall Flow Control on an Airfoil by Local Unsteady Forcing*, Journal of Fluid Mechanics, vol. 371, pp. 21-58, 1998.
- [13] Y. Tian, L.N. Cattafesta, R. Mittal, *Adaptive control of separated flow*, 44th AIAA aerospace Sciences meeting and Exhibit, Reno, 2006.
- [14] Raju, R., Mittal R., Cattafesta, L., *Dynamics of airfoil separation control using zero-net mass-flux forcing*, AIAA Journal, Vol. 46, No 12, December 2008.

- [15] Y. Guowei, W. Shanwu, L. Ningyu, Z. Lixian, *Control of unsteady vertical lift of an airfoil by leading-edge blowing-suction*, Acta Mechanica Sinica, vol. 13, no. 4, 2007.
- [16] P. Audier, A. Leroy, and D. Hong D, *Unsteady forcing of a post-stall flow over a NACA0012 airfoil by a surface DBD actuator*, AIAA 6th Flow Control Conference, New Orleans, AIAA paper 2012-3052, 2012.
- [17] A. Berendt, J. Podlinski, J. Mizeraczyk, *Elongated DBD with floating interelectrodes for actuators*, Eur. Phys. J. Appl. Phys, vol. 55, 13804, 2011.
- [18] A. Leroy, P. Audier, J. Podlinski, A. Berendt, D. Hong and J. Mizeraczyk, *Enhancement of lift and drag performances of NACA0012 airfoil by multi-DBD plasma actuator with additional floating interelectrodes*, proceedings in Int. Symp. on Electrohydrodynamics, Gdańsk, Poland, 2012.

# WING TIP VORTEX CONTROL BY PLASMA ACTUATORS

P. Molton<sup>1</sup>, A. Leroy-Chesneau<sup>2</sup>, J. Pons<sup>3</sup>, Y. Carpels<sup>1</sup>, P. Barricau<sup>4</sup>,  
C. Gleyze<sup>4</sup>, M. Forte<sup>4</sup> and D. Caruana<sup>4</sup>

<sup>1</sup>ONERA, 8 rue des Vertugadins, 92190 Meudon, France

<sup>2</sup>PRISME, University of Orleans, 8 rue Léonard de Vinci, 45072 Orléans cedex 2, France

<sup>3</sup>EPEE, CNRS / University of Orléans, BP 6744, 45067 Orléans Cedex 2, France

<sup>4</sup>ONERA, 2 Avenue Edouard Belin, 31055 Toulouse, France

## Abstract

Experiments studying the wing tip vortex, generated by a rectangular wing with a symmetric airfoil section and a straight tip, manipulated by surface plasma actuators (DBD) and plasma synthetic jets (PSJ) are presented in this paper. Objectives are focused on modifying vortex development to alter streamwise vorticity downstream of the wing trailing edge. Actual limitation of the ionic wind magnitude obtained with DBD actuators leads to investigate vortex control by action on the transverse component of the freestream flow velocity. Different DBD arrangements installed near the wing tip were tested to examine effects of momentum addition, firstly on the pressure and suction side surfaces, and secondly, simultaneously located more precisely on the main vortex separation and attachment lines. The objectives of the PSJ actuators were to create a fluidic layer similar to the effect of winglet. Different electrical control parameters were tested allowing for varying the exit flow velocity of the cavity. Stereoscopic PIV measurements were performed in different planes orthogonal to the vortex development axis to visualize and characterize wing tip vortices. Results of the actuation show a slight displacement of the wing tip vortex and a reduction of the mean streamwise vorticity level in its core.

## 1 Introduction

Reduction of wing tip vortices generated by an aircraft wing is of importance in practical engineering issues, such as saving fuel consumption and minimizing aircraft separation time during takeoff. On helicopter blades and propellers, tip vortices cause rotor noise and vibration [1, 2, 3, 4]. For these reasons many studies focusing on reducing their vorticity have been conducted during the last decades [5, 6]. Passive control techniques like winglets and active control techniques such as mobile flaps, suction or blowing devices [7, 8] have been used to reduce tip vortices. Corke et al [8] provided an overview of main capabilities of active control by surface Dielectric Barrier Discharge (DBD) actuators, discussing the optimization of design, placement and operation mode. Up to now, most applications of DBD actuators dedicated to flow control have focused on modifying the longitudinal component of the flow velocity by momentum addition in steady or burst mode. Investigations on modifying the transverse component of the flow velocity seem necessary to achieve a modification of wing tip vortices. The possibility of vortex flow control by DBD actuators on a delta-wing model was studied at high angles of attack and subsonic speed [9]. It was demonstrated that DBD actuators can be successfully applied to modify the vortex break-

down location but also to stabilize vortex when operating in burst mode. Plasma actuation on the wing tip vortex of rectangular wing [10, 11, 12] has been investigated experimentally and numerically and has shown different influences of the actuation on the wing tip vortex formation according to suction or blowing effect produced by actuators. Results on aerodynamic performance modification, lift increase [9] for example, differ with the study cases. More investigation is still necessary to find out optimized DBD arrangements.

According to the wing tip vortex topology [13, 14] and to results [15, 16] showing that particular steady blowing configurations near the wing tip are effective, this present study aims at experimentally investigating DBD and PSJ actuators devices for modifying the wing tip vortex of a rectangular wing placed with a straight tip at an incidence of  $6^\circ$  in a freestream flow of 10 m/s. Main objectives are to demonstrate actuator potentialities to modify the development, position and strength of these vortices, as well as to alter streamwise vorticity downstream of the wing trailing edge. Various DBD actuator arrangements were then implemented near the wing tip along the chord to generate a body-force field that couples with the momentum in the transverse direction of the main freestream flow.

The recent development of miniature plasma actuators [17] (PSJ) allowed the use of these devices for the control of aerodynamic flows [18], and studies of the power supplies of these devices [19], allow using this device for tests in a wind tunnel. The main objective of the PSJ actuators was to interact with the separation shear layers in order to modify the vortex formation and development. Different electrical operating parameters, positioning and number of actuators were tested. Flow investigation through the use of stereoscopic Particle Imaging Velocimetry (PIV) was performed to visualize and characterize wing tip vortices following planes orthogonal to the vortex development axis, on the wing and in the near wake. Control effectiveness while increasing the velocity of the freestream flow was also tested. After a presentation of the global experimental setup and actuator arrangements, results on the mean streamwise vorticity and turbulent kinetic energy are discussed according to DBD or PSJ arrangements to highlight effects of this active control.

## 2 Experimental setup

The tests were conducted in the F2 wind tunnel at the ONERA Fauga-Mauzac center, which is an atmospheric wind tunnel with a return circuit. The test section is 5-m-long, and has a 1.4-m-wide and 1.8-m-high rectangular cross section. The maximum freestream velocity is 100

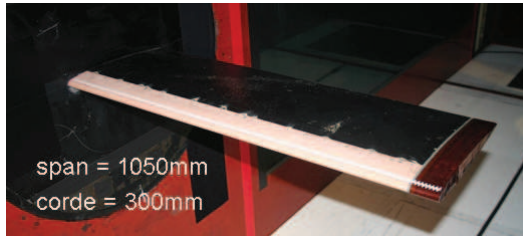


Figure 1: Rectangular wing in the test section

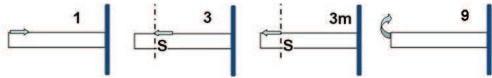


Figure 2: Schematic of DBD arrangements

m/s. The model consists in a rectangular wing having a symmetric profile (AFV82), a straight tip with sharp edges, a span equal to 1050 mm and a chord equal to 300 mm (see Figure 1). The angle of attack was set at  $6^\circ$  and the Reynolds number based on the chord length was chosen between  $2 \times 10^5$  and  $8.5 \times 10^5$ . A removable part for the wing tip was manufactured in order to implement actuators to be tested (PSJ and DBD). Stereoscopic PIV measurements were performed in different planes orthogonal to the vortex development axis on the wing and in the near wake, in order to visualize and characterize wing tip vortices with (case On) and without (case Off) actuation, and to consider the influence of geometry changes. The PIV system consisted of a pulsed Nd/YAG laser. Acquisition of the image pairs was performed by two PCO Imagerpro cameras. Each camera was equipped with a motorized Scheimpflug system, an auto-focus controller. The PIV cameras and laser device were located on a system of displacement along the three axes X, Y, and Z of the wind tunnel, allowing reproducible positions of the measurement planes. The flow was seeded with oil droplets emitted by a device implanted at the inlet of the diffuser downstream of the test section. Management of image acquisition was performed by the Davis software 7.2, and image processing was performed using the ONERA PIV software FOLKI [20, 21].

By using DBD actuators, investigations on modifying the transverse component of the main flow velocity have been achieved with different arrangements installed near the wing tip. They were tested to examine effects of momentum addition, firstly on the pressure and suction side surfaces, and secondly, simultaneously located more precisely on the main vortex separation and attachment lines. Four arrangements are presented in this paper (Figure 2). Firstly, results for the DBD actuators located along the chord on the suction sides near the wing tip (DBD 1, 3 and 3m) and secondly, results for the DBD 9 which was designed to reinforce action on the separation line of the primary vortex at the upper sharp edge. The direction of the ionic wind produced by DBDs is indicated by an arrow in the corresponding schemes. By using seventeen PSJ actuators implemented in the wingtip (see Figure 3), the objectives were to create a fluidic layer similar to the effect of winglets. The spacing between two actuators was equal to 11 mm, and the first actuator was located 30 mm downstream of the leading edge, leading to a fluidic layer length of 176 mm corresponding to 50% of the chord length. Different electrical operating parameters were tested (actuator pulse frequency, capacitor value), allowing for varying the exit

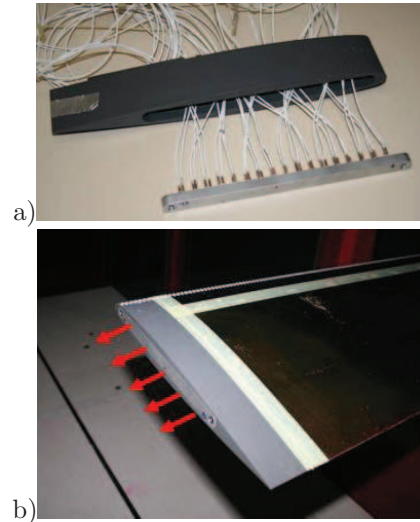


Figure 3: Schematic of DBD arrangements

flow velocity of the cavity.

### 3 Results

With DBD actuators, it has been established that the most effective reduction of vorticity was achieved by acting with inward flow arrangement on the separation line of the main primary vortex emitted on the wing [22]. For a freestream velocity of 10 m/s, Figure 4 shows non-dimensional mean streamwise vorticity contours obtained with DBD 1, 3 and 3m. Baseline flow topology, corresponding to the case off in the plane  $X/c = -0.25$ , shows the separating shear layer which is detached at the upper sharp edge and forms the main primary vortex. The presence of a secondary vortex which rotates in the opposite direction can also be noted. Velocity fluctuations are concentrated in the shear layer, in the vortex core, and at the detachment line of the secondary vortex. Downstream in the plane  $X/c = 0.5$ , the main wake vortex is formed. When actuator is on (DBD1), it can be observed in the plane  $X/c = -0.25$  that the ionic wind interacts with the separation layer and with the secondary vortex, leading to its displacement and vertical extension as well as a decrease of its streamwise vorticity. Consequently the same effects on the primary vortex can be observed, namely a small displacement and a vorticity decrease of 20% in its core. Downstream in the plane  $X/c = 0.5$ , significant diffusion of the streamwise vorticity can be noted in the vortex core. With DBD3, the ionic wind interacts with the secondary vortex by reducing its vorticity and its size. Thus, an enhancement of the primary vortex is here characterized by an increase of 15% in vorticity in the plane  $X/c = -0.25$  and downstream in the plane  $X/c = 0.5$  as well. This behavior was probably due to the position of the actuator with respect to the attachment line of the primary vortex. The DBD3m (DB3 modified) was then positioned so as to increase the transverse velocity at the attachment line of the main primary vortex even if the electrode position did not comply with the development of the conical main vortex. Indeed, DBD3m is effective only from  $X/c = -0.5$ . The results in the plane  $X/c = -0.25$  show an increase of the transverse velocity component near the wall of the model, which results in a decrease of the streamwise vorticity in the primary vortex core and a space reduction for the secondary vortex. This can be related to a stabilization of the vortex flow. Downstream in the plane

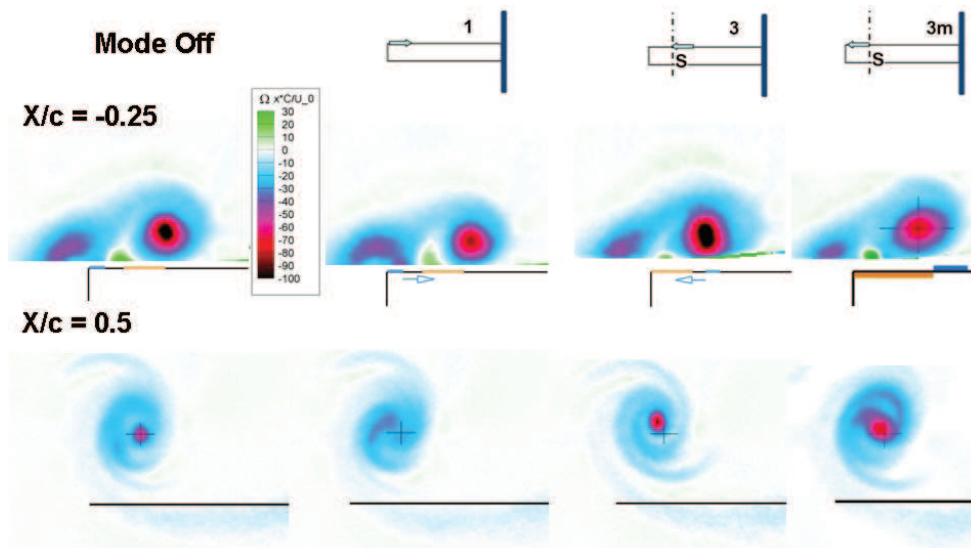


Figure 4: Streamwise vorticity contours for the DBD 1, 3 and 3m actuators. Free stream flow of 10 m/s

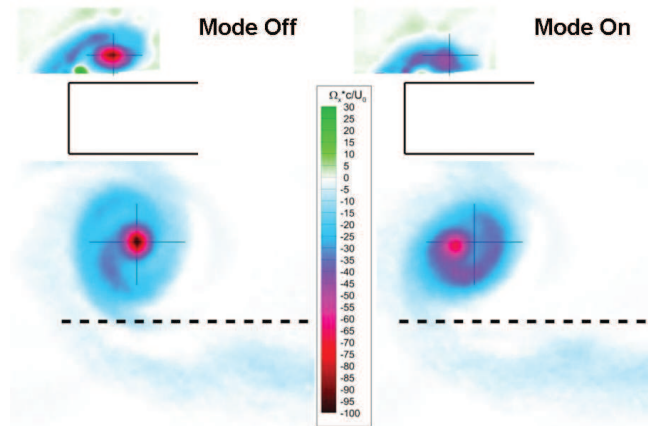


Figure 5: DBD 9, mean streamwise vorticity at  $X/c = -0.25$  and  $X/c = 0.5$ , mode Off and On

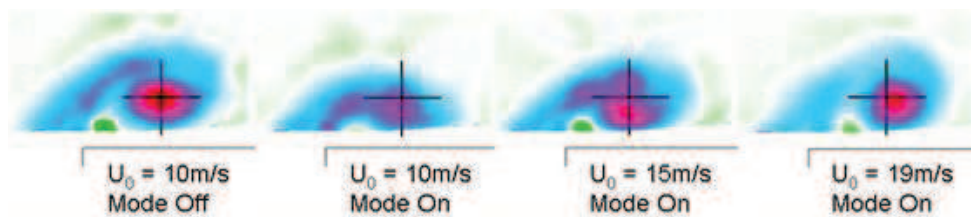


Figure 6: DBD 9, mean streamwise vorticity at  $X/c = -0.25$ . Freestream velocities  $U_0 = 10, 15$  and  $19$  m/s

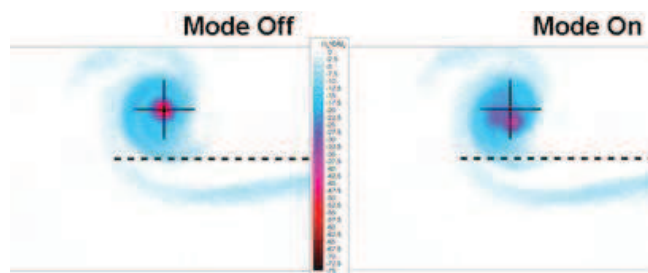


Figure 7: DBD 9, mean streamwise vorticity at  $X/c = 0.5$ . Freestream velocities  $U_0 = 19$  m/s

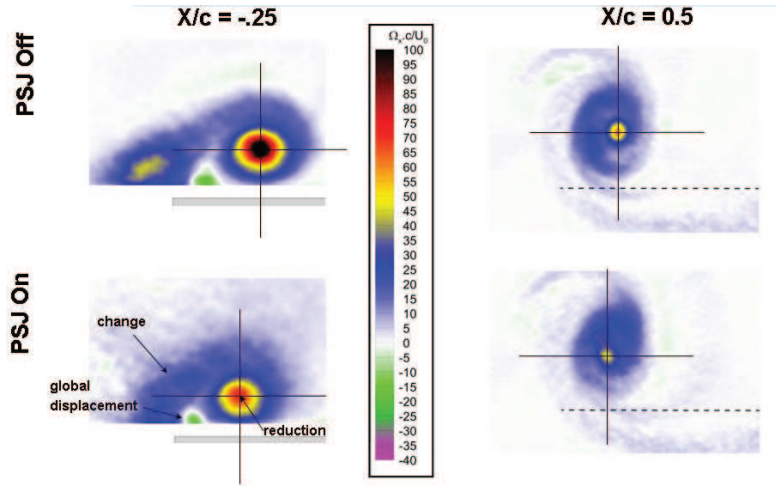


Figure 8: Streamwise vorticity contours for the PSJ actuators. Free stream flow of 10 m/s

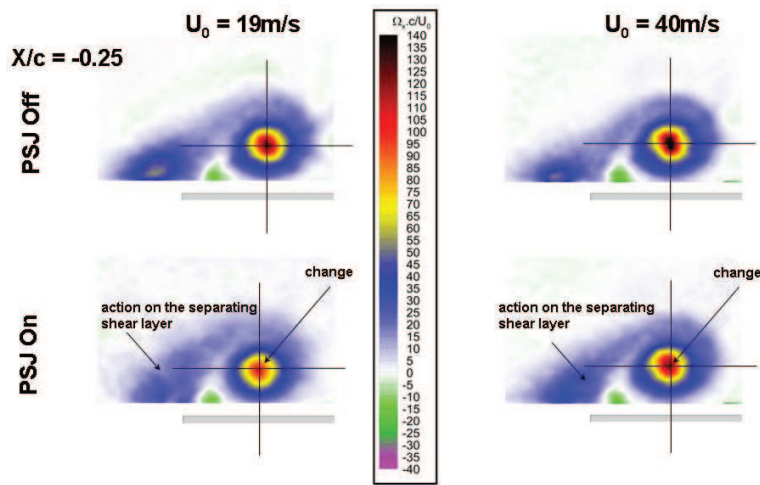


Figure 9: Streamwise vorticity contours for the PSJ actuators. Free stream flow of 10 m/s

$X/c = 0.5$ , weak effects of the actuator are absorbed by the main wake vortex without changing its characteristics significantly. Figure 5 shows streamwise vorticity contours obtained with DBD 9. Activation of control manifests itself in the model by changing the orientation of the separating shear layers, a decrease of the velocity transverse component near the wall and a change in the core location of the secondary vortex. These results denote a significant reduction in the formation of the vortex system. The effects of control persist downstream. Indeed a spatial shift of the vortex core can be observed, as well as a vorticity diffusion of the order of 30%.

Actuator influences on the flow field have been examined for higher free stream velocities. On the model ( $X/c = -0.25$ ) the flattening of the vortex system on the wing appears lower as the flow velocity increases (Figure 6). Control no longer modifies the secondary vortex. However a displacement of the main wake vortex and a reduction of its streamwise vorticity are still observed. Control effects persist downstream. In the plane  $X/c = 0.5$  (Figure 7), results show a shift of the main wake vortex, a reduction of its streamwise vorticity of about 45%. Finally, results have shown that the actuator authority decreases while the free stream velocity increases higher than 25 m/s.

The results obtained with PSJ actuators (Figure 8) show a modification of the mixed layer, a reduction of the level of the streamwise vorticity and a displacement

of the flow in the plane on the wing. These features are still observed in the near wake plane. In this case, the flow generated by the actuators can be compared to the effects of a winglet.

Similar effects are observed when the freestream velocity increases ( $U_0 = 19$  and 40m/s - Figure 9). However the actuator efficiency proportionally decreases as the freestream velocity increases.

## 4 Conclusion

The effects of plasma actuation on the wing tip vortex characteristics, size and strength, involving two different flow interaction mechanisms, were experimentally investigated by stereoscopic PIV. Different DBD arrangements near the wing tip were tested to examine and better understand effects of momentum addition on the formation and development of the vortex system emitted at the straight tip of a rectangular wing. The results obtained during the tests for a low freestream velocity show that effects of actuation mainly result in a local diffusion of the main wake vortex core and its displacement. The use of DBD actuators is quite convenient for a peripheral control of the vortex. It was established that the location of the DBD actuator remains a key parameter for optimizing control effects, as well as operating electrical parameters (frequency, amplitude, burst modulation of

the high voltage for example). However, their energy input remains too low to destabilize the formation of the wing tip vortex at higher speeds.

The effects of the plasma spark jets on the separating shear layer are lower as the freestream velocity increases. When the freestream velocity increases, the thickness of the separating shear layers is thinner and the jets actually cross the separating shear layer without significant interactions. Indeed the exit velocity of the jets is too high with respect to the thickness of the shear layer. Only the small potential cores interact with the shear layer. It therefore seems important to study in more details the interactions of the jets with the external flow. Indeed, two parameters seem have to be considered:

- the exit velocity of the jets with regard of the velocity in the shear layer,
- the jet orientation with regard to the main flow.

Moreover, it would be interesting to significantly reduce the frequency of jet emission because, on the one hand jets at high frequencies are more similar to a continuous stream, on the other hand the shear layer is subjected to higher stresses for low frequencies.

Circulation calculation around the whole wake vortex in the plane downstream has been performed and did not show significant differences with and without actuation. Aerodynamic load measurements were not available for these tests. It was not therefore possible to precisely quantify benefits of plasma actuation in terms of aerodynamic performances, such as lift increase or drag reduction for example. Nevertheless, for low free stream flow velocities, it has been demonstrated the capabilities of surface DBD actuators and JSP actuators to modify the wing tip vortex in order to reduce its strength.

## References

- [1] Margaris P., Gursul I., *Effect of Steady Blowing on Wing Tip Flowfield*, 2nd AIAA Flow Control Conference, 28 June - 1 July 2004, Portland, USA, paper n°2004-2619
- [2] Brooks T.F., Marcolini, M.A., *Airfoil Tip Vortex Formation Noise*, AIAA Journal, Vol. 24, N°2, 1986, pp. 246-252.
- [3] Hui Li, Burggraf, O.R., Conslisk, A.T., *Formation of a Rotor Tip Vortex*, Journal of Aircraft, Vol. 39, N°5, pp. 739-749, September-October2002.
- [4] Cousin, D., Morikone, M., Hirst, S., Elder, J., Ilie, M., *Experimental studies of tip-vortex formation; influence of blade-tip geometry on the vortex characteristics*, 49th AIAA Aerospace Sciences and Meeting including The New Horizons Forum and Aerospace Exposition, 4 - 7 January 2011, Orlando, Florida, paper n°2011-1253.
- [5] M. Mitchell, A., Délerly, J., *Research into vortex breakdown control*, Progress in Aerospace Sciences, Vol. 37, 2001, pp. 385-418.
- [6] D. Barberis, P. Molton, F. Renac, A. M. Mitchell. *Vortex control on delta wings*. 37th AIAA Thermophysics Conference - 34th AIAA Fluids Dynamics Conference and Exhibit - 2nd Flow Control Conference, Portland (U.S.A.), 28 June-1 July 2004
- [7] Ramaprian, B.R., Zheng, Y., *Measurements in Rollup region of the Tip Vortex from a Rectangular Wing*, AIAA Journal, Vol. 35, N°12, 1997, pp. 1837-1843.
- [8] Corke, T.C., Enloe, C.L., Wilkinson, S.P., *Dielectric barrier discharge plasma actuators for flow control*, Annual Review in Fluid Mechanics, Vol. 42, pp. 505-529, 2010.
- [9] Budovsky A.D., Sidorenko, A.A., Maslov, A.A., Zanin, B.Y., Zverkov, I.D., Postnikov, B.V., Kozlov, V.V., *Plasma Control Of Vortex Flow On Delta-Wing At High Angles Of Attack*, 47th AIAA Aerospace Sciences Meeting Including The New Horizons Forum and Aerospace Exposition, 5 - 8 January 2009, Orlando, Florida, paper n°2009-888.
- [10] Boesch, G., Vo, H.D., Savard, B., Wankot-Tchatchouang, C., Mureithi, N.W., *Flight Control Using Wing-Tip Plasma Actuation*, Journal of Aircraft, Vol. 47, No. 6, 2010.
- [11] Hasebe, H., Naka, Y., Fukagata, K., *An Attempt for Suppression of Wing-Tip Vortex Using Plasma Actuators*, Journal of Fluid Science and Technology, Vol. 6, No. 6, 2011.
- [12] Agibalova, S. A., Golub, V. V., Moralev, I. A., and Saveliev, A. S., *Effect of Dielectric Barrier Discharge on Wing Tip Vortex Formation*, Technical Physics Letters, Vol. 37, No. 11, pp. 1070-1073, 2011.
- [13] Birch, D., Lee, T., Mokhtarian, F. and Kafyeke, F., *Rollup and Near-Field Behavior of a Tip Vortex*, Journal of Aircraft, Vol. 40, N° 3, engineering notes, 2003.
- [14] Ghias, R., Mittal, R., Dong, H., S. Lund, T., *Study of Tip-Vortex Formation Using Large-Eddy Simulation*, 43th Fluid Dynamics Conference and Exhibit AIAA, 10- 13th January 2005, Reno, USA, paper n°2005-1280.
- [15] Margaris, P., Gursul, I., *Vortex topology of wing tip blowing*, Aerospace Science and Technology, Vol. 14, 2010, pp. 143-160.
- [16] Eric Coustols, Odile Labbé, Frédéric Moens, Pascal Molton & Laurent Jacquin. Status of ONERA Research on Wake Vortex Evolution and Elevation in the Framework of National Activities and European Collaboration. 8th. World Congress on Computational Mechanics (WCCM8), 5th. European Congress on Computational Methods in Applied Sciences and Engineering (ECCOMAS 2008). June 30 - July 5, 2008. Venice, Italy
- [17] D. Caruana & al. - The *Plasma Synthetic Jet* Actuator - Aero-thermodynamic characterisation and first Flow Control Application - AIAA-2009- 1307
- [18] Hardy P., Barricau P., Belinger A., Caruana D., Cambronne J.P. and Gleyzes C. (2010) *Plasma Synthetic Jet for flow control*, 40th AIAA Fluid Dynamics Conference and Exhibit, Chicago, Illinois, USA, 28 June - 1 July 2010, AIAA paper 2010-5103.
- [19] A. Belinger & al.- Influence of the energy dissipation rate in the discharge of a plasma synthetic jet actuator. J.Phys.D : Appl. Phys. 44

- [20] Leclaire, B., Jaubert, B., Champagnat, F., Le Besnerais, G., Le Sant, Y., *FOLKI-3C: a sample, fats and direct algorithm for stereo PIV*, Proceedings 8th International Symposium on PIV - PIV09, Melbourne, Victoria, Australia, August 25-28, 2009.
- [21] Champagnat, F., Plyer, A., Le Besnerais, G., Leclaire, B., and Le Sant, Y., *How to Calculate Dense PIV Vector Fields at Video Rates*, Proceedings of 8th International Symposium on Particle Image Velocimetry - PIV09, Melbourne, Australia, August 25-28, 2009.
- [22] Leroy A., Molton P., Carpels Y., Pons J. *Experimental Studies of DBD Actuator Effects on Wing Tip Vortex Topology*. 6th AIAA Flow Control Conference, 25-28 Juin 2012 - NEW ORLEANS - USA. AIAA-2012-2951

# BOUNDARY LAYER TRANSITION CONTROL WITH STEADY AND UNSTEADY DBD PLASMA ACTUATION

M. Forte<sup>1</sup>, A. Seraudie<sup>1</sup>, O. Vermeersch<sup>1</sup>, A. Kurz<sup>2</sup>, S. Grundmann<sup>2</sup>,  
C. Tropea<sup>2</sup>, J. Pons<sup>3</sup> and A. Leroy<sup>3</sup>

<sup>1</sup>ONERA, Aerodynamics & Energetics Modelling Department, 2 av. Edouard Belin., 31055, Toulouse, France

<sup>2</sup>Technische Universität Darmstadt, Centre of Smart Interfaces, Flughafenstr. 19, 64347, Griesheim, Germany

<sup>3</sup>University of Orléans, PRISME Laboratory, 8 Rue Léonard de Vinci, 45072, Orléans Cedex 2, France

## Abstract

This paper presents experimental and numerical investigations dealing with 2D boundary layer transition control on an ONERA-D airfoil using Dielectric Barrier Discharges actuators. The ability of this kind of plasma actuators to delay transition has been assessed using either steady or unsteady mode of actuation. On the one hand, wind tunnel investigations as well as linear stability analysis are conducted in order to study the effect of a steady operated DBD actuator on boundary layer stabilization. The results show a maximum transition delay of about 35% of chord for low freestream velocity ( $U_\infty = 7$  m/s). On the other hand, an experiment has been performed using the unsteady force produced by the DBD actuator to achieve Active Wave Cancellation in direct frequency mode. With the help of a closed loop control system, a significant transition delay has been achieved by damping artificially introduced TS waves for free-stream velocities up to  $U_\infty = 20$  m/s. This work has been conducted in the framework of the PlasmAero project funded by the European Commission.

## 1 Introduction

The main objective of this project is to study different kinds of plasma actuators and to assess their ability to control airflows in order to reduce environmental impact of air transport. One possible way to reduce aircraft fuel consumption is to delay boundary layer transition on wing profiles in order to reduce skin friction drag. Basically, the studies dealing with 2D boundary-layer transition delay can be sorted into two categories: on the one hand, steady actuation is used to modify the mean velocity profile in order to make the boundary layer more stable. Different kinds of actuation have demonstrated good results using this approach, like for instance steady suction. On the other hand, unsteady actuation is used to act (or counteract) directly on the instabilities growing within the boundary layer, the wellknown Tollmien-Schlichting (TS) waves, which lead to turbulence for low disturbance level airflow. This approach is called Active Wave Cancellation (AWC). The present study has focused on one specific kind of plasma actuator: Dielectric Barrier Discharge (DBD). This kind of actuator has been widely characterized in quiescent air for different ambient conditions. Moreover, many investigations have shown their ability to control airflows around different kind of bodies: flat plates, cylinders, airfoils. Most of these studies are reported in a recent review [1]. The goal here is to demonstrate the ability of DBD actuator to delay transition by means of either steady or unsteady

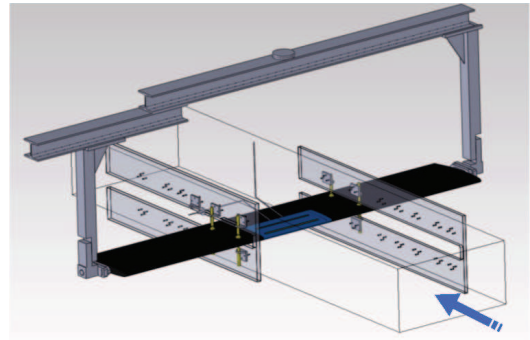


Figure 1: Two-dimensional model of the ONERA-D airfoil mounted inside the wind tunnel

actuation, as this actuator is able to induce either continuous or unsteady momentum addition to the boundary layer.

## 2 Experimental setup

The present experiment has been conducted in the subsonic open-return "Juju" wind tunnel located at the research facilities of ONERA Toulouse. It features a low turbulence level  $0.5 \times 10^{-3} < Tu < 0.5 \times 10^{-2}$  depending on the free-stream velocity, which ranges from 5 to 75 m/s. This facility operates at ambient conditions and is well suited for transition experiments. As illustrated in Figure 1, a two-dimensional model based on an ONERA-D profile, having a chord length of  $c = 0.35$  m, is mounted horizontally in the test-section of the wind tunnel.

This profile is symmetric and has been specifically designed for transition control investigations. The angle of attack can be adjusted between  $\alpha = -8^\circ$  and  $\alpha = +3^\circ$  in order to modify the upper side pressure gradient and thus the natural transition location. Additionally, the model is equipped with 15 pressure taps on the upper side.

Two different kinds of DBD actuator have been used during this experiment:

- 1) The first one, represented in Figure 2a), consists of a thick dielectric layer: a 5 mm-thick insert (the blue part in Figures 1 and 2) made of dielectric material Lab850 placed at the leading edge region and matching the model shape. This actuator insert allows the model to be outfitted with the desired number of DBD actuators, adhering electrodes asymmetrically on both sides of the Lab850 material which is used directly as the dielectric barrier. For example, Figure 2a) shows

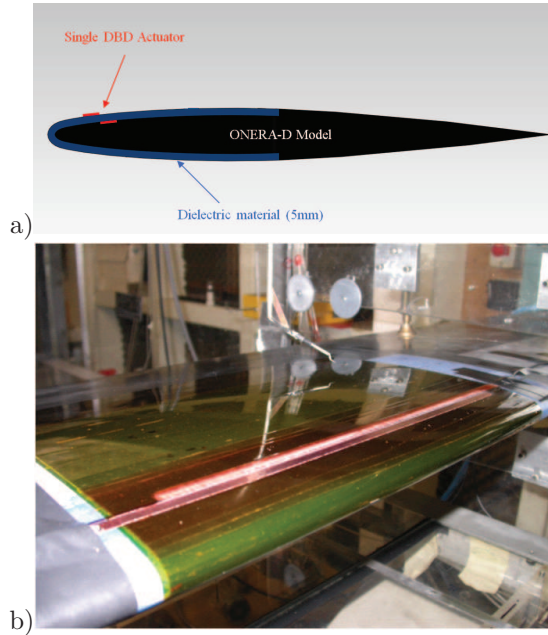


Figure 2: The two kinds of DBD actuator used in this study: a) a thick-dielectric actuator and b) the thin-dielectric actuator

one single DBD actuator located at  $x/c = 10\%$  (the downstream edge of the air-exposed electrode is taken as the location reference).

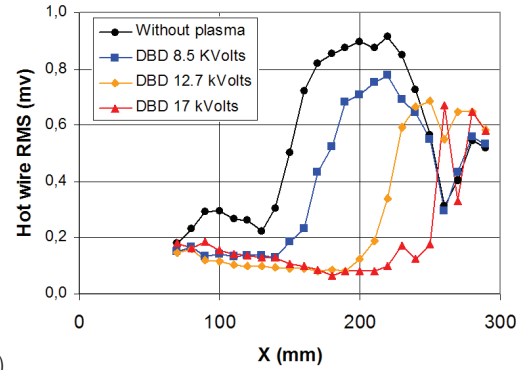
2) The second kind of actuator consists of a much thinner dielectric layer made of Kapton material ( $\approx 0.2$  mm-thick) which is flexible enough to outfit the model as shown in Figure 2b). Whatever the kind of actuator used, electrodes are 30 cm-long in spanwise direction and made of copper tape. Air-exposed electrodes are connected to a TREK power amplifier (model 30/20,  $\pm 30$  kV, 20 mA peak) and supplied with AC high voltage while other electrodes are grounded. Moreover, those air-exposed electrodes have been polished in order to reduce their thickness down to 0.05 mm to prevent them from promoting transition. Hot wire anemometry (Dantec Streamline, 90C10 CTA modules, 55P15 probes) has been employed for boundary-layer explorations.

### 3 Transition delay using steady DBD actuation

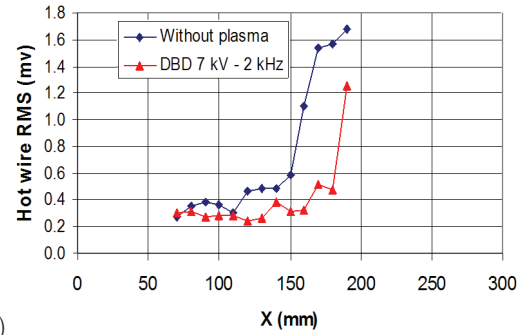
The study presented in this section is related to 2D boundary-layer stabilization using the plasma actuator in a continuous mode of operation. Using this approach, a quasi-steady momentum is added to the flow, directly acting on the mean velocity profile of the boundary layer in such a way that the amplification of the disturbances is impeded and transition can be delayed.

#### 3.1 Wind tunnel investigations

In a first step, boundary-layer transition delay is investigated experimentally using one single DBD actuator located at  $x/c = 10\%$  and operated continuously. The angle of attack of the model is set to  $\alpha = 2.5^\circ$  and the experiment has been performed for two different free-stream velocities  $U_\infty = 7$  & 12 m/s, using both thick and thin dielectric actuators for the lowest velocity but only the thick actuator for the highest velocity. The



a)



b)

Figure 3: Transition delay with steady DBD actuation for  $U_\infty = 7$  m/s : a) with the thick-dielectric actuator and b) with the thin-dielectric actuator

thin actuator is supplied with AC high voltage having an amplitude of  $V_{DBD} = 7$  kV while the thickest actuator is supplied with successively three different amplitudes  $V_{DBD} = 8.5; 12$  and 17 kV. For both actuators, the operating frequency is set to  $f_{DBD} = 2$  kHz. The maximum velocity of the ionic wind induced by the thickest actuator in quiescent air is about 4.5 m/s at the highest voltage amplitude. Figures 3 and 4 present typical results for  $U_\infty = 7$  & 12 m/s respectively. Velocity fluctuations are computed from boundary-layer explorations along the chord, moving the hot-wire probe at a constant distance from the wall, with and without control. The location of the transition is deduced from the fluctuation increase. The natural transition is located at  $x/c \approx 40\%$  for  $U_\infty = 7$  m/s and at  $x/c = 26\%$  for  $U_\infty = 12$  m/s. In all cases, the ignition of the plasma actuator leads to a transition delay. As expected, the transition is shifted progressively downstream when the amplitude of the voltage is increased since the mechanical effect of the actuator (ionic wind) increases. Maximum transition delay recorded during this experiment are 35% of chord for  $U_\infty = 7$  m/s and 20% of chord for  $U_\infty = 12$  m/s. The efficiency of the thin actuator could be largely improved by increasing the operating frequency of the supplied signal, which was not possible with our power amplifier.

#### 3.2 Numerical investigations

In order to confirm that this transition delay is due to the modification of the mean velocity profile, the control of the boundary layer with steady actuation has been investigated from a numerical point of view. At first, boundary-layer computations have been performed for the baseline cases (without plasma) using an ONERA code (3C3D). Then, an artificial ionic wind profile (with a simple model well described in [2]) has been numerically added at the location of the actuator

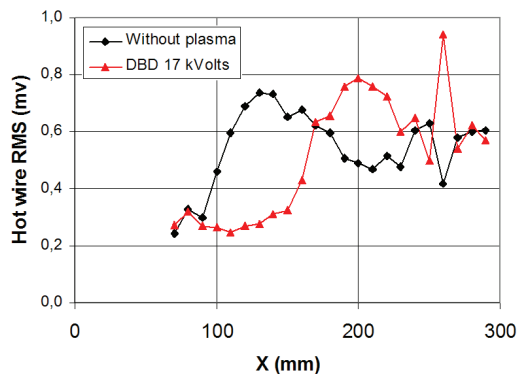


Figure 4: Transition delay with steady DBD actuation for  $U_\infty = 12$  m/s with the thick-dielectric actuator

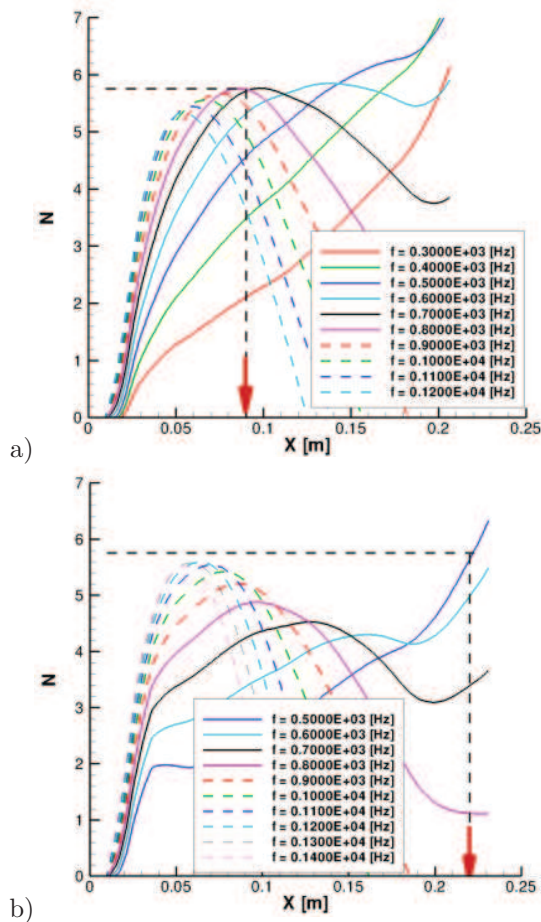


Figure 5: Evolution of the N-factor along the chord of the model ( $U_\infty = 12$  m/s,  $\alpha = 2.5^\circ$ ) without control (a) and with control (b)

( $x/c=10\%$ ) to the mean velocity profiles coming from these base flow computations in such a way that the resulting profiles fit the experimental ones. Finally, exact stability computations have been conducted on these modified profiles using the envelope strategy so as to compute the amplification N-factor with an ONERA code (Castet). Typical results of the linear stability analysis are given in Figure 5 which presents the evolutions of N-factor along the chord of the model for several instability frequencies in the baseline case (a) and for the controlled case (b).

The aerodynamic configuration is the same than for the case presented in Figure 4 with  $U_\infty = 12$  m/s. As the natural transition location is known from the experiment ( $x_t/c \sim 26\%$  or  $x_t = 0.09$  m), we can deduce the corresponding transition N-factor  $N_t = 5.8$ . Then, using this value in the controlled case plot, we can observe that transition location is shifted downstream ( $x_t = 0.22$  m), not far from what has been observed experimentally ( $x_t = 0.16$  m). In conclusion, stability computations as well as experiments show that DBD plasma actuator used in a steady mode has a stabilizing effect on the boundary layer. The modification of the mean velocity profiles is such that the amplification of the disturbances is impeded and transition can be delayed.

## 4 Transition delay using unsteady DBD actuation

One other possible way to delay 2D transition is to use unsteadily operated actuators to act (or counteract) directly on the Tollmien-Schlichting waves growing inside the boundary layer and triggering transition. This approach is called Active Wave Cancellation: the goal is to generate an artificial perturbation with an unsteady force production so as to damp natural TS waves by destructive interference. Transition is delayed because TS wave amplitude has been reduced locally. Grundmann and Tropea [3] have conducted experiments using this approach on a flat plate. They used a single high-frequency driven DBD actuator with square wave modulation to generate artificially introduced waves. Another possible solution is to make use of the DBD plasma actuator unsteady force production during one cycle of the operating frequency and to directly operate the cancellation actuator at the TS wave frequency. In fact, several recent studies [4] have shown that DBD actuator produces a local unsteady force mainly due to the different discharge regimes between the positive and the negative half cycles. This asymmetric behavior enables to use DBD actuator in direct frequency mode. A careful adjustment of the phase relation between the TS waves and the actuator excitation signal can thereby potentially cancel the waves. Thus, the use of a closedloop system, which detects the waves and optimizes the actuation, will be necessary.

The experimental set-up used for this study is quite the same than the one presented in the previous section except that the angle of attack is set to  $\alpha = 2^\circ$  and that the model is outfitted with two DBD actuators, as illustrated in Figure 6. The upstream actuator DBD1 ( $x/c = 10\%$ ) serves as disturbance source to artificially excite a single frequency TS wave train while DBD2 ( $x/c = 30\%$ ) is utilized as the transition control device. The experiments have been split into two phases. During an initial testing phase, the feasibility of the direct frequency mode for active wave cancellation had to be verified. In order to do so, a set-up employing a beat frequency approach without the use of a closed-loop controller was chosen, re-

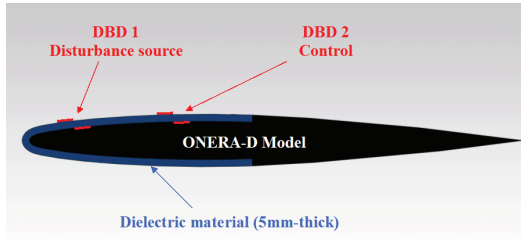


Figure 6: Experimental set-up for the Active Wave Cancellation study

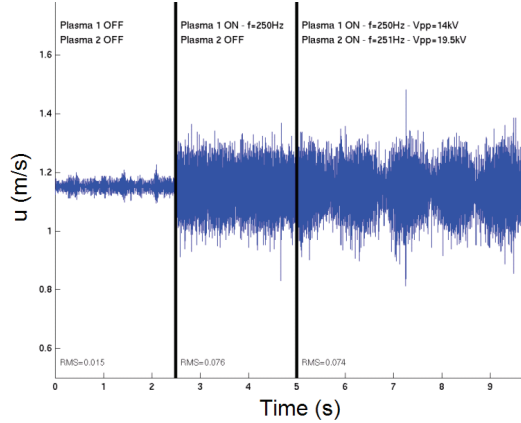


Figure 7: Time trace of  $u$  velocity component given by hot-wire probe located inside the boundary layer at  $x/c = 40\%$  for the base flow (left), with excitation (center) and with excitation and control (right)

producing the experiments of Grundmann and Tropea. This allows for time efficient parameter studies to find appropriate settings and the corresponding attenuation rates. In the second testing phase, transition delay on the wing model has been demonstrated with closed-loop control applied.

#### 4.1 AWC without closed-loop control

For this set of measurements the excitation frequency at the upstream actuator DBD1 has been set to a value close to the naturally occurring TS frequencies ( $f_{DBD1} = 250$  Hz). As the artificially excited waves travel downstream, they reach the control actuator (DBD2) which was operated at a slightly shifted frequency ( $f_{DBD2} = 251$  Hz) in order to create a beat frequency with the two signals due to the continuously changing phase relation. Some typical results from these experiments are presented in Figure 7 for a free-stream velocity of  $U_\infty = 7$  m/s.

The hot wire measurements shown were taken at  $x/c = 40\%$  inside the boundary layer at a wall-normal distance of  $y = 0.4$  mm. The base flow case (left part of the plot) exhibits a low fluctuation level within the hotwire signal of 0.015m/s. With excitation (middle part of the plot) this disturbance level is raised to 0.076m/s. Applying the control (right part of the plot) a slow oscillation of the amplitude of the TS waves farther downstream the second actuator develops, with a maximum amplitude above the one of the unaffected waves (amplification) and minimum amplitude below the unaffected wave (damping) resulting in an almost unchanged RMS-value of 0,074m/s in this case. Figure 8 shows a time trace of the excited TS wave signal with smaller time scale (dashed line) in comparison to the base flow case (solid

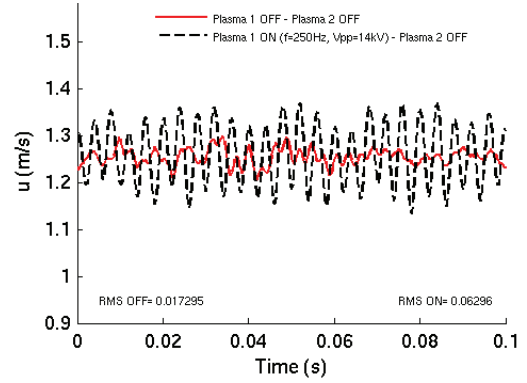


Figure 8: Time trace of  $u$  velocity component given by hot-wire probe located inside the boundary layer at  $x/c = 40\%$  for the base flow (solid line) and with DBD1 turned on (dashed line)

line), revealing that a clean TS wave train has been produced by DBD1. Two important results emerge from these experiments. First of all the unsteady momentum production of the plasma actuator can be utilized to excite TS waves, if applied at the appropriate position, amplitude and a frequency the flow is susceptible to. Secondly and most important, the direct frequency approach for flow control proved to be applicable and can be utilized for Active Wave Cancellation.

#### 4.2 AWC with closed-loop control

In order to have a permanent optimized phase shift between TS waves generated by DBD1 and the controlling unsteady force induced by DBD2, a robust extremum-seeking control algorithm has been used. This algorithm, which has previously been successfully applied for flow control purposes, was supplied by the TU Berlin.

The system utilizes the signal of a stationary hot wire probe ( $x/c = 40\%$ ,  $y = 0.2$  mm) as an error sensor to automatically optimize the control function. This control algorithm runs on a dSPACE real-time processing unit. Due to its robustness this algorithm is well suited to control artificially excited, single-frequency TS waves. By slowly and periodically deflecting the system out of its current operating point (perturbation), the gradient  $f'$  of the error signal according to a change of the controlled variable, which in this case is the phase shift, is determined. The phase relation between TS wave train and the flow structures created by the plasma actuator is then continuously adapted along this gradient, which drives the system into a minimum.

Following the promising beat frequency experiments, closed-loop control has been applied in order to demonstrate transition delay using the direct frequency approach. The free-stream velocity and the angle of attack remain at  $U_\infty = 7$  m/s and  $\alpha = 2^\circ$  respectively. A spectral analysis of the stationary hotwire signal reveals the frequency content of the flow, as shown in Figure 9. Plotted is the power spectral density in dB/Hz over frequency at a wall-normal position of  $y = 0.2$  mm. In the base flow case (DBD1 off, DBD2 off) two frequency peaks, one at 250 Hz and a wider peak around 340 Hz, are prominent. These frequencies represent the naturally occurring TS waves present in the boundary layer for the given flow situation. However, as it has been shown with linear stability analysis, well described in [5], frequencies around 340Hz are damped downstream of DBD2, with the limit for the unstable frequency band being about 300Hz. A

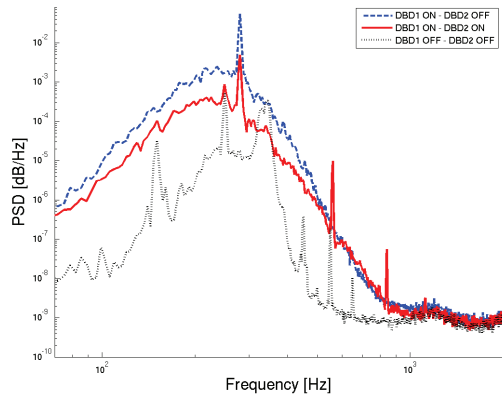


Figure 9: Spectral analysis of the error sensor signal ( $x/c = 40\%$ ,  $U_\infty = 7$  m/s) for the base flow (DBD1 off, DBD2 off), with excitation (DBD1 on, DBD2 off) and with closed-loop control (DBD1 on, DBD2 on)

frequency sweep in the unstable range revealed that an excitation at 280 Hz leads to the cleanest TS wave signal at the location of the error sensor. Consequently it was decided to use this frequency for the subsequent AWC experiments. Figure 9 shows that introducing the excitation at 10% chord (DBD1 on, DBD2 off) produces the expected peak around 280Hz as well as an overall increase in the turbulence level as transition is being promoted. This increase is visible at the error sensor, since its location is close to the point of transition for the excited case ( $\sim 47\%$  chord). Applying the control (DBD1 on, DBD2 on) the TS peak at 280Hz can be reduced by about one order of magnitude. This effect is accompanied by a decreased overall turbulence level. Figure 10 depicts a typical result of the transition delay studies. Plotted is the RMS-value of the longitudinal velocity fluctuations recorded at various downstream locations at a constant distance above the wall within the boundary layer. The dark blue curve ( $\diamond$ ) represents the natural transition case with the onset of transition at about 60% chord, i.e. neither the disturbance source nor the control actuator is operating. Turning on the disturbance source, the TS wave amplitude is significantly increased at  $f = 280$  Hz which moves the transition region upstream to about 40% chord ( $\square$ ). Then, with the control system active, the region of transition can be shifted downstream significantly by about 10% chord length ( $\circ$ ). Even though the unsteadiness of the force production of DBD plasma actuators is exploited in this work to conduct active wave cancellation it may not be neglected that a net force is produced, which modifies the mean flow, i.e. the boundary-layer velocity profile. This modification can by itself lead to a stabilization of the boundary layer as presented in section 3, hence delay transition. Complementary measurements have been carried out in order to exclude a possible boundary-layer stabilization due to continuous addition of momentum. To quantify this effect, the momentum generation of DBD2 has been measured in quiescent air using Pitot tube measurements. The maximum achievable velocity, 10 mm downstream of the active electrode, was determined to be  $\sim 0.6$  m/s at the prescribed plasma frequency of 280Hz using this electrode configuration, dielectric material and thickness. In order to deactivate the active wave cancellation and to quantify the effect of a pure momentum addition of this magnitude, the recorded average wall-jet velocity has been reproduced at a plasma frequency of 1 kHz using DBD2. This frequency is located well outside the unstable frequency range and is assumed not

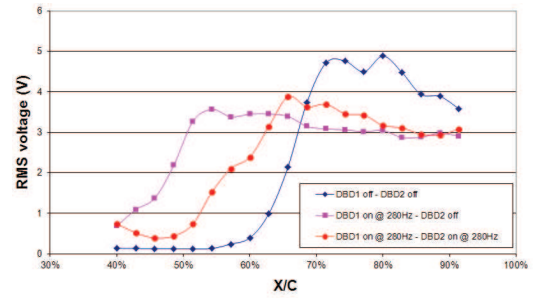


Figure 10: RMS value of hot-wire signal along the chord of the airfoil for the base flow, with excitation and with closed-loop control ( $U_\infty = 7$  m/s)

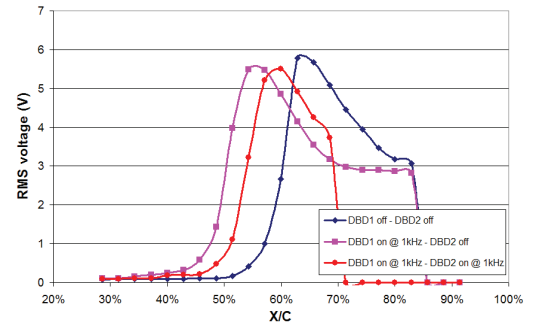


Figure 11: RMS value of hot-wire signal along the chord of the airfoil for the base flow, with excitation and with closed-loop control ( $U_\infty = 20$  m/s)

to have any destabilizing effect on the boundary layer. The transition delay due to continuous momentum addition is small compared to the effect of the active wave cancellation and is in the order of 1-2% of chord length. For higher Reynolds numbers it can be assumed that this effect will be reduced even further. This experiment proves that the achieved results can clearly be attributed to the unsteady force production of the DBD plasma actuator and are not the result of a modified mean flow.

The same experiment has been conducted with higher free-stream velocity  $U_\infty = 20$  m/s. The angle of attack has been slightly reduced to  $\alpha = 1.5^\circ$  in order to have the natural transition location near  $x/c = 60\%$  as for the previous case. This time the frequency of the disturbance source is set to  $f_{DBD1} = 1$  kHz which is close to the frequency of the most unstable perturbations for this aerodynamic configuration. The evolutions of velocity fluctuations along the chord, shown in Figure 11, prove that transition delay has been achieved (4% of chord) using DBD plasma actuator with a closed-loop control system. Detailed results about this last experiment will be given in a forthcoming paper.

## 5 Conclusion

In this paper, the ability of DBD actuator to delay 2D boundary-layer transition has been assessed by means of either steady or unsteady actuation. On one hand, wind tunnel investigations as well as linear stability analysis have shown that DBD actuator used in a steady mode has a stabilizing effect on the boundary layer. The modification of the mean velocity profiles is such that the amplification of the disturbances is impeded and transition can be delayed. A maximum transition delay of about 35% of chord has been achieved for low freestream velocity ( $U_\infty = 7$  m/s). On the other hand, an experiment

has been performed using the unsteady force produced by the DBD actuator to achieve Active Wave Cancellation in direct frequency mode. With the help of a closed loop control system, a significant transition delay has been achieved by damping artificial TS waves for free-stream velocities up to  $U_\infty = 20$  m/s.

## Acknowledgments

The present work has been performed within the framework of the PlasmAero project funded by the European Commission (Grant agreement nr. 234201). The authors would like to thank the members of this project for sharing their knowledge and the fruitful discussions. The authors would like to thank also N. Goldin and R. King from the Technische Universität Berlin for sharing their control algorithm [5] crucial for the AWC experiment as well as their help and advice.

## References

- [1] N. Bénard and E. Moreau, 2012, *EHD Force and Electric Wind Produced by Plasma Actuators Used for Airflow Control*, Proc. of the 6th AIAA Flow Control Conference, AIAA Paper 2012-3136, 2012.
- [2] A. Seraudie, O. Vermeersch and D. Arnal, *DBD plasma actuator effect on a 2D model laminar boundary layer. Transition delay under ionic wind effect*, Proc. of the 29th AIAA Applied Aerodynamics Conf., AIAA Paper 2011-3515, 2011.
- [3] S. Grundmann, and C. Tropea, *Active cancellation of artificially introduced Tollmien-Schlichting waves using plasma actuators*, Experiments in Fluids, Vol. 44, No. 5, pp. 795-806, 2008.
- [4] M. Forte, J. Jolibois, J. Pons, E. Moreau, G. Touchard and M. Cazalens, *Optimization of a dielectric barrier discharge actuator by stationary and non-stationary measurements of the induced flow velocity: application to airflow control*, Experiments in Fluids, Vol. 43, pp. 917-928, 2007.
- [5] A. Kurz, C. Tropea, S. Grundmann, M. Forte, O. Vermeersch, A. Seraudie, D. Arnal, N. Goldin and R. King, *Transition delay using DBD plasma actuators in direct frequency mode*, Proc. of the 6th AIAA Flow Control Conference, AIAA Paper 2012- 2945, 2012.

# ATTENUATION OF NOISE FROM AN AIRFOIL EQUIPPED WITH A HIGH-LIFT DEVICE USING PLASMA ACTUATORS

P. Chen, X. Zhang, S. Chappell, Z. Cai and D. Angland

*Faculty of Engineering and the Environment, University of Southampton, Southampton, SO17 1BJ, UK  
pc13v07@soton.ac.uk*

## Abstract

In this work, an experimental investigation was conducted into the attenuation of slat noise with a dielectric barrier discharge plasma actuator. To isolate the slat component of high lift device noise, initial tests were conducted using a two-element model comprised of a slat and main element. Following on from the two-element model, and to better represent the landing configuration, tests were also conducted using a three-element configuration. Near and far field acoustic data were acquired in an anechoic chamber at a freestream velocity of  $25 \text{ ms}^{-1}$ , corresponding to a Reynolds number of  $5.5 \times 10^5$  based on the main element chord. In both of the configurations tested (two-element and three-element), several tonal noise features with broadband components were apparent in the slat noise spectra. The angle of attack at which these noise features appeared depended on the model configuration. The mechanism behind the generation of the dominant tone was found to be related to the shedding of vorticity from the slat cusp, which subsequently rolled up to form vortices through the Kelvin-Helmholtz instability. The tonal features with broadband components were successfully suppressed using a plasma actuator located along the leading edge of the slat. For the two-element model, a quasi-static feedback control system was also developed wherein a controller was responsible for calculating the control inputs in terms of feedback signals. In the three-element model tests, a different form of closed-loop control was explored in which a proportional feedback controller was implemented. The experimental results showed that both of the feedback control methods worked effectively to suppress the slat tonal noise with broadband components.

## 1 Introduction

Aircraft noise has become an important consideration for civil aircraft manufacturers for a variety of reasons. Indeed, airline operations are restricted by the stringent nature of civil aviation noise regulations. Moreover, aircraft noise pollution has become a point of contention against the expansion of airports. Over the last several decades, research has been conducted into understanding the mechanisms of, and developing means of attenuating, aircraft noise [1–9]. The noise generated from aircraft comes mainly from two sources, the airframe and the engine. The main contributors to airframe noise are the high-lift devices and landing gears [2].

An important component of the high-lift system is the leading edge slat. Although the slat itself does not account for a major portion of the lift augmentation, it allows the main wing to operate effectively at higher angles of attack. However, the deployment of this device leads to extra radiated noise. Slat noise represents a

complex aeroacoustic problem and the underlying mechanisms governing its generation have been extensively explored over the past several decades [2]. Slat noise is generally agreed to be broadband in nature and in some cases is superimposed by tonal components [8, 10].

Several possible sources of slat tonal noise in two dimensional scale models have been identified [2]. Firstly, low frequency tonal noise due to coherent laminar flow separation at the leading edge of the slat can be mentioned. Second is the high frequency tonal noise thought to be due to Tollmien-Schlichting boundary layer instabilities at the slat suction side. Third is the high frequency tonal noise associated with the periodic vortex shedding off the trailing edge of the slat. The last possibility is the tonal noise generated by a mechanism similar to that observed in the production of cavity tones. For about a 1/10 scaled high-lift model, low frequency refers to approximately 1 kHz to 4 kHz and high frequency between 10 kHz and 20 kHz.

Experimental results [2] showed that the low frequency tonal noise could be attenuated, or even eliminated, by tripping the flow at the leading edge using a serrated strip. However, the use of such a passive device on an aircraft would have disadvantages, such as increasing drag at cruise. Active devices such as blowing are fragile and have installation and maintenance problems. Plasma actuators present an alternative actuation method. The easy and relatively low cost of manufacturing combined with the robustness of the device makes it a desirable technique for flow control. Indeed, in relation to aeroacoustics, the actuator has been proven to be an effective device for attenuating flow-induced noise [11, 12].

In the present work, several intense tones with broadband components appeared in the far field spectrum between a frequency range of 4.5 kHz to 6 kHz. The dominant tone was associated with the shedding of vorticity from the slat cusp that subsequently rolled up to form vortices through the Kelvin-Helmholtz instability. This current study aimed at developing effective methods for attenuating these tonal features with broadband components using a dielectric barrier discharge (DBD) plasma actuator.

## 2 Methodology

To isolate the slat component of high lift device noise, initial tests were conducted with a two-element model (Figure 1(a)). The model, comprised of the slat and main element, had a *RA16SC1* section [13]. Following on from the two-element model, and to better represent the landing configuration, tests were conducted using a three-element model (Figure 1(b)). For model dimensions refer to 1. For both configurations (two-element and three-element), tests were conducted with the flow untripped at a freestream velocity ( $U_\infty$ ) of  $25 \text{ ms}^{-1}$ . This

corresponded to a Reynolds number ( $Re$ ) of  $5.5 \times 10^5$  based on the main element chord.

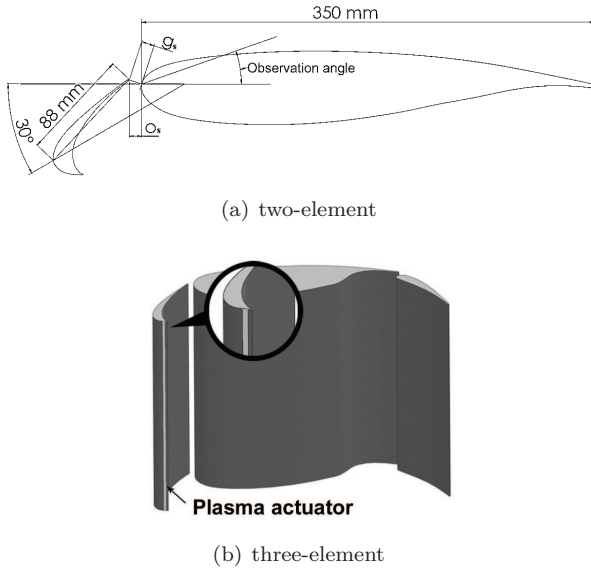


Figure 1: Wind tunnel models. Flow is from left to right.

Geometric feature	Value
Main element chord ( $c_w$ )	0.336 m
Slat chord ( $c_s$ )	0.08 m
Flap chord ( $c_f$ )	0.101 m
Slat deflection angle ( $\delta_s$ )	30 degrees
Slat horizontal gap ( $o_{hs}$ )	$0.035c_w$
Slat vertical gap ( $g_s$ )	$0.027c_w$
Flap deflection angle ( $\delta_f$ )	40 degrees
Flap horizontal gap ( $o_{hf}$ )	$0.013c_w$
Flap vertical gap ( $g_f$ )	$0.005c_w$

Table 1: Model dimensions.

The experiments were primarily conducted in the ISVR anechoic chamber at the University of Southampton. The chamber measures  $9.15 \text{ m} \times 9.15 \text{ m} \times 7.32 \text{ m}$  without wedges, free-field conditions exist at frequencies above 80 Hz. A DARP Open Jet Facility with a nozzle height of 540 mm and width of 350 mm was installed in the chamber and had a maximum attainable wind speed of  $40 \text{ ms}^{-1}$ . The incoming turbulence level was less than 0.2% outside of the shear layers.

In the experiments two microphones, one near field and another far field, were used to obtain the acoustic measurements. The location of these microphones for the three-element test is shown in 2. Near field measurements were acquired with a Bruel & Kjaer 4948 microphone, with a frequency range from 5 Hz to 20 kHz. This near field microphone was flush mounted inside the slat cavity at the mid-span point. The signal was amplified using an amplifier with an adjustable gain and acquired using a dSPACE system at a sampling frequency of 20 kHz. For the closed-loop control portion of the work, the RMS voltage of the near field microphone was the control output and the duty cycle the control input. The far field measurements were acquired with a Behringer ECM8000 omni-directional electret condenser microphone, which had a frequency range from 15 Hz to 20 kHz. The signal was pre-amplified using a DIGI-MAX FS and acquired using a National Instrument PXI-4472 data acquisition card. As with the near field microphone, data was acquired at a sampling frequency of 20 kHz. The calibration of the far field microphone was

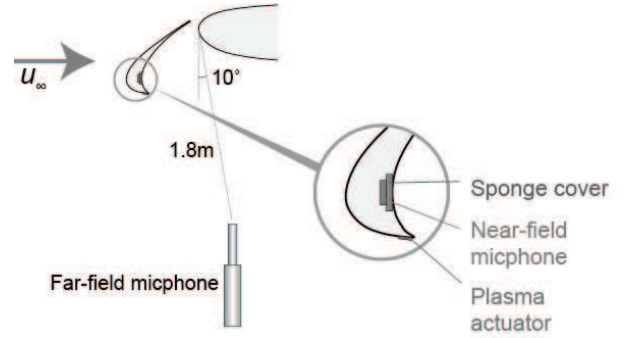


Figure 2: Set-up for the three-element test.

performed by comparison with a 1/2" BK 4961 standard microphone.

The effective sound pressure was determined using eq.1.

$$p_{rms}^2 = \frac{2 |FFT(p(t))|^2}{n^2} \quad (1)$$

where  $p(t)$  was the pressure signal measured,  $n = 4096$  was the number of samples per block and FFT the Fast Fourier Transform. This gave a frequency resolution of 4.8 Hz and the spectrum was averaged over 120 blocks. No windowing was applied during the FFT calculation. The sound pressure level (SPL) was then calculated using eq.2.

$$SPL = 10 \log_{10} \frac{p_{rms}^2}{p_{ref}^2} \quad (2)$$

where  $p_{ref} = 2 \times 10^{-5} \text{ Pa}$ .

The DBD actuator was placed at the slat cusp with the induced velocity in opposite sense to that of the freestream flow (Figure 1(b)) [14]. The actuator was constructed using a 0.5 mm thick silicon rubber dielectric and a 0.076 mm thick copper tape electrodes. The respective widths of the exposed and coated electrodes were 5 mm and 10 mm. The working frequency of the plasma was fixed at 12.5 kHz. The transformer had a transforming ratio of 500 and supplied a high AC voltage. The parameters of the DBD actuator, such as the length and position of the electrodes, were fixed for the duration of testing. The plasma actuator was controlled by a dSPACE (ds1104) system via the pulse width modulation (PWM) module. 3 shows the structure of the closed-loop control system.

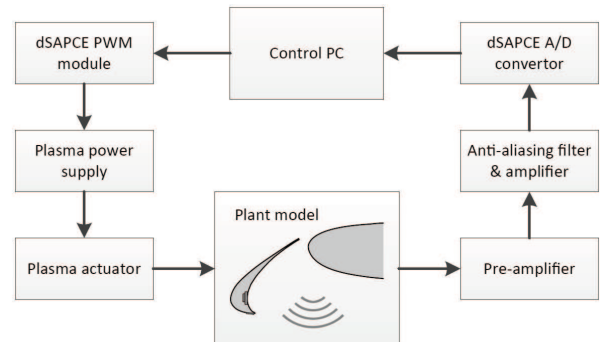


Figure 3: Implementation of closed-loop control.

In the frequency range of interest, the repeatability in OASPL was less than  $\pm 0.3$  dB for both the near and far field measurements. This was for all the cases tests - baseline, open-loop control and closed-loop control.

### 3 Results

4 shows the sound pressure level (SPL) of the slat noise in the far field at an angle of attack ( $\alpha$ ) of 4 degrees. The SPL can be seen to decrease gradually within the frequency range of 0.28 kHz to 2.95 kHz, followed by a significant increase up to a frequency ( $f$ ) of 4.4 kHz. Four obvious peaks, which corresponded to four intense tones with broadband components, appeared within the frequency range of 4.5 kHz to 6 kHz. At angles of attack of larger than 4 degrees, the tonal noise features with broadband components were no longer apparent in the slat spectrum. This result was in accordance with previous results [2]. Based on this observation, the focus of the two-element model tests was at an angle of attack of 4 degrees. To gain insight into the mech-

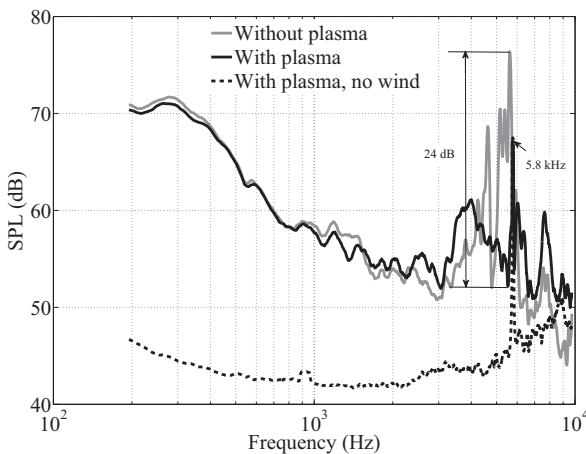


Figure 4: Two-element model slat noise in the far field,  $\alpha = 4$  degrees and  $U_\infty = 25 \text{ ms}^{-1}$ . Steady actuation at an applied voltage of 15 kV and duty cycle of 40 %.

anism of the slat tonal noise generation, a strip with a thickness of 0.5 mm was mounted at positions A, B, C, D shown in 5. The tonal noise was suppressed only when the strip was positioned at location A. Leading to the conclusion that the tones were closely related to the flow around the slat cusp, rather than other parts of the slat. Then, from high speed particle image velocimetry measurements, the generation of the dominant tone was found to be related to the shedding of vorticity from the slat cusp, which subsequently rolled up to form vortices through the Kelvin-Helmholtz instability. This mechanism of noise generation, the shedding of vorticity from the slat cusp, was different to that previously suggested, a mechanism similar to that seen in cavity flow.

Based on the results obtained with the 0.5 mm thick strip, a plasma actuator was flush mounted at position A. The aim of doing so was to investigate whether the slat tonal features with broadband components could be suppressed with a plasma actuator. 4 demonstrates the noise reduction in the far field at  $\alpha = 4$  degrees,  $U_\infty = 25 \text{ ms}^{-1}$ . According to the measurements, the self-noise of the actuator appeared nearly flat within the frequency range of 0.2 to 5 kHz and was followed by a sharp peak at  $f = 5.8$  kHz. The peak was regarded as the consequence of the first subharmonic of the plasma actuator driving

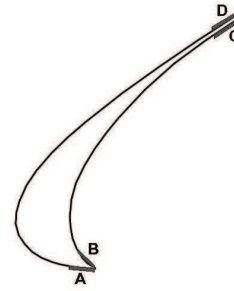


Figure 5: Strip mounted at several positions across the slat.

signal because the frequency of the peak was nearly half that of the driving frequency of the actuator. Above the frequency  $f = 5.8$  kHz and until  $f = 9$  kHz, the self-noise tended to increase with the frequency rise. Regarding the slat peaks, it can be seen that the first four peaks in the spectrum were significantly reduced when control was applied. This was especially the case for the fourth peak in which a reduction of 24 dB was achieved. Lastly, it was observed that the noise within the frequency range of 1.5 to 4.5 kHz increased, whereas the noise within the frequency of 0.825 to 1.5 kHz was attenuated. 6 shows the comparison of the RMS of acoustic pressure in the far field at various duty cycles. The RMS experienced a rapid decrease as the duty cycle was increased from 0 to 0.3. Nevertheless, a slow decrease, similar to an asymptote, occurred within a duty cycle range of 0.3 to 0.45.

Open-loop control with a plasma actuator was found

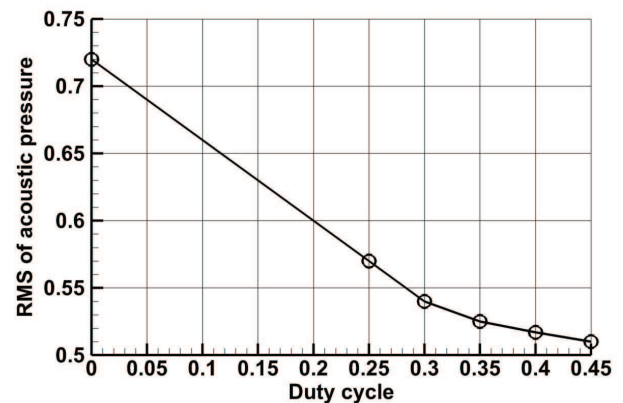


Figure 6: Variation in the far field RMS of acoustic pressure with duty cycle. Two-element model at  $\alpha = 4$  degrees and  $U_\infty = 25 \text{ ms}^{-1}$ .

to reduce the slat noise with larger duty cycle values giving greater reductions. However, in some cases there is a need for a trade-off between the noise reduction and the power consumption. In addition, the system needs to be able to remain stable under various external disturbances. Under these circumstances, a feedback control system would be more suitable than that of open-loop. To successfully implement a feedback control system for the two-element model, several steps were taken. Firstly, the plant of the slat noise was identified by an ARX algorithm, wherein a total of 600 input/output data pairs were used. Then, the input data was generated from the duty cycle and the output data from the near field microphone's RMS of acoustic pressure. It was found that a polynomial model with three poles and two zeros described the plant. Finally, based on the identified model, a quasi-static feedback control system with a LQG servo

controller was developed. 7 shows the comparison of the output voltages in the far field between controller on and controller off. From this figure, it can be seen that the acoustic pressure reduced when feedback control was turned on. Following on from the two-element model

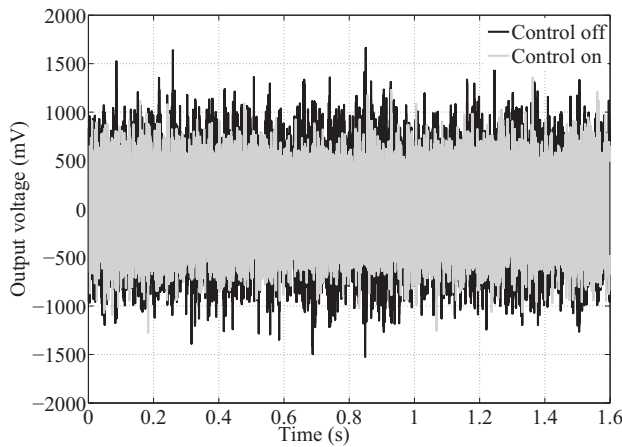


Figure 7: Time history of the output voltage of the far field microphone at the output port of the amplifier.

tests, to better represent the landing configuration, tests were conducted using a three-element model. Deployment of the flap was found to alter the angle of attack at which the tonal features with broadband components were present. It was suggested that the inclusion of the flap altered the pressure distribution around the wing. At a geometric angle of attack of 2 degrees, two distinct tonal features were present in the spectrum (8). These tones were attenuated with the application of the plasma actuator, with a 20 dB reduction observed in the dominant tone.

During tests with the three-element model, a different form of closed-loop control was explored in which a proportional feedback controller was implemented (9). The details of the results obtained with the three-element model have been described in Chappell et al. [14]. A parametric study of the Proportional (P) controller was conducted by varying the set point, fixed time step, proportional gain, and duty cycle range. The set point value was defined as the controller's target output RMS voltage which was proportional to acoustic pressure. The proportional gain made changes to the output that was proportional to the current error value. The fixed time step determined the response time of the actuator. A set point value of 0, fixed time step of 0.2 s, proportional gain of -60 and a duty cycle range of 10% to 15% was found to provide the best performance, with regards to the attenuation of the tonal features. The performance of the actuator was determined to be highly dependent on both its duty cycle and applied voltage. As was observed in the two-element model tests, when the closed-loop control was switched on, the acoustic pressure was found to be significantly attenuated (8).

## 4 Conclusions

An experimental investigation was conducted into the attenuation of slat noise with a DBD plasma actuator. The tests were initially undertaken using a two-element model comprised of a slat and main element. For the final phase of the project, to represent the landing configuration, the model was updated to include a flap. Tests were

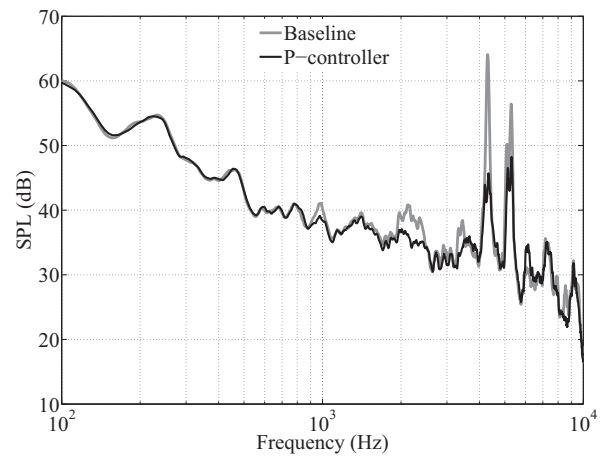


Figure 8: SPL of three-element model at  $\alpha = 2$  degrees.

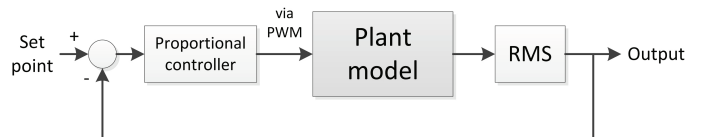


Figure 9: Closed-loop P-controller.

conducted at a Reynolds number of  $5.5 \times 10^5$ , based on the main element chord, with the flow untripped. To attenuate the slat noise, and based on preliminary tests with a passive device, the plasma actuator was applied to the leading edge of a slat. The performance of both open-loop and closed-loop forms of control were examined using near and far field acoustic measurements obtained in an anechoic chamber.

In tests with the two-element model and at an angle of attack of 4 degrees, tonal features with broadband energy content were present in the far field spectrum. From high-speed PIV measurements, the dominant noise was concluded as being closely associated with the shedding of vorticity from the slat cusp. To suppress these noise features, a plasma actuator was developed wherein the plasma intensity was regulated by means of a duty cycle signal that was generated by a dSPACE system. The noise was successfully suppressed by the use of a plasma actuator in an open-loop control system. A maximum reduction of 24 dB was achieved at a frequency of approximately 5.6 kHz. A feedback control system was also implemented to effectively attenuate the slat noise. In the three-element model tests, the tonal features were most apparent at an angle of attack of 2 degrees. A different form of closed-loop control was explored in which a proportional feedback controller was implemented. Both controllers were shown to be successful in the suppression of the slat tonal noise with broadband content.

## Acknowledgment

The research leading to these results has received funding from the European Community's Seventh Framework Programme FP7/2007-2013 under Grant Agreement nr. 234201 [www.plasmaero.eu](http://www.plasmaero.eu).

## References

- [1] X. Zhang, "Airframe noise: high lift device noise," in *Encyclopedia of Aerospace Engineering*, Edited

- by Blockley, R. and Shyy, W., ISBN 978-0-470-75440-5, Willy, vol. 6, pp. 3541–3551, 2008.
- [2] W. Dobrzynski, “Almost 40 years of airframe noise research - what did we achieve?,” *Journal of Aircraft*, vol. 47, no. 2, pp. 353–367, 2010.
- [3] C. Andreou, W. Graham, and H. Shin, “Aeroacoustic study of airfoil leading edge high-lift devices,” AIAA Paper 2006-2515, 2006.
- [4] S. Olson, F. Thomas, and R. Nelson, “A preliminary investigation into slat noise production mechanisms in a high-lift configuration,” AIAA Paper 2000-4508, 2000.
- [5] W. Dobrzynski, B. Gehlhar, and H. Buchholz, “Model and full scale high-lift wing wind tunnel experiments dedicated to airframe noise reduction,” *Aerospace Science Technology*, vol. 5, pp. 27–33, 2001.
- [6] W. Horne, K. James, N. Burnside, and S. Jaeger, “Measurements of 26% scale 777 airframe noise in the NASA ames 40 by 80 foot wind tunnel,” NASA/TP-2004-212802, 2004.
- [7] M. Herr and W. Dobrzynski, “Experimental investigations in low-noise trailing-edge design,” AIAA Paper 2004-2804, 2004.
- [8] M. Choudhari, D. Lockard, M. Macaraeg, B. Singer, C. Streett, G. Neubert, R. Stoker, J. Underbrink, M. Berkman, M. Khorrami, and S. Sadowski, “Aeroacoustic experiments in the langley low-turbulence pressure tunnel,” NASA TM-211432, 2002.
- [9] M. Khorrami and M. Choudhari, “Application of passive porous treatment to slat trailing edge noise,” NASA/TM-2003-212416, 2003.
- [10] W. Dobrzynski, K. Nagakura, B. Gehlhar, and A. Buschbaum, “Airframe noise studies on wings with deployed high-lift devices,” AIAA Paper 1998-2337, 1998.
- [11] X. Huang, S. Chan, and X. Zhang, “Atmospheric plasma actuators for aeroacoustic applications,” *IEEE Transactions on Plasma Science*, vol. 35, no. 3, pp. 693–695, 2007.
- [12] S. Chan, X. Zhang, and S. Gabriel, “The attenuation of cavity tones using plasma actuators,” AIAA Paper 2005-2802, 2005.
- [13] A. Arnott, G. Schneider, K. Neitzke, J. Agocs, B. Sammler, A. Schroder, and J. Kompenhans, “Multi-window PIV for high-lift measurements,” 20th International Congress on Instrumentation in Aerospace Simulation Facilities ICIASF, Goettingen, August, 2003.
- [14] S. Chappell, Z. Cai, X. Zhang, and D. Angland, “Slat noise feedback control with a dielectric barrier discharge plasma actuator,” AIAA Paper 2012-2806, 2012.

# HIGH VOLTAGE PULSED DBD EFFECTS ON THE AERODYNAMIC PERFORMANCES AND ON THE SHOCK BUFFET

A. Marino<sup>1</sup>, P. Peschke<sup>2</sup>, F. De Gregorio<sup>1</sup>, P. Leyland<sup>2</sup>, P. Ott<sup>2</sup>,  
C. Hollenstein<sup>2</sup> and R. S. Donelli<sup>1</sup>

<sup>1</sup>Italian Aerospace Research Centre (CIRA), Via Maiorise snc, 81043, Capua (CE), Italy

<sup>2</sup>Ecole Polytechnique Fédérale de Lausanne (EPFL), CH-1015 Lausanne, Switzerland

## Nomenclature

DBD	= Dielectric Barrier Discharge
FRP	= Fast Rising Voltage Pulse
P1	= Clean Configuration of the model
P2	= Configuration of the model installing electrodes at $x/c=0.45$
P3	= Configuration of the model installing electrodes at $x/c=0.575$
PT-1	= Pilot Transonic CIRA Wind Tunnel
M	= Mach number
Re	= Reynolds Number
c	= Model Chord
$V_\infty$	= Free Stream Velocity
$\alpha$	= Angle of attack
U	= Volt
Cp	= Pressure Coefficient
rms	= Root Mean Square
f	= Frequency
$\omega = \frac{2\pi fc}{2V_\infty}$	= Reduced Frequency
PSD	= Power Spectra Density

## 1 Introduction

The applications of surface dielectric barrier discharge plasma actuators, (DBD), have known a considerable interest recently in the field of flow control. In general, such actuators consist of two electrodes separated by an insulation covering the lower electrode entirely, while the upper electrode remains exposed to the flow. This actuator is driven either by a high frequency AC-voltage or by fast rising voltage pulses. In the former case, a sinusoidal voltage of several kilovolts with frequencies of a few hundred to several thousand Hertz is applied to the electrodes. The actuator generates a body force tangentially to the surface which provides a variety of possibilities to manipulate or to create flows. Inside an existing mean flow, the actuator can be used to impart momentum into a boundary layer and to alter the velocity, the turbulence distribution or to control the transition from laminar to turbulent. The amplitude of the force, created by the plasma actuator can be altered by varying the driving voltage. In the case of the fast rising voltage pulse (FRP) driven DBD actuators, pulses with an amplitude of several kilovolts and with a rise/decay time (from 10%-90% max. voltage) of a few nanoseconds are applied. The wall jet's velocities of these actuators are quite low, and the actuator acts as an equivalent additional energy source. A weak compression wave is generated at the edge of the flow/air-exposed electrode which prevails whatever the flow regime, and seems to be the predominant mechanism of these FRP actuators.

A major part of the experimental work up to now using surface dielectric barrier discharge (DBD) actuators was

carried out in flow speeds up to 30 m/s, mostly with actuators driven by AC-voltage. The main identified mechanism of successful control with such actuators at such low speeds is the induced ionic wind effect, which can attain velocities limited to a few meters per second, hence influencing mainly only very low speed flows [8]. With increasing flow speed, however, this influence becomes insufficient and the actuator's control capacity generated by these AC-driven DBD has not yet achieved expectations [2]. Recently, DBD actuators driven by nanosecond pulsed FRP-DBD have been successfully used to reattach leading edge separation in high speed flows [1]. Even though this is not a phenomenon frequently encountered under realistic flight conditions these findings encouraged to investigate possible effects of FRP-DBD on shock buffet, which is a problem pertaining to transonic cruise flight conditions, and is of interest in compressor design.

In order to evaluate whether FRP-DBD actuators have beneficial effects on the aerodynamic performance in high subsonic flows and in particular in mitigating shock buffeting phenomena, a series of experimental investigations has been carried out in the CIRA PT-1 transonic wind tunnel. The flow speed was varied between  $M=0.4$  and  $M=0.85$  at angles of attack from  $-2^\circ$  to  $8^\circ$  and Reynolds numbers between  $Re = 1.7 \times 10^6$  and  $Re = 2.5 \times 10^6$ . Tests were performed on a constant wing span model of a BAC 3-11 supercritical airfoil, with 11% of maximum thickness, able to reach shock buffet conditions at Mach numbers in the range ( $M=0.75-0.88$ ), at low angles of attack ( $0-5^\circ$ ) and Reynolds number about 2 - 3 million [3, 4]. During the tests, steady and unsteady pressure measurements were acquired to obtain quantitative measurements.

This paper provides a short description of the experimental setup, presents the main results regarding the effect of the plasma presence on the aerodynamic performance and on the shock buffet phenomenon.

## 2 Model and instrumentation

The test campaign has been performed in the PT-1 facility. This is a transonic and supersonic pressurized wind tunnel, which operates in a closed-circuit. It has two drive systems: a 145 kW fan, for continuous tests in the low subsonic flow speed range ( $M<0.35$ ), and a compressed air injection system for intermittent transonic and supersonic operation. In the high subsonic-transonic flow regime the wind tunnel reaches Mach numbers between [0.35-1.1], while in supersonic condition only one Mach number is achievable [ $M=1.4$ ]. The maximum total pressure reachable in the wind tunnel is 1.85 bar and the possible range test time is of 150 seconds. Tests were performed on the BAC3-11 wind tunnel model with a model chord of 0.12 m and a span of 0.45 m. The model

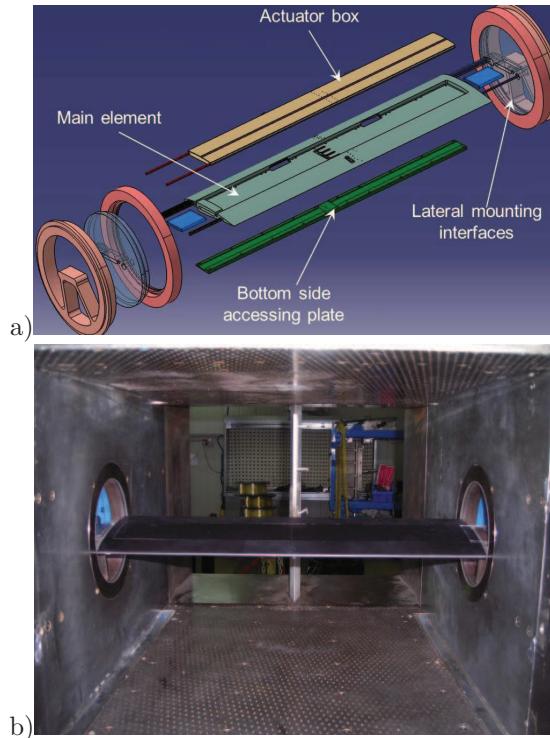


Figure 1: BAC3-11 airfoil: a) Main model components; b) Assembled model installed in the wind tunnel

has been designed to house the DBD actuator on the suction side, as shown in Figure 1.

Three different configurations have been tested: the first called P1, is a metallic insert that represents clean BAC3-11 shape (no actuators installed) to be used as reference test case; the second called P2, is a DBD actuator insert with 2 electrodes in an asymmetric configuration separated by dielectric material. The trailing edge of the exposed electrode is at 45% of the chord in this configuration. Figure 1 illustrates the exploded view of the model with the main model components (a) and the assembled manufactured model installed in the wind tunnel test section. Moreover, in order to evaluate if the relative position between the electrodes and the shock wave can influence the aerodynamic performance, another DBD actuator, called "P3", with a different electrode position (at 57% chord length) has been tested.

The actuator inserts consist of two parts. The first is a support realised by stereo lithography. Its upper side shape corresponds to the BAC 3-11 geometry. The DBD actuator is made of flexible printed circuit boards with a thickness of 0.2 mm, glued on top of the support. Thus a smooth surface following the profile shape was produced. In order to allow quantitative measurements during experiments, pressure taps were drilled into the dielectric (Figure 2). However, no pressure taps could be included into the electrode structure due to the risk of arc breakdown. In particular, for the Kulite pressure transducers, arcing and electromagnetic interferences posed a problem for the sensors located close to the electrodes; an issue that has been approached and solved by developing special shielding. In all, a total of 45 pressure taps (29 on the upper surface and 16 on the lower surface) and 10 high frequency pressure transducers (Kulite transducers XCS-062-25A) located on the upper surface of the model (Figure 3) could be implemented.

Figure 3 shows the distribution of steady pressure taps and of the points individuated for unsteady pressure measurements. For the P2 configuration, measurements

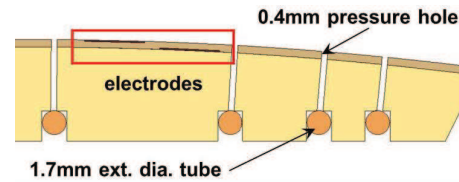


Figure 2: Solution for steady and unsteady pressure measurement near electrodes

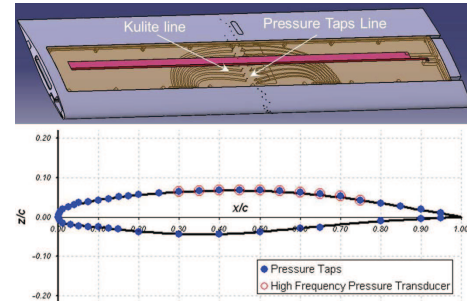


Figure 3: Distribution of steady and unsteady measurement points on the model

points located at  $x/c = 0.45$  and  $x/c = 0.5$  are omitted due to the presence of the electrodes at these locations. The experiments with nanosecond pulse-driven DBD actuators require a power supply capable of generating these short, fast-rising voltage pulses. The core of the system used in the present study is a Behlke HTS 111-06-GSM fast high-voltage transistor switch, composed of two identical Mosfet switching paths forming a so-called push-pull circuit. It produces voltage pulses of up to 10 kV, at a pulse width of  $t_w = 200$  ns, with rise and fall times down to 20 ns. An upgraded version of the power supply is today able to work with frequencies up to  $f_p = 10$  kHz. Figure 4 and Figure 5 show the waveforms of a typical voltage pulse and Figure 6 the resulting discharge on the assembled model. For the present activity, tests were performed with FRP DBD actuators at a voltage of  $U_p = 8$  kV and a pulsing frequency of  $f_p = 970$  kHz.

Finally, since the laminar-turbulent transition of the boundary layer is a significant parameter for the shock - boundary layer interaction, the boundary layer transition was triggered at a line of 5-7% chord, on both upper and lower surfaces, by means of carborundum grains located along the whole model span. This helped to limit the number of variables that could affect the test. Hence more realistic simulations at high Reynolds number can be performed.

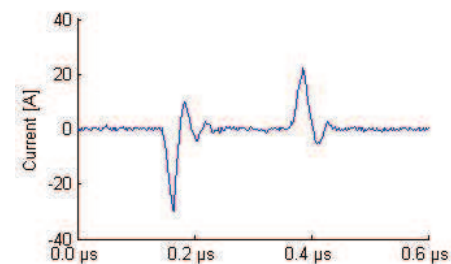


Figure 4: Current waveform of a typical pulse

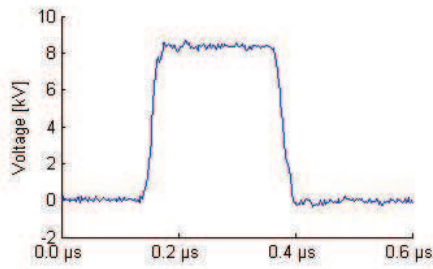


Figure 5: Voltage waveform of a typical pulse

### 3 Effect of the plasma on the main aerodynamic performances

In order to evaluate whether FRP DBD actuators have beneficial effects on the aerodynamic performance, several tests were performed in the Mach range  $M = 0.4$  to  $M = 0.85$ , at angles of attack from  $\alpha = -2^\circ$  to  $\alpha = 8^\circ$  and with Reynolds numbers varying between  $Re = 1.7 \times 10^6$  and  $Re = 2.5 \times 10^6$ . During the tests the total pressure of the free stream was acquired via a RUSKA 7222 absolute transducer with a full scale of 26 PSI and an accuracy of 0.01% FS. The atmospheric pressure was measured by using a DRUCK DPI 740 barometer with accuracy  $\pm 15$  Pa. Steady pressure measurements on the model were acquired by means of the PSI 8400 system connected to differential electro-scanner with 15 PSI FS. The total temperature was measured by a United Sensor USNH-B-106 total temperature probe installed in the settling chamber.

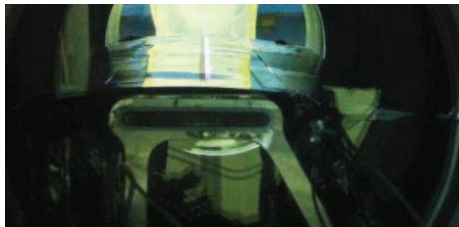


Figure 6: Plasma activated on the model during a wind tunnel test - Plasma "P2" ( $x_{plasma} = 0.45C$ )

Figure 7 shows the experimental pressure coefficients on the model carried-out at  $M = 0.5$  for different angles of attack, on the clean model ("P1") and on the model equipped with plasma at  $x/c=45$  ("P2"). In order to evaluate the quality of wind tunnel data, experimental measurements were compared with numerical data referring to the clean configuration P1 obtained with the UZEN code [7].

From the analysis of results, a good matching between numerical and experimental data was observed indicating a good quality of wind tunnel data. Small discrepancies between the experimental pressure coefficients measured on the clean configuration and on the model equipped with the plasma inserts (plasma off) are present. This is a result of wind tunnel measurement errors, of the manufacturing tolerance of the plasma inserts (which slightly changed the model shape), of the model assembly and of the plasma inserts deformation under the aerodynamic loads (which again slightly changed the model shape). Experimental measurements carried-out

in subsonic conditions with the activated plasma show no evident effect on the general surface pressure distribution with respect to measurements obtained in the same Mach-Re-a conditions without plasma.

A similar analysis was performed also at high subsonic/transonic Mach numbers in order to check whether the plasma effects the shock wave position and intensity. Figures 8 present the experimental pressure coefficients on the model, measured at  $M = 0.8$  for different angles of attack, on the clean model ("P1") and on the model equipped with plasma at  $x/c = 45\%$  ("P2"). In the pictures, results are compared with numerical data referred to the clean configuration obtained with the UZEN code.

Only small discrepancies between the experimental pressure coefficients measured on the clean configuration without insert and on the model equipped with the plasma insert but with the plasma off were observed. Also, a good match between wind tunnel and CFD data has been found except for the lower pressure expansion showed by the experimental data. The measured shock wave position and intensity are comparable to what was expected. From the analysis of steady pressure measurements carried out with and without plasma, it was not evident that the plasma produced effects on shock wave position and intensity. As these are steady state analyses, it is not possible at this stage to analyse eventual effects of the plasma on the oscillation of the shock wave and in particular on the buffet conditions.

### 4 Effect of the plasma on the shock buffet phenomenon

The steady pressure measurements reported in the Figures 8 can help to highlight the onset of buffet when, in presence of a strong shock wave, the local pressure at the trailing edge fails to recover positive values, remaining slightly at negative values [6]. Following this approach, it seems clear that the case  $M = 0.8$ ,  $\alpha = 4^\circ$  is characterised by strong shock wave oscillations compared to the condition  $M=0.8$  and  $\alpha=0^\circ$ . As shown in Figure 9 this can be easily detected by plotting the instantaneous time responses of the Kulite transducers. More in detail, Figure 9 displays the instantaneous pressure distributions measured by the Kulite transducers on the clean configuration "P1" in two different points of time at  $M = 0.8$ ,  $\alpha = 0^\circ$  and at  $M = 0.8$ ,  $\alpha = 4^\circ$ . For each condition, the reference times have been selected to show the maximum fluctuation of the pressure in the shock wave position.

The results show that in both conditions, the averaged pressure measured by the Kulite transducers are quite comparable with steady pressure measurements and, as expected, the case at  $\alpha=4^\circ$  is characterized by a stronger shock wave oscillation around the mean position compared the case at  $\alpha=0^\circ$ . In general, a strong pressure oscillation is measured by Kulite transducers close the shock wave position under buffeting conditions. This can be quantitatively measured by analysing the root mean square of pressure coefficient ( $C_{p_{rms}}$ ) along the model as shown in the Figures 10 the values of  $C_{p_{rms}}$  were calculated from the pressure signals considering a time period of 0-3 seconds.

From results reported in Figure 10, it can be noticed that the standard deviation of the pressure coefficient  $C_{p_{rms}}$ , which can be regarded as a measure of the wave intensity, shows very low pressure fluctuation values upstream of  $x/c \cong 0.55$ , then increases up to 4% at the

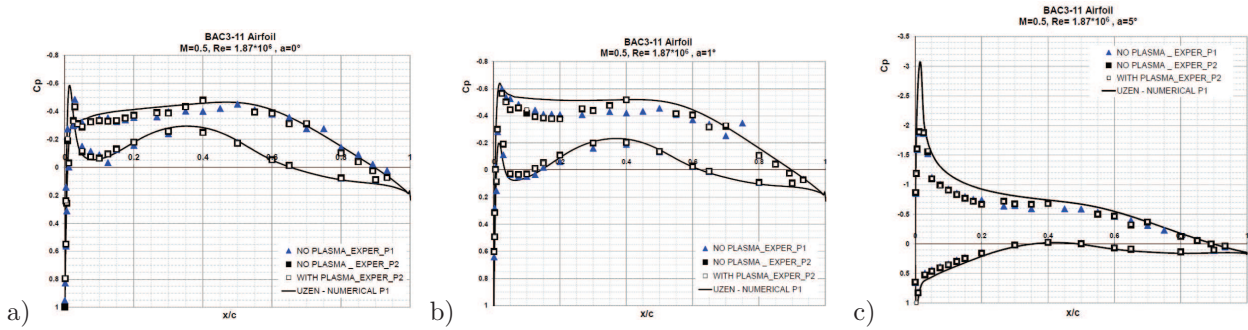


Figure 7: Effect of the plasma on the average  $C_p$  distribution for a) zero incidence; b) Angle of attack of  $1^\circ$ ; c) Experimental results obtained at  $M = 0.5$  on the clean configuration "P1" and with DBD insert "P2" ( $x_{plasma} = 0.45C$ )

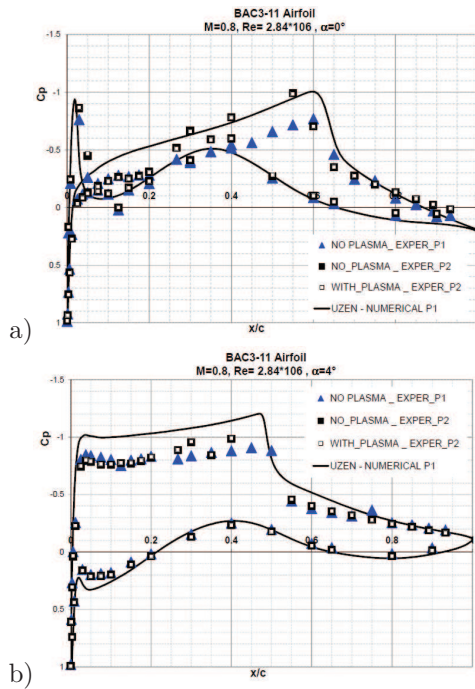


Figure 8: Effect of the plasma on the average  $C_p$  distribution. Experimental results were obtained at  $M = 0.8$  on the clean configuration "P1" and with DBD insert "P2" ( $X_{plasma} = 0.45C$ )

shock wave position and return to decrease downstream to values lower than 1%. In the case of oscillating shock waves (Figure 10 b), high values of pressure fluctuations are measured in a wider region of the model respect to other conditions. Finally, comparing results obtained with and without plasma at different conditions, it was systematically recognized that a lower value of pressure fluctuation is registered at the shock wave position on both tested configurations in presence of plasma. This seems to indicate a benefit of plasma in terms of reduction of both intensity and oscillation of the shock wave, hence a stabilisation of the shock wave. These measured differences with and without plasma are quite small and could be confused with measurement errors. Further tests are necessary to achieve a more confident conclusion.

In order to further improve the understanding of the plasma effect on the shock buffet phenomenon, the analysis of Kulite transducer data was performed in the frequency domain. The signals were filtered at 10 kHz by means of the GLE/SGA- 4 conditioner system and amplified with a gain of 10, in order to have an output sig-

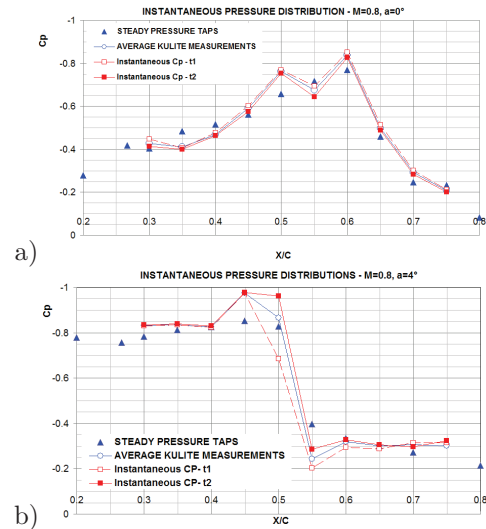


Figure 9: Shock wave position oscillations: a) config. P1 with  $M = 0.8$ ,  $\alpha = 0^\circ$  conditions; b) config. P1 with  $M = 0.8$ ,  $\alpha = 4^\circ$  conditions

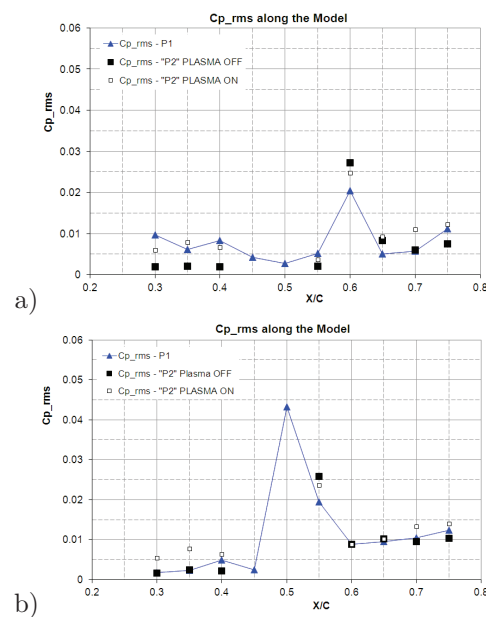


Figure 10: Root mean square of the pressure coefficient  $C_{p_{rms}}$  Top:  $M = 0.8$ ,  $\alpha = 0^\circ$ ; Below:  $M = 0.8$ ,  $\alpha = 4^\circ$

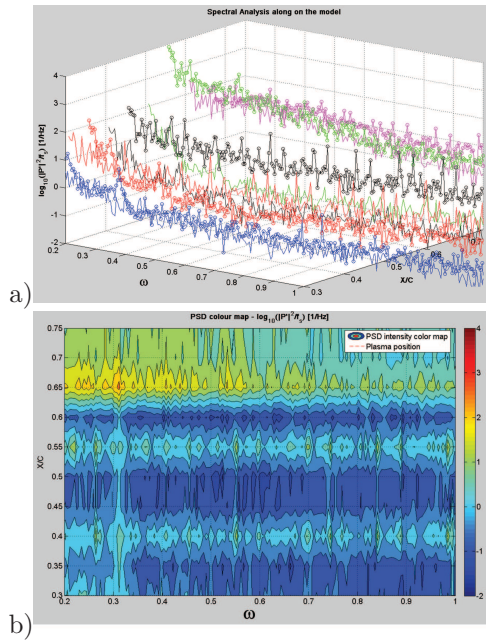


Figure 11: a) 3D spectral plot of PSD along the model chord. Clean configuration "P1" at  $M = 0.8$ ,  $\alpha = 0^\circ$ ; b) Contour map corresponding to plot a) of PSD along the model chord

nal between 0 and 1 Volt. The signals were sampled at 30'000 samples/sec/channel over 3 seconds. The spectral analysis was done by using Welch's method with block sizes of 8192. Moreover, the smoothing of the transforms was accomplished using 25% overlap block averaging. In this way the chord-wise distribution of the resulting squared modulus of the unsteady component of the upper surface pressure versus frequency (or reduced frequency  $\omega$ ) was evaluated for each chord wise pressure tap location from  $x/c = 0.3$  to  $x/c = 0.75$ . Figure 11a and Figure 12 report the power spectral density (PSD) of pressure fluctuations referring to the cases of Figure 9 (with  $M = 0.8$ ,  $\alpha = 0^\circ$  and  $M = 0.8$ ,  $\alpha = 4^\circ$ ). The different trends measured by each Kulite transducer along the model chord were finally interpolated obtaining the colour maps reported in Figure 11b and Figure 12b. Most of the graphs presented in the following are limited to the range of reduced frequencies  $0.20 < \omega < 1$  since this is considered to be the interesting range for the study of buffet phenomena. At lower frequencies, the signal of some Kulite transducers contained significant electrical noise occurring at the dominating frequencies 50 Hz or 100 Hz. Spectral plots are shown in the following Figures, 11-12. From the analysis of the spectral plots, it was recognized that in absence of buffeting conditions ( $M = 0.8$ ,  $\alpha = 0^\circ$ ), the spectral signals show a typical decreasing trend versus reduced frequency without showing predominant peaks. Near the shock wave position the signal shows a similar trend but with higher PSD intensity. In presence of oscillating shock waves ( $M = 0.8$ ,  $\alpha = 4^\circ$ ), the amplitude in the shock wave position are much higher compared to the previous case. In particular, the signal amplitude results increased in the reduced frequency range  $\omega \in [0.2 : 0.45]$ . Although reduced in amplitude, this feature is also observed at all stations downstream of the shock wave.

Regarding the main characteristics of shock oscillation, the coherence analysis between Kulite transducers located at  $x/c = 0.5$  and  $x/c = 0.55$  showed prominent spectral peaks at reduced frequency  $\omega = 0.27$  and  $\omega = 0.31$  corresponding respectively to  $f = 180\text{Hz}$  and  $f =$

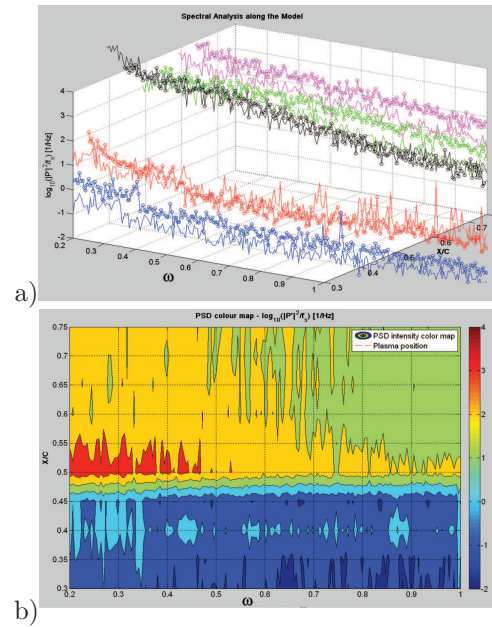


Figure 12: PSD along the model chord. Clean configuration "P1" at  $M = 0.8$ ,  $\alpha = 4^\circ$  a) 3D plot; b) contour map

215Hz. These peaks are well evident in Figure 13 which reports the same data of Figures 11 and 12 in a different way. The first peak is well in accordance with literature data for which, in 2D flows, the BAC3-11 airfoil exhibits shock buffet conditions at Mach numbers  $M = 0.75-0.88$  at low angles of attack ( $0^\circ-5^\circ$ ), oscillating at reduced frequencies between  $0.25 \leq \omega \leq 0.29$  [5]. In order to evaluate the effects of the plasma in the frequency domain, a similar analysis was performed in the presence of plasma. Figures 14 show the PSD colour map of the configuration "P2" with and without plasma in the same flow conditions as in Figure 12. The colour map between  $x/c = 0.4$  and  $x/c = 0.55$  is omitted because no pressure transducers were included at these locations due to electrodes. The results reported in Figure 14a, related to the P2 configuration without plasma, are quite well in accordance with the ones reported in Figure 12b, which relate to the P1 "clean" configuration. Only some PSD peaks not present on the P1 configuration are observed between  $0.25 < \omega < 0.5$  downstream at the model abscissa higher than  $x/c = 0.55$ . This is due to the manufacturing tolerance of the plasma inserts, the model assembly and the plasma insert deformation under the aerodynamic loads which alter the flow field around the model (generating for example different fluid dynamic structures and/or vortex shedding in the separation zone). In the presence of plasma, (Figure 14b), an increased background noise was measured on all transducers. This produces a slight increase in the mean value of the PSD intensities. This effect is clear at location  $x/c < 0.4$  where a low intensity signal, comparable to the background noise is measured. However, at the shock wave position, the presence of plasma seems to reduce the intensity of peaks registered in absence of plasma (Figure 14a). PSD peaks are themselves in fact limited to the range of reduced frequencies  $0.3 < \omega < 0.4$ . Figure 15 shows the PSD of the pressure fluctuations measured by the Kulite transducer located at  $x/c = 0.55$  on the P2 configuration with and without plasma. The results are compared with the data measured on the clean P1 configuration. The PSD intensity measured on the P2 configuration is in both cases much higher than the one measured on the P1 con-

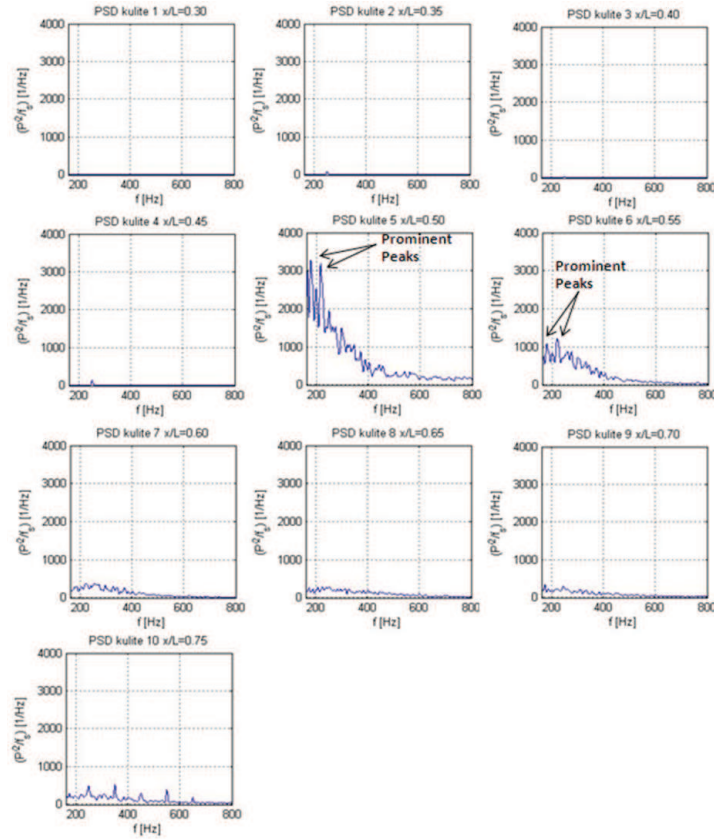


Figure 13: Oscillation frequency of the shock wave for the P1 configuration ( $M = 0.8$ ,  $\alpha = 4^\circ$ )

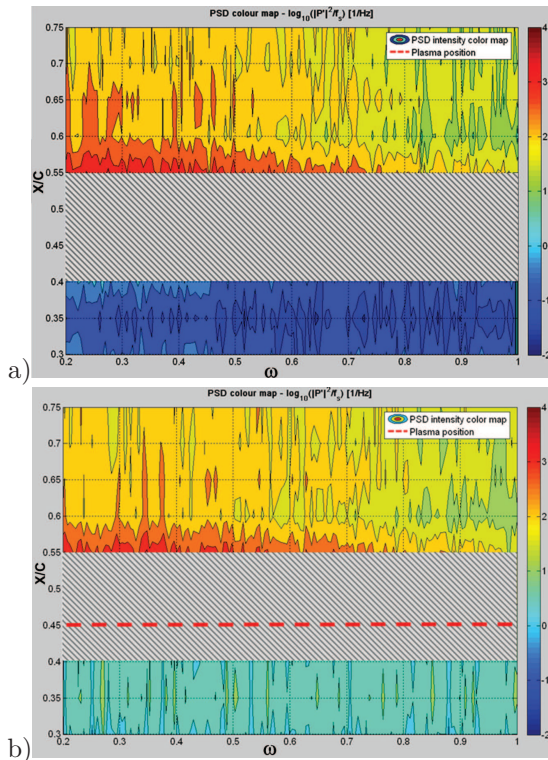


Figure 14: PSD along the model chord. Configuration “P2” at  $M = 0.8$ ,  $\alpha = 4^\circ$ ; a) plasma off; b) plasma on

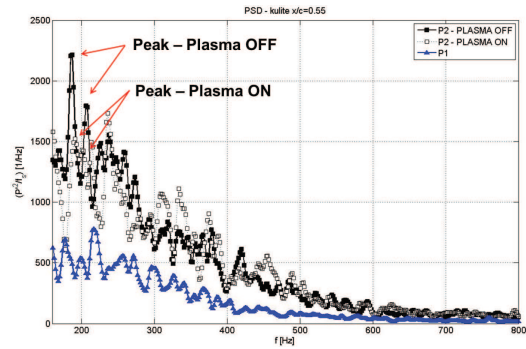


Figure 15: Effect of Plasma on the Oscillating frequency of Shock wave for the P2 Configuration at  $M=0.8$ ,  $\alpha = 4^\circ$

figuration. This indicates that on the P2 configuration the oscillating shock wave moves around a mean position located farther downstream than on the clean P1 configuration, hence closer to the pressure transducer at  $x/c = 0.55$ . Moreover, the PSD trend of the P2 configuration without plasma shows predominant peaks at  $f = 190$  Hz and at  $f = 210$  Hz, corresponding to reduced frequencies of  $\omega = 0.28$  and  $\omega = 0.30$  respectively. Note that these values are slightly different than the ones measured on the P1 configuration. Again, this could be associated to the different position, intensity and characteristic of the shock wave acting on the P2 configuration compared to the one measured on the clean configuration. Finally, when comparing PSD trends obtained with and without plasma, it is evident that the presence of plasma reduces the PSD intensity of both peaks. From a physical point of view, this seems to confirm that the presence of the plasma reduces the pressure fluctuation intensity of the oscillating shock wave. However, higher values of

PSD intensity are registered at higher frequencies indicating that in this case, stronger fluid dynamic structures and/or vortex shedding are generated in the separation zone in the presence of plasma.

## 5 Conclusions

In order to evaluate whether pulsed DBD actuators have beneficial effects on the aerodynamic performance in high subsonic flows and in particular in mitigating shock buffeting phenomena, a series of experimental investigations was carried out in the CIRA PT-1 transonic wind tunnel. The flow speed was varied between  $M = 0.4$  and  $M = 0.85$  at angles of attack from  $-2^\circ$  to  $8^\circ$  and Reynolds numbers between  $Re = 1.7 \times 10^6$  and  $Re = 2.5 \times 10^6$ . Tests were performed on a two dimensional BAC 3-11 profile, a supercritical airfoil with 11% of maximum thickness able to reach shock buffet conditions at Mach numbers ranging between  $M = 0.75$  and  $M = 0.88$ , at low angles of attack ( $0-5^\circ$ ) and Reynolds number about 2 - 3 million. Different configurations have been tested: the first called P1, a metallic insert that is representative of the clean BAC3-11 shape (no actuators installed) to be used as reference test case; the second called P2 is an insert with DBD actuator consisting of two electrodes in an asymmetric configuration separated by dielectric material. The discharge area of the P2 configuration was located at 45% chord length. In order to allow quantitative measurements during experiments, special solutions for steady pressure taps and instantaneous pressure sensors close to the electrodes were developed. This allowed having 45 pressure taps (29 on the upper surface and 16 on the lower surface) and 10 high frequency pressure transducers (Kulite transducers XCS-062-25A) located on the upper surface of the model. For the present activity, tests were performed with nanosecond pulse-driven DBD actuators powered with voltage pulses of  $U_p = 8$  kV and at a pulsing frequency of  $f_p = 970$  Hz.

Experimental measurements carried out in subsonic and transonic conditions with plasma show no immediate effect of the Plasma on the main surface pressure distribution or on the shock wave position and intensity compared to measurements obtained in the same conditions obtained without plasma.

From the analysis of pressure fluctuations in the presence of a shock wave, the pressure fluctuations registered at the shock wave position were reduced in the presence of plasma. This indicates a benefit of plasma in terms of reduction of both intensity and oscillation of the shock wave, hence a stabilising effect. However, since the measured differences with and without plasma are quite small there is a risk of uncertainties due to measurement errors. Further tests are necessary to achieve a more confident conclusion.

In shock buffet conditions the PSD signals of Kulite transducers measured on both P1 and P2- plasma off configurations shows spectral peaks that are well in accordance with literature data, for which the BAC3-11 airfoil is characterized by oscillating reduced frequency between  $0.25 \leq \omega = \frac{2\pi fc}{2V_\infty} \leq 0.29$  in 2D flows. The presence of plasma seems to reduce the intensity of these peaks indicating, from a physical point of view a reduction of the pressure fluctuation intensity of the oscillating shock wave. However, higher values of PSD intensity appear at higher frequencies which are probably associated to fluid dynamic structures and/or vortex shedding generated in the separation zone by the plasma.

## References

- [1] Roupassov D.V., Nikipelov A.A., Nudnova M.M., Starikovskii A.Y., *Flow Separation Control by Plasma Actuator with Nanosecond Pulsed-Periodic Discharge*, AIAA Journal, 47 (1), 2009.
- [2] S- Pavon, J-L. Dorier, C. Hollenstein, P. Ott, P. Leyland *Effects of high-speed airflows on a surface dielectric barrier discharge*, J. Phys. D: Appl. Phys. 40. No 6.2 1733-1741, 2007.
- [3] A. Alshabu, V. Hermes,y I. Klioutchnikovz - *Highly Transient Phenomena on an Airfoil at Transonic Flow Conditions* - AIAA Paper 2007-4000, 2007.
- [4] Atef Alshabu, Herbert Olivier, Viktor Herms, and Igor Klioutchnikov - *Wave Processes on a Supercritical Airfoil* - 26th International Symposium on Shock Waves.
- [5] P.C. Steimle, W. SchrÄüder, and M. Klaas - *Unsteady Transonic Fluid Structure Interaction at the BAC 3-11 High Aspect Ratio Swept Wing* - Summary of Flow Modulation and Fluid-Structure Interaction Findings, Volume 109, 2010, pp 325-361, 2010.
- [6] Robert E. Bartels and John W. Edwards - *Cryogenic Tunnel Pressure Measurements on a Supercritical Airfoil for Several Shock Buffet Conditions* - NASA -TM-110272.
- [7] Catalano, P., and Amato, M., *An Evaluation of RANS Turbulence Modeling for Aerodynamic Applications*, Aerospace Science and Technology, Vol. 7, No. 7, pp. 493-590.doi:10.1016/S1270-9638(03)00061-0, 2003
- [8] Eric Moreau - *Airflow control by non-thermal plasma actuators* - Journal of Physic - D: Appl. Phys. Vol.40 605 doi:10.1088/0022- 3727/40/3/S01, 2007

# UNMANNED AERIAL VEHICLE FOR PLASMA FLOW CONTROL

W. Friedrichs<sup>1</sup>, S. Grundmann<sup>1</sup>, C. Tropea<sup>1</sup>

<sup>1</sup>Center of Smart Interfaces, Technische Universität Darmstadt, Flughafenstr. 19, 64347 Griesheim, Germany

## Abstract

In the course of the PLASMAERO project an unmanned aerial vehicle was designed and built to enable experiments with plasma actuators under realistic flight conditions. On the basis of the requirements and preliminary tests to ensure a flow control effect of DBD plasma actuators, a kite configuration with 2.4 m wingspan, 0.3 m chord and a flight weight of 10 kg was chosen. The propulsion system consists of two electric motors with pusher propellers behind the wing. The UAV is mostly made out of fibre-reinforced plastic. The wing consists of 5 sections on a continuous spar which can be exchanged to allow for different profiles and flow control configurations for the experiments. The fuselage offers space for the integration of different payloads.

To record data and automatically control the UAV during the experiments a flight control system is used. The system was developed by the "Institute of Flight Systems and Automatic Control" at the TU Darmstadt. The sensors on board the UAV include a dynamic and barometric pressure sensor, inertial measurement unit, magnet field sensor and a GPS receiver. The system uses this data as input for an autopilot and flight control system to autonomously control the plane. Additionally the data is sent to a ground station for monitoring and is recorded for post flight analysis.

Two small high voltage generators can be carried on the sides of the fuselage underneath the wing. They can be used for standard or conformable DBD actuators with a length of up to 0.9 m and supply a voltage of up to 12 kV. Other types of high voltage generators can be installed in the payload section of the fuselage. During the PLASMAERO project two different actuator configurations were developed by the partners for use on the UAV platform. The "University of Nottingham" developed a vortex-generating DBD plasma actuator for control of trailing edge separation on a NACA 0015 profile. The second actuator is a multi-DBD arrangement from the "Instytut Maszyn Przeplywowych" which also aims to control separation on this profile.

## 1 Introduction

The motivation for the current work arose after building and testing a UAV to demonstrate separation control with the help of DBD plasma actuators [1]. This plane had a wingspan of 1800 mm, a payload of about 4 kg and a mean chord of about 180 mm, resulting in Reynolds numbers of around 140,000. Actuators were applied over a total of 900 mm wingspan on both sides. The stall speeds for the unactuated and actuated cases were measured using a pitot-static tube on the the left wing. The measurements and data recording were done by a small logging system designed for model aircraft use.

Although successful test flights were performed with that UAV, several areas for improvement were identified and these were realized in a new design known as the

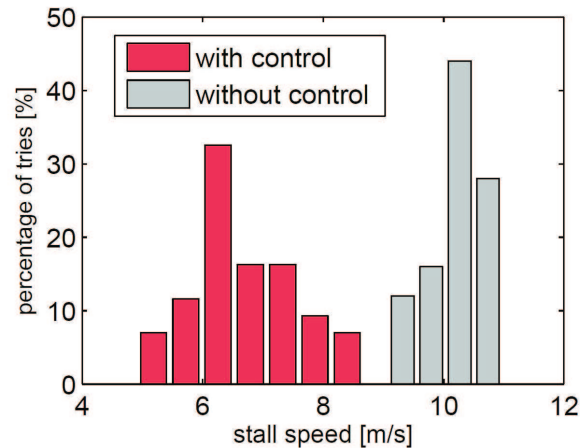


Figure 1: Results of 68 stall speed measurements with the existing UAV from [1].

PLASMAERO UAV:

- The electric system, especially the measurement equipment, was prone to electrical interference from the plasma actuation. Several electric motors, batteries and data recording devices were strongly affected or even permanently damaged.
- The measurement results exhibited high variability. This can be explained by two factors: Gusts, and the influence of the pilot. Gusts can only be avoided by flying in relatively calm air, usually in the morning and evening. However, the influence of the pilot can be diminished by using a system for autonomous control for the experimental maneuvers.
- During the PLASMAERO project different flow control concepts and high voltage generators were to be developed. The existing UAV could not provide sufficient payload or space for such developments. Moreover, to incorporate different configurations and electronics a more modular platform was desirable.

## 2 The PLASMAERO UAV

The most obvious and important requirement the PLASMAERO UAV has to fulfill is the ability to carry the necessary equipment while being able to demonstrate plasma flow control in flight. On the one hand the UAV needs relatively heavy plasma actuator equipment, mainly the high voltage generators, as well as additional measurement and flight control equipment. This requires a relatively high payload and space, especially since different components from different partners were foreseen, some with unknown specifications at the design phase. On the other hand the control authority of plasma actuators for flow diminishes severely with increasing Reynolds

number, ultimately contradictory to the requirement of a high payload. Most successful DBD plasma actuator experiments were done at Reynolds numbers around or below 200.000.

Although an advancement of the control authority by the partners in the course of the project was anticipated, a wind tunnel study was conducted in the "Niedergeschwindigkeitswindkanal" at the TUD to ensure at least one successful experiment at the chosen Reynolds number. A wing with a span of 1.2 m, consisting of three 400 mm segments was tested at velocities of 5 - 30 m/s. Three different chords of 200, 400 and 500 mm and different flow control concepts, namely leading and trailing edge separation control, "Gurney-flap" plasma actuators and control of a forced separation by a bump were investigated. Although only provisional and sketchy, the experiments showed a change in lift of up to  $\Delta c_l = 0.1$  over a range of  $\Delta\alpha = 10^\circ$  for the 400 mm forced separation case at a Reynolds number of 290.000. Although not an elegant or efficient way to achieve flow control, it ensures the feasibility of at least one experiment at this Reynolds number. Other than the control



Figure 2: PLASMAERO UAV in flight.

authority of the plasma actuator there were also many other requirements regarding placement of sensors and flow control experiments in undisturbed flow, electromagnetic compatibility, crash safety and manufacturing.

## 2.1 Layout

The general layout chosen is a kite configuration with a rectangular shoulder wing with a chord of 300 mm and a span of just under 2400 mm. This chord combined with an anticipated stall speed of 10-15 m/s, depending on the flight weight results in a minimum Reynolds number between 215,000 and 320,000.

Due to the relatively high wing the plane is stable along the roll axis without adding any dihedral. The wing therefore can be as simple as possible to allow modular interchangeability. The propulsion system consists of two propellers in a pusher configuration, mounted in-board on the wing. This allows the mounting of sensors, e.g. pitot-static tube, in the front of the fuselage, and a relatively undisturbed airflow at the flow control sections on the wing. A structural weight of approximately 6 kg and a flight weight of 10 kg have been achieved. The fuselage has the function to hold variable payloads and to connect to the wing and tail sections, bearing the according loads. It consists of a lightweight, laser-cut GRP-foam sandwich frame, covered by laser-sintered plastic and styrofoam parts which gives the outer form of the

Table 1: Overview of UAV measurements.

Wingspan	2384	mm
Span of actuator segment	400	mm
Span of aileron segment	400	mm
Wing chord	300	mm
Wing area	0.72	m <sup>2</sup>
Flight weight	10	kg

fuselage and can absorb some energy in case of a crash and thereby protect the payload. The main segment of the fuselage has a square cross section, beginning at the nose and ending below the wing. The interior dimensions are 540x166x166 mm, a removable cover plate on the top ensures easy access to the payload. The payload can be installed on the ground plate or on intermediate plates mounted to the side walls. The frame is relatively long to accommodate payloads of different sizes and weights, while ensuring a tolerable position of the center of gravity. The nose cone is made of laser-sintered plastic and is mounted to the front spar of the frame. It has ventilation ducts as well as a fixture for a pitot-static tube probe with an outer diameter of 3 mm. Other sensors could be mounted as well by rapidly building new nose cones with added fixtures with the laser-sintering machine. The plane features a tricycle landing gear.

The tail boom is removable and connected via an aluminium tube glued into feed holes in three ribs below the wing, ensuring short paths for the force transmission to the wing and the fuselage frame. The tail boom itself consists of a wound carbon fibre tube, the control surfaces consist of a CRP tube as spar and styrofoam covered with a plastic sheet. An all-flying tail was chosen as horizontal control, while the rudder is divided due to structural and clearance reasons. For good stability and control authority a horizontal tail volume of about 0.35 to 0.45 is needed, both can be adjusted by the length of the tail boom. The servo motors for the control surfaces are installed in the tail to avoid electromagnetic disturbances by the high voltage generators in the fuselage. This adds weight with a long lever towards the center of gravity, which has to be accounted for with weight in the front of the fuselage, by shifting the payload forward.

The wing sits on top of the frame behind the payload section and is connected to it by 6 screw joints. The wing has a rectangular planform and no aerodynamic or geometric twist. The profile used is a model aircraft profile with 2.5 % camber and 15 % thickness. To allow for the use different experiments the wing consists of several sections which can be exchanged. To dimension the spar for the wing an analysis of the loads was carried out. First an assumption regarding the maximum load was made, due to manoeuvring or gusts the load on the wing can be increased several fold. In this case a load factor of  $n=10$  was assumed, setting the design manoeuvring speed  $V_A$  to  $3.16 V_S$  (stall speed). To calculate the resulting bending moment an assumption of the lift distribution has to be made. The easiest one would be a constant distribution along the wing span. Since the outboard sections do produce a smaller part of the lift this assumption would lead to a significantly higher bending moment, resulting in a over dimensioned spar. To get a better assumption a simple model of the airplane was evaluated using the software XFLR5. The calculated lift distribution shows an anticipated smaller lift outboards

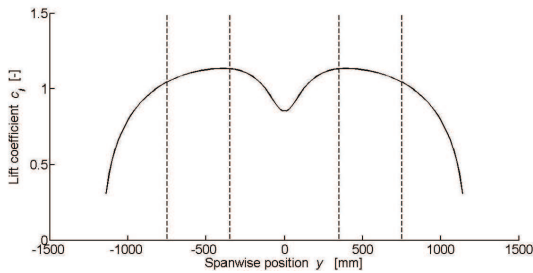


Figure 3: Lift distribution over the span of the wing for calculation of maximum loads.

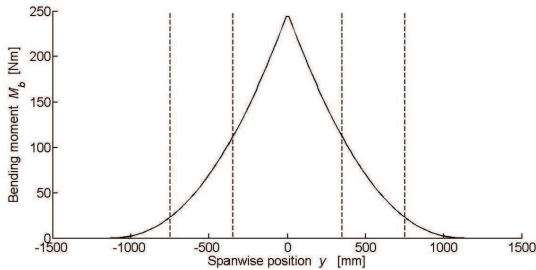


Figure 4: Resulting bending moment at maximum load.

as well as a drop in the vicinity of the fuselage. The self-weight of the wing was neglected, leading to a rather conservative assumption. Especially the peak bending moment at the fuselage is reduced by the weight of the engines and propulsion system on the inboard sections.

The spar consists of a balsa wood bar with CRP caps and several layers of GRP shear web. The required amount of carbon fibres was calculated and the according number of roving was applied to the spar caps, with the number increasing towards the middle of the wing. After curing the GRP shear web was applied and the spar was put in a metal mould to achieve an exact size. The individual wing sections can be slid on the spar, allowing for an easy exchange of experiments. To achieve this a GRP sleeve is built into each wing section which serves as guide for the spar.

For the wing covering 400 mm span moulds are used, the laminate consists of a GRP-foam sandwich. Recesses for the installation of the plasma actuators are attained by placing wax plates into the moulds before laminating. In between the section wing fences can be installed to minimize three-dimensional effects due to different profiles used in the actuated sections. The wing tips are covered with a laser-sintered plastic part with a small wing tip fence.

The propulsion system consists of two electric motors and airscrews. Electric motors were chosen because of the easier handling, safety issues and fewer vibrations when compared to internal combustion engines as well as no contaminations by fuel or exhaust. The placement of the propeller in a pusher configuration behind the wing was chosen to ensure an unchanged flow field at the fuselage for sensor placement and on the wings for experiments. To minimize electrical losses and sensitivity to electromagnetic disturbances, these components are installed in the engine mount directly in front of the motor. This setup yields flight times of 8 minutes at maximum power to around 12 minutes at more efficient speeds. Since the propulsion system is above the center of gravity a pitching moment cannot be avoided. It is not critical, but has to be kept in mind, especially during manoeuvres near the ground with drastic changes in propulsion power, i.e. the abortion of a landing.

## 2.2 Flight control and data recording system

To achieve repeatable results an automated flight control system was acquired. Predefined maneuvers for the different experiments can be flown without pilot intervention or errors. The flight control system was developed at the "Institute of Flight Systems and Automatic Control" (FSR) at the TU Darmstadt [2]. It is a highly modular and flexible system which is in use on different platforms, including quadcopter and ground vehicles. Sensors include a barometer, air speed, temperature sensor and magnetometer, a GPS device and an inertial guidance unit. All data is passed via an ethernet connection to the mini-PC, which uses it to compute the actual flight situation and the required servo outputs for control. The most crucial data is sent to the ground station for telemetry purposes. Additionally, the data is saved onboard to enable a complete post-flight analysis.

The controllers for the autonomous flight control unit were designed and implemented using Matlab Simulink Release 2011b, a graphical environment to analyze and design systems within Matlab. The software of the flight control system uses the "Open robot control software OROCOS". All sensor inputs are used to compute the actual flight situation. The control algorithm is divided into a navigation, autonomous guidance and flight controller loop in a cascade. The most important for our purposes is the flight controller, airspeed, height and azimuth are controlled by it. The elevator deflection is

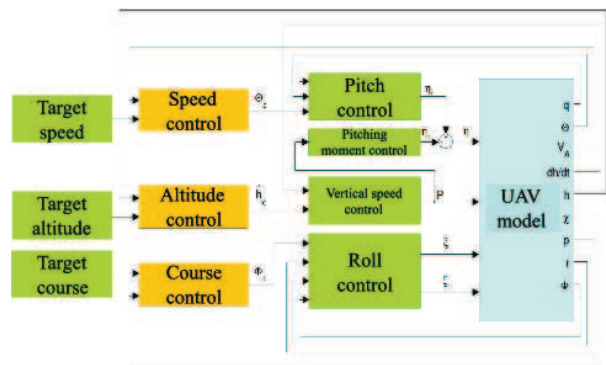


Figure 5: Overview of the flight controller.

used to control the airspeed of the plane. The height is controlled by the power of the propulsion system. Since the propulsion has a pitching moment as well as an influence on the airspeed at the elevator, the propulsion power has to be included when computing the elevator deflection. The control of the lateral movement of the UAV, i.e. yaw and roll control, can be decoupled from the longitudinal movement. The roll control uses the ailerons to fly a given heading, while the yaw control uses the rudder to avert a sideslip of the plane. All deflections are limited to an amount that ensures that the physically maximal deflections are not reached and that the plane cannot fly too severe manoeuvres. Additionally, bank angle and climb rate are limited as well. Additional information on the system can be found in [2].

The rest of the system consists of standard model radio control parts, controlled either automatically via the flight control unit or manually piloted by remote control. The control surfaces are actuated by servo motors, the propulsion motors are driven by controllers. For the flight testing of the UAV platform as well as start and landing the plane has to be controlled remotely by a pilot. For flights with the flight control unit a 7 channel

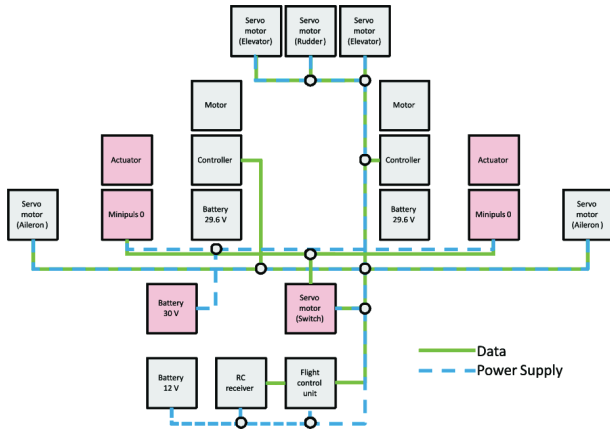


Figure 6: Overview of the electrical system of the UAV.

satellite receiver is used which operates in the 2,4 GHz frequency band. The signal is transmitted to the flight control unit and split into the according servo signal outputs with a pulse-width modulation. If the plane is controlled remotely the signal is passed through without any modification by the flight control unit. Altogether 7 servo motors are installed in the plane to actuate the aerodynamic control surfaces, the steerable front gear and the high voltage devices.

The 2,4 GHz connection from the remote control as well as the pulse width modulated signal to the servo motors were tested for interference introduced by plasma actuation. The only critical disturbances found were from malfunctioning plasma actuators. Otherwise disturbances and noise can be found in the signals, but without effecting the position of the servo motors.

### 2.3 High voltage generators for plasma actuation

The Minipuls 0.1 high voltage generator is an improved version of the MP 0 generator. It consists of two units, a control board and a high voltage board, and needs 15 - 35 V input voltage. It has a maximum peak-to-peak voltage of 12 kV with a plasma frequency of 5 - 20 kHz. Actuators with a capacity of 100 pF and 50 pF, corresponding to about 900 or 450 mm typical actuator length, can be operated. The signal can be pulsed with a duty cycle of 0 - 100 % and a pulse frequency of 10 - 230 Hz. For a duty cycle of more than 50 % the transformer cascade has to be cooled, either by external ventilation or by the airflow in flight experiments. The device can be partially controlled in flight. Pulse frequency, duty cycle and output voltage can be controlled by analog input signal between 0 and 5 V. It was specifically designed for use on the UAV and weighs only around 340 g. The UAV is able to carry two "GBS Elektronik" Minipuls 0 or 0.1 high voltage generators at the side of the fuselage under the wing, or other generators inside the fuselage. The covering over the Minipuls devices consists of laser-sintered plastic parts with cut-outs for easy access of the potentiometers on the signal generator board and ducts for the ventilation of the devices. The fillet between the last rib of the fuselage frame and the tail boom consists of the same material and has outlet ducts for ventilation. The ducts are in front of the propellers, which increase the air flow by suction. The high voltage is transferred by cables in ductwork to the actuator sections of the wings on each side. Other types of high voltage generators can be carried in the payload segment in the fuselage. The

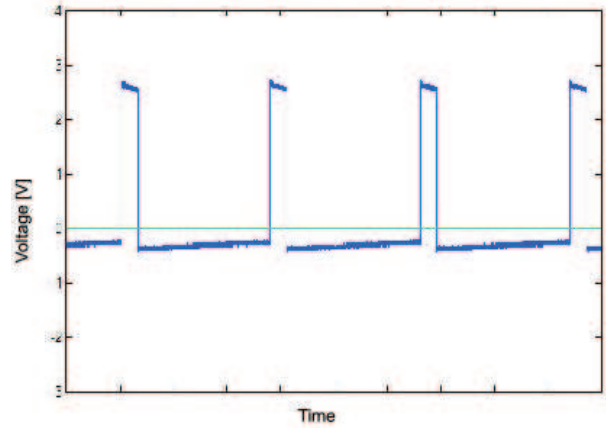


Figure 7: Pulse width modulated servo signal. The servo position is controlled by the length of the pulse, ranging from 1000 to 2000  $\mu$  s. A pulse is sent approximately every 20 ms.

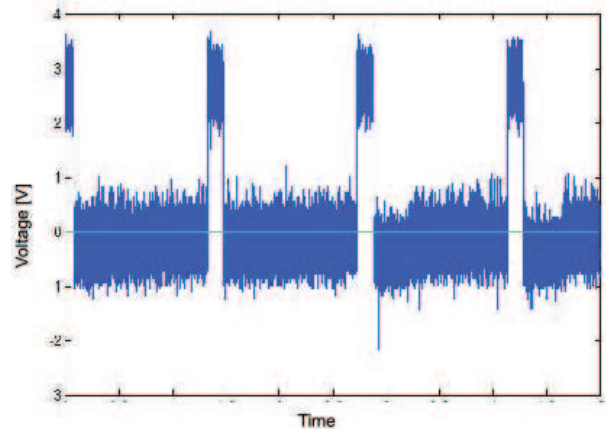


Figure 8: Pulse width modulated servo signal with disturbances introduced by placing the connection cable next to the plasma actuator.

flight control unit is installed in the front of the fuselage, leaving a space of 300x166x166 mm with an opening of 130 mm width on top for HV generators or other equipment. However, since all planned experiments use the Minipuls 0.1 generator, this segment is not in use.

## 3 Experiments

Several partners of the PLASMAERO project are carrying out flight experiments on the UAV platform. The "University of Nottingham" (UNOTT) is investigating the effect of vortex-generating DBD plasma actuator on the trailing edge separation on a NACA 0015 profile. Co- and counter-rotating vortex generators are used to reduce the recirculation zone. The "Instytut Maszyn Przepływowych" (IMP) is also using this profile to test multi-DBD actuator arrangements for separation control. Since the NACA 0015 has no camber, the angle of incidence in this section had to be increased by 3°. Although this leads to an equal lift coefficient as the other wing sections, the profile will encounter flow separation at a much smaller angle of attack. Therefore the stall speed is increased and the plane is very difficult to control at low speeds.



Figure 9: Minipuls 0.1 high voltage generator installed in fuselage.

Due to changes in the German air law in May 2012 an authorization had to be acquired for the UAV. The major problem was to find a suitable airfield for the experiments. Although the TUD owns an airfield in Griesheim, an agreement for the flights there could not be acquired since it is also a nature reserve. Many model aircraft fields in the vicinity are not big enough or are obstructed. Eventually an airfield was found. However, the field has some restrictions and disadvantages. Due to the crowded airspace of the Frankfurt and Egelsbach airports the usable airspace is restricted and the altitude is limited to 100 m above ground level. Additionally the field is relatively small and has a forest on one side, which complicates the landing approaches. The pilot of the UAV is a student employed at the TUD, who is an experienced model aircraft pilot. Also, a representative of the model aircraft field has to be present during the experiments out of safety and regulatory issues.

The experiments can only be conducted under favourable weather conditions. The visibility has to be high enough to clearly see the UAV during the entire flight. The wind and gusts should be weak for the experiments, although the plane is able to fly and was also tested at higher wind velocities. Additionally, the wind has to be from the right direction for the landing approach at the relatively small model airfield.

The first flights were made with different configurations and actuators to test the system and ensure a safe flight with plasma actuation. During the flights the flight control unit was first operated as a passive data recording and monitoring device collecting all available sensor data and remote-control signals. The telemetry system transmitted the data to the ground station where the operator was controlling the system such that the pilot could focus only on flying the UAV.

### 3.1 IMP actuator

The IMP multi-DBD actuator configuration used on the airplane consists of two actuators, each covering half of the span of the wing section. This configuration was chosen due to the restricted power output of the Minipuls 0.1 high voltage supply, each actuator half is driven by one of the Minipuls units on board of the UAV. The actuators consist of several grounded electrodes on top of the dielectric and several floating interelectrodes in-between. The dielectric material used was 300  $\mu\text{m}$  thick Cirlex. Details of the actuator and the tests performed at IMP can be found in [3].

The actuator was installed in a NACA 0015 wing section built for it with a recess of 1 mm depth and 50 mm length, beginning at 40% chord. It was tested using two Minipuls 0.1 power supplies. Various tests were performed to find the maximum power attainable since it is a smaller version than the one used at IMP for the

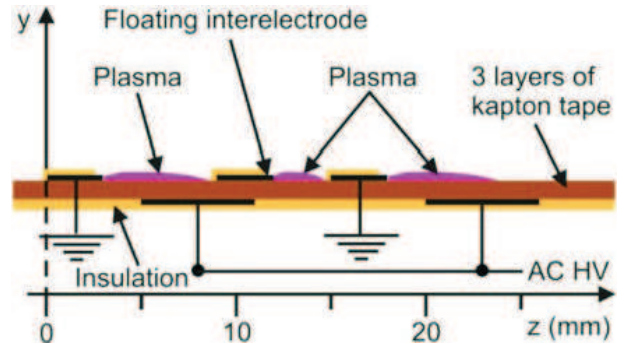


Figure 10: Sketch of IMP multi-DBD actuator configuration. (From [3])

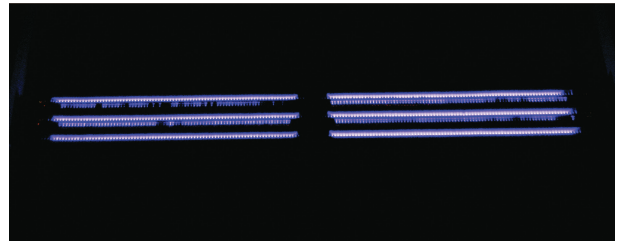


Figure 11: IMP multi-DBD actuator configuration operated by two Minipuls 0.1 high voltage generators.

windtunnel experiments. The specifications of this actuator required 100% duty cycle, also meaning that burst frequency was not a factor. Testing began at a low input voltage of 22 V and was carried forth until reaching 32 V, short of the maximum allowable input voltage on the Minipuls of 35 V. Any input voltage higher than 26.5 V was found sufficient and resulted in both Minipuls and both sides of the actuator to operate at 10 kV at 10 kHz. The IMP actuator arrived at TUD in late October. Due

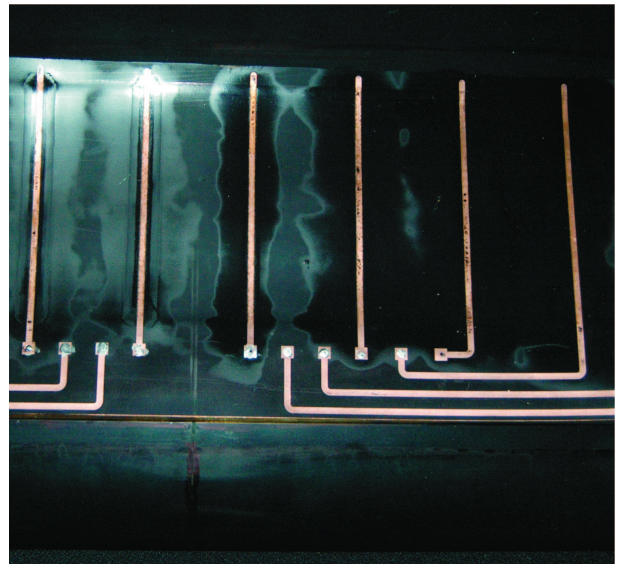


Figure 12: UNOTT vortex generating DBD actuator configuration.

to the arrival of the actuator in late autumn the weather conditions were not favourable and up to date only one test flight could be made. The weather during this flight was relatively windy and gusty. The flight lasted around 10 minutes; during the flight 12 experiments with plasma actuators were conducted.

The pilot attempted to fly at a low speed and rela-

tively high angle of attack and turns on the actuators. A change in lift coefficient on the actuated side of the wing should lead to a roll moment. The pilot can then act against this moment by an aileron control input or let the plane fly a curve. In comparison to this idealized simulation the real situation, suffers from difficult weather conditions during this test flight. Due to the gusty winds the UAV experiences continuously alternating roll rates and the pilot is quite active with the aileron. As a result of the difficult conditions no clear effect of the actuator on the flight mechanical properties could be found.

### 3.2 UNOTT actuator

At the "University of Nottingham" counter-rotating DBD vortex generators were developed for the use on the UAV. The actuator consists of 8 streamwise oriented upper electrodes, which are 45 mm apart from each other. The dielectric material used is 0.25 mm thick Cirlex, covering the grounded electrode which extends across the whole span of the wing segment. The streamwise length of the actuator is 100 mm, extending from 30 to 63% of the chord. Due to the plasma actuator streamwise vortices are generated, entraining the high speed flow from outside into the boundary layer and thereby canceling separation. Details about this actuator configuration and wind tunnel testing can be found in [4].

Due to the late availability of the wing section from UNOTT it was not possible to conduct test flights with this actuator until the end of M39. Additionally the wind tunnel tests of UNOTT were conducted with a different power supply than the Minipuls device. In contrast to the wind tunnel tests with the IMP actuator, a combination of operation voltage and frequency used were not possible to be generated with the Minipuls 0.1. Therefore it was not guaranteed that the same control authority of the actuator on the flow can be achieved. However, preliminary ground tests with the UNOTT-actuator arrays were promising and indicated that similar control authority can be achieved with this generator-actuator combination.

## 4 Conclusion and outlook

The UAV developed during the project is a highly modular system for diverse experiments and flow configurations. The exchangeable wing segments allow the use of different airfoils and flow control configurations. The

first test flight can be considered as a successful conclusion of the project since the UAV has proven to meet all requirements necessary to be able to capture any effect of plasma actuators for flow control in flight. Even the smallest effects on the flight mechanics of the UAV can be captured by numerous sensors without a noticeable interference of the high-voltage system with the measurement equipment. Overall the UAV enables the transfer of successful wind tunnel tests to in-flight experiments under realistic conditions and thereby moving closer to actual applications. Further flight experiments with suitable weather conditions will be conducted in the next months and a thorough data analysis will elaborate detailed information on the flow-control success.

## Acknowledgment

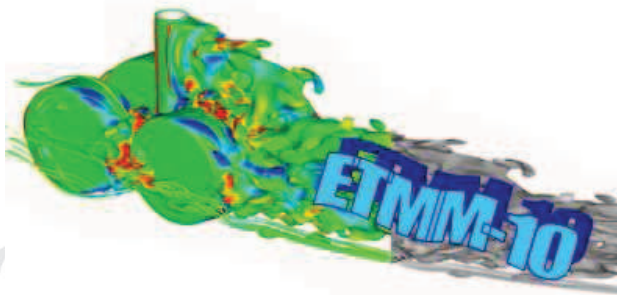
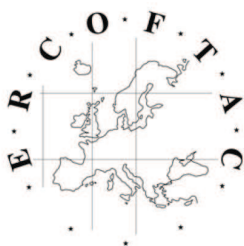
The research leading to these results has received funding from the European Community's Seventh Framework Programme FP7/2007-2013 under grant agreement nr. 234201.

## References

- [1] S. Grundmann, M. Frey, and C. Tropea, "Unmanned Aerial Vehicle (UAV) with Plasma Actuators for Separation Control," in *AIAA-2009-698; 47th AIAA Aerospace Science Meeting; Orlando, Florida, USA, 2009*.
- [2] J. Meyer and A. Strobel, "A Flexible Real-Time Control System for Autonomous Vehicles," in *Proceedings of the joint conference of the 41st International Symposium on Robotics (ISR 2010) and the 6th German Conference on Robotics (ROBOTIK 2010)*, 2010.
- [3] A. Leroy, P. Audier, D. Hong, J. Podlinski, A. Berendt, and J. Mizeraczyk, "Fully Separated Flow Control Using DBD Plasma Actuators Located at the Leading Edge of an Airfoil," *Ercoftac Bulletin*, 2013.
- [4] R. D. Whalley, A. Debien, T. N. Jukes, K.-S. Choi, N. Benard, and E. Moreau, "Trailing-edge separation control of a NACA 0015 airfoil using dielectric-barrier-discharge plasma actuators," in *Proc. Joint ERCOFTAC-PLASMAERO WORKSHOP*, 2012.

## *ERCOFTAC Workshops and Summer Schools*

<b>Title</b>	<b>Location</b>	<b>Date</b>	<b>Organisers</b>	<b>Email addresses</b>
ERCOFTAC Workshop – Direct and Large Eddy Simulation 9	Dresden, Germany	3/04/2013 - 5/04/2013	Fröhlich, J. Giesecke, A.	<a href="mailto:Jochen.Froehlich@tu-dresden.de">Jochen.Froehlich@tu-dresden.de</a>
Design Optimization II : Methods and Applications	Wolfsburg, Germany	10/04/2013 - 11/04/2013	Giannakoglou, K. Haase, W.	<a href="mailto:kgianna@central.ntua.gr">kgianna@central.ntua.gr</a>
2nd ERCOFTAC Workshop "Turbulent flows: Fundamentals and Applications" – workshop	Poitiers, France	15/04/2013 - 16/04/2013	Fortuné, V.	<a href="mailto:veronique.fortune@univ-poitiers.fr">veronique.fortune@univ-poitiers.fr</a>
Non Homogeneous Turbulence in the Atmosphere - International Workshop and course on Environmental Turbulence – summer school	Warsaw, Poland	25/04/2013 - 30/04/2013	Bajer, K.	<a href="mailto:konrad.bajer@fuw.edu.pl">konrad.bajer@fuw.edu.pl</a>
Transition Modelling II – course	Munich, Germany	22/05/2013 - 23/05/2013	Dick, E.	<a href="mailto:richard.seoud-leo@ercofac.org">richard.seoud-leo@ercofac.org</a>
10th ERCOFTAC SIG 33 Workshop	Sandhamn, Sweden	29/05/2013 - 31/05/2013	Hanif, A. Henningson, D.	<a href="mailto:ardeshir.hanifi@foi.se">ardeshir.hanifi@foi.se</a>
Current Status and Future Research Directions in the Development of Immersed Boundary Methods – workshop	Leiden, Netherlands	17/06/2013 – 19/06/2013	Breugem, W.P.	<a href="mailto:w.p.breugem@tudelft.nl">w.p.breugem@tudelft.nl</a>
Unsteady Separation in Fluid-Structure Interaction	Mykonos, Greece	17/06/2013 - 21/06/2013	Braza, M. Bottaro, A.	<a href="mailto:mariana.braza@imif.fr">mariana.braza@imif.fr</a> <a href="mailto:alessandro.bottaro@unige.it">alessandro.bottaro@unige.it</a>
Non-normal and non-linear effects in aero and thermoacoustics	Munich, Germany	18/06/2013 - 21/06/2013	Polifke, W.	<a href="mailto:polifke@td.mw.tum.de">polifke@td.mw.tum.de</a>
3d Heat Flux Burner Workshop – workshop	Lund, Sweden	24/06/2013	De Goey, L.P.H. Hermanns, R. Voss, S.	<a href="mailto:l.m.verhoven@tue.nl">l.m.verhoven@tue.nl</a>
Non-ideal Particles and Aggregates in Complex Flow – summer school	Udine, Italy	24/06/2013 - 28/06/2013	Marchioli, C.	<a href="mailto:marchioli@uniud.it">marchioli@uniud.it</a>
Small scale numerical methods for multiphase flows	Pessac, France	28/08/2013 - 30/08/2013	Vincent, S.	<a href="mailto:vincent@enscbb.fr">vincent@enscbb.fr</a>
J M Burgers Centre Course on Combustion	Eindhoven, The Netherlands	4/11/2013 - 7/11/2013	De Goey, L.P.H. Van Oijen, J.A. Roekaerts, D.	<a href="mailto:l.p.h.d.goey@tue.nl">l.p.h.d.goey@tue.nl</a> <a href="mailto:j.a.v.oijen@tue.nl">j.a.v.oijen@tue.nl</a> <a href="mailto:d.j.e.m.rokaerts@tuedelft.nl">d.j.e.m.rokaerts@tuedelft.nl</a>
4th Wrkshp on Turbulent Combustion Sprays	Cesme-Izmir, Turkey	8/09/2013	Guthelil, E. Masri, A.	<a href="mailto:guthelil@iwr.uni-heidelberg.de">guthelil@iwr.uni-heidelberg.de</a> <a href="mailto:assaad.masri@sydney.edu.au">assaad.masri@sydney.edu.au</a>
Buoyancy Driven Mixing	Cambridge, UK	26/09/2013 - 27/09/2013	Woods, A.	<a href="mailto:andy@bpi.cam.ac.uk">andy@bpi.cam.ac.uk</a>
Biological Fluid Mechanics – course	Delft, The Netherlands	?/10/2013	Poelma, Ch. van de Vosse, F.	<a href="mailto:c.poelma@tudelft.nl">c.poelma@tudelft.nl</a>
10th International ERCOFTAC Symposium on Engineering Turbulence Modelling and Measurements	Marbella, Spain	17/09/2014 - 19/09/2014	Leschziner, M. Rodi, W.	<a href="mailto:fgarcia@eventisimo.com">fgarcia@eventisimo.com</a>



## **ETMM 10**

### **10th International ERCOFTAC Symposium on Engineering Turbulence Modelling and Measurements**

**17 - 19 September 2014**

**Don Carlos Resort, Marbella, Spain**

---

#### **Organizers**

Prof. Michael Leschziner, Chairman, Imperial College  
Prof. Wolfgang Rodi, Co-chairman, Karlsruhe Institute of Technology  
The ETMM Series of Conferences

#### **Aims**

The ETMM series of symposia aims to provide a bridge between researchers and practitioners in Flow, Turbulence and Combustion by reporting progress in the predominantly applied, industrially-oriented areas of turbulence research. This includes the development, improvement and application of statistical closures, simulation methods and experimental techniques for complex flow conditions that are relevant to engineering practice; the modelling of interactions between turbulence and chemistry, dispersed phases and solid structures; and the symbiosis of modelling, simulation and experimental research.

#### **Major Themes**

- Novel modelling and simulation methods for practically relevant turbulent flows, including interaction with heat and mass transfer, rotation, combustion and multi-phase transport
- Novel experimental techniques for flow, turbulence and combustion and new experimental studies and data sets
- Innovative applications of modelling, simulation and experimental techniques to complex flows, industrial configurations and optimisation problems
- High-speed aerodynamics, acoustics and flow control with emphasis on turbulence processes
- Modelling, simulation and measurements of environmental and bio-spherical flows



RECENT TABLE OF CONTENTS OF FLOW TURBULENCE AND COMBUSTION  
AN INTERNATIONAL JOURNAL PUBLISHED BY SPRINGER  
IN ASSOCIATION WITH ERCOFTAC

EDITOR-IN-CHIEF: K. HANJALIĆ

EDITORS: J.J. CHEN, M. REEKS, W. RODI, L. VERVISCH

HONORARY EDITOR: J.C.R HUNT

FOUNDING EDITOR: F. NIEUWSTADT

## VOLUME 90, NUMBER 1, JANUARY 2013

### Explicit Friction Factor Accuracy and Computational Efficiency for Turbulent Flow in Pipes

*H.K. Winning, T. Coole*

### Immersed Boundaries in Large Eddy Simulation of Compressible Flows

*C. Merlin, P. Domingo, L. Vervisch*

### Development of a Low-Reynolds-number k- Model for FENE-P Fluids

*P.R. Resende, F.T. Pinho, B.A. Younis, K. Kim, R. Suresh Kumar*

### Near Field Round Jet Flow Downstream from an Abrupt Contraction Nozzle with Tube Extension

*X. Grandchamp, A. Van Hirtum*

### Characteristics of Oscillations in Supersonic Open Cavity Flows

*H. Wang, M. Sun, N. Qin, H. Wu, Z. Wang*

### Statistical Analysis and a-priori Modelling of Flame Surface Density Transport in Turbulent Stratified Flames: A Direct Numerical Simulation Study

*S.P. Malkeson, N. Chakraborty*

### Stochastic Simulation of Scalar Mixing Capturing Unsteadiness and Small-scale Structure Based on Mean-flow Properties

*S. Sannan, T. Weydahl, A.R. Kerstein*

## VOLUME 90, NUMBER 2, JANUARY 2013

*Special Issue:*

*Recent Advances in Modelling Turbulent Flames*

*Guest Editors: Assaad Masri, Epaminondas Mastorakos*

### Preface

*A.R. Masri, E. Mastorakos*

### Investigation of the TECFLAM Non-premixed Flame Using Large Eddy Simulation and Proper Orthogonal Decomposition

*S. Ayache, E. Mastorakos*

### A-Priori Direct Numerical Simulation Modelling of Co-variance Transport in Turbulent Stratified Flames

*S.P. Malkeson, N. Chakraborty*

### Effect of Partial Premixing on Stabilization and Local Extinction of Turbulent Methane/Air Flames

*E. Baudoïn, X.S. Bai, B. Yan, C. Liu, R. Yu, A. Lantz, S.M. Hosseini, B. Li, A. Elbaz, M. Sami, Z.S. Li, R. Collin, G. Chen, L. Fuchs, M. Aldn, M.S. Mansour*

### Development of Chemistry Coordinate Mapping Approach for Turbulent Partially Premixed Combustion

*M. Jangi, R. Yu, X.-S. Bai*

### Analysis of Algebraic Closures of the Mean Scalar Dissipation Rate of the Progress Variable Applied to Stagnating Turbulent Flames

*H.Q. Dong, V. Robin, A. Mura, M. Champion*

### Turbulent Methane/Air Premixed Flame Structure at High Karlovitz Numbers

*J. Savre, H. Carlsson, X.S. Bai*

### Dynamic Response of Turbulent Low Emission Flames at Different Vortex Breakdown Conditions

*F. Biagioli, B. Paikert, F. Genin, N. Noiray, S. Bernero, K. Syed*

### Joint PDF Closure of Turbulent Premixed Flames

*M.L. Hack, P. Jenny*

### Towards an Extension of TFC Model of Premixed Turbulent Combustion

*V.A. Sabelnikov, A.N. Lipatnikov*

### Transition from Countergradient to Gradient Scalar Transport in Developing Premixed Turbulent Flames

*A.N. Lipatnikov, V.A. Sabelnikov*

### Acetone Droplet Behavior in Reacting and Non Reacting Turbulent Flow

*M. Chrigui, J. Gounder, A. Sadiki, J. Janicka, A.R. Masri*

### Large Eddy Simulation of Reactive Two-Phase Flow in an Aeronautical Multipoint Burner

*G. Hannebique, P. Sierra, E. Riber, B. Cuenot*

---

## ERCOFTAC Special Interest Groups

---

### 1. Large Eddy Simulation

*Geurts, B.J.*  
University of Twente, Holland.  
Tel: +31 534 894 125  
b.j.geurts@utwente.nl

### 4. Turbulence in Compressible Flows

*Dussauge, Jean-Paul*  
IUSTI, Marseille  
jean-paul.dussauge  
@polytech.univmrs.fr

### 5. Environmental Fluid Mechanics

*Armenio, V.*  
Universit di Trieste, Italy.  
Tel: +39 040 558 3472  
Fax: +39 040 572 082  
armenio@dica.units.it

### 10. Transition Modelling

*Dick, E.,*  
University of Ghent, Belgium.  
Tel: +32 926 433 01  
Fax: +32 926 435 86  
erik.dick@ugent.be

### 12. Dispersed Turbulent Two Phase Flows

*Sommerfeld, M.*  
Martin-Luther University, Germany.  
Tel: +49 346 146 2879  
Fax: +49 346 146 2878  
martin.sommerfeld@iw.uni-halle.de

### 14. Stably Stratified and Rotating Flows

*Redondo, J.M.*  
UPC, Spain.  
Tel: +34 934 017 984  
Fax: +34 934 016 090  
redondo@fa.upc.edu

### 15. Turbulence Modelling

*Jakirlic, S.*  
Darmstadt University of Technology, Germany.  
Tel: +49 615 116 3554  
Fax: +49 615 116 4754  
s.jakirlic@sla.tu-darmstadt.de

### 20. Drag Reduction and Flow Control

*Choi, K-S.*  
University of Nottingham, England.  
Tel: +44 115 951 3792  
Fax: +44 115 951 3800  
kwing-so.choi@nottingham.ac.uk

### 24. Variable Density Turbulent Flows

*Anselmet, F.*  
IMST, France.  
Tel: +33 491 505 439  
Fax: +33 491 081 637  
anselmet@irphe.univ-mrs.fr

### 28. Reactive Flows

*Tomboulides, A.*  
University of Western Macedonia.  
Tel: +30 246 105 6630  
Fax: +30 246 105 6631  
atompoulidis@uowm.gr  
ananiast@auth.gr

### 32. Particle Image Velocimetry

*Stanislas, M.*  
Ecole Centrale de Lille, France.  
Tel: +33 320 337 170  
Fax: +33 320 337 169  
Michel.Stanislas@ec-lille.fr

### 33. Transition Mechanisms, Prediction and Control

*Hanifi, A.*  
FOI, Sweden.  
Tel: +46 855 503 197  
Fax: +46 855 503 397  
ardeshir.hanifi@foi.se

### 34. Design Optimisation

*Giannakoglou, K.*  
NTUA, Greece.  
Tel: +30 210 772 1636  
Fax: +30 210 772 3789  
kgianna@central.ntua.gr

### 35. Multipoint Turbulence Structure and Modelling

*Cambon, C.*  
ECL Ecully, France.  
Tel: +33 472 186 161  
Fax: +33 478 647 145  
claude.cambon@ec-lyon.fr

### 36. Swirling Flows

*Braza, M.*  
IMFT, France.  
Tel: +33 534 322 839  
Fax: +33 534 322 992  
braza@imft.fr

### 37. Bio-Fluid Mechanics

*Poelma, C.*  
Delft University of Technology, Holland.  
Tel: +31 152 782 620  
Fax: +31 152 782 947  
c.poelma@tudelft.nl

### 38. Micro-thermofluidics

*Borhani, N.*  
EPFL, Switzerland.  
Tel: +41 216 933 503  
Fax: +41 216 935 960  
navid.borhani@epfl.ch

### 39. Aeroacoustics

*Bailly, C.*  
Ecole Centrale de Lyon, France.  
Tel: +33 472 186 014  
Fax: +33 472 189 143  
christophe.bailly@ec-lyon.fr

### 40. Smoothed Particle Hydrodynamics

*Le Touze, D.*  
Ecole Centrale de Nantes, France  
Tel: +33 240 371 512  
Fax: +33 240 372 523  
David.LeTouze@ec-nantes.fr

### 41. Fluid Structure Interaction

*Longatte, E.*  
EDF, France.  
Tel: +33 130 878 087  
Fax: +33 130 877 727  
elisabeth.longatte@edf.fr

### 42. Synthetic Models in Turbulence

*Nicolleau, F.*  
University of Sheffield, England.  
Tel: +44 114 222 7867  
Fax: +44 114 222 7890  
f.nicolleau@sheffield.ac.uk

### 43. Fibre Suspension Flows

*Prof Lundell, F.*  
The Royal Institute of Technology, Sweden  
frederik@mech.kth.se

### 44. Fundamentals and Applications of Fractal Turbulence

*Fortune, V.*  
Universit de Poitiers, France.  
Tel: +33 549 454 044  
Fax: +33 549 453 663  
veronique.fortune@lea.univ-poitiers.fr

### 45. Uncertainty Quantification in Industrial Analysis and Design

*Meyers, J.*  
Katholieke Universiteit Leuven, Belgium.  
Tel: +32 163 225 02  
Fax: +32 163 229 85  
johan.meyers@mech.kuleuven.be

## ERCOFTAC Pilot Centres

### Alpe - Danube - Adria

*Dr. Gergely Kristóf*  
Department of Fluid Mechanics,  
Budapest University of Technology and  
Economics  
Bertalan L. utca 4-6  
1111 Budapest, Hungary  
Tel: +36 1 463 4073  
Fax: +36 1 463 4072  
kristof@ara.bme.hu

### Belgium

*Geuzaine, P.*  
Cenaero,  
CFD Multi-physics Group,  
Rue des Frères Wright 29,  
B-6041 Gosselies,  
Belgium.  
Tel: +32 71 919 334  
philippe.geuzaine@cenaero.be

### Czech Republic

*Bodnar, T.*  
Institute of Thermomechanics AS CR,  
5 Dolejskova,  
CZ-18200 Praha 8,  
Czech Republic.  
Tel: +420 224 357 548  
Fax: +420 224 920 677  
bodnar@marian.fsik.cvut.cz

### France - Henri Bénard

*Cambon, C.*  
Ecole Centrale de Lyon.  
LMFA, B.P. 163,  
F-69131 Ecully Cedex,  
France.  
Tel: +33 4 72 18 6161  
Fax: +33 4 78 64 7145  
claude.cambon@ec-lyon.fr

### France South

*Braza, M.*  
IMF Toulouse,  
CNRS UMR - 5502,  
Allée du Prof. Camille Soula 1,  
F-31400 Toulouse Cedex, France.  
Tel: +33 534 322 839  
Fax: +33 534 322 992  
Braza@imft.fr

### France West

*Danaila, L.*  
CORIA, University of Rouen,  
Avenue de l'Université BP12,  
76801 Saint Etienne du Rouvray  
France.  
Tel: +33 232 953 702  
luminita.danaila@coria.fr

### Germany North

*Gauger, N.R.*  
Computational Mathematics  
Group  
RWTH Aachen University  
Schinkelstr. 2  
D-52062 Aachen, Germany  
Tel: +49 241 80 98 660  
Fax: +49 241 80 92 600  
gauger@mathcces.rwth-aachen.de

### Germany South

*PD Dr. Ing. Stefan Becker*  
Universität Erlangen, IPAT  
Cauerstr. 4  
91058 Erlangen  
Germany  
Tel: +49 9131 85 29451  
Fax: +49 9131 85 29449  
sb@ipat.uni-erlangen.de

### Greece

*Prof. M. Founti.*  
National Tech. University Of Athens,  
School of Mechanical Engineering,  
Lab. of Steam Boilers and  
Thermal Plants,  
Heroon Polytechniou 9,  
15780 Zografou, Athens, Greece  
Tel: +30 210 772 3605  
Fax: +30 210 772 3663  
mfou@central.ntua.gr

### Iberian East

*Oñate, E.*  
Universitat Politècnica de Catalunya,  
Edificio C-1, Campus Norte,  
Gran Capitan s/n,  
E-08034 Barcelona,  
Spain.  
Tel: +34 93 401 6035  
Fax: +34 93 401 6517  
onate@cimne.upc.es

### Iberian West

*Theofilis, V.*  
Research Professor of Fluid Mechanics  
School of Aerospace Engineering  
Technical University of Madrid (UPM)  
Tel: +34 91 336 3298  
Fax: +34 91 336 3295  
vassilios.theofilis@upm.es

### Italy

*Bottaro, A.*  
DIMSET, Università di Genova,  
Tel: +39 010 353 2540  
alessandro.bottaro@unige.it

### Netherlands

*Ooms, G.*  
J.M. Burgerscentrum,  
National Research School for Fluid  
Mechanics,  
Mekelweg 2,  
NL-2628 CD Delft, Netherlands.  
Tel: +31 15 278 1176  
Fax: +31 15 278 2979  
g.ooms@tudelft.nl

### Nordic

*Wallin, S.*  
Swedish Defence Research Agency FOI,  
Information and Aeronautical Systems,  
S-16490 Stockholm,  
Sweden.  
Tel: +46 8 5550 3184  
Fax: +46 8 5550 3062  
stefan.wallin@foi.se

### Poland

*Rokicki, J.*  
Warsaw University of Technology,  
Inst. of Aeronautics & Applied  
Mechanics,  
ul. Nowowiejska 24,  
PL-00665 Warsaw, Poland.  
Tel: +48 22 234 7444  
Fax: +48 22 622 0901  
jack@meil.pw.edu.pl

### Switzerland

*Prof Thome, J.R.*  
Swiss Federal Institute of Technology  
Lausanne (EPFL),  
Switzerland.  
Tel: +41 216 935 981  
john.thome@epfl.ch

### United Kingdom

*Standingford, D.*  
Zenotech Ltd.  
University Gate East, Park Row,  
Bristol, BS1 5UB  
England.  
Tel: +44 117 302 8251  
Fax: +44 117 302 8007  
david.standingford@zenotech.com



# Best Practice Guidelines for Computational Fluid Dynamics of Dispersed Multi-Phase Flows

## Editors

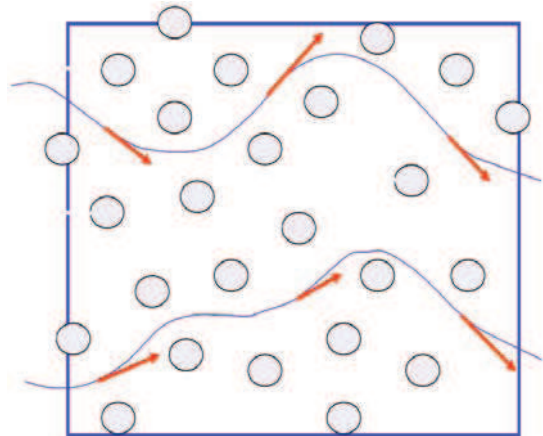
Martin Sommerfeld, Berend van Wachem  
&  
René Oliemans

The simultaneous presence of several different phases in external or internal flows such as gas, liquid and solid is found in daily life, environment and numerous industrial processes. These types of flows are termed multiphase flows, which may exist in different forms depending on the phase distribution. Examples are gas-liquid transportation, crude oil recovery, circulating fluidized beds, sediment transport in rivers, pollutant transport in the atmosphere, cloud formation, fuel injection in engines, bubble column reactors and spray driers for food processing, to name only a few. As a result of the interaction between the different phases such flows are rather complicated and very difficult to describe theoretically. For the design and optimisation of such multiphase systems a detailed understanding of the interfacial transport phenomena is essential. For single-phase flows Computational Fluid Dynamics (CFD) has already a long history and it is nowadays standard in the development of air-planes and cars using different commercially available CFD-tools.

Due to the complex physics involved in multiphase flow the application of CFD in this area is rather young. These guidelines give a survey of the different methods being used for the numerical calculation of turbulent dispersed multiphase flows. The Best Practice Guideline (BPG) on Computational Dispersed Multiphase Flows is a follow-up of the previous ERCOFTAC BPG for Industrial CFD and should be used in combination with it. The potential users are researchers and engineers involved in projects requiring CFD of (wall-bounded) turbulent dispersed multiphase flows with bubbles, drops or particles.

## Table of Contents

1. Introduction
2. Fundamentals
3. Forces acting on particles, droplets and bubbles
4. Computational multiphase fluid dynamics of dispersed flows
5. Specific phenomena and modelling approaches
6. Sources of errors
7. Industrial examples for multiphase flows
8. Checklist of 'Best Practice Advice'
9. Suggestions for future developments



Copies of the Best Practice Guidelines can be acquired electronically from the ERCOFTAC website:

[www.ercoftac.org](http://www.ercoftac.org)

Or from:

ERCOFTAC CADO  
Crown House  
72 Hammersmith Road  
London W14 8TH, United Kingdom

Tel: +44 207 559 1429

Fax: +44 207 559 1428

Email: [Richard.Seoud-ieo@ercoftac.org](mailto:Richard.Seoud-ieo@ercoftac.org)

The price per copy (not including postage) is:

ERCOFTAC members

First copy	Free
Subsequent copies	65 Euros
Students	49 Euros

Non-ERCOFTAC academics	90 Euros
Non-ERCOFTAC industrial	230 Euros